Modelling chemical and transfer processes in a silicon carbide reactor

Brady Metherall
Mansfield College
University of Oxford

A thesis submitted for the degree of
Doctor of Philosophy
Michaelmas 2024

Acknowledgements

First and foremost, I would like to express my gratitude to my supervisors, Chris Breward, Colin Please, and Jim Oliver, for their invaluable guidance, patience, and support throughout this journey. Your insights and expertise have been instrumental in shaping this work. Also, thank you to Cora Cartis for the conversations about optimization, which enhanced my understanding of the subject.

I am also thankful to my industrial supervisors at Elkem ASA—Aasgeir Valderhaug, Anne Gry Messenlein, Harry Reynolds, Ben Sloman, and Jan Inge Meling—for their practical insights and collaboration, which added value to my research.

To my officemates, Matthew and Georgia, your camaraderie, coffee trips, and support have made long days in the office much more enjoyable. I would also like to thank Anna, James, my fellow Cohort 6 members, and everyone in OCIAM and InFoMM for their academic companionship and support.

To Eva and Sophie H., your encouragement and friendship have meant the world to me. Lastly, I am profoundly grateful to my mom for her endless love, belief in me, and unwavering support, without which this journey would not have been possible.

Abstract

Traditional refining of silicon generates carbon dioxide emissions that are released into the atmosphere. An alternative pathway under experimental exploration processes quartz and carbon into silicon carbide. We present mathematical models for the chemical and transfer processes within a silicon carbide reactor. We consider both a single pellet model and multiphase model. We then optimize the the multiphase model for silicon yield.

We first examine a quartz particle coated in a layer of porous carbon as the raw material. We derive governing equations for the key chemical species silicon monoxide, carbon monoxide, and carbon dioxide, along with conservation laws on the surface of the quartz. We reduce our model to an industrially relevant distinguished limit and identify two distinct behaviours: reaction-limited and diffusion-limited. We find that the diffusion-limited regime obtains higher silicon yield and carbon utilization.

We then develop a multiphase model for a homogenous bed of quartz and carbon particles in a laboratory-scale crucible. We model the phases of carbon, silicon carbide, quartz, and the gas mixture. We also consider the motion of the solid, and model the gas flow with Darcy's law. Both analytical and numerical methods are employed to explore the effects of the dimensionless parameters on system behaviour. The dependence of silicon yield, carbon utilization, and maximum pressure on dimensionless parameters is understood through parameter sweeps. We find that a high silicon yield is primarily achieved by balancing the relative speed of the reactions, while maintaining a safe gas pressure requires balancing the ratio of transport to reaction speed.

Finally, we focus on optimizing the multiphase model to maximize silicon yield while maintaining safe pressures. We further examine the parameter space around the optimum point with parameter sweeps and sensitivity analysis. We find that maximizing the speed of the silicon carbide reaction most significantly contributes to a high silicon yield. We then explore the effect of dimensional parameters, such as the initial bed height, on the maximum silicon yield achievable within an industrially relevant timeframe.

Statement of Originality

All of the work that is presented in this thesis has been carried out by the author. The quartz–carbon pellet model presented in Chapter 2 has been published in [1]. Portions of the multiphase model presented in Chapter 3 have been published in [2].

Contents

List of Figures

List of Tables

Chapter 1

Introduction

Silicon is the second most abundant element in the Earth's crust [3]. Silicon naturally occurs in quartz, as silicon dioxide, and is usually obtained by processing quartz, or sometimes quartzite [4]. Elkem ASA is one company involved in the processing of silicon, which is then used in a variety of industries. The silicon can be used for semiconductors for use in electronics such as solar panels, to produce silicone, and also to produce alloys [4]. Quartz is often processed into silicon in a submerged-arc furnace, and similar furnaces are also used for producing ferrosilicon [4], phosphorus [5], and titanium oxide [6]. A typical industrial furnace has a diameter of about 10 m, and a height of about 3 m; we show a schematic of the cross-section of an industrial submerged-arc furnace in Figure 1.1. The furnace is continually filled with a mixture of solid quartz and a form of carbon—usually a combination of charcoal, coal, woodchips, and coke. The quartz and carbon aggregate is called the charge. In the centre of the furnace there are typically three carbon electrodes arranged in a circle [7] that are about 1.2 m in diameter. A large three-phase alternating current passes between the electrodes and the bottom of the furnace. The current heats up the charge due to the charge's resistance and Ohmic heating, and the quartz begins to melt, initiating chemical reactions—some of which produce off-gases. As the quartz melts and the charge is partially converted into gases, a gaseous region around each electrode is formed, called the crater. The crater is the hottest part of the furnace at over 2000 °C. The electric arc continues to pass through the gas-filled crater, with some current also passing through the charge. Furthermore, the electrical effects are coupled to the thermal effects since the conductivity of the charge and crater increase with temperature [8]. Heat generated by the arc is transferred to the charge by radiation and the flow of hot gas out of the crater into the charge [8]. The charge slowly moves down through the furnace replacing what is consumed in the crater.

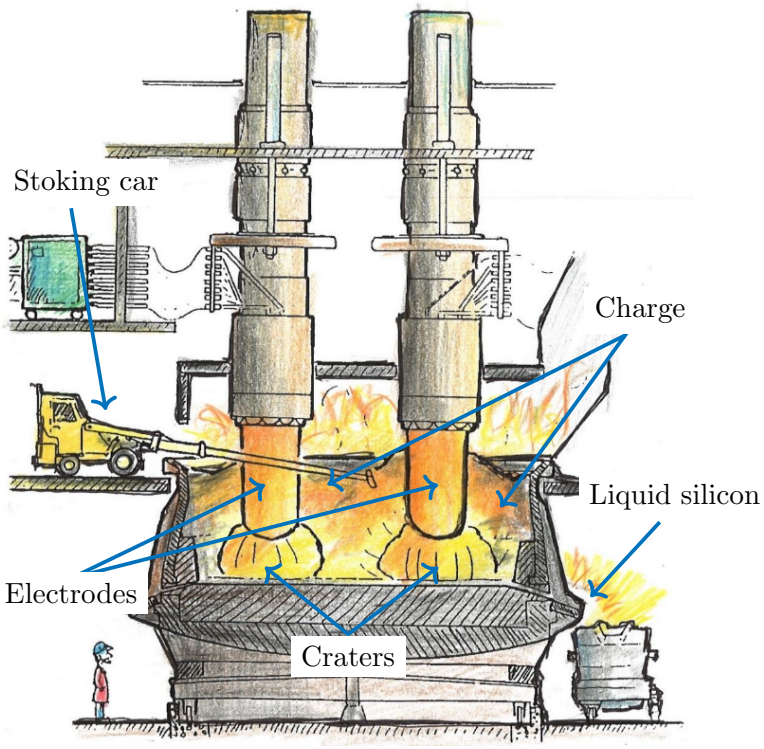

Figure 1.1: Schematic of an industrial furnace, see text for details. Reproduced from [9].

Approximately every 10 to 15 minutes additional charge material is added to the top of the furnace to balance the consumption in the crater.

The main chemical reactions within an industrial silicon furnace, once the quartz has melted, are [10]

$$\mathrm{SiO_2}(l) + \mathrm{C}(s) \longrightarrow \mathrm{SiO}(g) + \mathrm{CO}(g), \tag{1.1}$$

$$\mathrm{SiO}(g) + 2\mathrm{C}(s) \longrightarrow \mathrm{SiC}(s) + \mathrm{CO}(g), \tag{1.2}$$

$$2\mathrm{SiO}(g) \rightleftharpoons \mathrm{SiO_2}(l) + \mathrm{Si}(l), \tag{1.3}$$

$$\mathrm{SiO}(g) + \mathrm{SiC}(s) \longrightarrow 2\mathrm{Si}(l) + \mathrm{CO}(g). \tag{1.4}$$

Initially, the quartz and the carbon react to form silicon monoxide and carbon monoxide. The silicon monoxide is then able to react with carbon to form silicon carbide and additional carbon monoxide, or condense to form liquid quartz and silicon. Finally, the silicon monoxide can also react with silicon carbide to yield liquid silicon and carbon monoxide gas. The liquid silicon is tapped off at the side of the furnace [4, 11–13], and the gaseous silicon monoxide and carbon monoxide vent up through the charge.

As the gases rise through the charge they begin to cool; some of the silicon monoxide condenses on the surface of the charge and forms a viscous liquid of quartz and

silicon by reaction (1.3). This 'condensate' has the potential to limit or stop the venting of the off-gases, which can cause the pressure in the crater to increase to the point of an explosion. The charge is 'stoked' approximately hourly; the charge is broken up manually by a long bar attached to a 'stoking car' to redistribute the charge and create new channels through the charge (see Figure 1.1). The remaining silicon monoxide and carbon monoxide combust once outside of the furnace into silicon dioxide and carbon dioxide, respectively. As the silicon dioxide and carbon dioxide cool further, the silicon dioxide condenses into microsilica, which can be captured and sold to be used to strengthen concrete [4, 14], whereas the carbon dioxide is released into the atmosphere [4]. Metal, and metalloid, factories are among the most intensive and concentrated sources of greenhouse gas emissions in the world [15]. Typically about 6.1–6.5 kg of carbon dioxide is released into the atmosphere for every 1 kg of silicon produced [4]. Moreover, this figure does not take into account the emissions involved in the production of the carbon sources used in the furnace [14]. The main controllable variables are the carbon material used, the carbon to quartz mole ratio of the input charge, and the current through and vertical position of the electrodes. Understanding the underlying physical and chemical effects is required in order to optimize the silicon process. For example, Elkem ASA may want to maximize the production of liquid silicon or microsilica, or to minimize the amount of silicon carbide produced or carbon dioxide emitted. However, taking measurements within an industrial silicon furnace is impractical. The high temperatures within the furnace make it difficult to obtain accurate measurements. Furthermore, the furnaces run continuously, only stopping production for periodic maintenance. The rare stoppages do allow for excavations of the furnace to be analyzed, but these occur after the charge has cooled, so may not be representative of operational furnace behaviour. Elkem ASA use 'pilot furnace process simulators', or pilot furnaces, as one alternative.

1.1 Pilot furnaces

One type of pilot furnace is a cylindrical crucible with an inner height and diameter of about 43 cm and 13 cm, respectively, which is filled with the charge material and heated by an inductive furnace from room temperature. The pilot furnace is heated to a similar temperature as an industrial furnace, then the temperature is held constant for a specified amount of time, and then the inductive heating is turned off and the pilot furnace is allowed to cool down. After the experiment, the pilot furnace is injected with epoxy and the epoxy is allowed to solidify. The slab of epoxy can then

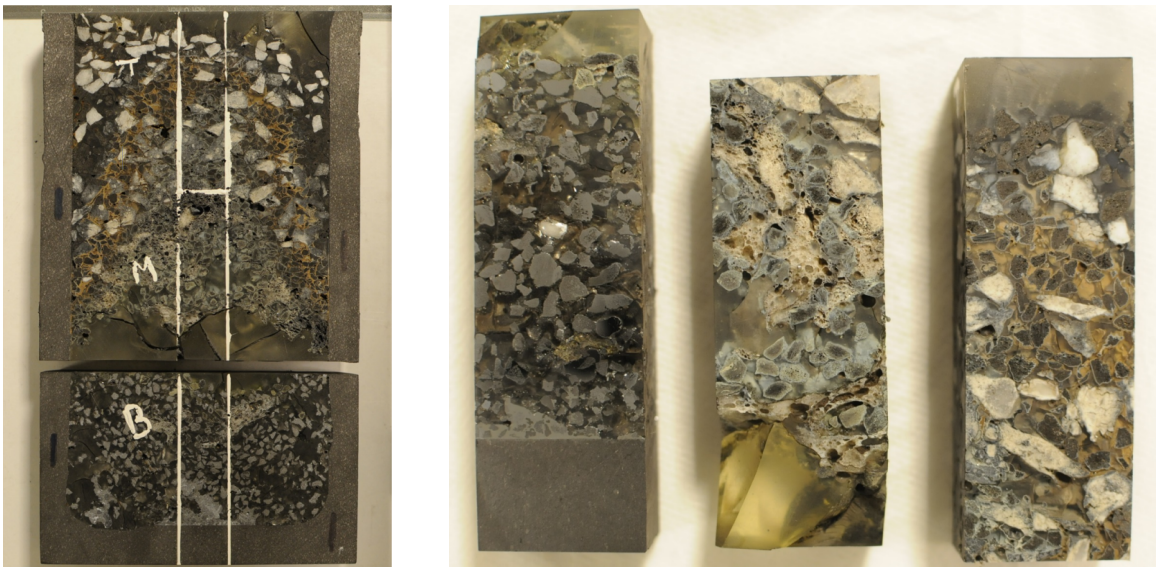

(a) Full pilot furnace cross-section.

(b) Bottom, middle, and top central slices of pilot furnace.

Figure 1.2: This pilot furnace cross-section is about 13 cm in width and 26 cm in height; the slices are about 2.5 cm wide and 9 cm tall. We acknowledge Harald Wegge from Elkem ASA for the photographs.

be cut open to reveal the exact cross-section of the pilot furnace at the end of the experiment. A sample cross-section is shown in Figure 1.2. In this pilot furnace the liquid silicon is not tapped off and instead remains in the crucible. There are no electrical arcs or currents since the furnace is heated by induction, and so the results are not completely representative of an industrial furnace. However, pilot experiments give valuable insight nonetheless. Larger pilot furnaces with different setups are used for various experiments.

1.2 Silicon carbide reactor

Recall that a by-product of the traditional silicon process in a submerged-arc furnace is carbon dioxide, which is released into the atmosphere. In order to reduce, or neutralize, the carbon footprint of silicon production, Elkem ASA is developing alternate reactors for the silicon process.

A possible alternative is a silicon carbide reactor. Quartz and carbon are preprocessed into either quartz–carbon pellets or preprocessed into a homogenous mixture with a prescribed particle size. The quartz and carbon is then added to the silicon carbide reactor to produce silicon carbide. The silicon carbide can then be post-processed efficiently into the final silicon.

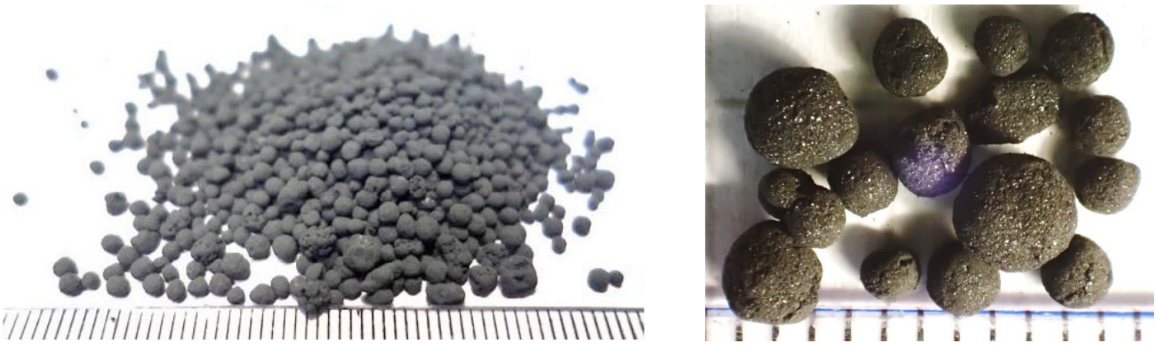

(a) Hatch marks at 1 mm increments. Note these pellets are about 1–3 mm in diameter, whereas the pellets we are interested in are around 400 μm in diameter.

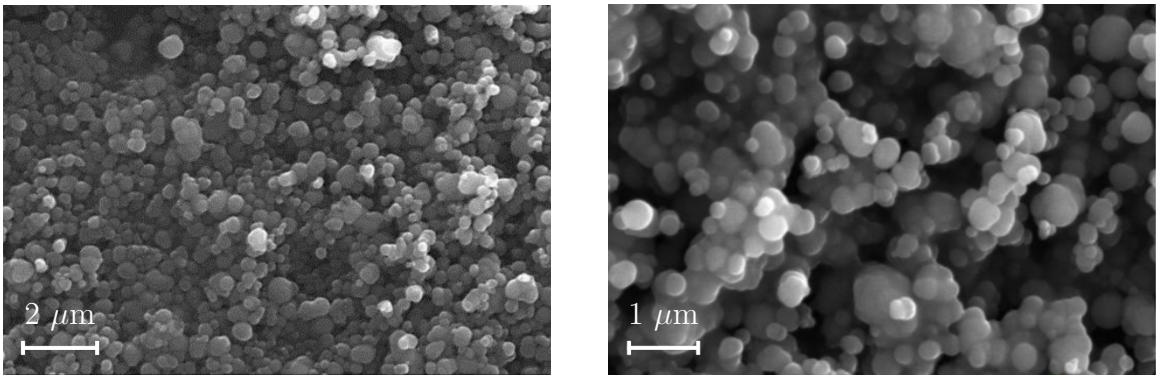

(b) Electron microscope image of carbon black coating.

Figure 1.3: Quartz–carbon pellets. Reproduced with permission from Elkem ASA.

One setup involves granular quartz–carbon pellets, as shown in Figure 1.3. The pellets are created by depositing carbon from renewable methane onto a quartz core [16]. Methane gas has a great reducing capability [15], and has been studied for use as a metal oxide reducing agent. Methane gas has been used to reduce oxides of aluminium, calcium, chromium, iron, magnesium, manganese, titanium, and zinc [15, 17, 18]. More specific to silicon production, cool methane gas has been injected into a furnace to reduce and capture silicon monoxide gas [19]. Also, natural gas (primarily methane) has been used to reduce quartz directly into silicon carbide [20]. Using quartz–carbon pellets potentially improves the energy efficiency, and may significantly decrease greenhouse gas emissions [15]. Moreover, since the carbon layer is deposited by a chemical reaction, the carbon is extremely pure [15, 16], unlike more traditional forms of carbon. Higher purity carbon also allows for higher purity in the final silicon [16].

The deposited carbon forms a porous layer surrounding the solid quartz core. Due to the current method used to deposit the carbon onto the quartz, the thickness of the

carbon layer is about 10 μm regardless of the size of the quartz particle, and the total radius of the quartz–carbon pellets is about 200 μm. We show electron microscope images of the porous carbon layer in Figure 1.3b.

Another alternative approach involves using a bed of a homogeneous mixture comprising small quartz particles and very fine carbon particles. This setup offers some advantages over the quartz–carbon pellets. First, it eliminates the need for the time consuming preprocessing of depositing carbon on the quartz. Second, it is easier to adjust or modify the sizes of the quartz and carbon particles, as well as their ratio, without encountering limitations related to the carbon deposition. Furthermore, the carbon coating can be susceptible to cracking under heating or during experimental conditions, diminishing its effectiveness in trapping silicon monoxide and reducing overall efficiency [21]. In contrast, the homogeneous mixture approach avoids these potential drawbacks associated with carbon coating integrity, offering a potentially more robust and adaptable solution for silicon production processes.

The geometry of the silicon carbide reactor has not yet been decided since it is unclear what would be best. One possibility is essentially a larger version of a pilot reactor. The pellets would be added to a large crucible and converted to silicon carbide. The crucible would then be emptied and the silicon carbide would be refined into silicon elsewhere. In this case, the silicon carbide is produced in large batches. Another option is a continuous setup. The pellets or mixture could be continuously loaded onto a conveyor belt and transported through a furnace. The pellets or mixture would react as they travel through the furnace and silicon carbide would come out. In contrast to the first method, the silicon carbide is produced continuously instead of in discrete batches. Elkem ASA have recently started pilot experiments with the quartz–carbon pellets, and it is not clear which of these two setups would be more beneficial for converting the quartz–carbon pellets to silicon carbide. Due to the infancy of the development of the silicon carbide reactor, mathematical modelling is a cost and time effective tool for making predictions of the dynamics compared to pilot reactor experiments. Mathematical modelling can also help Elkem ASA choose parameter values to optimize particular features of the process such as carbon dioxide emissions or silicon carbide yield.

The silicon carbide reactor is cooler than an industrial silicon furnace, at around 1600 °C, and the set of chemical reactions is different. In this thesis we focus on modelling three particular reactions. The silicon monoxide–carbon reaction,

$$\mathrm{SiO}(g) + 2\mathrm{C}(s) \longrightarrow \mathrm{SiC}(s) + \mathrm{CO}(g), \tag{1.5}$$

the Boudouard reaction,

$$\mathrm{CO_2}(g) + \mathrm{C}(s) \longrightarrow 2\mathrm{CO}(g), \tag{1.6}$$

and the carbon monoxide–quartz surface reaction,

$$\mathrm{SiO_2}(s) + \mathrm{CO}(g) \longrightarrow \mathrm{SiO}(g) + \mathrm{CO_2}(g). \tag{1.7}$$

The reactions (1.5)–(1.7) were initially proposed as the mechanism for the carbothermal reduction of quartz by Lee, Miller, and Cutler [22].

It is uncertain what the initial reaction is at 1600 °C [10]. However some believe

$$\mathrm{SiO_2}(s) + \mathrm{C}(s) \longrightarrow \mathrm{SiO}(g) + \mathrm{CO}(g) \tag{1.8}$$

is the initial reaction [10, 21]. Notice this reaction is the same as (1.1), but the quartz is solid since the melting temperature of quartz is about 1700 °C, depending on the crystalline structure. Reaction (1.8) only happens for a very short time since it is a solid–solid reaction—the two solids lose contact once the first layer of atoms have reacted. The silicon monoxide formed by reaction (1.8) is then able to react with the carbon either as it is transported out of the quartz–carbon pellet or a neighbouring carbon particle, by reaction (1.5). Conversely, the carbon monoxide reacts with the surface of the quartz core via (1.7). Finally, we consider the Boudouard reaction, (1.6), since carbon dioxide will be present in our system owing to (1.7).

Reaction (1.7) is slow, and the Boudouard reaction, (1.6), is limited by reaction (1.7) due to the carbon monoxide. For this reason, reactions (1.5)–(1.7) are sometimes combined to yield the net reaction

$$\mathrm{SiO_2}(s) + 3\mathrm{C}(s) \longrightarrow \mathrm{SiC}(s) + 2\mathrm{CO}(g). \tag{1.9}$$

Reaction (1.9) has been widely studied in the literature [22–34]. In general, the effective reaction rate depends on temperature, particle size, and the removal of the carbon monoxide to prevent side reactions.

1.3 Literature review

Wiik's thesis [10] investigated many of the reactions involving quartz and carbon for silicon processing, and provides a thorough background. Wiik's main focus used

coarse-grain charge particles in crucibles and attempted to understand the reaction mechanisms and reaction kinetics associated with the reactions in an industrial silicon furnace. Wiik performed thermogravity experiments for their simplicity. Thermogravimetric analysis measures the weight change of a sample over a range of temperatures and time. The vacuum thermobalance consisted of a graphite tube-furnace, a vacuum system, a pyrometer to measure temperature, an electronic weighing system, and equipment for mixing gases. An x-ray diffractometer was later used for phase identification. In addition he varied the partial pressure and make-up of the background gas that the experiments were done in, and found that the partial pressure of carbon monoxide and carbon dioxide affect the rate of the reactions. Wiik found that the material of the crucible had an influence on the experiments. Furthermore, he concluded that the carbon monoxide–quartz reaction, (1.7), and the Boudouard reaction, (1.6), were the initial reaction mechanisms between quartz and carbon. His experiments had very little silicon carbide formation, intentionally, and so he concluded that the reactions in the presence of silicon carbide required further study. However, his work was limited to the higher temperatures in a traditional furnace, rather than the lower temperatures in our silicon carbide reactor.

Weimer *et al.* [35] used a dilute flow vertical reactor [36] to study the dynamics of composite particles of quartz and carbon over rapid heating and short timescales. They created spheres approximately 60 μm in diameter made of quartz and carbon particles about 1 μm in diameter, with a slight excess of carbon at a $3.1 : 1$ mole ratio. Weimer *et al.* found that a substantial amount of silicon monoxide exited the reactor. The generation of silicon monoxide gas was deduced to be fast compared to reaction (1.5), the process being limited by the formation of silicon carbide. Finally, they used the simple shrinking core model developed by Yagi and Kunii [37], where a reactant core is converted to a porous product shell, to estimate the intrinsic reaction rate.

Agarwal and Pal [23] used similar composite particles to Weimer *et al.* However, they used carbon black particles about 68 nm in diameter and quartz particles about 10 μm in diameter, which they pressed together into spheres 1.9 cm in diameter using a pressure of over 600 atm. Agarwal and Pal instead found that no silicon monoxide leaked out of the reactor, and that with an excess of carbon and the small particles sizes, nearly all of the quartz was converted into silicon carbide. Furthermore, the overall kinetics depended on the mole ratio of carbon and quartz, the individual particle sizes, the composite particle size, and the pressure used to compress the composite particles.

More recently, Li [21] has studied composite pellets as well as Elkem ASA's quartz–

carbon pellets. Li studied composite particles made with carbon black, charcoal, coke, coal, and pre-heated coal. For the composite pellets the quartz and the carbon were ground into a powder, thoroughly mixed, and bound together with water into particles with a diameter of 1–3 mm. The composite pellets were then dried for 12 hours in an oven to evaporate all of the water. The final composite pellets had a carbon content of about 15% by weight. The experiments for both the composite pellets and the quartz–carbon pellets were conducted with about 5 g of pellets with a temperature between 1625 °C and 1675 °C, a 0.5 L/min. flow of carbon monoxide, and a pressure of 1 atm. He found similar behaviour for each form of carbon, but that the reactivity of carbon black best matched the other reactions, and so carbon black minimized the loss of silicon monoxide and maximized the yield of silicon carbide. Li also investigated the shape and size change of the pellets while the pellets were heated to their final temperature. He found that the particles became more spherical as they were heated and also shrank as the reactions began. Li primarily focused on measuring the mass loss as a function of time for various pellets and background gases, and the final composition after the experiments. Generally, the particles were consumed in a $3 : 1$ ratio of carbon to quartz, in line with (1.9), and each of the carbon coatings behaved similarly. Finally, he fit his data to a simple Arrhenius model to estimate the reaction rates from his experiments. In addition to his thesis, Li published papers focusing on the composite pellets [38], the quartz–carbon pellets [39], and comparisons between the two [40, 41].

1.3.1 Silicon furnace modelling

Owing to the long history and industrial significance of silicon production, modelling and simulating the related processes have been widely studied. This comprehensive research encompasses various aspects of the production process, from the behaviour of electrodes to the optimization of heat and mass transfer in industrial furnaces.

Heat and mass transport, along with chemical processes, are modelled and studied in the thesis [42] and in the papers [43–46]. Specific areas of focus include reactions and transport, as well as asymptotic analysis of a vertical slice of a silicon furnace [43, 44], a grain model for an aggregate of quartz and carbon [45], and the flow and melting of the charge [46]. Additionally, energy balances within the furnace crater have been studied in [47–49].

Some silicon monoxide is lost due to its transport out of the crater and up through the charge, typically combusting into microsilica, which has historically been a major

source of air pollution [4]. However, microsilica has since found applications in the concrete and oil industries [50, 51]. Between 10% and 25% of the initial silicon in quartz is converted into microsilica [50]. Therefore, modelling the formation of microsilica as silicon monoxide cools and combusts is important. The formation, growth, and transport of microsilica have been studied in the thesis [14] and associated paper [52].

The electrodes used in an industrial furnace are primarily made of carbon. Due to the high temperatures and their carbon composition, these electrodes are continuously consumed within the crater. Consequently, the electrodes are continuously formed higher up from a paste, which bakes due to the furnace's high temperature [53, 54]. Understanding the softening and baking processes is essential to ensure that the electrodes achieve optimal, and uniform, material properties [55, 56]. The temperature distribution within the electrodes has been studied to understand the effects of temperature on material properties [54, 57, 58]. Mathematical models of the electrodes include the segregation model [59], the briquette model [60], the thermo-electrical stability model [61], and the baking model [62]. Additionally, time-dependent and steady-state solutions for the flow and temperature have been explored in the thesis [63].

The electrical properties and currents within the crater significantly impact the silicon production process. The electrical system and control processes have been studied in the thesis [7] and through equivalent-circuit models [7, 64]. Additionally, the electromagnetic fields in a furnace have been simulated in two and three dimensions [65–68]. Magnetohydrodynamics and computational fluid dynamics simulations have also been conducted, assuming a compressible, turbulent flow [69–71]. However, these studies often neglect the coupling of the electrical and thermal systems to the chemical processes. This coupling has been explored in the thesis [8] and associated papers [72–75].

The consumption of the charge induces a downward motion of the solid charge material in the furnace. Simultaneously, net gas production and high temperatures in the crater create an upward flow of hot gas, resulting in a counter-current flow within the charge material. Counter-current flows are common in various industrial settings, such as urology [76], bioreactors [77], separation of chemicals [78], blood flow [79], coolant systems [80], catalytic converters [81], filtration combustion [82], and rocket fuel combustion [83].

Compressible gas flow in narrow channels also has been studied for applications to blast furnaces [84], cooling systems for superconducting magnets [85], carbon dioxide

capture [86], and micro-fluidic devices [87]. Additionally, the hot gas can react with the surfaces of the charge channels by reaction (1.3). Models of multi-component gases reacting with channel walls [88, 89] is therefore useful for understanding this process. Furthermore, a model for the counter-current flow and gas dynamics within the charge material, assuming an idealized channel microstructure, is studied in the thesis [90].

Similar heat and mass transfer models have also been applied to other metallurgical processes, such as the dissolution of an alumina particle in a cryolite bath [91].

As we develop mathematical models we will review the most relevant literature as we progress.

1.4 Thesis outline

In Chapter 2, we consider a single quartz–carbon pellet. We derive governing equations for the concentration of silicon monoxide, carbon monoxide, and carbon dioxide, and conservation equations on the moving quartz interface. We then focus on a reduced model in an industrially relevant distinguished limit, and solve numerically the resulting leading-order system. We show examples of reaction-limited behaviour as well as diffusion-limited behaviour. Both regimes are physically admissible due to the large potential range of the parameters. Finally, we sweep through the parameter space, and characterize the dynamics based on the utilization of the carbon and the silicon yield. We find that the diffusion-limited regime is best for carbon utilization and silicon yield, as the silicon monoxide reacts with the carbon before it is transported out of the pellet.

In Chapter 3, we consider a bed comprising a mixture of quartz and carbon particles and derive multiphase governing equations for the system, including the phases of carbon, quartz, silicon carbide, and gas. Within the gas phase, we account for silicon monoxide, carbon monoxide, and carbon dioxide. Additionally, we consider the pressure-driven flow of the gas using Darcy's law and the ideal gas law. The motion of the solid phase, resulting from the consumption and net decrease in volume, is also taken into account. The model is then non-dimensionalized for further analysis. We explore two paradigm problems: a one-reaction system with solid advection and a three-reaction system representative of our chemistry. Both analytical and numerical analysis of these paradigm problems are conducted. Finally, we solve numerically the full model in a physically relevant parameter region and perform parameter sweeps to better understand how the dimensionless parameters affect carbon utilization, silicon

yield, consumption time, and maximum pressure.

In Chapter 4, we optimize the multiphase model developed in Chapter 3. We begin with a brief introduction to optimization methods, focusing on those most appropriate for our problem. Our primary goal is to optimize silicon yield within the parameter space for physically relevant maximum pressures of 1.2 and 3.0 atm. We perform parameter sweeps around these optimum points and compute the Hessian matrix to understand the sensitivity of the dimensionless parameters, identifying which parameters have the largest effect on the objective near the optimum. We conduct dimensional parameter sweeps on the most relevant parameters, such as initial bed height. This approach introduces constraints on the dimensionless parameters, thereby reducing the feasible region of the parameter space. This analysis reveals how parameters, such as the height of the bed of particles or its permeability, affect the maximum silicon yield achievable.

In Chapter 5, we summarize the key findings from the quartz–carbon system, highlighting the insights gained from the single pellet model, the multiphase bed model, and the subsequent optimization studies. We emphasize the importance of the diffusion-limited regime for maximizing carbon utilization and silicon yield. Additionally, we discuss the implications of our optimization results, noting how specific parameters such as bed height and permeability influence the outcomes. Looking forward, we propose potential avenues for future work, including experimental validation of our models and further refinement of the optimization techniques to enhance industrial applicability.

Chapter 2

Single pellet model

In this chapter, we will model the mass transfer within a single quartz–carbon pellet to estimate the consumption of the carbon and the conversion of quartz to silicon carbide to predict the efficiency. We will present a mathematical model of the chemical reactions and transport, and then non-dimensionalize the model in Section 2.1. We will then reduce the model by considering a physically relevant regime in Section 2.2. The resulting simplified model allows us to partially solve the model analytically. We will explore the simplified model to understand the reaction-limited and diffusion-limited behaviour in Section 2.3. We will then investigate sweeps of the parameter space to better understand the transition between the reaction-limited and diffusion-limited behaviour. Furthermore, we will quantify the behaviour by evaluating how much of the initial carbon is consumed, as well as how much of the initial quartz is converted to silicon carbide. Finally, we will summarize our results and give our concluding thoughts in Section 2.4.

2.1 Mathematical model

We consider an idealized case of an isolated spherical quartz particle with a concentric, porous carbon shell surrounding the quartz, as shown in Figure 2.1. Our geometry consists of three spatial domains. Initially, a solid, impermeable quartz core of radius $r = R_1$ is surrounded by a porous carbon layer, extending from $r = R_1$ to $r = R_2$. We neglect the effect of gravity, since we wish to maintain the critical spherical symmetry. We assume all regions initially contain an inert gas (such as nitrogen or argon [10, 24, 33, 35]) and some externally supplied carbon monoxide with a concentration of c_0. In order to sustain the reactions, we continue to provide the external source of carbon monoxide in the far-field. As time progresses, the carbon monoxide–quartz

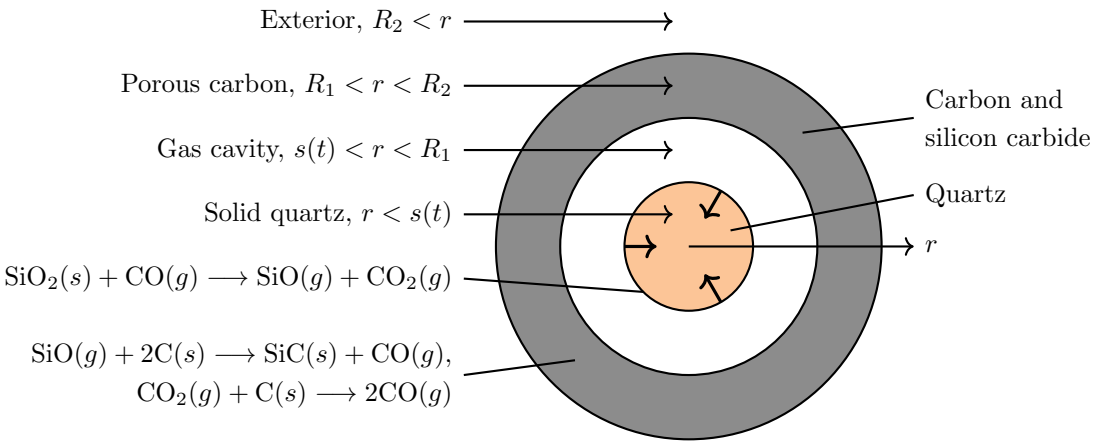

Figure 2.1: Cross-section of a single, spherically symmetric, quartz–carbon pellet. A quartz core is initially surrounded by a porous carbon layer and the gaseous exterior. The quartz core shrinks owing to reaction (1.7), creating an internal gaseous region in the pellet between the quartz and the carbon.

reaction, (1.7), consumes the quartz core—reducing the size—and we denote the resulting radius of the quartz core by $r = s(t)$. As the radius of the quartz shrinks, an interior gaseous cavity is formed in the region $s(t) < r < R_1$.

We assume the gas mixture contains four components: silicon monoxide, carbon monoxide, carbon dioxide, and inert nitrogen. We denote the gaseous concentration of silicon monoxide by C_{SiO}, carbon monoxide by C_{CO}, and carbon dioxide by $C_{\mathrm{CO_2}}$, each with units of mol / m^3 *of gas*. Furthermore, we assume that the gas mixture is dominated by the inert gas in the sense that the inert gas concentration is much larger than the concentrations of the other gases. Thus, it is reasonable to assume the gas mixture has constant density.

For simplicity we assume the system is isothermal, since the pellet's relatively small size suggests that the temperature will be uniform throughout the pellet, and for simplicity we assume that the temperature remains constant.

In the exterior of the pellet, $r > R_2$, the assumed spherical symmetry implies conservation of mass for each of the reactive species reads

$$\frac{\partial C^E_{\mathrm{SiO}}}{\partial t} + \frac{1}{r^2}\frac{\partial}{\partial r}\left(r^2 q^E_{\mathrm{SiO}}\right) = 0, \tag{2.1}$$

$$\frac{\partial C^E_{\mathrm{CO}}}{\partial t} + \frac{1}{r^2}\frac{\partial}{\partial r}\left(r^2 q^E_{\mathrm{CO}}\right) = 0, \tag{2.2}$$

$$\frac{\partial C^E_{\mathrm{CO_2}}}{\partial t} + \frac{1}{r^2}\frac{\partial}{\partial r}\left(r^2 q^E_{\mathrm{CO_2}}\right) = 0, \tag{2.3}$$

where the fluxes q_i^E are defined to be [92, 93]

$$q_i^E = u^E C_i^E - \mathscr{D}_i \frac{\partial C_i^E}{\partial r} \tag{2.4}$$

for $i \in \{\text{SiO, CO, CO}_2\}$; here u^E is the radial mass-averaged speed of the gas mixture, and $\mathscr{D}_i$ is the diffusivity of species i in nitrogen, which we take to be constant. The superscript E on the dependent variables is to make it clear these quantities are defined in the exterior region, $r > R_2$. Instead of directly modelling the concentration of the inert gas, we appeal to conservation of total mass of the gas and the assumption of constant density, and write down

$$\frac{1}{r^2}\frac{\partial}{\partial r}\left(r^2 u^E\right) = 0. \tag{2.5}$$

In the gap between the quartz and carbon, $s(t) < r < R_1$, which we call the gas cavity, we have the same dynamics as in the exterior, and hence, our model in the gas cavity is identical to (2.1)–(2.5), but with the superscript I, for interior gas cavity, labelling the dependent variables.

Within the porous layer the silicon monoxide–carbon reaction, (1.5), and the Boudouard reaction, (1.6), take place. The expressions representing conservation of mass in the porous layer, $R_1 < r < R_2$, are given by

$$\frac{\partial}{\partial t}(\phi C_{\text{SiO}}^P) + \frac{1}{r^2}\frac{\partial}{\partial r}\left(r^2 q_{\text{SiO}}^P\right) = -\mathscr{R}_1, \tag{2.6}$$

$$\frac{\partial}{\partial t}(\phi C_{\text{CO}}^P) + \frac{1}{r^2}\frac{\partial}{\partial r}\left(r^2 q_{\text{CO}}^P\right) = \mathscr{R}_1 + 2\mathscr{R}_2, \tag{2.7}$$

$$\frac{\partial}{\partial t}\left(\phi C_{\text{CO}_2}^P\right) + \frac{1}{r^2}\frac{\partial}{\partial r}\left(r^2 q_{\text{CO}_2}^P\right) = -\mathscr{R}_2, \tag{2.8}$$

$$\rho_0\left(\frac{\partial \phi}{\partial t} + \frac{1}{r^2}\frac{\partial}{\partial r}\left(r^2 u^P \phi\right)\right) = -m_{\text{SiO}}\mathscr{R}_1 + m_{\text{CO}}(\mathscr{R}_1 + 2\mathscr{R}_2) - m_{\text{CO}_2}\mathscr{R}_2, \tag{2.9}$$

where ϕ is the porosity of the porous layer, ρ_0 is the density of the gas and the intrinsic fluxes q_i^P are defined to be [94, 95]

$$q_i^P = u^P \phi C_i^P - \mathscr{D}_i^p \phi \frac{\partial C_i^P}{\partial r}. \tag{2.10}$$

The superscript P denotes these quantities are defined in the porous layer. Since C_{SiO}^P is measured in mol m^{-3} *of gas*, ϕC_{SiO}^P is the extrinsic concentration of silicon monoxide per unit volume of porous media (in mol / m^3). Here, $\mathscr{R}_1$ and $\mathscr{R}_2$ are the reaction rates of the silicon monoxide–carbon reaction, (1.5), and of the Boudouard reaction,

(1.6), respectively—we will specify constitutive laws for the rates in Section 2.1.2—and $\mathscr{D}_i^p$ is the diffusivity of species i in the void space of the porous medium, which we again assume to be constant. On the scale of the pores within the porous medium, we consider reactions (1.5) and (1.6) to be surface reactions. However, since the reactions take place throughout the porous medium, we consider $\mathscr{R}_1$ and $\mathscr{R}_2$ to be bulk reactions on the scale of the porous medium.

Within the solid phase of the porous layer, we assume the carbon and silicon carbide are immobile, and that any volume change due to reaction (1.5) results in a change in porosity the porous medium. It then follows that conservation of mass simply reads

$$\frac{\partial}{\partial t}((1-\phi)C_{\mathrm{C}}) = -2\mathscr{R}_1 - \mathscr{R}_2, \tag{2.11}$$

$$\frac{\partial}{\partial t}((1-\phi)C_{\mathrm{SiC}}) = \mathscr{R}_1, \tag{2.12}$$

where C_{C} and C_{SiC} are the concentration of carbon and silicon carbide in mol / m^3 *of solid*, respectively. We note that $(1-\phi)C_{\mathrm{C}}$ is the extrinsic concentration of carbon per volume of porous media and since the solid is made of only carbon and silicon carbide, we have

$$\frac{m_{\mathrm{C}}}{\rho_{\mathrm{C}}}C_{\mathrm{C}} + \frac{m_{\mathrm{SiC}}}{\rho_{\mathrm{SiC}}}C_{\mathrm{SiC}} = 1, \tag{2.13}$$

where m_{C} and m_{SiC} are the molar mass of carbon and silicon carbide, respectively, and ρ_{C} and ρ_{SiC} are the density of carbon and silicon carbide, respectively. Multiplying (2.13) by $1-\phi$, and taking the time derivative, we find

$$\frac{\partial \phi}{\partial t} = \frac{m_{\mathrm{C}}}{\rho_{\mathrm{C}}}\left(-\mathscr{R}_1\left(\frac{m_{\mathrm{SiC}}}{m_{\mathrm{C}}}\frac{\rho_{\mathrm{C}}}{\rho_{\mathrm{SiC}}} - 2\right) + \mathscr{R}_2\right), \tag{2.14}$$

by (2.11) and (2.12). The $\mathscr{R}_1$ term represents the difference in volume caused when two carbon atoms are replaced by one silicon carbide molecule, while the $\mathscr{R}_2$ term is the volume lost owing to the Boudouard reaction. We neglect any structural issues that may arise in the limit $\phi \to 1$. There may be some maximum porosity, $\phi_{\max} < 1$, above which, the carbon layer disintegrates. Additionally, in our numerical implementation, we will use (2.14) in place of (2.12), and use (2.13) to find the concentration of silicon carbide *a posteriori*.

We note that we assume the thickness of the porous layer is constant. As the carbon is consumed, some of the carbon is replaced by silicon carbide. As a result,

the region $R_1 \leq r \leq R_2$ maintains the same thickness, with a different porosity. Thus, this region is porous with $\phi < 1$, even if the carbon consumption is concentrated at the boundaries. Experimental evidence has shown the thickness does not vary.

2.1.1 Boundary conditions

We recall that we denote the boundary of the solid quartz core by $r = s(t)$, and the inner and outer boundary of the porous layer by $r = R_1$ and $r = R_2$, respectively. As $r \to \infty$, we assume the concentration of carbon monoxide approaches a constant, and the concentrations of silicon monoxide and carbon dioxide tend to zero, so that

$$C^E_{\mathrm{SiO}} \to 0, \quad C^E_{\mathrm{CO}} \to c_0, \quad C^E_{\mathrm{CO_2}} \to 0 \quad \text{as } r \to \infty, \tag{2.15}$$

where c_0 is the concentration of the external supply of carbon monoxide.

On the interface between the exterior and the porous layer we assume the concentrations are continuous, so that

$$C^E_{\mathrm{SiO}} = C^P_{\mathrm{SiO}}, \quad C^E_{\mathrm{CO}} = C^P_{\mathrm{CO}}, \quad C^E_{\mathrm{CO_2}} = C^P_{\mathrm{CO_2}} \quad \text{on } r = R_2. \tag{2.16}$$

We also assume continuity of flux of silicon monoxide, carbon monoxide, carbon dioxide, and mass, so that

$$q^E_{\mathrm{SiO}} = q^P_{\mathrm{SiO}}, \quad q^E_{\mathrm{CO}} = q^P_{\mathrm{CO}}, \quad q^E_{\mathrm{CO_2}} = q^P_{\mathrm{CO_2}}, \quad u^E = \phi u^P \quad \text{on } r = R_2. \tag{2.17}$$

Similarly, on $r = R_1$, the boundary between the gas cavity of the pellet and the porous layer, we have analogous boundary conditions to (2.16) and (2.17).

On $r = s(t)$, the quartz interface, we consider the effect of the carbon monoxide–quartz reaction, (1.7). We assume no gas enters the solid quartz core, and so the five boundary conditions needed are obtained from considering conservation of the three gas species, the total mass of the gas, and the mass of the quartz. Conservation of silicon monoxide relative to the moving interface yields

$$q^I_{\mathrm{SiO}} - \frac{\mathrm{d}s}{\mathrm{d}t} C_{\mathrm{SiO}} = \mathscr{R}_3 \quad \text{on } r = s(t), \tag{2.18}$$

where $\mathscr{R}_3$ is the reaction rate of the carbon monoxide–quartz reaction, (1.7), to be

specified in the following subsection. Similarly, we have the boundary conditions

$$q^I_{\mathrm{CO}} - \frac{\mathrm{d}s}{\mathrm{d}t} C_{\mathrm{CO}} = -\mathscr{R}_3 \qquad \text{on } r = s(t), \tag{2.19}$$

$$q^I_{\mathrm{CO_2}} - \frac{\mathrm{d}s}{\mathrm{d}t} C_{\mathrm{CO_2}} = \mathscr{R}_3 \qquad \text{on } r = s(t), \tag{2.20}$$

$$\left(u^I - \frac{\mathrm{d}s}{\mathrm{d}t}\right)\rho_0 = -\rho_{\mathrm{SiO_2}} \frac{\mathrm{d}s}{\mathrm{d}t} \qquad \text{on } r = s(t) \tag{2.21}$$

for conservation of carbon monoxide, carbon dioxide, and the total gas mass respectively, where $\rho_{\mathrm{SiO_2}}$ is the density of quartz. We note that the right-hand side of (2.19) is negative, since carbon monoxide is consumed by reaction (1.7). The rate that the quartz is consumed is related to the carbon monoxide–quartz reaction, (1.7), by

$$\frac{\rho_{\mathrm{SiO_2}}}{m_{\mathrm{SiO_2}}} \frac{\mathrm{d}s}{\mathrm{d}t} = -\mathscr{R}_3, \tag{2.22}$$

where $m_{\mathrm{SiO_2}}$ is the molar mass of quartz. Unlike the constant thickness of the porous layer, the quartz layer decreases in size. By producing solid silicon carbide, the thickness of the porous layer remains constant, whereas the products of reaction (1.7) are all gaseous, and therefore the quartz shrinks.

2.1.2 Rates of reaction

We now specify the form of the rates of reaction $\mathscr{R}_1$, $\mathscr{R}_2$, and $\mathscr{R}_3$. The particular rates of reaction involving quartz and carbon are complicated and not well understood [10]. For simplicity, we assume reactions (1.5)–(1.7) are elementary reactions, and model the reaction rates with the law of mass action by assuming

$$\mathscr{R}_1 = k_1 \phi C^P_{\mathrm{SiO}} (1 - \phi) C_{\mathrm{C}}, \tag{2.23}$$

$$\mathscr{R}_2 = k_2 \phi C^P_{\mathrm{CO_2}} (1 - \phi) C_{\mathrm{C}}, \tag{2.24}$$

where k_1 and k_2 are the associated rate constants, with units m^3 / (mol s). In reality, k_1 and k_2 will be temperature dependent, however, we assume they are constant by our isothermal assumption. We note that we assume $\mathscr{R}_1$ and $\mathscr{R}_2$ are linear in C_{C} since the rate limiting step is the gas reaching the solid, see [96]. The carbon atoms are densely packed compared to the gas, and so, whenever a silicon monoxide molecule interacts with a carbon atom, there is always an adjacent carbon atom to allow the silicon monoxide–carbon reaction, (1.5), to proceed.

For the carbon monoxide–quartz reaction, (1.7), we assume the form

$$\mathscr{R}_3 = k_3 C^I_{\mathrm{CO}} H(s), \tag{2.25}$$

where k_3 is the associated rate constant, with units m / s, and $H(x)$ is the Heaviside function. We do not explicitly track the quartz concentration in (2.25) since it is constant, and instead is contained in k_3, as is usually done. Once again, in reality k_3 will depend on the temperature, but we assume k_3 is constant. Note, the carbon monoxide–quartz reaction, (1.7), is a surface reaction, whereas reactions (1.5) and (1.6) are bulk reactions. Hence, the Heaviside function is required to turn off the reaction once the quartz has been fully consumed, and we transition from modelling a quartz–carbon pellet to modelling a hollow carbon shell. Once we are in the latter regime, the partial differential equations that were imposed for $s(t) < r < R_1$ must now be imposed on $0 < r < R_1$. The boundary conditions on $r = s(t)$ are then replaced in our symmetric geometry by the condition that the concentrations are bounded and that $u^I \to 0$ as $r \to 0^+$.

2.1.3 Initial conditions

Initially, the quartz core extends to the porous carbon layer, and so

$$s(0) = R_1. \tag{2.26}$$

The solid is taken to be composed entirely of carbon. Thus, at $t = 0$ we have

$$C_{\mathrm{C}} = \frac{\rho_{\mathrm{C}}}{m_{\mathrm{C}}}, \quad C_{\mathrm{SiC}} = 0, \quad \phi = \phi_0 \quad \text{for } R_1 \leq r \leq R_2, \tag{2.27}$$

where ϕ_0 is the initial porosity. We assume no silicon monoxide or carbon dioxide is present in the system initially and the carbon monoxide concentration is uniform, and thus write

$$C_{\mathrm{SiO}} = 0, \quad C_{\mathrm{CO}} = c_0, \quad C_{\mathrm{CO_2}} = 0 \quad \text{for } r > R_1 \tag{2.28}$$

at $t = 0$; we note that these initial concentrations are consistent with the far-field boundary conditions given in (2.15).

Table 2.1: Nominal parameter values. We estimate the density of the gas with the ideal gas law at a temperature of 1600 °C. The values of R_1 and R_2 were provided by Elkem ASA.

Parameter	Description	Range	Value assumed	Units	Ref.
ρ_{C}	Density of carbon	-	2.27×10^3	kg / m^3	[42]
ρ_{SiC}	Density of silicon carbide	-	3.21×10^3	kg / m^3	[42]
$\rho_{\mathrm{SiO_2}}$	Density of quartz	-	2.65×10^3	kg / m^3	[42]
ρ_0	Density of gas[1]	-	0.18	kg / m^3	
m_{C}	Molar mass of carbon	-	12	g / mol	[97]
m_{SiC}	Molar mass of silicon carbide	-	40	g / mol	[97]
$m_{\mathrm{SiO_2}}$	Molar mass of quartz	-	60	g / mol	[97]
m_{SiO}	Molar mass of silicon monoxide	-	44	g / mol	[97]
m_{CO}	Molar mass of carbon monoxide	-	28	g / mol	[97]
$m_{\mathrm{CO_2}}$	Molar mass of carbon dioxide	-	44	g / mol	[97]
m_{bg}	Molar mass of inert gas[1]	-	28	g / mol	[97]
k_1	Rate constant of reaction (1.5)	10^{-3}–1	0.1	m^3 / (mol s)	
k_2	Rate constant of reaction (1.6)	10^{-3}–1	0.1	m^3 / (mol s)	
k_3	Rate constant of reaction (1.7)	10^{-3}–1	0.1	m / s	
$\mathscr{D}$	Diffusion coefficient	10^{-5}–10^{-3}	10^{-4}	m^2 / s	[32, 98]
$\mathscr{D}^p$	Porous diffusion coefficient	10^{-5}–10^{-3}	10^{-4}	m^2 / s	
R_1	Inner radius of carbon layer	50–400	1.6×10^2	μm	
R_2	Outer radius of carbon layer	60–500	2×10^2	μm	
c_0	Initial carbon monoxide concentration	0.064–6.4	0.64	mol / m^3	
ϕ_0	Initial porosity of carbon layer	0.2–0.4	0.3	-	[21]

[1] Assuming the experiment is done in a nitrogen atmosphere.

2.1.4 Parameter values

We now consider typical sizes for our various parameters; the values are given in Table 2.1. The uncertainty of the value of each parameter varies considerably from parameter to parameter. Physical constants, such as the density of carbon or the molar mass of silicon carbide, are accurately known. However, the rate constants are not known experimentally, and their values must be estimated from related experiments. We expect the physical range of the rate constants to be much narrower than reported in Table 2.1, however, we consider this wide range to ensure we capture the correct value in our simulations. In the experiments, the pellets have a total diameter of about 400 μm. However, the radius of the quartz core and the thickness of the carbon layer can be varied. We wish to explore the dynamics over a range of R_1 and R_2 values. The initial carbon monoxide concentration can also easily be varied; we impose a 10% molar concentration.

2.1.5 Dimensionless model

We non-dimensionalize the model (2.1)–(2.28) in the following way. We scale r and s with the outer radius of the pellet,

$$r = R_2\tilde{r}, \quad s = R_2\tilde{s}. \tag{2.29}$$

In each region we scale C_{SiO}, C_{CO}, and $C_{\mathrm{CO_2}}$ by the initial concentration of carbon monoxide, and write

$$C_{\mathrm{SiO}} = c_0\tilde{C}_{\mathrm{SiO}}, \quad C_{\mathrm{CO}} = c_0\tilde{C}_{\mathrm{CO}}, \quad C_{\mathrm{CO_2}} = c_0\tilde{C}_{\mathrm{CO_2}}. \tag{2.30}$$

Multiple possible timescales are embedded in our model. We choose to scale time with the timescale of conversion of carbon to silicon carbide, found by balancing terms in (2.11). We choose the velocity scale to balance the flow generated on the surface of the quartz with the speed of the quartz interface in (2.21), noting that $\rho_{\mathrm{SiO_2}} \gg \rho_0$. We thus write

$$t = \frac{1}{k_1 c_0}\tilde{t}, \quad u = \left(\frac{\rho_{\mathrm{SiO_2}}}{\rho_0} - 1\right) k_1 c_0 R_2 \tilde{u}. \tag{2.31}$$

Finally, we scale the concentrations of carbon and silicon carbide by the initial concentration of carbon, and write

$$C_{\mathrm{C}} = \frac{\rho_{\mathrm{C}}}{m_{\mathrm{C}}}\tilde{C}_{\mathrm{C}}, \quad C_{\mathrm{SiC}} = \frac{\rho_{\mathrm{C}}}{m_{\mathrm{C}}}\tilde{C}_{\mathrm{SiC}}. \tag{2.32}$$

After dropping the tildes, the dimensionless model in the exterior, from (2.1)–(2.5), is

$$\frac{\partial C^E_{\mathrm{SiO}}}{\partial t} + \frac{\mathrm{Da}_{\mathrm{SiO}}}{r^2}\frac{\partial}{\partial r}\big(r^2 q^E_{\mathrm{SiO}}\big) = 0, \tag{2.33}$$

$$\frac{\partial C^E_{\mathrm{CO}}}{\partial t} + \frac{\mathrm{Da}_{\mathrm{CO}}}{r^2}\frac{\partial}{\partial r}\big(r^2 q^E_{\mathrm{CO}}\big) = 0, \tag{2.34}$$

$$\frac{\partial C^E_{\mathrm{CO_2}}}{\partial t} + \frac{\mathrm{Da}_{\mathrm{CO_2}}}{r^2}\frac{\partial}{\partial r}\big(r^2 q^E_{\mathrm{CO_2}}\big) = 0, \tag{2.35}$$

$$\frac{1}{r^2}\frac{\partial}{\partial r}\big(r^2 u^E\big) = 0, \tag{2.36}$$

for $r > 1$, where

$$q^E_i = \mathrm{Pe}_i u^E C^E_i - \frac{\partial C^E_i}{\partial r}, \tag{2.37}$$

$$\mathrm{Da}_i = \frac{\mathscr{D}_i}{k_1 c_0 R_2^2}, \quad \mathrm{Pe}_i = \left(\frac{\rho_{\mathrm{SiO_2}}}{\rho_0} - 1\right)\mathrm{Da}_i^{-1}. \tag{2.38}$$

Here, q^E_i are the dimensionless fluxes, and Da_i and Pe_i are Damköhler numbers [99, 100] and Péclet numbers.

In the interior gas cavity we have analogous equations to (2.33)–(2.36) which hold in the dimensionless region $s(t) < r < s_0$, where

$$s_0 = \frac{R_1}{R_2}. \tag{2.39}$$

In the porous layer, the dimensionless equations for the concentration of carbon and silicon carbide, and the porosity, (2.11), (2.12), and (2.14), respectively, are

$$\frac{\partial}{\partial t}((1-\phi)C_{\mathrm{C}}) = -\phi(1-\phi)C_{\mathrm{C}}(2C^P_{\mathrm{SiO}} + \mathcal{K}C^P_{\mathrm{CO_2}}), \tag{2.40}$$

$$\frac{\partial}{\partial t}((1-\phi)C_{\mathrm{SiC}}) = \phi(1-\phi)C^P_{\mathrm{SiO}}C_{\mathrm{C}}, \tag{2.41}$$

$$\frac{\partial \phi}{\partial t} = \phi(1-\phi)C_{\mathrm{C}}\big(-\mathcal{M}_1 C^P_{\mathrm{SiO}} + \mathcal{K}C^P_{\mathrm{CO_2}}\big), \tag{2.42}$$

which hold in the dimensionless region $s_0 \leq r \leq 1$. We have introduced the two

dimensionless parameters

$$\mathcal{M}_1 = \frac{m_{\mathrm{SiC}}}{m_{\mathrm{C}}}\frac{\rho_{\mathrm{C}}}{\rho_{\mathrm{SiC}}} - 2, \quad \mathcal{K} = \frac{k_2}{k_1}, \tag{2.43}$$

which are the relative volume change when two carbon atoms are replaced by one silicon carbide molecule, and the ratio of the rate constants for the silicon monoxide–carbon reaction, (1.5), and the Boudouard reaction, (1.6), respectively. The equations governing the gas concentrations, (2.6)–(2.8), and continuity of mass, (2.9), become

$$\delta\left(\frac{\partial}{\partial t}(\phi C^P_{\mathrm{SiO}}) + \frac{\mathrm{Da}_{\mathrm{SiO}}}{r^2}\frac{\partial}{\partial r}\big(r^2 q^P_{\mathrm{SiO}}\big)\right) = -\phi(1-\phi)C_{\mathrm{C}}C^P_{\mathrm{SiO}}, \tag{2.44}$$

$$\delta\left(\frac{\partial}{\partial t}(\phi C^P_{\mathrm{CO}}) + \frac{\mathrm{Da}_{\mathrm{CO}}}{r^2}\frac{\partial}{\partial r}\big(r^2 q^P_{\mathrm{CO}}\big)\right) = \phi(1-\phi)C_{\mathrm{C}}\big(C^P_{\mathrm{SiO}} + 2\mathcal{K}C^P_{\mathrm{CO_2}}\big), \tag{2.45}$$

$$\delta\left(\frac{\partial}{\partial t}\big(\phi C^P_{\mathrm{CO_2}}\big) + \frac{\mathrm{Da}_{\mathrm{CO_2}}}{r^2}\frac{\partial}{\partial r}\big(r^2 q^P_{\mathrm{CO_2}}\big)\right) = -\mathcal{K}\phi(1-\phi)C_{\mathrm{C}}C^P_{\mathrm{CO_2}}, \tag{2.46}$$

$$\delta\left(\frac{\partial \phi}{\partial t} + \frac{\mathrm{Da}_{\mathrm{SiO}}\mathrm{Pe}_{\mathrm{SiO}}}{r^2}\frac{\partial}{\partial r}(r^2\phi u^P)\right) = \mathcal{C}\phi(1-\phi)C_{\mathrm{C}}\big(-\mathcal{M}_2 C^P_{\mathrm{SiO}} + \mathcal{M}_3\mathcal{K}C^P_{\mathrm{CO_2}}\big), \tag{2.47}$$

where

$$q^P_i = \mathrm{Pe}_i u^P \phi C^P_i - \mathscr{d}_i \phi \frac{\partial C^P_i}{\partial r}, \tag{2.48}$$

$$\delta = \frac{c_0}{(\rho_{\mathrm{C}}/m_{\mathrm{C}})}, \quad \mathscr{d}_i = \frac{\mathscr{D}^p_i}{\mathscr{D}_i}, \quad \mathcal{C} = \frac{c_0}{(\rho_0/m_{\mathrm{bg}})}, \tag{2.49}$$

$$\mathcal{M}_2 = \frac{m_{\mathrm{SiO}} - m_{\mathrm{CO}}}{m_{\mathrm{bg}}}, \quad \mathcal{M}_3 = \frac{2m_{\mathrm{CO}} - m_{\mathrm{CO_2}}}{m_{\mathrm{bg}}}. \tag{2.50}$$

We have introduced five additional dimensionless parameters. Firstly, δ is the initial concentration ratio of carbon monoxide to carbon. Secondly, the $\mathscr{d}_i$ are the ratios of the diffusivity in the porous layer to that in the interior and exterior. Thirdly, the mole fraction of carbon monoxide in the inert gas is denoted by $\mathcal{C}$. Finally, $\mathcal{M}_2$ and $\mathcal{M}_3$ are the normalized mass differences of the silicon monoxide–carbon reaction, (1.5), and the Boudouard reaction, (1.6), respectively.

2.1.6 Dimensionless boundary conditions

Our far-field boundary conditions, (2.15), become

$$C^E_{\mathrm{SiO}} \to 0, \quad C^E_{\mathrm{CO}} \to 1, \quad C^E_{\mathrm{CO_2}} \to 0 \quad \text{as } r \to \infty. \tag{2.51}$$

On the interface $r = 1$ between the porous media and the exterior environment, (2.16) and (2.17), become

$$C^E_{\mathrm{SiO}} = C^P_{\mathrm{SiO}}, \quad C^E_{\mathrm{CO}} = C^P_{\mathrm{CO}}, \quad C^E_{\mathrm{CO_2}} = C^P_{\mathrm{CO_2}}, \tag{2.52}$$

$$\frac{\partial C^E_{\mathrm{SiO}}}{\partial r} = \cancel{d}_{\mathrm{SiO}}\phi\frac{\partial C^P_{\mathrm{SiO}}}{\partial r}, \quad \frac{\partial C^E_{\mathrm{CO}}}{\partial r} = \cancel{d}_{\mathrm{CO}}\phi\frac{\partial C^P_{\mathrm{CO}}}{\partial r}, \quad \frac{\partial C^E_{\mathrm{CO_2}}}{\partial r} = \cancel{d}_{\mathrm{CO_2}}\phi\frac{\partial C^P_{\mathrm{CO_2}}}{\partial r}, \tag{2.53}$$

$$u^E = \phi u^P. \tag{2.54}$$

Similarly, on the interface $r = s_0$ between the porous media and the gas cavity, we have

$$C^I_{\mathrm{SiO}} = C^P_{\mathrm{SiO}}, \quad C^I_{\mathrm{CO}} = C^P_{\mathrm{CO}}, \quad C^I_{\mathrm{CO_2}} = C^P_{\mathrm{CO_2}}, \tag{2.55}$$

$$\frac{\partial C^I_{\mathrm{SiO}}}{\partial r} = \cancel{d}_{\mathrm{SiO}}\phi\frac{\partial C^P_{\mathrm{SiO}}}{\partial r}, \quad \frac{\partial C^I_{\mathrm{CO}}}{\partial r} = \cancel{d}_{\mathrm{CO}}\phi\frac{\partial C^P_{\mathrm{CO}}}{\partial r}, \quad \frac{\partial C^I_{\mathrm{CO_2}}}{\partial r} = \cancel{d}_{\mathrm{CO_2}}\phi\frac{\partial C^P_{\mathrm{CO_2}}}{\partial r}, \tag{2.56}$$

$$u^I = \phi u^P. \tag{2.57}$$

On the surface of the quartz, $r = s(t)$, boundary conditions (2.18)–(2.21), become

$$q^I_{\mathrm{SiO}} - \mathrm{Da}^{-1}_{\mathrm{SiO}}\frac{\mathrm{d}s}{\mathrm{d}t}C^I_{\mathrm{SiO}} = \mathcal{R}_{\mathrm{SiO}}C^I_{\mathrm{CO}}H(s), \tag{2.58}$$

$$q^I_{\mathrm{CO}} - \mathrm{Da}^{-1}_{\mathrm{CO}}\frac{\mathrm{d}s}{\mathrm{d}t}C^I_{\mathrm{CO}} = -\mathcal{R}_{\mathrm{CO}}C^I_{\mathrm{CO}}H(s), \tag{2.59}$$

$$q^I_{\mathrm{CO_2}} - \mathrm{Da}^{-1}_{\mathrm{CO_2}}\frac{\mathrm{d}s}{\mathrm{d}t}C^I_{\mathrm{CO_2}} = \mathcal{R}_{\mathrm{CO_2}}C^I_{\mathrm{CO}}H(s), \tag{2.60}$$

$$u^I = -\frac{\mathrm{d}s}{\mathrm{d}t}, \tag{2.61}$$

where the constants

$$\mathcal{R}_i = \frac{k_3 R_2}{\mathcal{D}_i} \quad \text{for } i \in \{\mathrm{SiO},\ \mathrm{CO},\ \mathrm{CO_2}\} \tag{2.62}$$

measure how fast the carbon monoxide–quartz reaction, (1.7), proceeds relative to how quickly the gases diffuse on the surface of the quartz. Finally, the quartz consumption rate, (2.22), simply becomes

$$\frac{\mathrm{d}s}{\mathrm{d}t} = -\mathcal{S}C^I_{\mathrm{CO}}H(s), \tag{2.63}$$

where

$$\mathcal{S} = \frac{k_3 m_{\mathrm{SiO_2}}}{k_1 R_2 \rho_{\mathrm{SiO_2}}} \tag{2.64}$$

is proportional to the ratio of the rate constants for the carbon monoxide–quartz reaction, (1.7), and the silicon monoxide–carbon reaction, (1.5).

We note that not all of our dimensionless parameter groups are independent of each other. In particular,

$$\mathrm{Da}_i \,\mathrm{Pe}_i = \left(\frac{\rho_{\mathrm{SiO_2}}}{\rho_0} - 1\right), \quad \frac{\mathcal{S}}{\mathrm{Da}_i \,\mathcal{R}_i} = \frac{c_0}{\rho_{\mathrm{SiO_2}}/m_{\mathrm{SiO_2}}}. \tag{2.65}$$

We consider the gas density ρ_0, the far-field carbon monoxide concentration c_0, and the density and molar mass of quartz to be constant. We thus consider the independent dimensionless parameters to be Da_i, s_0, $\mathcal{K}$, and $\mathcal{S}$, and we determine Pe_i and $\mathcal{R}_i$ by (2.65).

2.1.7 Dimensionless initial conditions

The dimensionless versions of the initial conditions at $t = 0$, from (2.27) and (2.28), are

$$C_{\mathrm{C}} = 1, \qquad C_{\mathrm{SiC}} = 0, \qquad \phi = \phi_0 \qquad \text{for } s_0 \leq r \leq 1, \tag{2.66}$$

$$C_{\mathrm{SiO}} = 0, \qquad C_{\mathrm{CO}} = 1, \qquad C_{\mathrm{CO_2}} = 0 \qquad \text{for } s_0 < r, \tag{2.67}$$

with

$$s(0) = s_0 \tag{2.68}$$

by (2.26).

2.2 Quasi-steady regime

We estimate the values of the dimensionless parameters in Table 2.2. The wide range of some of the parameter values is primarily due to the uncertainty of the rate constants and radius of the pellets. Industrially, the most relevant limit is where the supplied concentration of carbon monoxide is low. Thus, in order to gain insight into the behaviour in an industrially relevant regime, we consider the regime where

Table 2.2: Range of values for the dimensionless parameters. The typical values are computed using the 'value assumed' in Table 2.1.

Parameter	Description	Minimum	Typical	Maximum
$\mathrm{Da}_i = \mathscr{D}_i/(k_1 c_0 R_2^2)$	Damköhler number	10	10^4	10^7
$\mathcal{C} = c_0 m_{\mathrm{bg}}/\rho_0$	Carbon monoxide mole fraction	10^{-4}	0.1	1
$s_0 = R_1/R_2$	Dimensionless quartz radius	0.1	0.8	1
$\mathscr{d}_i = \mathscr{D}_i^p/\mathscr{D}_i$	Diffusivity ratio	0.01	1	1
$\delta = c_0/(\rho_{\mathrm{C}}/m_{\mathrm{C}})$	Initial gas to solid concentration ratio	3×10^{-7}	3×10^{-6}	3×10^{-5}
$\mathcal{K} = k_2/k_1$	Ratio of rate constants for (1.6) and (1.5)	10^{-3}	1	10^3
$\mathcal{S} = k_3 m_{\mathrm{SiO_2}}/(k_1 R_2 \rho_{\mathrm{SiO_2}})$	Dimensionless speed of (1.7)	2×10^{-4}	0.1	2×10^2
$\mathcal{M}_1 = (m_{\mathrm{SiC}}/m_{\mathrm{C}})(\rho_{\mathrm{C}}/\rho_{\mathrm{SiC}}) - 2$	Relative volume change of (1.5)	-	0.36	-
$\mathcal{M}_2 = (m_{\mathrm{SiO}} - m_{\mathrm{CO}})/m_{\mathrm{bg}}$	Normalized mass difference of (1.5)	-	0.57	-
$\mathcal{M}_3 = (2m_{\mathrm{CO}} - m_{\mathrm{CO_2}})/m_{\mathrm{bg}}$	Normalized mass difference of (1.6)	-	0.43	-

$\delta \ll \mathcal{C} \ll 1$. Furthermore, we consider the distinguished limit where each of Pe_i, s_0, $\mathcal{K}$, $\mathscr{d}_i$, $\mathcal{R}_i$ and $\mathcal{S}$ are $\mathcal{O}(1)$, and Da_i is $\mathcal{O}(\delta^{-1})$ to recover the richest possible dynamics. The resulting evolution of the gas concentrations are quasi-steady at leading order. The consumption of the carbon layer and quartz surface remain time dependent. There are three timescales within our system. The short timescale, the timescale that we non-dimensionalized with, and the long timescale. Equilibration of the gas concentrations happens on the short timescale. Due to the density difference between the gases and the solids, the solids do not evolve on the short timescale. On the scale we have chosen to non-dimensionalize the system with, the carbon and quartz is consumed by the reactions and the gas dynamics are quasi-steady. On the long timescale, all of the quartz will be consumed and thus, no silicon monoxide or carbon dioxide will be present in the system. On this scale, the system is static since no quartz remains and there is no silicon monoxide or carbon dioxide to react with any remaining carbon.

We take the limit in which $\mathcal{C} \ll 1$ and $\delta \ll 1$ in (2.33)–(2.36). In the exterior the leading-order quasi-steady model reads

$$\frac{1}{r^2}\frac{\partial}{\partial r}\left(r^2 q^E_{\mathrm{SiO}}\right) = 0, \tag{2.69}$$

$$\frac{1}{r^2}\frac{\partial}{\partial r}\left(r^2 q^E_{\mathrm{CO}}\right) = 0, \tag{2.70}$$

$$\frac{1}{r^2}\frac{\partial}{\partial r}\left(r^2 q^E_{\mathrm{CO_2}}\right) = 0, \tag{2.71}$$

$$\frac{1}{r^2}\frac{\partial}{\partial r}\left(r^2 u^E\right) = 0, \tag{2.72}$$

for $r > 1$; analogous equations hold in the interior gas cavity. The equations (2.40)–(2.42) for the evolution of carbon, silicon carbide, and the porosity remain the same in the limit $\delta \ll 1$. However, (2.44)–(2.47), the conservation equations for the gases in the porous media $s_0 < r < 1$, become

$$\frac{\delta \mathrm{Da}_{\mathrm{SiO}}}{r^2}\frac{\partial}{\partial r}\left(r^2 q^P_{\mathrm{SiO}}\right) = -\phi(1-\phi)C_{\mathrm{C}}C^P_{\mathrm{SiO}}, \tag{2.73}$$

$$\frac{\delta \mathrm{Da}_{\mathrm{CO}}}{r^2}\frac{\partial}{\partial r}\left(r^2 q^P_{\mathrm{CO}}\right) = \phi(1-\phi)C_{\mathrm{C}}\left(C^P_{\mathrm{SiO}} + 2\mathcal{K}C^P_{\mathrm{CO}_2}\right) \tag{2.74}$$

$$\frac{\delta \mathrm{Da}_{\mathrm{CO}_2}}{r^2}\frac{\partial}{\partial r}\left(r^2 q^P_{\mathrm{CO}_2}\right) = -\mathcal{K}\phi(1-\phi)C_{\mathrm{C}}C^P_{\mathrm{CO}_2}, \tag{2.75}$$

$$\frac{1}{r^2}\frac{\partial}{\partial r}\left(r^2 \phi u^P\right) = 0. \tag{2.76}$$

All the boundary conditions remain the same, except the boundary conditions (2.58)–(2.61), which simplify to

$$q^I_{\mathrm{SiO}} = \mathcal{R}_{\mathrm{SiO}}C^I_{\mathrm{CO}}H(s), \tag{2.77}$$

$$q^I_{\mathrm{CO}} = -\mathcal{R}_{\mathrm{CO}}C^I_{\mathrm{CO}}H(s), \tag{2.78}$$

$$q^I_{\mathrm{CO}_2} = \mathcal{R}_{\mathrm{CO}_2}C^I_{\mathrm{CO}}H(s), \tag{2.79}$$

$$u^I = -\frac{\mathrm{d}s}{\mathrm{d}t}. \tag{2.80}$$

2.3 Analysis of the quasi-steady model

We analyze our quasi-steady model assuming $\mathrm{Da}_{\mathrm{SiO}} = \mathrm{Da}_{\mathrm{CO}} = \mathrm{Da}_{\mathrm{CO}_2}$ and $\not{d}_{\mathrm{SiO}} = \not{d}_{\mathrm{CO}} = \not{d}_{\mathrm{CO}_2}$ for simplicity, and so $\mathrm{Pe}_{\mathrm{SiO}} = \mathrm{Pe}_{\mathrm{CO}} = \mathrm{Pe}_{\mathrm{CO}_2}$ and $\mathcal{R}_{\mathrm{SiO}} = \mathcal{R}_{\mathrm{CO}} = \mathcal{R}_{\mathrm{CO}_2}$ as a consequence. The analysis can be done in the general case, however, the manipulation is algebraically tedious and we do not expect the diffusivities to vary greatly among the three gas species. We drop the subscripts in the subsequent analysis. In the gas cavity and exterior of the pellet, we will solve explicitly the simple form of the partial differential equations governing the gas concentrations and, using these analytical expressions, we will reduce the problem to one posed in only the porous layer, with appropriate boundary conditions at $r = s_0$ and $r = 1$. A numerical solution is then required only for $s_0 \le r \le 1$.

We first integrate the gas flow equations, namely (2.72) and its interior analogue,

as well as (2.76), to find

$$u^I = \frac{\alpha(t)}{r^2} \qquad \text{for } s(t) < r < s_0, \tag{2.81}$$

$$u^P = \frac{\alpha(t)}{\phi r^2} \qquad \text{for } s_0 < r < 1, \tag{2.82}$$

$$u^E = \frac{\alpha(t)}{r^2} \qquad \text{for } 1 < r, \tag{2.83}$$

where we have used the boundary conditions (2.54) and (2.57). The velocities are thus determined by $\alpha(t)$, the function of integration interpreted as the time-dependent advective flux induced by the reactions. The $\alpha(t)$ is determined as a part of the solution, found later by (2.93).

We substitute (2.81) and (2.83) into (2.69)–(2.71) to find that the concentration of gases in the gas cavity are

$$C^I_{\mathrm{SiO}}(r,t) = \beta^I_{\mathrm{SiO}}(t) + \gamma^I_{\mathrm{SiO}}(t)\exp(-\alpha(t)\mathrm{Pe}/r), \tag{2.84}$$

$$C^I_{\mathrm{CO}}(r,t) = \beta^I_{\mathrm{CO}}(t) + \gamma^I_{\mathrm{CO}}(t)\exp(-\alpha(t)\mathrm{Pe}/r), \tag{2.85}$$

$$C^I_{\mathrm{CO_2}}(r,t) = \beta^I_{\mathrm{CO_2}}(t) + \gamma^I_{\mathrm{CO_2}}(t)\exp(-\alpha(t)\mathrm{Pe}/r) \tag{2.86}$$

for $s(t) < r < s_0$, while in the exterior they are

$$C^E_{\mathrm{SiO}}(r,t) = \beta^E_{\mathrm{SiO}}(t) + \gamma^E_{\mathrm{SiO}}(t)\exp(-\alpha(t)\mathrm{Pe}/r), \tag{2.87}$$

$$C^E_{\mathrm{CO}}(r,t) = \beta^E_{\mathrm{CO}}(t) + \gamma^E_{\mathrm{CO}}(t)\exp(-\alpha(t)\mathrm{Pe}/r), \tag{2.88}$$

$$C^E_{\mathrm{CO_2}}(r,t) = \beta^E_{\mathrm{CO_2}}(t) + \gamma^E_{\mathrm{CO_2}}(t)\exp(-\alpha(t)\mathrm{Pe}/r) \tag{2.89}$$

for $r > 1$, where the $\beta_i(t)$ and $\gamma_i(t)$ are to be determined. Eliminating $\beta_i(t)$ and $\gamma_i(t)$ using the boundary conditions (2.77)–(2.80) and (2.63), we find that, on the inner surface of the porous media, $r = s_0$, the concentrations of the gases satisfy the conditions

$$\phi\frac{\partial C^P_{\mathrm{SiO}}}{\partial r} = \frac{\alpha(t)\mathrm{Pe}}{s_0^2}\left(C^P_{\mathrm{SiO}} - \frac{\mathcal{R}}{\mathrm{Pe}}\right), \tag{2.90}$$

$$\phi\frac{\partial C^P_{\mathrm{CO}}}{\partial r} = \frac{\alpha(t)\mathrm{Pe}}{s_0^2}\left(C^P_{\mathrm{CO}} + \frac{\mathcal{R}}{\mathrm{Pe}}\right), \tag{2.91}$$

$$\phi\frac{\partial C^P_{\mathrm{CO_2}}}{\partial r} = \frac{\alpha(t)\mathrm{Pe}}{s_0^2}\left(C^P_{\mathrm{CO_2}} - \frac{\mathcal{R}}{\mathrm{Pe}}\right), \tag{2.92}$$

as well as the additional requirement that

$$C_{\mathrm{CO}}^{P} = -\frac{\mathcal{R}}{\mathrm{Pe}} + \left(\frac{\alpha(t)}{s^2} + \frac{\mathcal{R}}{\mathrm{Pe}}\right) \exp\left(\alpha(t)\mathrm{Pe}\left(\frac{1}{s} - \frac{1}{s_0}\right)\right) \tag{2.93}$$

to determine $\alpha(t)$, which may be shown to be unique and non-negative by inverting (2.93). Similarly, on the exterior boundary, $r = 1$, we have

$$\mathcal{d}\phi \frac{\partial C_{\mathrm{SiO}}^{P}}{\partial r} = \frac{\alpha(t)\mathrm{Pe}}{1 - \exp(\alpha(t)\mathrm{Pe})} C_{\mathrm{SiO}}^{P}, \tag{2.94}$$

$$\mathcal{d}\phi \frac{\partial C_{\mathrm{CO}}^{P}}{\partial r} = \frac{\alpha(t)\mathrm{Pe}}{1 - \exp(\alpha(t)\mathrm{Pe})} (C_{\mathrm{CO}}^{P} - 1), \tag{2.95}$$

$$\mathcal{d}\phi \frac{\partial C_{\mathrm{CO_2}}^{P}}{\partial r} = \frac{\alpha(t)\mathrm{Pe}}{1 - \exp(\alpha(t)\mathrm{Pe})} C_{\mathrm{CO_2}}^{P}. \tag{2.96}$$

We have reduced the model to a problem posed in just the porous layer, but we cannot reduce any further the system (2.40), (2.42), (2.63), and (2.73)–(2.75), with boundary conditions (2.90)–(2.96), and initial conditions (2.66) and (2.68). Hence, we seek a numerical solution using the method of lines using second-order central differences in space. This discretization turns the differential equations (2.73)–(2.75), and the boundary conditions (2.90)–(2.96) into a set of algebraic constraints, which combined with (2.40), (2.42), and (2.63), leaves us with a set of differential-algebraic equations (DAEs) to solve. We specify the resulting DAE system in Julia [101, 102], and solve the system with the DAE solver `IDA` of SUNDIALS [103] using adaptive-step time integrations. Furthermore, we use the `ModelingToolkit` package [104] to efficiently and quickly compute the sparse Jacobian.

We first consider the time evolution with the parameters given by the representative values in Table 2.2, shown in Figure 2.2. We find that the carbon monoxide diffuses through the porous layer and reacts with the quartz core. As time goes on, the concentration rises since the reaction with the quartz slows as the carbon monoxide is consumed, and also because carbon monoxide is produced in the porous layer by reactions (1.5) and (1.6). The dynamics of the silicon monoxide is the converse of the carbon monoxide. The concentration of silicon monoxide is largest at $t = 0$, and decreases with time. Less silicon monoxide is produced on the surface of the quartz with time, and the carbon consumes the silicon monoxide by reaction (1.5). Since $\mathcal{K} = 1$, the dynamics of carbon dioxide is identical to silicon monoxide. Overall, there is not a large variation in the concentration of silicon monoxide throughout the porous layer. As such, the carbon is consumed, and silicon carbide is produced,

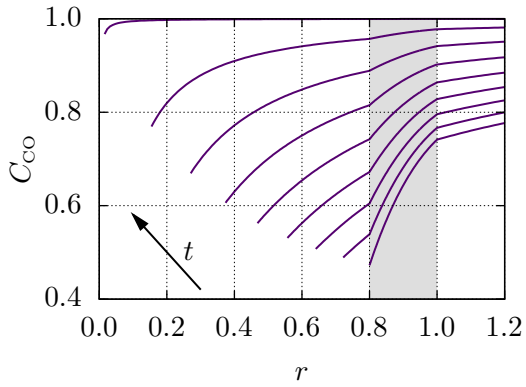

(a) Concentration of carbon monoxide. The shaded region denotes the porous layer.

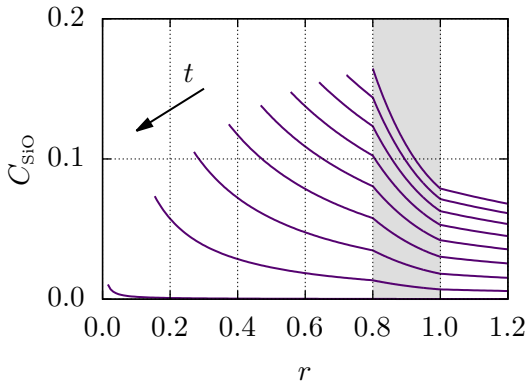

(b) Concentration of silicon monoxide. The shaded region denotes the porous layer.

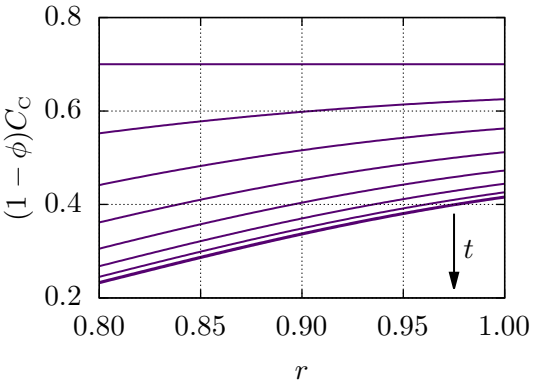

(c) Concentration of carbon.

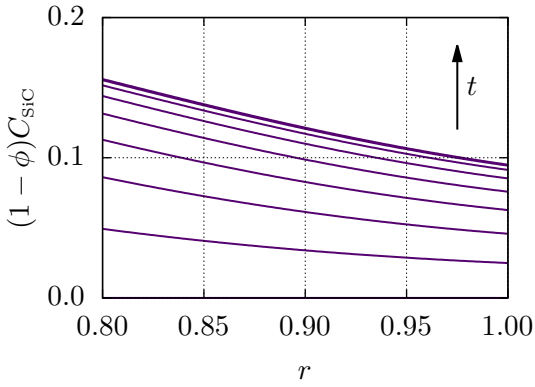

(d) Concentration of silicon carbide.

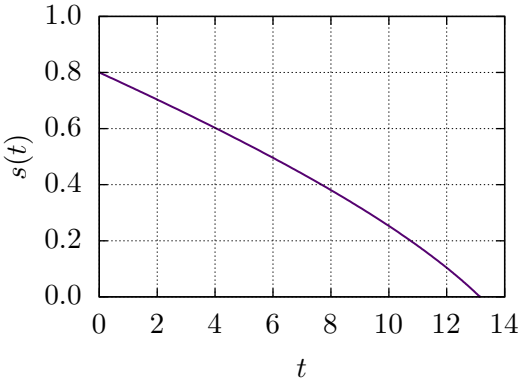

(e) Consumption of the quartz core.

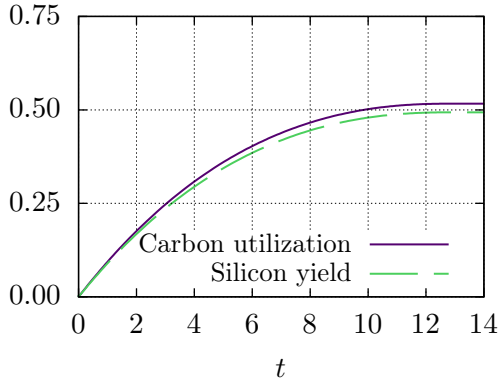

(f) Carbon utilization and silicon yield.

Figure 2.2: Results from the numerical simulation of the reduced system consisting of (2.40), (2.42), (2.63), and (2.73)–(2.75), with boundary conditions (2.90)–(2.96), and initial conditions (2.66) and (2.68). Parameter values taken from Table 2.2.

fairly uniformly. Since the concentration of silicon monoxide is largest at $r = 0.8$, the carbon is consumed, and the silicon carbide is produced, the fastest here. The radius of the quartz core decreases approximately linearly, since there is not a large variation in time of the concentration of carbon monoxide on $r = s(t)$. However, since the concentration of carbon monoxide increases with time, the quartz core shrinks slightly faster as time increases.

In order to better quantify the utilization of the carbon and the production of silicon carbide, we introduce two macroscale metrics. The first metric is the carbon utilization fraction

$$U_{\mathrm{C}}(t) = 1 - \frac{3}{(1-\phi_0)(1-s_0^3)} \int_{s_0}^{1} (1-\phi) C_{\mathrm{C}} r^2 \, \mathrm{d}r, \tag{2.97}$$

which is the normalized amount of carbon used, and is a measure of how much of the initial carbon reacts by either the silicon carbide reaction or the Boudouard reaction. The second metric is the silicon yield

$$Y_{\mathrm{SiC}}(t) = \frac{3 m_{\mathrm{SiO_2}} \rho_{\mathrm{SiC}}}{s_0^3 \rho_{\mathrm{SiO_2}} m_{\mathrm{SiC}}} \int_{s_0}^{1} (1-\phi)(1-C_{\mathrm{C}}) r^2 \, \mathrm{d}r, \tag{2.98}$$

which is the amount of silicon carbide produced normalized by the initial quartz—it is the fraction of the initial quartz that has successfully been converted to silicon carbide. In the example shown in Figure 2.2, $U_{\mathrm{C}} = 0.517$ and $Y_{\mathrm{SiC}} = 0.494$ at the quartz consumption time. Only half of the carbon is used and the rest is wasted, and only half of the quartz is converted to silicon carbide and the rest is lost to silicon monoxide exiting the pellet.

The relative strength of diffusion to the reactions within the porous layer is key to predicting the dynamics. As we saw, a significant amount of silicon may be lost to the transport of silicon monoxide out of the pellet. We now examine two limits of the simulations. We begin with the reaction-limited case, which we show in Figure 2.3. In this case, we use the parameter values in Table 2.2, but with $\mathrm{Da} = 10^5$. The choice $\mathrm{Da} = 10^5$ is sufficient to highlight the reaction-limited behaviour, despite Table 2.2 suggesting we choose $\mathrm{Da} = 10^7$. Generally, we find the same qualitative behaviour as in the previous example. However, the spacial variation in the concentrations is reduced. Any silicon monoxide (or carbon dioxide) produced by the quartz reaction quickly diffuses through the porous layer and is lost, leading to slow consumption of carbon and production of silicon carbide. The loses are further reflected in the carbon utilization and silicon yield. At the quartz consumption

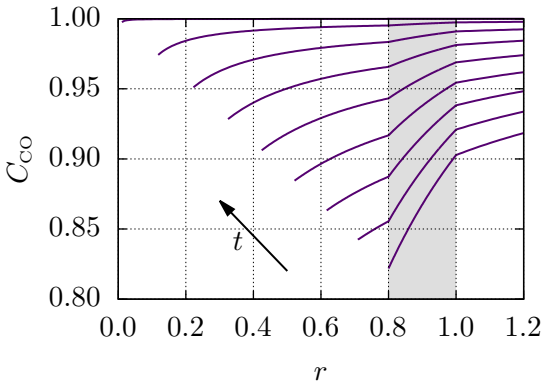

(a) Concentration of carbon monoxide. The shaded region denotes the porous layer.

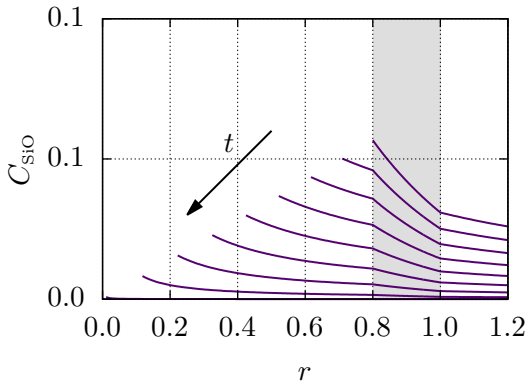

(b) Concentration of silicon monoxide. The shaded region denotes the porous layer.

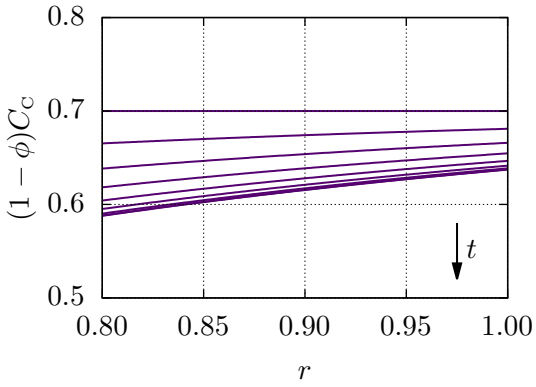

(c) Concentration of carbon.

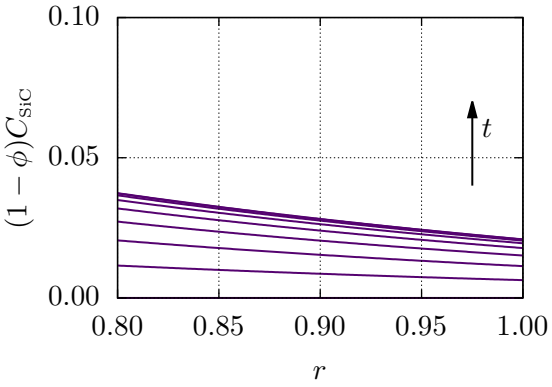

(d) Concentration of silicon carbide.

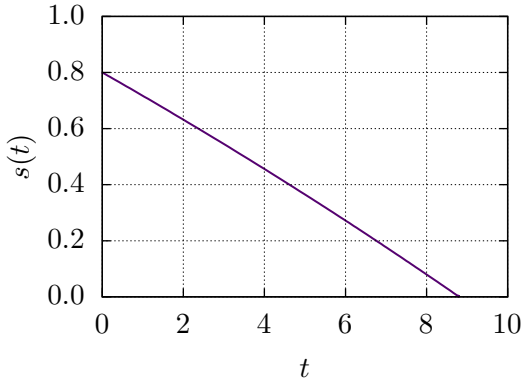

(e) Consumption of the quartz core.

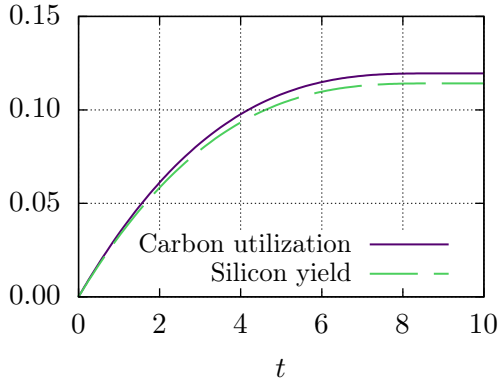

(f) Carbon utilization and silicon yield.

Figure 2.3: Results from the numerical simulation of the reduced system consisting of (2.40), (2.42), (2.63), and (2.73)–(2.75), with boundary conditions (2.90)–(2.96), and initial conditions (2.66) and (2.68). Parameter values taken from Table 2.2, with $\mathrm{Da} = 10^5$.

time $U_C = 0.120$ and $Y_{SiC} = 0.114$.

We now examine the diffusion-limited case by using the typical values found in Table 2.2, but with $\mathrm{Da} = 10^2$, with results shown in Figure 2.4. Again, we choose Da to show the diffusion-limited structure, not necessarily the minimum possible value. The concentration of carbon monoxide at the quartz interface is small, since the reaction dominates diffusion—almost all carbon monoxide that reaches the quartz surface reacts immediately. In turn, a considerable amount of silicon monoxide is produced. The concentration of silicon monoxide sharply decreases in the porous layer, since most of the silicon monoxide is consumed before it is able to diffuse to the exterior of the pellet. We find a rapid consumption of carbon and production of silicon carbide. In this case, we find a moving front—behind which, all the carbon has reacted—instead of the relatively uniform consumption we saw in the previous examples. Owing to the moving front nature of the carbon, once all the carbon at a particular radius has been consumed, no more silicon carbide can be formed there. This can be seen with the highlighted curves in Figures 2.4c and 2.4d. All the carbon has been consumed for $r \lesssim 0.9$ and corresponds to where the silicon carbide curve begins to deviate from the maximum. The silicon carbide profile remains the same for $r \lesssim 0.9$ for all later times because the carbon has been fully exhausted in this region, and no additional silicon carbide can be produced. In this example, the carbon utilization and silicon yield at the quartz consumption time are $U_C = 1.000$ and $Y_{SiC} = 0.955$. Since the reactions dominate diffusion, all the carbon is reacted, and almost all the initial quartz is converted into silicon carbide.

We now explore the parameter space, and use the carbon utilization, (2.97), and silicon yield, (2.98), *at the quartz consumption time* to characterize the effectiveness of the process.

In Figure 2.5 we show the carbon utilization and silicon yield at the quartz consumption time for three characteristic planes within the parameter space. The base parameter values are $\mathrm{Da} = 10^4$, $s_0 = 0.8$, $\mathcal{K} = 1$, and $\mathcal{S} = 0.1$, as in Table 2.2. We begin with the Da–s_0 plane (Figure 2.5a). For $\mathrm{Da} < 10^3$ we find a transition around $s_0 \approx 0.8$ from maximal silicon yield to full carbon utilization. Since $\mathcal{K} = 1$, the silicon carbide reaction, (1.5), and the Boudouard reaction, (1.6), dominate diffusion equally. Each mole of quartz is able to consume three moles of carbon—two moles by the silicon carbide reaction, and one mole by the Boudouard reaction. The initial carbon : quartz mole ratio is given by

$$(1 - \phi_0)\frac{\rho_C}{\rho_{SiO_2}}\frac{m_{SiO_2}}{m_C}\left(s_0^{-3} - 1\right). \tag{2.99}$$

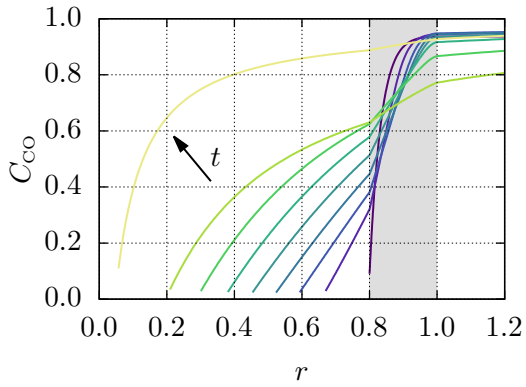

(a) Concentration of carbon monoxide. The shaded region denotes the porous layer.

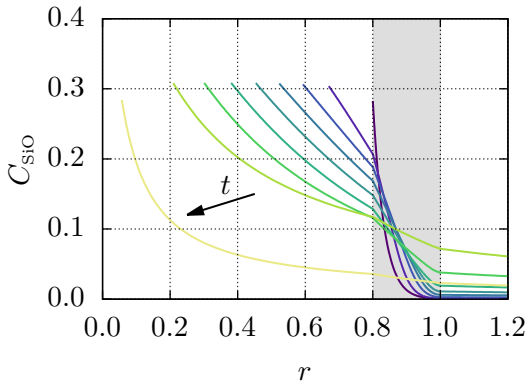

(b) Concentration of silicon monoxide. The shaded region denotes the porous layer.

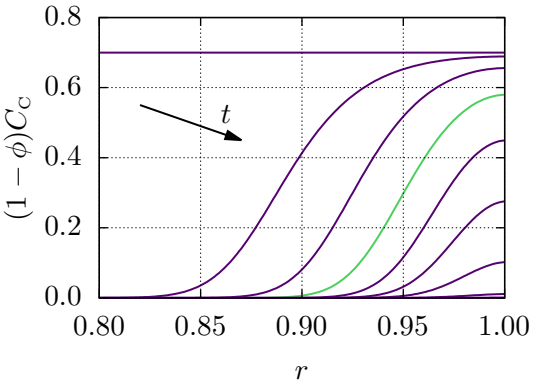

(c) Concentration of carbon.

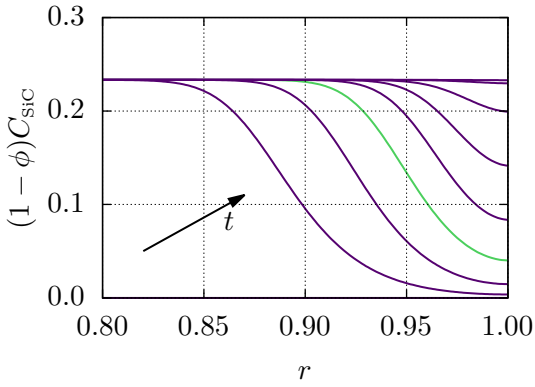

(d) Concentration of silicon carbide.

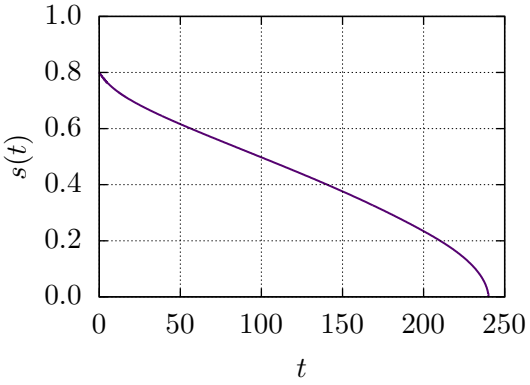

(e) Consumption of the quartz core.

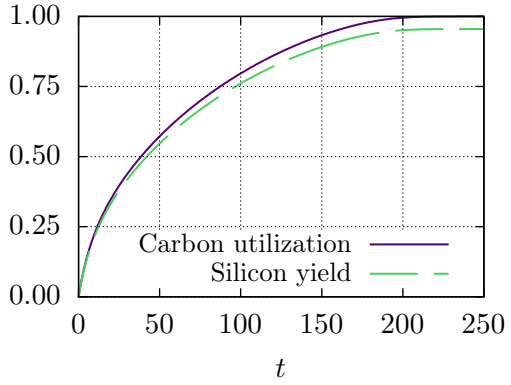

(f) Carbon utilization and silicon yield.

Figure 2.4: Results from the numerical simulation of the reduced system consisting of (2.40), (2.42), (2.63), and (2.73)–(2.75), with boundary conditions (2.90)–(2.96), and initial conditions (2.66) and (2.68). Parameter values taken from Table 2.2, with $\mathrm{Da} = 10^2$.

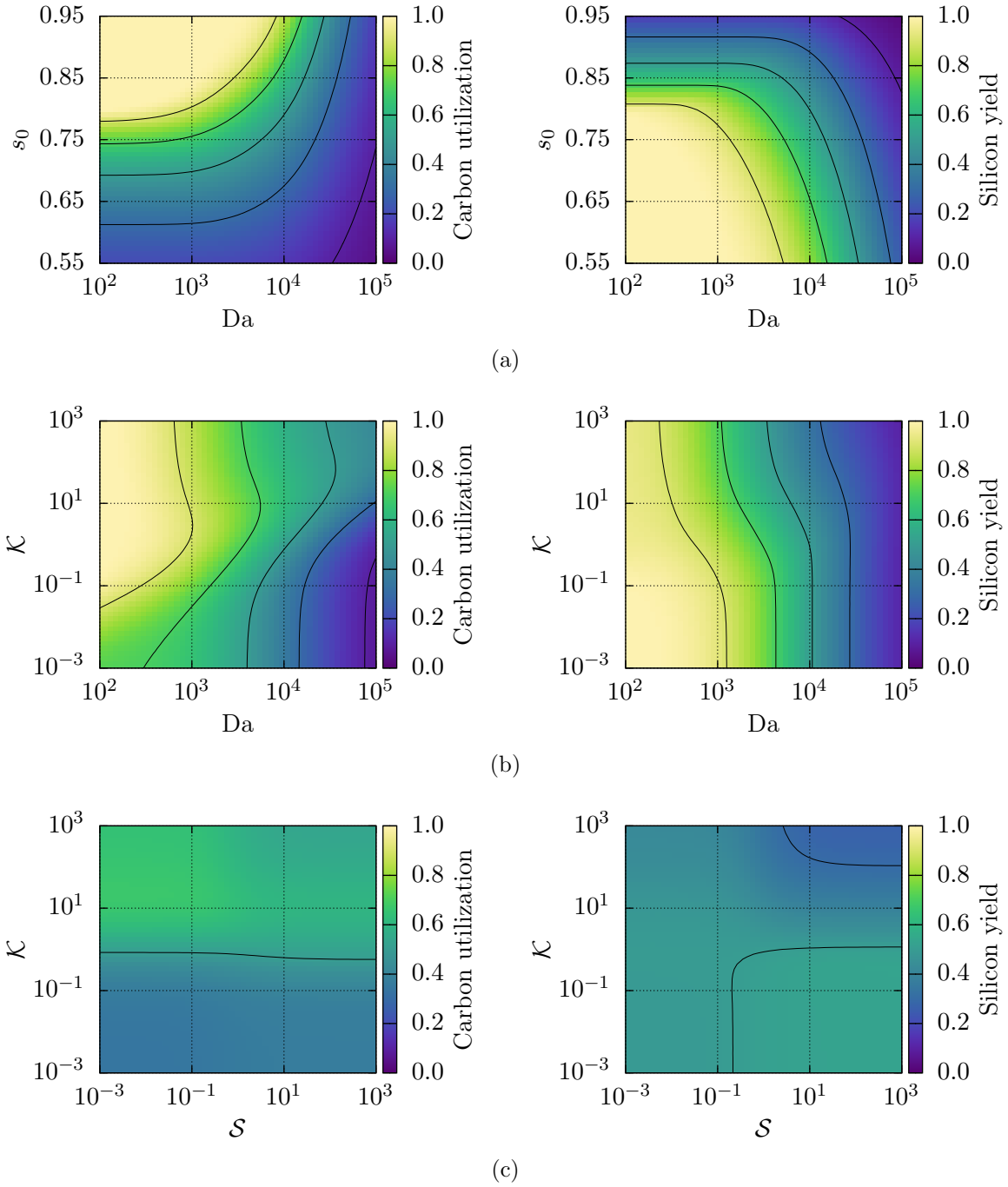

Figure 2.5: Plots of the carbon utilization and silicon yield as given by (2.97) and (2.98), at the quartz consumption time. The default values are as in Table 2.2, $\mathrm{Da} = 10^4$, $s_0 = 0.8$, $\mathcal{K} = 1$, and $\mathcal{S} = 0.1$. We use slightly different parameter ranges than in Table 2.2 to better highlight the variations within the parameter space.

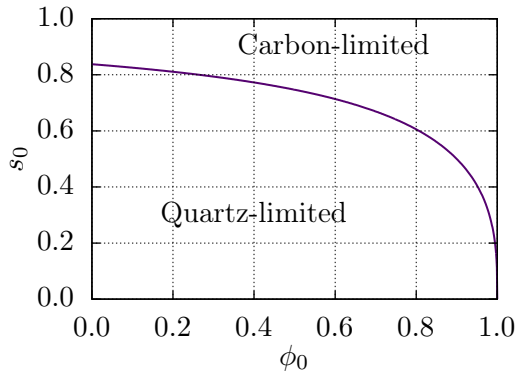

Figure 2.6: Critical s_0 value as a function of initial porosity, ϕ_0, found by solving (2.99) for an initial mole ratio of 3.

Thus, an initial mole ratio of 3 carbon : 1 quartz corresponds to an initial quartz radius of $s_0 = 0.793$. Therefore, the pellet is quartz-limited for $s_0 < 0.793$, and carbon-limited for $s_0 > 0.793$, in the case of $\mathcal{K} = 1$. We highlight the dependence of this critical s_0 value on the initial porosity in Figure 2.6. Above the critical line the carbon : quartz ratio is less than 3, and the pellet is carbon-limited. Conversely, below the line the carbon : quartz ratio is greater than 3, and the pellet is quartz-limited. Hence, the silicon yield in Figure 2.4f is less than 1 since the system is carbon-limited with $s_0 = 0.8$. We also find that, for large Da values, the carbon utilization and silicon yield are reduced. The reduction is caused by diffusion dominating the reactions; silicon monoxide and carbon dioxide more easily escape the porous layer—slowing the carbon reactions, and reducing both the carbon utilization and silicon yield fractions.

Moving to Figure 2.5b, the Da–$\mathcal{K}$ plane, we see different behaviour. Generally, as $\mathcal{K}$ increases, the carbon utilization increases. By increasing $\mathcal{K}$, the Boudouard reaction begins to dominate the silicon carbide reaction, and so more of the carbon is consumed. However, increasing $\mathcal{K}$ reduces the silicon yield, albeit weakly. As the rate of the Boudouard reaction increases, there is less available carbon for the silicon carbide reaction, and so the production of silicon carbide is slowed slightly. We see that increasing Da decreases the carbon utilization and silicon yield. The carbon utilization behaviour is more interesting than in Figure 2.5a, there is not a simple transition at a particular Da value, instead the transition depends on $\mathcal{K}$. Increasing $\mathcal{K}$ increases the speed of the Boudouard reaction, and so Da must correspondingly increase in order for diffusion to dominate.

The final plane we will look at in detail is the $\mathcal{S}$–$\mathcal{K}$ plane, as shown in Figure 2.5c. We recall that $\mathcal{S}$ compares the speed of the quartz reaction to the silicon carbide

reaction. The plane is split into four distinct regions depending on which reaction(s) dominate(s). In the lower left region $\mathcal{S} \ll 1$ and $\mathcal{K} \ll 1$ and so the silicon carbide reaction is the fastest of the three reactions. Here, only about a third of the carbon is consumed and only about half of the quartz is converted to silicon carbide. Neither of the metrics approach 1 owing to the reasonably large Da value—a non-negligible amount of the silicon monoxide diffuses through the carbon having not reacted. In the lower right portion of Figure 2.5c, the reactions are dominated by the quartz reaction. The carbon utilization and silicon yield increase here owing to the higher concentration of silicon monoxide caused by the faster quartz reaction. The upper left region is instead dominated by the Boudouard reaction, (1.6). Any carbon monoxide created by the quartz reaction quickly reacts with the carbon via the Boudouard reaction, thus, the carbon utilization fraction is highest in this region. However, the faster consumption of the carbon prohibits the formation of silicon carbide, and the yield is correspondingly reduced. Finally, in the upper right region, the silicon carbide reaction is dominated by both the quartz reaction and the Boudouard reaction. The silicon yield is lowest in this region, since the silicon carbide reaction is the slowest of the three reactions. Interestingly, the carbon utilization fraction is not largest here. The dynamics within this region are diffusion-limited, and so we recover a moving front within the carbon layer, and the carbon layer shrinks from the inside. In turn, the capacity of the carbon to react with the silicon monoxide and the carbon dioxide is reduced. The gases can diffuse out of the pellet more easily—reducing the amount of carbon that is utilized.

2.4 Conclusions

We have formulated and analyzed a model for the evolution of a single quartz–carbon pellet under experimental exploration for use in a silicon carbide furnace. The aim is to identify how the quartz can be efficiently converted to silicon carbide. We have developed a spherically symmetric model describing the relevant chemical reactions and mass transfer within a single pellet. We then reduced the model to a quasi-steady regime, and solved the reduced model numerically. The quasi-steady model has four independent non-dimensional parameters, which allows us to explore the dynamics and parameter space relatively efficiently.

We found two distinct regions in the parameter space—a reaction-limited regime and a diffusion-limited regime. In the reaction-limited regime, most of the silicon monoxide produced on the surface of the quartz diffuses out of the pellet and is lost.

However, in the diffusion-limited regime, most of the silicon monoxide is converted to silicon carbide owing to the reactions dominating the transport of the gas. We characterized the dynamics using two metrics, the carbon utilization fraction and the silicon yield at the time that the quartz is fully consumed. The carbon utilization fraction told us how much of the carbon had reacted. The silicon yield told us how much of the initial quartz was converted to silicon carbide, and thus, how much silicon monoxide escaped from the pellet. We numerically found a critical ratio of initial quartz radius to pellet radius of about 0.8. Here, the pellet transitions from being carbon-limited to being quartz-limited for our choice of ϕ_0. The 0.8 value is in agreement with a calculation based on the initial mole ratio. A diffusion-limited system maximizes the carbon utilization and silicon yield, since the silicon monoxide reacts with the carbon before diffusing out of the pellet.

To maximize silicon yield—Elkem ASA's primary objective—the system should operate in the diffusion-limited regime. This ensures that most of the silicon monoxide produced reacts with carbon to form silicon carbide rather than being lost to the atmosphere. To achieve or move closer to this regime the dimensionless diffusion, $\mathcal{D}$, should be reduced. A straightforward way to accomplish this is by increasing the radius of the pellet, thereby increasing the diffusion path length and reducing silicon monoxide loss. Additionally, based on both simulations and an analytical calculation, the radius of the quartz core should not exceed approximately 80% of the total pellet radius. This constraint ensures a sensible initial mole ratio for the reaction.

Chapter 3

A multiphase model for silicon carbide production

We now consider a macroscale multiphase model describing laboratory- or industrial-scale experiments. Multiphase models have a wide range of applications in scientific and engineering disciplines, often in understanding fluid dynamics. Multiphase models have been applied to studying flow in exothermic chemical reactions, which play a role in combustion processes [82, 105]. These models have also previously been employed in analyzing silicon furnaces [42, 43]. Furthermore, in reactive flows [100], and droplet problems [106], including evaporating droplets [100]. Multiphase models have been utilized in the study of multi-component gas flows through capillaries and porous solids [107], and the derivation of conservation laws for such systems [93]. Multiphase models also find applications in biological contexts, such as avascular tumour growth [108], the dynamics of egg yolk in amphibian embryos [109], and biofilm growth modelled with solvent–polymer interactions [110]. Other areas of applications include the study of poroviscous drops on substrates [111], geosciences modelling viscous anisotropic flows in magma and rock [112, 113], and even ice cream [114] and the flow in a pint of Guinness [115]. For more details see the classical works [116, 117].

Quartz particles ($\sim$ 1 mm diameter) and carbon particles ($\sim$ 50 μm diameter) are mixed, and in laboratory-scale experiments are added to a cylindrical crucible as shown in Figure 3.1. Within the crucible is a homogenous mixture of the quartz particles and carbon particles with space between them for gases to flow. The crucible is placed in an inductive furnace, and the quartz and carbon are heated up from room temperature [42]. The particles are held at around 1600 °C for about an hour, and then the inductive heating is turned off and the crucible is allowed to cool down [21].

In this chapter, we will model the mass transfer and chemical reactions within

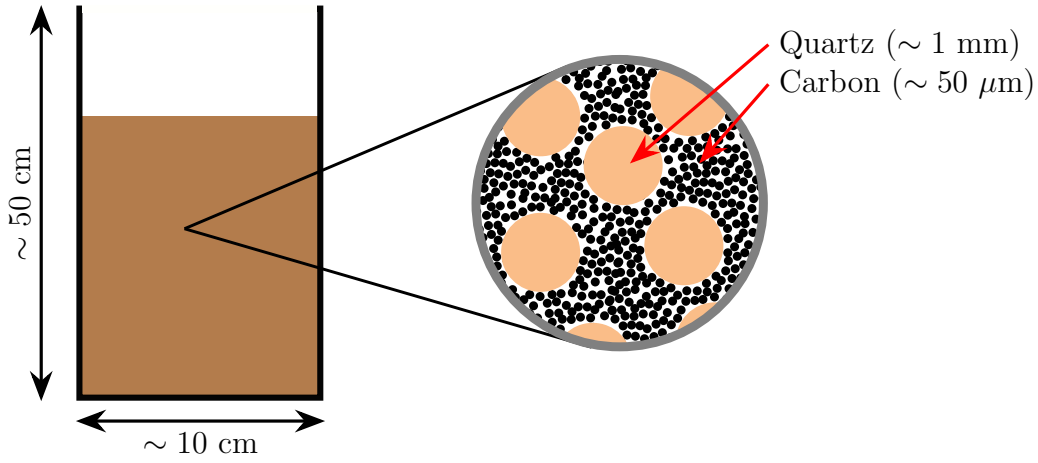

Figure 3.1: Cross section of a laboratory-scale experimental setup.

a crucible of quartz and carbon particles in Section 3.1. Additionally, we specify the initial conditions and boundary conditions, and we then non-dimensionalize the model. In order to gain insight into the model, we pose and solve two paradigm problems analytically and numerically in Section 3.3. We then return to the full model in Section 3.4, where we examine the dependence of the carbon utilization and silicon yield on the dimensionless parameters. Finally, we summarize our results in Section 3.5.

3.1 Mathematical model

Since the crucible is long and thin (typically 43 cm tall, with a diameter of 13 cm), we do not expect radial or angular variations in the solid volume fractions or gas concentrations and so we consider variations in the z direction only and derive a 1D multiphase model for a crucible filled with a mixture of small quartz particles and carbon particles, as shown in Figure 3.1. We suppose that the only gas present in the crucible initially is an inert gas (*e.g.* nitrogen or argon [10, 24, 33, 35]) and we continuously inject a small concentration of carbon monoxide though an inlet at the bottom. The top of the crucible is unsealed, and so expect an outward flow of gas through the top of the bed of particles. We assume that the temperature is uniform, at 1600 °C, so that the parameters in the model may be taken to be constant.

In the crucible, we assume that the gases produced react with the quartz and carbon by reactions (1.5)–(1.7). As the reactions proceed, the overall volume of the solid mixture decreases, leading to a downward motion of the solid materials due to gravity. This downward flow ensures that voids do not form in the crucible as

the quartz and carbon are consumed. Simultaneously, the generation of gas from the reactions increases the pressure within the system. Pressure gradients drive an upward gas flow. To model the behaviour, we track the volume fractions of carbon, silicon carbide, and quartz, as well as the solid velocity, and the gas concentrations. Additionally, since the reaction rates depend on the surface area of quartz and carbon particles, we express the surface area in terms of the number density of these particles. As a consequence, we also need to track the number density of both carbon and quartz particles to capture the evolution of the system.

We begin the derivation of our multiphase model by appealing to conservation of carbon. We assume that the solid materials move downward under gravity as they are consumed and we denote by α_{C} the volume fraction of carbon and by u_s the speed at which the solid moves due to the consumption of the material. Conservation of carbon takes the form

$$\frac{\rho_{\mathrm{C}}}{m_{\mathrm{C}}}\left(\frac{\partial \alpha_{\mathrm{C}}}{\partial t}+\frac{\partial}{\partial z}(\alpha_{\mathrm{C}} u_s)\right)=-2\mathscr{R}_{\mathrm{SiC}}-\mathscr{R}_{\mathrm{Boud}}, \tag{3.1}$$

where ρ_{C} is the density of carbon, m_{C} is the molar mass of carbon (so that $\rho_{\mathrm{C}}/m_{\mathrm{C}}$ is the molar density, or concentration, of solid carbon), and $\mathscr{R}_{\mathrm{SiC}}$ and $\mathscr{R}_{\mathrm{Boud}}$ describe mass transfer due to reactions (1.5) and (1.6). We will define their functional forms in Section 3.1.1. Similarly, we denote by α_{SiC} the volume fraction of silicon carbide and by $\alpha_{\mathrm{SiO_2}}$ the volume fraction of quartz, appealing to conservation of mass for silicon carbide and quartz we find that

$$\frac{\rho_{\mathrm{SiC}}}{m_{\mathrm{SiC}}}\left(\frac{\partial \alpha_{\mathrm{SiC}}}{\partial t}+\frac{\partial}{\partial z}(\alpha_{\mathrm{SiC}} u_s)\right)=\mathscr{R}_{\mathrm{SiC}}, \tag{3.2}$$

$$\frac{\rho_{\mathrm{SiO_2}}}{m_{\mathrm{SiO_2}}}\left(\frac{\partial \alpha_{\mathrm{SiO_2}}}{\partial t}+\frac{\partial}{\partial z}(\alpha_{\mathrm{SiO_2}} u_s)\right)=-\mathscr{R}_{\mathrm{SiO_2}}, \tag{3.3}$$

respectively. Here, ρ_{SiC} is the density of silicon carbide, m_{SiC} is the molar mass of silicon carbide, $\rho_{\mathrm{SiO_2}}$ is the density of quartz, $m_{\mathrm{SiO_2}}$ is the molar mass of quartz, and $\mathscr{R}_{\mathrm{SiO_2}}$ describes mass transfer due to reaction (1.7).

The reaction rates $\mathscr{R}_{\mathrm{SiC}}$, $\mathscr{R}_{\mathrm{Boud}}$, and $\mathscr{R}_{\mathrm{SiO_2}}$ depend on the surface area of the carbon and quartz particles. If we consider a crucible containing densely packed identical carbon spheres, then the volume fraction of carbon is constant regardless of the size of the individual particles. The surface area, however, is not constant, since we observe that a very fine carbon powder will have a much larger surface area than a single large particle, for a given overall volume. Therefore, we need an additional

variable to characterize the surface area, and we choose to use the number density of carbon particles, n_{C}, and quartz particles, $n_{\mathrm{SiO_2}}$. Other choices to characterize the surface area are the radius of the particles or the surface area itself. If a particle is fully consumed, we consider it to be a particle with zero radius, and so the number of particles is conserved, but $\alpha \to 0$. Thus, conservation of particles gives us

$$\frac{\partial n_{\mathrm{C}}}{\partial t} + \frac{\partial}{\partial z}(n_{\mathrm{C}} u_s) = 0, \tag{3.4}$$

$$\frac{\partial n_{\mathrm{SiO_2}}}{\partial t} + \frac{\partial}{\partial z}(n_{\mathrm{SiO_2}} u_s) = 0. \tag{3.5}$$

Since silicon carbide is only a product and not a reactant in our system, we do not need to track the number density of silicon carbide particles since we do not need to capture the surface area of silicon carbide.

We now turn to the gas phases. We assume that the gaseous mixture fills the void space created by the three solid phases. We denote by α_{gas} the volume fraction that the gaseous mixture occupies. With all of the volume fractions defined, we assume that there are no voids, and so we write

$$\alpha_{\mathrm{C}} + \alpha_{\mathrm{SiC}} + \alpha_{\mathrm{SiO_2}} + \alpha_{\mathrm{gas}} = 1. \tag{3.6}$$

Denoting the *intrinsic* concentrations[1] of silicon monoxide, carbon monoxide, carbon dioxide, and the inert background gas by C_{SiO}, C_{CO}, $C_{\mathrm{CO_2}}$, and C_{bg}, respectively, and the gas velocity by u, conservation of silicon monoxide, carbon monoxide, and carbon dioxide take the form

$$\frac{\partial}{\partial t}(\alpha_{\mathrm{gas}} C_{\mathrm{SiO}}) + \frac{\partial q_{\mathrm{SiO}}}{\partial z} = -\mathscr{R}_{\mathrm{SiC}} + \mathscr{R}_{\mathrm{SiO_2}}, \tag{3.7}$$

$$\frac{\partial}{\partial t}(\alpha_{\mathrm{gas}} C_{\mathrm{CO}}) + \frac{\partial q_{\mathrm{CO}}}{\partial z} = \mathscr{R}_{\mathrm{SiC}} - \mathscr{R}_{\mathrm{SiO_2}} + 2\mathscr{R}_{\mathrm{Boud}}, \tag{3.8}$$

$$\frac{\partial}{\partial t}(\alpha_{\mathrm{gas}} C_{\mathrm{CO_2}}) + \frac{\partial q_{\mathrm{CO_2}}}{\partial z} = \mathscr{R}_{\mathrm{SiO_2}} - \mathscr{R}_{\mathrm{Boud}}, \tag{3.9}$$

where

$$q_i = \alpha_{\mathrm{gas}} u C_i - \mathscr{D}_i \alpha_{\mathrm{gas}} \rho_{\mathrm{gas}} \frac{\partial}{\partial z}\left(\frac{C_i}{\rho_{\mathrm{gas}}}\right) \tag{3.10}$$

is the flux of species i taken from concentrated gas theory [92, 93, 100, 118, 119],

[1] Microscale concentrations in units of mol / m^3 *of gas*.

including advection and diffusion, where $\mathscr{D}_i$ is the diffusion coefficient of species i, and

$$\rho_{\text{gas}} = m_{\text{SiO}} C_{\text{SiO}} + m_{\text{CO}} C_{\text{CO}} + m_{\text{CO}_2} C_{\text{CO}_2} + m_{\text{bg}} C_{\text{bg}} \tag{3.11}$$

is the density of the gas mixture. Instead of explicitly considering an analogous equation for conservation of mass of the inert background gas, we instead write down the continuity equation for the gaseous mixture, which is the sum of all the individual gas conservation equations, and reads

$$\begin{aligned} \frac{\partial}{\partial t}(\alpha_{\text{gas}}\rho_{\text{gas}}) + \frac{\partial}{\partial z}(\alpha_{\text{gas}}\rho_{\text{gas}} u) = (-m_{\text{SiO}} + m_{\text{CO}})\mathscr{R}_{\text{SiC}} + \\ (2m_{\text{CO}} - m_{\text{CO}_2})\mathscr{R}_{\text{Boud}} + (m_{\text{SiO}} - m_{\text{CO}} + m_{\text{CO}_2})\mathscr{R}_{\text{SiO}_2}. \end{aligned} \tag{3.12}$$

We note that the gaseous mixture is transported by advection only. We assume that the local flow has low enough Reynolds number so that the gas flow is governed by Darcy's law

$$u - u_s = -\frac{\kappa}{\mu}\frac{\partial P}{\partial z}, \tag{3.13}$$

where $\kappa = \kappa(\alpha_{\text{C}}, \alpha_{\text{SiC}}, \alpha_{\text{SiO}_2}, n_{\text{C}}, n_{\text{SiO}_2})$ is the permeability of the porous structure formed by the carbon, silicon carbide, and quartz, $\mu = \mu(C_{\text{SiO}}, C_{\text{CO}}, C_{\text{CO}_2}, C_{\text{bg}})$ is the viscosity of the gas mixture, and P is the pressure of the gas. We relate the pressure to the intrinsic concentrations using the ideal gas law [120, 121]

$$P = RT(C_{\text{SiO}} + C_{\text{CO}} + C_{\text{CO}_2} + C_{\text{bg}}), \tag{3.14}$$

where R is the gas constant, and T is the (constant) temperature. We eliminate the concentration of the background gas, C_{bg}, from (3.14) using (3.11), so that the pressure is

$$P = RT\left(\frac{\rho_{\text{gas}}}{m_{\text{bg}}} + \sum_{i\in\mathcal{G}}\left(1 - \frac{m_i}{m_{\text{bg}}}\right)C_i\right), \tag{3.15}$$

where $\mathcal{G} = \{\text{SiO, CO, CO}_2\}$ is the set of reactive gases. We then eliminate the pressure from (3.13) using (3.15). Thus,

$$u - u_s = -\frac{\kappa}{\mu}\frac{\partial}{\partial z}\left[RT\left(\frac{\rho_{\text{gas}}}{m_{\text{bg}}} + \sum_{i\in\mathcal{G}}\left(1 - \frac{m_i}{m_{\text{bg}}}\right)C_i\right)\right]. \tag{3.16}$$

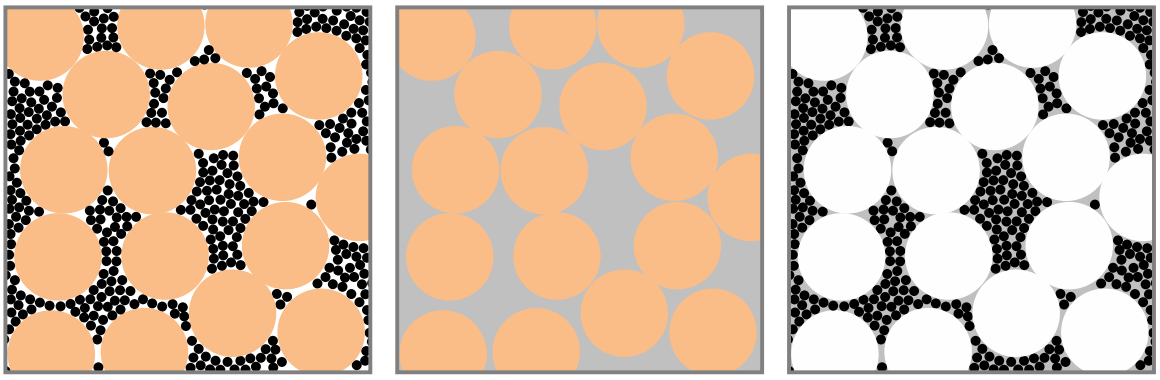

(a) (b) (c)

Figure 3.2: The initial micro-structure (a) may be decomposed into the quartz particles and the region occupied by the carbon and the gas, denoted by the grey region in (b). Within the grey region we assume the carbon particles are densely packed (c).

We now turn our attention to describing how the solid moves. One possible way to model conservation of momentum of the solid is by treating it as a granular flow [122]. In such models, the solids are treated as a continuum with the micro-scale structure and dynamics incorporated using nonlinear relationships between the components of the stress tensor [123, 124]. Here, for simplicity, we assume the flow is dominated by gravity so that the solids remain well-packed for all time. Since the carbon particles are much smaller and much more numerous initially than the quartz particles, we assume that the carbon is densely packed in the space unoccupied by quartz and silicon carbide, as we show in Figure 3.2a. The grey region in Figure 3.2b highlights the volume fraction unoccupied by the quartz, $1 - \alpha_{\mathrm{SiO_2}}$. We assume that the grey region is densely packed with carbon particles, as shown in Figure 3.2c. We assume η is the packing fraction of carbon in the grey region, which will depend on α_{C}, α_{SiC}, $\alpha_{\mathrm{SiO_2}}$, n_{C}, $n_{\mathrm{SiO_2}}$, and the geometry of the particles[2]. Moreover, the formation of silicon carbide further decreases the available volume for the carbon particles. Therefore, we replace the dynamics with the constitutive relation

$$\alpha_{\mathrm{C}} = \eta(1 - \alpha_{\mathrm{SiO_2}} - \alpha_{\mathrm{SiC}}). \tag{3.17}$$

[2]For spheres of equal radius, typical experiments find a random packing fraction of $\eta = 0.6366$ [125–127], and some authors have suggested the exact value of $\eta = 2/\pi$ [128, 129]. However, random packing fraction may not be well defined and instead depend on the method of packing [130]. As a result, the range $0.642 \leq \eta \leq 0.649$ is sometimes reported [131, 132].

3.1.1 Rates of reaction

We now discuss forms of the reaction rates. Despite extensive investigation [10], the reaction kinetics are not well understood. Let us first consider the silicon carbide reaction, (1.5). We expect the reaction rate to depend both on the amount of available silicon monoxide and the surface area of carbon. The amount of available silicon monoxide is given by the *extrinsic* mixture concentration[3], $\alpha_{\text{gas}} C_{\text{SiO}}$. The surface area requires more careful consideration. For a single particle of volume V the surface area scales as $V^{2/3}$ with the coefficient depending on the geometry.

For particles with characteristic radius r, the surface area per volume S and volume fraction α scale as

$$S \propto r^2 n, \quad \alpha \propto r^3 n, \tag{3.18}$$

so that

$$r \propto \left(\frac{\alpha}{n}\right)^{1/3}, \tag{3.19}$$

and so

$$S \propto (n\alpha^2)^{1/3}. \tag{3.20}$$

Thus, we take the form of the reaction rate for reaction (1.5) to be

$$\mathscr{R}_{\text{SiC}} = k_1 \left(n_{\text{C}} \alpha_{\text{C}}^2\right)^{1/3} (\alpha_{\text{gas}} C_{\text{SiO}}) \tag{3.21}$$

by the law of mass action, where k_1 is the rate constant with units of m / s. Moreover, using the same argument for the other reactions, recalling (1.6) and (1.7), we write

$$\mathscr{R}_{\text{Boud}} = k_2 \left(n_{\text{C}} \alpha_{\text{C}}^2\right)^{1/3} (\alpha_{\text{gas}} C_{\text{CO}_2}), \tag{3.22}$$

$$\mathscr{R}_{\text{SiO}_2} = k_3 \left(n_{\text{SiO}_2} \alpha_{\text{SiO}_2}^2\right)^{1/3} (\alpha_{\text{gas}} C_{\text{CO}}). \tag{3.23}$$

3.1.2 Initial conditions

Initially, the crucible contains no silicon carbide, thus, we write

$$\alpha_{\text{SiC}} = 0, \quad \text{at } t = 0. \tag{3.24}$$

[3] Macroscale concentration in units mol / m^3 *of mixture*.

Physically, we can control the initial radii of the carbon and quartz particles, as well as the initial carbon : quartz mole ratio. Thus, we need to determine the initial volume fractions and number densities of carbon and quartz from their radii and mole ratio. We assume the carbon and quartz particles are spherical, so that initially we have that

$$\alpha_{\mathrm{C}} = \alpha_{\mathrm{C}}^0 = \frac{4}{3}\pi(r_{\mathrm{C}}^0)^3 n_{\mathrm{C}}^0, \quad \alpha_{\mathrm{SiO_2}} = \alpha_{\mathrm{SiO_2}}^0 = \frac{4}{3}\pi(r_{\mathrm{SiO_2}}^0)^3 n_{\mathrm{SiO_2}}^0, \quad \text{at } t = 0, \tag{3.25}$$

where we use the superscript 0 to indicate an initial value, as well as

$$\alpha_{\mathrm{C}}^0 = \eta(1 - \alpha_{\mathrm{SiO_2}}^0), \quad \text{at } t = 0, \tag{3.26}$$

from (3.17). Additionally, with a prescribed initial stoichiometric ratio ν between carbon and quartz we write

$$\frac{\rho_{\mathrm{C}}}{m_{\mathrm{C}}}\alpha_{\mathrm{C}}^0 = \nu\frac{\rho_{\mathrm{SiO_2}}}{m_{\mathrm{SiO_2}}}\alpha_{\mathrm{SiO_2}}^0. \tag{3.27}$$

Since our goal is to convert the silicon in quartz to silicon carbide, we want to ensure all the quartz is consumed. The theoretical mole ratio is $\nu = 3$ by (1.9), however, experiments typically use the range $3 < \nu \leq 5$ [23] to guarantee full quartz consumption. In our analysis we take $\nu = 3.5$.

Solving the linear system (3.25)–(3.27) for the initial volume fraction and number density of carbon and quartz we find that

$$\alpha_{\mathrm{C}}^0 = \frac{\eta\nu m_{\mathrm{C}}\rho_{\mathrm{SiO_2}}}{\eta m_{\mathrm{SiO_2}}\rho_{\mathrm{C}} + \nu m_{\mathrm{C}}\rho_{\mathrm{SiO_2}}}, \qquad n_{\mathrm{C}}^0 = \frac{3\eta\nu m_{\mathrm{C}}\rho_{\mathrm{SiO_2}}}{4\pi(r_{\mathrm{C}}^0)^3(\nu m_{\mathrm{C}}\rho_{\mathrm{SiO_2}} + \eta m_{\mathrm{SiO_2}}\rho_{\mathrm{C}})}, \tag{3.28}$$

$$\alpha_{\mathrm{SiO_2}}^0 = \frac{\eta m_{\mathrm{SiO_2}}\rho_{\mathrm{C}}}{\eta m_{\mathrm{SiO_2}}\rho_{\mathrm{C}} + \nu m_{\mathrm{C}}\rho_{\mathrm{SiO_2}}}, \qquad n_{\mathrm{SiO_2}}^0 = \frac{3\eta\nu m_{\mathrm{SiO_2}}\rho_{\mathrm{C}}}{4\pi(r_{\mathrm{SiO_2}}^0)^3(\nu m_{\mathrm{C}}\rho_{\mathrm{SiO_2}} + \eta m_{\mathrm{SiO_2}}\rho_{\mathrm{C}})}. \tag{3.29}$$

Since $\alpha_{\mathrm{SiC}} = 0$ at $t = 0$, (3.6) reads

$$\alpha_{\mathrm{gas}} = \alpha_{\mathrm{gas}}^0 = 1 - \alpha_{\mathrm{C}}^0 - \alpha_{\mathrm{SiO_2}}^0, \quad \text{at } t = 0. \tag{3.30}$$

We assume that the crucible contains only the background gas initially, so that

$$C_{\mathrm{SiO}} = 0, \quad C_{\mathrm{CO}} = 0, \quad C_{\mathrm{CO_2}} = 0, \quad \rho_{\mathrm{gas}} = m_{\mathrm{bg}}\left(\frac{P_{\mathrm{atm}}}{RT}\right), \quad \text{at } t = 0, \tag{3.31}$$

where P_{atm} is atmospheric pressure. Finally, we assume that the initial height of the

bed of pellets is known and given by

$$H = H^0, \quad \text{at } t = 0. \tag{3.32}$$

3.1.3 Boundary conditions

At the bottom of the crucible, located at $z = 0$, we assume a prescribed flux of carbon monoxide and background gas, and that there is no flux of silicon monoxide or carbon dioxide, so that we write

$$q_{\mathrm{CO}} = q_{\mathrm{CO}}^{\mathrm{in}}, \quad u\alpha_{\mathrm{gas}}\rho_{\mathrm{gas}} = m_{\mathrm{CO}}q_{\mathrm{CO}}^{\mathrm{in}} + m_{\mathrm{bg}}q_{\mathrm{bg}}^{\mathrm{in}}, \quad q_{\mathrm{SiO}} = 0, \quad q_{\mathrm{CO_2}} = 0, \quad \text{at } z = 0. \tag{3.33}$$

We also assume there is no solid flow through the bottom of the crucible so that

$$u_s = 0, \quad \text{at } z = 0. \tag{3.34}$$

At the top of the bed of pellets, at $z = H(t)$, care must be taken to write down the boundary conditions. A common approach is to prescribe no diffusive flux across the interface, for example in [90], so that

$$-\mathscr{D}_i\alpha_{\mathrm{gas}}\rho_{\mathrm{gas}}\frac{\partial}{\partial z}\left(\frac{C_i}{\rho_{\mathrm{gas}}}\right) = 0. \tag{3.35}$$

However, since we have concentrated compressible gas, this is insufficient and degenerate. The overall diffusive flux is zero everywhere, by construction, and so this can only be considered three boundary conditions—a fourth is still needed. Therefore, we need an additional boundary condition for the gas mixture as well. This additional boundary condition would need to be consistent with the three no diffusive flux conditions.

Instead, following [134], we assume that the gas above the bed of pellets is well-mixed and that

$$q_i - \frac{\mathrm{d}H}{\mathrm{d}t}\alpha_{\mathrm{gas}}C_i = \theta_i\alpha_{\mathrm{gas}}(C_i - C_i^{\mathrm{out}}), \tag{3.36}$$

where θ_i is the mass transfer coefficient of species i and C_i^{out} is a known (constant) concentration outside of the crucible. The mass transfer coefficient θ_i is a simple way

Table 3.1: Parameters, their descriptions, values, and units.

Parameter	Description	Value	Units	Ref.
ρ_{C}	Density of carbon	2270	kg / m^3	[42]
ρ_{SiC}	Density of silicon carbide	3210	kg / m^3	[42]
$\rho_{\mathrm{SiO_2}}$	Density of quartz	2650	kg / m^3	[42]
m_{C}	Molar mass of carbon	12	g / mol	[97]
m_{SiC}	Molar mass of silicon carbide	40	g / mol	[97]
$m_{\mathrm{SiO_2}}$	Molar mass of quartz	60	g / mol	[97]
m_{SiO}	Molar mass of silicon monoxide	44	g / mol	[97]
m_{CO}	Molar mass of carbon monoxide	28	g / mol	[97]
$m_{\mathrm{CO_2}}$	Molar mass of carbon dioxide	44	g / mol	[97]
m_{bg}	Molar mass of inert gas[1]	28	g / mol	[97]
k_1	Rate constant of reaction (1.5)	10^{-2}	m / s	Estimated
k_2	Rate constant of reaction (1.6)	10^{-2}	m / s	Estimated
k_3	Rate constant of reaction (1.7)	10^{-2}	m / s	Estimated
$\mathscr{D}_i$	Diffusion coefficient of species i	10^{-4}	m^2 / s	[32, 98]
$r^0_{\mathrm{SiO_2}}$	Initial radius of quartz particles	1	mm	Elkem ASA
r^0_{C}	Initial radius of carbon particles	50	μm	Elkem ASA
κ	Permeability	10^{-10}	m^2	Estimated
μ	Viscosity of the gas	10^{-4}	kg / (m s)	[133]
R	Gas constant	8.314	J / (K mol)	
T	Temperature	1600	°C	Elkem ASA
η	Packing fraction	0.64	-	[131, 132]
ν	Initial mole ratio	3.5	-	Elkem ASA
P_{atm}	Atmospheric pressure	10^5	Pa	
H^0	Initial height of particles	50	cm	Elkem ASA
$q^{\mathrm{in}}_{\mathrm{CO}}$	Inlet flux of carbon monoxide	1	mol / (m^2 s)	Est. from [21]
$q^{\mathrm{in}}_{\mathrm{bg}}$	Inlet flux of background gas	9	mol / (m^2 s)	Est. from [21]
θ_i	Mass transfer coefficient of species i	0.1	m / s	Estimated
$C^{\mathrm{out}}_{\mathrm{bg}}$	External background gas concentration	6.0	mol / m^3	Estimated

[1] Assuming the experiment is done in a nitrogen atmosphere.

of modelling a more complex interaction [134, 135]. Thus, we write

$$q_{\mathrm{SiO}} - \frac{\mathrm{d}H}{\mathrm{d}t}\alpha_{\mathrm{gas}}C_{\mathrm{SiO}} = \theta_{\mathrm{SiO}}\alpha_{\mathrm{gas}}C_{\mathrm{SiO}}, \tag{3.37}$$

$$q_{\mathrm{CO}} - \frac{\mathrm{d}H}{\mathrm{d}t}\alpha_{\mathrm{gas}}C_{\mathrm{CO}} = \theta_{\mathrm{CO}}\alpha_{\mathrm{gas}}C_{\mathrm{CO}}, \tag{3.38}$$

$$q_{\mathrm{CO_2}} - \frac{\mathrm{d}H}{\mathrm{d}t}\alpha_{\mathrm{gas}}C_{\mathrm{CO_2}} = \theta_{\mathrm{CO_2}}\alpha_{\mathrm{gas}}C_{\mathrm{CO_2}}, \tag{3.39}$$

$$u\alpha_{\mathrm{gas}}\rho_{\mathrm{gas}} - \frac{\mathrm{d}H}{\mathrm{d}t}\alpha_{\mathrm{gas}}\rho_{\mathrm{gas}} = \alpha_{\mathrm{gas}}\left(\sum_{i\in\mathcal{G}}\theta_i m_i C_i + \theta_{\mathrm{bg}}m_{\mathrm{bg}}(C_{\mathrm{bg}} - C_{\mathrm{bg}}^{\mathrm{out}})\right). \tag{3.40}$$

We note that (3.37)–(3.39) take the same form as (3.36), except we take $C_i^{\mathrm{out}} = 0$.

Since no solid moves through the top surface, we impose the kinematic condition that the rate of change of the height of the bed of particles is equal to the solid velocity at the top, and so we write

$$\frac{\mathrm{d}H}{\mathrm{d}t} = u_s, \quad \text{at } z = H(t). \tag{3.41}$$

3.1.4 Parameter values

We now consider typical sizes for our various dimensional parameters; the values are given in Table 3.1. The uncertainty of the value of each parameter varies considerably from parameter to parameter. Physical constants, such as the density of carbon or the molar mass of silicon carbide, are accurately known. However, the rate constants must be estimated from related experiments.

3.1.5 Dimensionless model

We non-dimensionalize the model (3.1)–(3.17), reaction rates (3.21)–(3.23), initial conditions (3.24)–(3.32), and boundary conditions (3.33)–(3.41) in the following way. We scale z and the height of the bed of particles with the initial bed height, and so we write

$$z = H^0\widetilde{z}, \quad H = H^0\widetilde{H}, \tag{3.42}$$

where $\widetilde{\cdot}$ denotes a dimensionless variable. We scale the number densities by their initial values, and so we write

$$n_{\mathrm{C}} = n_{\mathrm{C}}^0\widetilde{n}_{\mathrm{C}}, \quad n_{\mathrm{SiO_2}} = n_{\mathrm{SiO_2}}^0\widetilde{n}_{\mathrm{SiO_2}}. \tag{3.43}$$

We balance the gas velocity with the pressure gradient in Darcy's law (3.16). We thus use the scaling

$$u = \frac{\kappa P_{\text{atm}}}{\mu H^0}\widetilde{u}, \tag{3.44}$$

where we have scaled the pressure by P_{atm}. The gas concentrations C_{SiO}, C_{CO}, and C_{CO_2} are scaled using the intrinsic scalings

$$C_{\text{SiO}} = c^*_{\text{SiO}}\widetilde{C}_{\text{SiO}}, \quad C_{\text{CO}} = c^*_{\text{CO}}\widetilde{C}_{\text{CO}}, \quad C_{\text{CO}_2} = c^*_{\text{CO}_2}\widetilde{C}_{\text{CO}_2}, \tag{3.45}$$

where

$$c^*_{\text{CO}} = \frac{q^{\text{in}}_{\text{CO}}\mu H^0}{\kappa P_{\text{atm}}} \tag{3.46}$$

comes from balancing the inlet flux, (3.33), with the advective flux, (3.10). Since our system has no extrinsic scaling for the concentration of silicon monoxide or carbon dioxide, we choose

$$c^*_{\text{SiO}} = \frac{k_3 c^*_{\text{CO}}}{k_1}\left(\frac{n^0_{\text{SiO}_2}}{n^0_{\text{C}}}\right)^{1/3}, \quad c^*_{\text{CO}_2} = \frac{k_3 c^*_{\text{CO}}}{k_2}\left(\frac{n^0_{\text{SiO}_2}}{n^0_{\text{C}}}\right)^{1/3} \tag{3.47}$$

so that each of the three reaction terms balance with each other. Furthermore, we scale the gas density with the initial density,

$$\rho_{\text{gas}} = m_{\text{bg}}\left(\frac{P_{\text{atm}}}{RT}\right)\widetilde{\rho}_{\text{gas}}. \tag{3.48}$$

There are multiple timescales we could choose in our system. We choose to scale time using the quartz consumption timescale,

$$t = \left(\frac{\rho_{\text{SiO}_2}/m_{\text{SiO}_2}}{k_3(n^0_{\text{SiO}_2})^{1/3}c^*_{\text{CO}}}\right)\widetilde{t}, \tag{3.49}$$

found by balancing the first term with the reaction term in (3.3). Finally, we scale the solid velocity in such a way that (3.41) is preserved. We thus use the scaling

$$u_s = H^0\left(\frac{k_3(n^0_{\text{SiO}_2})^{1/3}c^*_{\text{CO}}}{\rho_{\text{SiO}_2}/m_{\text{SiO}_2}}\right)\widetilde{u}_s. \tag{3.50}$$

After dropping the tildes, the dimensionless versions of the model for the solid

volume fractions and number densities (3.1)–(3.5) incorporating (3.21)–(3.23) reads

$$\frac{\partial \alpha_{\mathrm{C}}}{\partial t} + \frac{\partial}{\partial z}(\alpha_{\mathrm{C}} u_s) = -\alpha_{\mathrm{gas}} \mathcal{M}_{\mathrm{C}} \big(n_{\mathrm{C}} \alpha_{\mathrm{C}}^2\big)^{1/3} (2C_{\mathrm{SiO}} + C_{\mathrm{CO_2}}), \tag{3.51}$$

$$\frac{\partial \alpha_{\mathrm{SiC}}}{\partial t} + \frac{\partial}{\partial z}(\alpha_{\mathrm{SiC}} u_s) = \alpha_{\mathrm{gas}} \mathcal{M}_{\mathrm{SiC}} \big(n_{\mathrm{C}} \alpha_{\mathrm{C}}^2\big)^{1/3} C_{\mathrm{SiO}}, \tag{3.52}$$

$$\frac{\partial \alpha_{\mathrm{SiO_2}}}{\partial t} + \frac{\partial}{\partial z}(\alpha_{\mathrm{SiO_2}} u_s) = -\alpha_{\mathrm{gas}} \big(n_{\mathrm{SiO_2}} \alpha_{\mathrm{SiO_2}}^2\big)^{1/3} C_{\mathrm{CO}}, \tag{3.53}$$

$$\frac{\partial n_{\mathrm{C}}}{\partial t} + \frac{\partial}{\partial z}(n_{\mathrm{C}} u_s) = 0, \tag{3.54}$$

$$\frac{\partial n_{\mathrm{SiO_2}}}{\partial t} + \frac{\partial}{\partial z}(n_{\mathrm{SiO_2}} u_s) = 0, \tag{3.55}$$

where we have introduced the two dimensionless parameters

$$\mathcal{M}_{\mathrm{C}} = \frac{\rho_{\mathrm{SiO_2}}/m_{\mathrm{SiO_2}}}{\rho_{\mathrm{C}}/m_{\mathrm{C}}}, \quad \mathcal{M}_{\mathrm{SiC}} = \frac{\rho_{\mathrm{SiO_2}}/m_{\mathrm{SiO_2}}}{\rho_{\mathrm{SiC}}/m_{\mathrm{SiC}}}, \tag{3.56}$$

which are molar density ratios of quartz to carbon and to silicon carbide, respectively. The gas concentration equations (3.7)–(3.9) incorporating (3.21)–(3.23) become

$$\delta \mathcal{C}_{\mathrm{SiO}} \left(\frac{\partial}{\partial t}(\alpha_{\mathrm{gas}} C_{\mathrm{SiO}}) + \frac{\partial q_{\mathrm{SiO}}}{\partial z} \right) = \alpha_{\mathrm{gas}} \Big(- \big(n_{\mathrm{C}} \alpha_{\mathrm{C}}^2\big)^{1/3} C_{\mathrm{SiO}} + \big(n_{\mathrm{SiO_2}} \alpha_{\mathrm{SiO_2}}^2\big)^{1/3} C_{\mathrm{CO}} \Big), \tag{3.57}$$

$$\delta \left(\frac{\partial}{\partial t}(\alpha_{\mathrm{gas}} C_{\mathrm{CO}}) + \frac{\partial q_{\mathrm{CO}}}{\partial z} \right) = \alpha_{\mathrm{gas}} \Big(\big(n_{\mathrm{C}} \alpha_{\mathrm{C}}^2\big)^{1/3} (C_{\mathrm{SiO}} + 2C_{\mathrm{CO_2}}) - \big(n_{\mathrm{SiO_2}} \alpha_{\mathrm{SiO_2}}^2\big)^{1/3} C_{\mathrm{CO}} \Big) \tag{3.58}$$

$$\delta \mathcal{C}_{\mathrm{CO_2}} \left(\frac{\partial}{\partial t}(\alpha_{\mathrm{gas}} C_{\mathrm{CO_2}}) + \frac{\partial q_{\mathrm{CO_2}}}{\partial z} \right) = \alpha_{\mathrm{gas}} \Big(\big(n_{\mathrm{SiO_2}} \alpha_{\mathrm{SiO_2}}^2\big)^{1/3} C_{\mathrm{CO}} - \big(n_{\mathrm{C}} \alpha_{\mathrm{C}}^2\big)^{1/3} C_{\mathrm{CO_2}} \Big), \tag{3.59}$$

where the dimensionless fluxes q_i are given by

$$q_i = \mathrm{Da} \left(\alpha_{\mathrm{gas}} u C_i - \frac{1}{\mathrm{Pe}_i} \alpha_{\mathrm{gas}} \rho_{\mathrm{gas}} \frac{\partial}{\partial z} \left(\frac{C_i}{\rho_{\mathrm{gas}}} \right) \right), \tag{3.60}$$

and we have introduced a further seven dimensionless parameters, namely

$$\begin{gathered} \delta = \frac{c^*_{\mathrm{CO}}}{\rho_{\mathrm{SiO_2}}/m_{\mathrm{SiO_2}}}, \quad \mathcal{C}_{\mathrm{SiO}} = \frac{c^*_{\mathrm{SiO}}}{c^*_{\mathrm{CO}}}, \quad \mathcal{C}_{\mathrm{CO_2}} = \frac{c^*_{\mathrm{CO_2}}}{c^*_{\mathrm{CO}}}, \\ \mathrm{Da} = \frac{\kappa P_{\mathrm{atm}}}{\mu (H^0)^2} \left(\frac{\rho_{\mathrm{SiO_2}}/m_{\mathrm{SiO_2}}}{k_3 (n^0_{\mathrm{SiO_2}})^{1/3} c^*_{\mathrm{CO}}} \right), \quad \mathrm{Pe}_i = \frac{\kappa P_{\mathrm{atm}}}{\mathscr{D}_i \mu} \quad i \in \mathcal{G}. \end{gathered} \tag{3.61}$$

Here, δ is the ratio of the intrinsic concentration scale of carbon monoxide to quartz,

$\mathcal{C}_{\mathrm{SiO}}$ and $\mathcal{C}_{\mathrm{CO_2}}$ are the ratios of the intrinsic concentration scales of silicon monoxide and carbon dioxide to carbon monoxide, Da is the Damköhler number [99, 100], and Pe_i are the Péclet numbers.

The no voids condition, (3.6), and the constitutive relation (3.17) remain the same in dimensionless form. The continuity equation (3.12) and Darcy's law (3.16) become

$$\delta\left(\frac{\partial}{\partial t}(\alpha_{\mathrm{gas}}\rho_{\mathrm{gas}}) + \mathrm{Da}\frac{\partial}{\partial z}(\alpha_{\mathrm{gas}}\rho_{\mathrm{gas}}u)\right) = \varrho\mathcal{M}_3\alpha_{\mathrm{gas}}\Big[-\mathcal{M}_1\big(n_{\mathrm{C}}\alpha_{\mathrm{C}}^2\big)^{1/3}C_{\mathrm{SiO}} + \mathcal{M}_2\big(n_{\mathrm{C}}\alpha_{\mathrm{C}}^2\big)^{1/3}C_{\mathrm{CO_2}} + \big(n_{\mathrm{SiO_2}}\alpha_{\mathrm{SiO_2}}^2\big)^{1/3}C_{\mathrm{CO}}\Big], \tag{3.62}$$

$$u - \frac{u_s}{\mathrm{Da}} = -\frac{\partial}{\partial z}\left(\rho + \varrho\sum_{i\in\mathcal{G}}\sigma_i\mathcal{C}_iC_i\right), \tag{3.63}$$

respectively, and we introduce seven further dimensionless parameters, namely

$$\varrho = \frac{c_{\mathrm{CO}}^*RT}{P_{\mathrm{atm}}}, \quad \mathcal{M}_1 = \frac{m_{\mathrm{SiO}} - m_{\mathrm{CO}}}{m_{\mathrm{SiO_2}}}, \quad \mathcal{M}_2 = \frac{2m_{\mathrm{CO}} - m_{\mathrm{CO_2}}}{m_{\mathrm{SiO_2}}}, \quad \mathcal{M}_3 = \frac{m_{\mathrm{SiO_2}}}{m_{\mathrm{bg}}}, \tag{3.64}$$

$$\sigma_{\mathrm{SiO}} = 1 - \frac{m_{\mathrm{SiO}}}{m_{\mathrm{bg}}}, \quad \sigma_{\mathrm{CO}} = 1 - \frac{m_{\mathrm{CO}}}{m_{\mathrm{bg}}}, \quad \sigma_{\mathrm{CO_2}} = 1 - \frac{m_{\mathrm{CO_2}}}{m_{\mathrm{bg}}}. \tag{3.65}$$

Here, ϱ is the ratio of intrinsic carbon monoxide concentration scale to the concentration of a gas at atmospheric pressure. The $\mathcal{M}_i$ are the normalized mass differences of the products and reactants in reactions (1.5)–(1.7), and the σ_i are normalized molar mass differences between i and the background gas.

3.1.6 Dimensionless initial conditions

The initial volume fractions are given by (3.28), (3.29), (3.24), with α_{gas}^0 given by (3.6). The initial number densities of carbon and quartz are

$$n_{\mathrm{C}} = 1, \quad n_{\mathrm{SiO_2}} = 1, \quad \text{at } t = 0, \tag{3.66}$$

while the dimensionless initial gas concentrations, gas density, and height of the bed are given by

$$C_{\mathrm{SiO}} = 0, \quad C_{\mathrm{CO}} = 0, \quad C_{\mathrm{CO_2}} = 0, \quad \rho_{\mathrm{gas}} = 1, \quad H = 1, \quad \text{at } t = 0. \tag{3.67}$$

3.1.7 Dimensionless boundary conditions

At $z = 0$, the boundary conditions (3.33) become

$$q_{\mathrm{CO}} = 1, \quad u\alpha_{\mathrm{gas}}\rho_{\mathrm{gas}} = \omega, \quad q_{\mathrm{SiO}} = 0, \quad q_{\mathrm{CO_2}} = 0, \quad u_s = 0, \tag{3.68}$$

where we introduce the dimensionless parameter

$$\omega = \frac{\mu H^0 RT}{\kappa m_{\mathrm{bg}} P_{\mathrm{atm}}^2}(m_{\mathrm{CO}} q_{\mathrm{CO}}^{\mathrm{in}} + m_{\mathrm{bg}} q_{\mathrm{bg}}^{\mathrm{in}}), \tag{3.69}$$

which is the normalized inlet mass flux.

At $z = H(t)$, we impose the dimensionless boundary conditions

$$q_{\mathrm{SiO}} - \frac{\mathrm{d}H}{\mathrm{d}t}\alpha_{\mathrm{gas}} C_{\mathrm{SiO}} = \chi_{\mathrm{SiO}}\alpha_{\mathrm{gas}} C_{\mathrm{SiO}}, \tag{3.70}$$

$$q_{\mathrm{CO}} - \frac{\mathrm{d}H}{\mathrm{d}t}\alpha_{\mathrm{gas}} C_{\mathrm{CO}} = \chi_{\mathrm{CO}}\alpha_{\mathrm{gas}} C_{\mathrm{CO}}, \tag{3.71}$$

$$q_{\mathrm{CO_2}} - \frac{\mathrm{d}H}{\mathrm{d}t}\alpha_{\mathrm{gas}} C_{\mathrm{CO_2}} = \chi_{\mathrm{CO_2}}\alpha_{\mathrm{gas}} C_{\mathrm{CO_2}}, \tag{3.72}$$

$$\begin{aligned} \mathrm{Da}\, u\alpha_{\mathrm{gas}}\rho - \frac{\mathrm{d}H}{\mathrm{d}t}\alpha_{\mathrm{gas}}\rho_{\mathrm{gas}} = {} & \chi_{\mathrm{bg}}(\alpha_{\mathrm{gas}}\rho_{\mathrm{gas}} - \alpha_{\mathrm{gas}}\psi) + \\ & \varrho \sum_{i\in\mathcal{G}} (\chi_i - \chi_{\mathrm{bg}})\mathcal{C}_i(1-\sigma_i)\alpha_{\mathrm{gas}} C_i, \end{aligned} \tag{3.73}$$

obtained from (3.37)–(3.40), where we introduce the final five dimensionless parameters

$$\chi_i = \frac{\theta_i}{H^0}\left(\frac{\rho_{\mathrm{SiO_2}}/m_{\mathrm{SiO_2}}}{k_3 (n^0_{\mathrm{SiO_2}})^{1/3} c^*_{\mathrm{CO}}}\right) \quad i \in \mathcal{G}, \tag{3.74}$$

$$\chi_{\mathrm{bg}} = \frac{\theta_{\mathrm{bg}}}{H^0}\left(\frac{\rho_{\mathrm{SiO_2}}/m_{\mathrm{SiO_2}}}{k_3 (n^0_{\mathrm{SiO_2}})^{1/3} c^*_{\mathrm{CO}}}\right), \quad \psi = \frac{C^{\mathrm{out}}_{\mathrm{bg}} RT}{P_{\mathrm{atm}}}. \tag{3.75}$$

Here, χ_i and χ_{bg} are the dimensionless mass transfer coefficients, and ψ is the normalized background gas concentration above the surface of particles. Finally, in dimensionless form the height of the bed of particles satisfies

$$\frac{\mathrm{d}H}{\mathrm{d}t} = u_s, \quad \text{at } z = H(t). \tag{3.76}$$

3.2 Model summary

In summary, our dimensionless model comprises equations (3.6), (3.17), (3.51)–(3.55), (3.57)–(3.59), (3.62), (3.63), and (3.76); initial conditions (3.24), (3.28), (3.29), (3.66), and (3.67); and boundary conditions (3.68) and (3.70)–(3.73), for the 13 dependent variables α_{C}, α_{SiC}, $\alpha_{\mathrm{SiO_2}}$, α_{gas}, n_{C}, $n_{\mathrm{SiO_2}}$, C_{SiO}, C_{CO}, $C_{\mathrm{CO_2}}$, u_s, u, ρ, and H, and depends on 22 dimensionless parameters.

We estimate the values of the dimensionless parameters in Table 3.2. We consider the regime where $\delta \ll 1$ and the rest of the parameters are $\mathcal{O}(1)$ to recover the richest possible dynamics. We will see that the resulting evolution of the gas concentrations are quasi-steady at leading order in δ, while the consumption of the carbon and quartz particles remain time dependent. We also identify two time-scales within our system: (1) a short time-scale over which the gas concentrations equilibrate, but the quartz and carbon do not react. Due to the density difference between the gases and the solids, the solids do not evolve on the short time-scale. (2) The time-scale that we non-dimensionalized with, on which the gas concentrations are quasi-steady, but the reactions with the quartz and carbon occur.

3.3 Paradigm models

We investigate two paradigm problems in detail in order to understand the mathematical structure of problems related to ours. The paradigm problems will give us insight into the interplay of transport and reactions in certain parameter regimes of the full model. We begin with a one-reaction system involving motion of the solid, and will then move on to study a three-reaction system, before then solving the full model.

3.3.1 One-reaction system involving solid advection

We will first consider the paradigm problem of a single gas, $\mathcal{G}$, reacting with a single solid, $\mathcal{S}_1$, to form a solid product, $\mathcal{S}_2$, in the simple reaction

$$\mathcal{S}_1 + \mathcal{G} \longrightarrow \mathcal{S}_2. \tag{3.77}$$

We assume that the porosity of the solid mixture is constant for simplicity, but allow a molar density difference between the reactant solid and the product solid so that the solid particles move in such a way to keep the porosity constant. We also assume that the gas flow speed is constant and that the gas mixture density is constant. We

Table 3.2: Values for the dimensionless parameters, computed using the values in Table 3.1.

Parameter	Description	Typical value
$\delta = \dfrac{c^*_{\mathrm{CO}}}{\rho_{\mathrm{SiO_2}}/m_{\mathrm{SiO_2}}}$	Gas to solid concentration ratio	10^{-4}
$\mathcal{M}_{\mathrm{C}} = \dfrac{\rho_{\mathrm{SiO_2}}/m_{\mathrm{SiO_2}}}{\rho_{\mathrm{C}}/m_{\mathrm{C}}}$	Normalized concentration of carbon	0.233
$\mathcal{M}_{\mathrm{SiC}} = \dfrac{\rho_{\mathrm{SiO_2}}/m_{\mathrm{SiO_2}}}{\rho_{\mathrm{SiC}}/m_{\mathrm{SiC}}}$	Normalized concentration of silicon carbide	0.550
$\mathcal{C}_{\mathrm{SiO}} = c^*_{\mathrm{SiO}}/c^*_{\mathrm{CO}}$	Silicon monoxide concentration ratio	1
$\mathcal{C}_{\mathrm{CO_2}} = c^*_{\mathrm{CO_2}}/c^*_{\mathrm{CO}}$	Carbon dioxide concentration ratio	1
$\mathrm{Da} = \dfrac{\kappa P_{\mathrm{atm}}}{\mu (H^0)^2}\left(\dfrac{\rho_{\mathrm{SiO_2}}/m_{\mathrm{SiO_2}}}{k_3 (n^0_{\mathrm{SiO_2}})^{1/3} c^*_{\mathrm{CO}}}\right)$	Damköhler number	493.5
$\mathrm{Pe}_i = \dfrac{\kappa P_{\mathrm{atm}}}{\mathscr{D}_i \mu}$	Péclet number of species i	100
$\varrho = \dfrac{c^*_{\mathrm{CO}} RT}{P_{\mathrm{atm}}}$	Background gas concentration ratio	0.83
$\mathcal{M}_1 = (m_{\mathrm{SiO}} - m_{\mathrm{CO}})/m_{\mathrm{SiO_2}}$	Normalized mass difference of (1.5)	0.267
$\mathcal{M}_2 = (2m_{\mathrm{CO}} - m_{\mathrm{CO_2}})/m_{\mathrm{SiO_2}}$	Normalized mass difference of (1.6)	0.200
$\mathcal{M}_3 = m_{\mathrm{SiO_2}}/m_{\mathrm{bg}}$	Molar mass ratio of quartz and background gas	2.14
$\sigma_{\mathrm{SiO}} = 1 - m_{\mathrm{SiO}}/m_{\mathrm{bg}}$	Silicon monoxide molar mass ratio	-0.571
$\sigma_{\mathrm{CO}} = 1 - m_{\mathrm{CO}}/m_{\mathrm{bg}}$	Carbon monoxide molar mass ratio	0.00
$\sigma_{\mathrm{CO_2}} = 1 - m_{\mathrm{CO_2}}/m_{\mathrm{bg}}$	Carbon dioxide molar mass ratio	-0.571
$\omega = \dfrac{\mu H^0 RT}{\kappa m_{\mathrm{bg}} P^2_{\mathrm{atm}}}(m_{\mathrm{CO}} q^{\mathrm{in}}_{\mathrm{CO}} + m_{\mathrm{bg}} q^{\mathrm{in}}_{\mathrm{bg}})$	Dimensionless inlet mass flux	8.3
$\chi_i = \dfrac{\theta_i \rho_{\mathrm{SiO_2}}/m_{\mathrm{SiO_2}}}{H^0 k_3 (n^0_{\mathrm{SiO_2}})^{1/3} c^*_{\mathrm{CO}}}$	Dimensionless mass transfer of species i	500
$\psi = \dfrac{C^{\mathrm{out}}_{\mathrm{bg}} RT}{P_{\mathrm{atm}}}$	Normalized outlet background gas concentration	1

neglect any dependence of reaction rates on the number density of solid particles.

We thus consider the dimensionless model

$$\frac{\partial S_1}{\partial t} + \frac{\partial}{\partial z}(u_s S_1) = -\mathcal{M} S_1^{2/3} g, \tag{3.78}$$

$$\frac{\partial S_2}{\partial t} + \frac{\partial}{\partial z}(u_s S_2) = S_1^{2/3} g, \tag{3.79}$$

$$\delta\left(\frac{\partial g}{\partial t} + \mathcal{U}\frac{\partial g}{\partial z} - \mathcal{D}\frac{\partial^2 g}{\partial z^2}\right) = -S_1^{2/3} g, \tag{3.80}$$

$$S_1 + S_2 = 1 - \phi_0, \tag{3.81}$$

where S_1 and S_2 are the volume fractions of $\mathcal{S}_1$ and $\mathcal{S}_2$, and g is the gas concentration of $\mathcal{G}$. Futhermore, $\mathcal{M}$ relates the molar densities of S_1 and S_2, ϕ_0 is the (constant) porosity, δ is the concentration ratio of gas to S_2, and $\mathcal{U}$ and $\mathcal{D}$ are the advection and diffusion Damköhler numbers. We consider the case where $\mathcal{M}$, ϕ_0, $\mathcal{U}$, and $\mathcal{D}$ are $\mathcal{O}(1)$, and $\delta \ll 1$.

By adding (3.78) and (3.79), and substituting for S_2 from (3.81) we find that

$$(1 - \phi_0)\frac{\partial u_s}{\partial z} = -(\mathcal{M} - 1) S_1^{2/3} g. \tag{3.82}$$

If the product solid has a higher molar density than the reactant solid, then $\mathcal{M} > 1$ and thus $u_s < 0$. In our analysis we use (3.82) in place of (3.79).

We pose the initial conditions

$$g(z,0) = 0, \quad S_1(z,0) = 1 - \phi_0, \quad S_2(z,0) = 0, \quad H(0) = 1, \tag{3.83}$$

where $H(t)$ is the height of the particles, and the boundary conditions

$$g(0,t) = 1, \quad u_s(0,t) = 0 \quad \text{at } z = 0, \tag{3.84}$$

and

$$g(H(t),t) = 0, \quad \frac{\mathrm{d}H}{\mathrm{d}t} = u_s(H(t),t) \quad \text{at } z = H(t). \tag{3.85}$$

This represents the situation where there is not gas in the crucible initially, and we supply some at the lower boundary.

We seek a numerical solution using the method of lines using second-order central differences in space for the diffusion terms, and an upwind scheme for the advective terms. Due to the moving boundary at the top of the particles, we transform to a

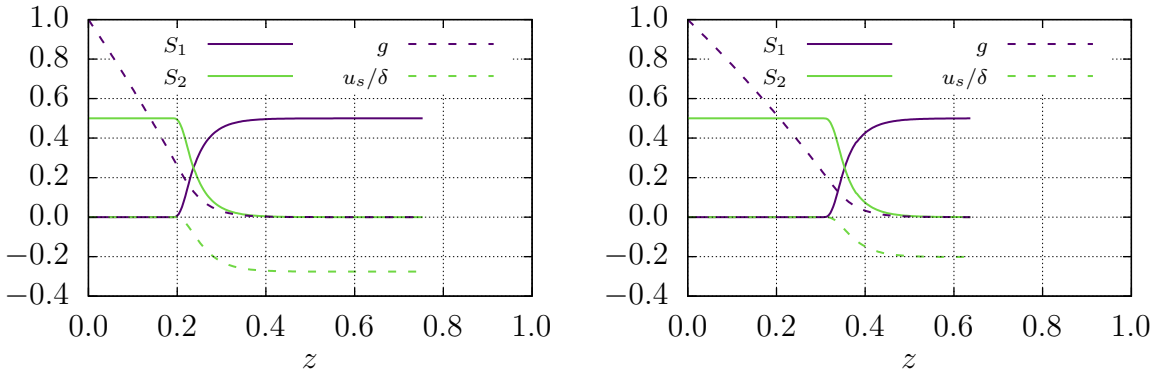

(a) (b)

Figure 3.3: Numerical solution of the problem (3.78)–(3.85) at (a) $t = 500$ and (b) $t = 1000$. The parameter values are $\mathcal{D} = 1$, $\mathcal{U} = 1$, $\phi_0 = 0.5$, $\mathcal{M} = 2$, and $\delta = 10^{-3}$. Note that we plot u_s/δ rather than u_s for ease of visualization.

fixed domain by

$$\tau = t, \quad \xi = \frac{z}{H(t)}. \tag{3.86}$$

This discretization turns (3.82) into a set of algebraic constraints, and so we have a set of differential-algebraic equations (DAEs) to solve. We specify the resulting DAE system in Julia [101, 102], and solve the system with the DAE solver `IDA` of SUNDIALS [103] using adaptive-step time integrations.

We show the solution to (3.78)–(3.85) in Figure 3.3, where we plot u_s/δ rather than u_s for ease of visualization. We see that a reaction front forms, which we say is located at $z = h(t)$ such that $S_1 = (1 - \phi)/2$, with $h(0) = 0$. The reaction front separates the gas and reacted solid from the unreacted solid and that the upper surface moves downward as material is consumed, as expected. Within the reaction front, the gas concentration is $\mathcal{O}\big(\delta^{1/2}\big)$, as we can see around $z = 0.25$ in Figure 3.3a. Furthermore, we see that the system evolves slowly due to the large density difference between the gas and solids. Guided by the numerical solution, we scale to a long timescale by using $T = \delta t$, and let

$$S_1 = S_1^0 + \delta^{3/2} S_1^1 + \dots, \qquad h = h^0 + \dots, \qquad g = g^0 + \dots, \tag{3.87}$$

$$S_2 = S_2^0 + \delta^{3/2} S_2^1 + \dots, \qquad u_s = u_s^0 + \delta u_s^1 + \dots, \tag{3.88}$$

so that the reaction balances the gas transport. Then, taking the limit as $\delta \to 0$, the

leading-order equations are

$$\frac{\partial}{\partial z}\left(u_s^0 S_1^0\right) = -\mathcal{M}(S_1^0)^{2/3} g^0, \tag{3.89}$$

$$0 = -(S_1^0)^{2/3} g^0, \tag{3.90}$$

$$(1-\phi_0)\frac{\partial u_s^0}{\partial z} = -(\mathcal{M}-1)(S_1^0)^{2/3} g^0, \tag{3.91}$$

$$S_1^0 + S_2^0 = 1 - \phi_0. \tag{3.92}$$

From (3.90) we must have $S_1^0 = 0$ or $g^0 = 0$, which agrees with the numerical solution away from the reaction front: $g^0 = 0$ ahead of the front (*i.e.* the gas has not penetrated that far) and $S_1^0 = 0$ and $S_2^0 = 1 - \phi_0$ behind the front (*i.e.* all the reactant has been consumed). Furthermore, substituting (3.90) into (3.91) leads to the conclusion that $u_s^0 = 0$ behind the front (*i.e.* the layer has completely reacted). However, the leading-order system does not yield g^0 behind the front.

Ahead of the front (*i.e.* in $z > h^0(T)$), since $g^0 = 0$, (3.89) tells us that the solid does not react, and therefore when combined with (3.91) and the upstream boundary conditions (3.85) we have

$$S_1^0 = 1 - \phi_0, \quad S_2^0 = 0. \tag{3.93}$$

Finally,

$$u_s^0 = u_s^{*,0}(T) \tag{3.94}$$

for $z > h^0(T)$, where $u_s^{*,0}(T)$ is yet to be determined.

In order to find g^0 behind the reaction front, we must look at the next-order versions of (3.78)–(3.82). We find that

$$\delta^{5/2}\frac{\partial}{\partial z}\left(u_s^1 S_1^1\right) = -\delta\mathcal{M}(S_1^1)^{2/3} g^0, \tag{3.95}$$

$$\delta\left(\mathcal{U}\frac{\partial g^0}{\partial z} - \mathcal{D}\frac{\partial^2 g^0}{\partial z^2}\right) = -\delta(S_1^1)^{2/3} g^0, \tag{3.96}$$

$$\delta(1-\phi_0)\frac{\partial u_s^1}{\partial z} = -\delta(\mathcal{M}-1)(S_1^1)^{2/3} g^0, \tag{3.97}$$

$$S_1^1 + S_2^1 = 0, \tag{3.98}$$

where we have used the fact that $S_1^0 = 0$ and $u_s^0 = 0$ for $z < h^0(T)$. In order for both S_1^1 and u_s^1 to be non-zero, we must have a balance in (3.95). However, (3.95) does not

balance and implies that either $S_1^1 = 0$ or $g^0 = 0$ for $z < h^0(T)$. It is not possible to balance the reaction terms in (3.95)–(3.97) simultaneously, regardless of our choice of asymptotic expansion. Thus, $S_1^1 = 0$ and $u_s^1 = 0$. Therefore, writing $\mathrm{Pe} = \mathcal{U}/\mathcal{D}$, g^0 satisfies

$$\mathrm{Pe}\,\frac{\partial g^0}{\partial z} - \frac{\partial^2 g^0}{\partial z^2} = 0 \tag{3.99}$$

by (3.96), where $g^0(0) = 1$ and $g^0(h^0) = 0$, which has the solution

$$g^0 = \frac{\mathrm{e}^{\mathrm{Pe}\,h^0} - \mathrm{e}^{\mathrm{Pe}\,z}}{\mathrm{e}^{\mathrm{Pe}\,h^0} - 1}. \tag{3.100}$$

We explore the behaviour of the moving reaction front using the substitutions

$$\zeta = \frac{z - h(\tau)}{\delta^{1/2}}, \quad \tau = T, \quad G = \frac{g}{\delta^{1/2}}, \tag{3.101}$$

in order to preserve the gradients and given the observation that $g = \mathcal{O}\big(\delta^{1/2}\big)$ in the reaction layer, so that

$$\delta^{1/2}\frac{\partial S_1}{\partial \tau} - \frac{\mathrm{d}h}{\mathrm{d}\tau}\frac{\partial S_1}{\partial \zeta} + \frac{\partial}{\partial \zeta}(u_s S_1) = -\mathcal{M} S_1^{2/3} G, \tag{3.102}$$

$$\delta\left(\delta\frac{\partial G}{\partial \tau} - \delta^{1/2}\frac{\mathrm{d}h}{\mathrm{d}\tau}\frac{\partial G}{\partial \zeta} + \delta^{1/2}\mathcal{U}\frac{\partial G}{\partial \zeta} - \frac{\mathcal{D}}{\delta}\frac{\partial^2 G}{\partial \zeta^2}\right) = -S_1^{2/3} G, \tag{3.103}$$

$$(1 - \phi_0)\frac{\partial u_s}{\partial \zeta} = -(\mathcal{M} - 1) S_1^{2/3} G, \tag{3.104}$$

$$S_1 + S_2 = 1 - \phi_0. \tag{3.105}$$

Taking the leading-order behaviour, we find

$$-\frac{\mathrm{d}h^0}{\mathrm{d}\tau}\frac{\partial S_1^0}{\partial \zeta} + \frac{\partial}{\partial \zeta}\big(u_s^0 S_1^0\big) = -\mathcal{M}(S_1^0)^{2/3} G^0, \tag{3.106}$$

$$-\mathcal{D}\frac{\partial^2 G^0}{\partial \zeta^2} = -(S_1^0)^{2/3} G^0, \tag{3.107}$$

$$\frac{\partial u_s^0}{\partial \zeta} = -\left(\frac{\mathcal{M} - 1}{1 - \phi_0}\right)(S_1^0)^{2/3} G^0, \tag{3.108}$$

$$S_1^0 + S_2^0 = 1 - \phi_0. \tag{3.109}$$

Combining (3.106) and (3.107) we find

$$-\mathcal{D}\frac{\partial^2 G^0}{\partial \zeta^2} = \frac{1}{\mathcal{M}}\frac{\partial}{\partial \zeta}\left(\left(u_s^0 - \frac{\mathrm{d}h^0}{\mathrm{d}\tau}\right)S_1^0\right), \tag{3.110}$$

and thus,

$$-\mathcal{D}\mathcal{M}\frac{\partial G^0}{\partial \zeta} = \left(u_s^0 - \frac{\mathrm{d}h^0}{\mathrm{d}\tau}\right)S_1^0 + A(\tau) \tag{3.111}$$

after integrating. Taking the limit $\zeta \to \infty$, and matching to the outer solution ahead of the front, in which $g^0 = 0$ and (3.93) holds, we find

$$A(\tau) = -\left(u_s^{*,0} - \frac{\mathrm{d}h^0}{\mathrm{d}\tau}\right)(1-\phi_0), \tag{3.112}$$

and, therefore

$$-\mathcal{D}\mathcal{M}\frac{\partial G^0}{\partial \zeta} = \left(u_s^0 - \frac{\mathrm{d}h^0}{\mathrm{d}\tau}\right)S_1^0 - \left(u_s^{*,0} - \frac{\mathrm{d}h^0}{\mathrm{d}\tau}\right)(1-\phi_0). \tag{3.113}$$

Considering $\zeta \to -\infty$, where $S_1^0 \to 0$, we find that

$$\mathcal{D}\mathcal{M}\frac{\partial G^0}{\partial \zeta} = \left(u_s^{*,0} - \frac{\mathrm{d}h^0}{\mathrm{d}\tau}\right)(1-\phi_0), \tag{3.114}$$

which provides a matching condition for the outer solution behind the reaction front and relates the gas flux into the reaction front with the speed of the reaction front.

In order to determine $u_s^{*,0}$, we eliminate the reaction terms between (3.106) and (3.108) to find that

$$\frac{1}{\mathcal{M}}\frac{\partial}{\partial \zeta}\left(\left(u_s^0 - \frac{\mathrm{d}h^0}{\mathrm{d}\tau}\right)S_1^0\right) = \left(\frac{1-\phi_0}{\mathcal{M}-1}\right)\frac{\partial u_s^0}{\partial \zeta}, \tag{3.115}$$

which we integrate to find

$$\frac{\mathcal{M}}{\mathcal{M}-1}u_s^0 = \frac{\left(u_s^0 - \dfrac{\mathrm{d}h^0}{\mathrm{d}\tau}\right)}{(1-\phi_0)}S_1^0 + B(\tau). \tag{3.116}$$

As $\zeta \to -\infty$, since $u_s^0 \to 0$ and $S_1^0 \to 0$ we find $B(\tau) = 0$ and, hence as $\zeta \to \infty$,

we find that

$$u_s^{*,0} = -(\mathcal{M}-1)\frac{\mathrm{d}h^0}{\mathrm{d}\tau}, \tag{3.117}$$

since $u_s^0 \to u_s^{*,0}$ and $S_1^0 \to 1-\phi_0$. The speed of the solid advection is proportional to the speed of the reaction front, weighted by the volume difference of the reactant solid and product solid.

Having determined $u_s^{*,0}$, we may then determine the height of the bed of particles. We recall that

$$\frac{\mathrm{d}H^0}{\mathrm{d}\tau} = u_s^0(H^0,\tau) = u_s^{*,0}(\tau). \tag{3.118}$$

Then,

$$H^0(\tau) = 1 + \int_0^\tau u_s^{*,0}(t)\,\mathrm{d}t = 1-(\mathcal{M}-1)h^0(\tau), \tag{3.119}$$

by (3.117), and we have a relationship between the height of the bed and the position of the reaction front.

To determine $h^0(\tau)$, we return to the outer region behind the reaction front. From the matching condition (3.114) we find

$$-\mathcal{M}\mathcal{U}\frac{\mathrm{e}^{\mathrm{Pe}\,h^0}}{\mathrm{e}^{\mathrm{Pe}\,h^0}-1} = \left(u_s^{*,0} - \frac{\mathrm{d}h^0}{\mathrm{d}\tau}\right)(1-\phi_0), \tag{3.120}$$

$$= -\mathcal{M}(1-\phi_0)\frac{\mathrm{d}h^0}{\mathrm{d}\tau} \tag{3.121}$$

by (3.117). Thus, rearranging (3.121) we find that h^0 satisfies the nonlinear ODE

$$\frac{\mathcal{U}}{1-\phi_0} = \left(1-\mathrm{e}^{-\mathrm{Pe}\,h^0}\right)\frac{\mathrm{d}h^0}{\mathrm{d}\tau}, \tag{3.122}$$

with $h^0(0)=0$. Thus,

$$\frac{\mathcal{U}\,\mathrm{Pe}}{1-\phi_0}\tau + 1 = \mathrm{Pe}\,h^0 + \mathrm{e}^{-\mathrm{Pe}\,h^0}. \tag{3.123}$$

In the large Péclet number limit, the transport of the gas is advection dominated and so

$$h^0(\tau) \sim \frac{\mathcal{U}\tau}{1-\phi_0}, \tag{3.124}$$

while for small Péclet numbers, we find that

$$h^0(\tau) \sim \left(\frac{2\mathcal{D}\tau}{1-\phi_0}\right)^{1/2}, \tag{3.125}$$

since the transport is diffusion dominated.

Inverting (3.123), we find the position of the reaction front to be explicitly given by

$$h^0(\tau) = \frac{1}{\mathrm{Pe}}\left[\frac{\mathcal{U}\,\mathrm{Pe}}{1-\phi_0}\tau + 1 + W\left(-\exp\left(-\frac{\mathcal{U}\,\mathrm{Pe}}{1-\phi_0}\tau - 1\right)\right)\right], \tag{3.126}$$

where W is the principal branch of the Lambert W function [136]. From (3.119), we determine the height of the solid mixture to be given by

$$H^0(\tau) = 1 - \frac{(\mathcal{M}-1)}{\mathrm{Pe}}\left[\frac{\mathcal{U}\,\mathrm{Pe}}{1-\phi_0}\tau + 1 + W\left(-\exp\left(-\frac{\mathcal{U}\,\mathrm{Pe}}{1-\phi_0}\tau - 1\right)\right)\right]. \tag{3.127}$$

Finally, to work out $u_s^{*,0}$ we first take the time derivative of (3.126) to find the speed of the front to be

$$\frac{\mathrm{d}h^0}{\mathrm{d}\tau}(\tau) = \frac{\mathcal{U}}{1-\phi_0}\left[1 + W\left(-\exp\left(-\frac{\mathcal{U}\,\mathrm{Pe}}{1-\phi_0}\tau - 1\right)\right)\right]^{-1}, \tag{3.128}$$

and therefore, from (3.117), we find that

$$u_s^{*,0}(\tau) = -\frac{\mathcal{U}(\mathcal{M}-1)}{1-\phi_0}\left[1 + W\left(-\exp\left(-\frac{\mathcal{U}\,\mathrm{Pe}}{1-\phi_0}\tau - 1\right)\right)\right]^{-1}. \tag{3.129}$$

We show a numerical solution to the long time re-scaled version of the system (3.78)–(3.85) as well as the solution of the leading-order boundary layer system (3.106)–(3.108) (dashed) in Figure 3.4. We see that the asymptotic solution closely approximates the full solution.

In Figure 3.5 we compare the position of the reaction front extracted from the simulation with the prediction from (3.126). We find great agreement between the two until $t \approx 1.7$, at which point h extracted from the numerics flattens. At this point all the S_1 has been consumed and the reaction stops. We compare u_s^* in the simulation with our prediction (3.129) in Figure 3.6. We find good agreement between the two until $t \approx 1.5$, when the reaction front begins to interact with the upper boundary.

The key insights we draw from this paradigm problem is that we identify a travelling wave solution due to the reaction. Furthermore, we found that the speed of the reaction front is proportional to the flux of the gas into the reaction front. Having

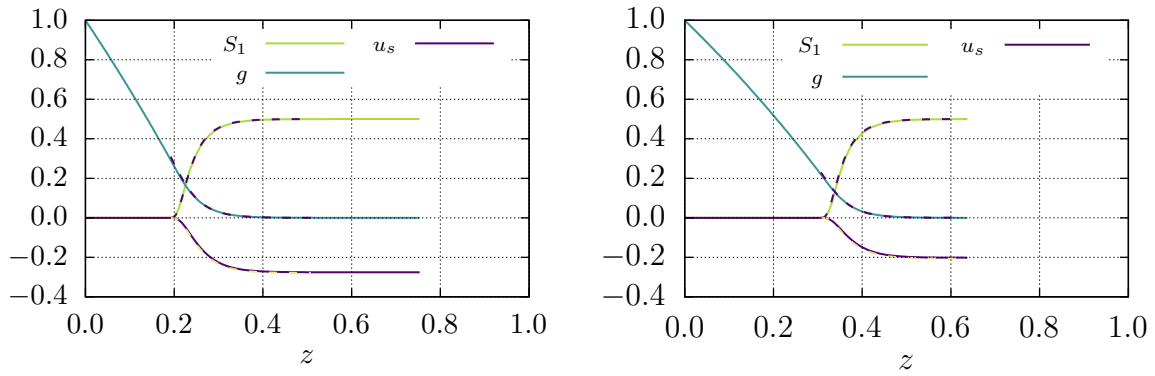

Figure 3.4: Numerical solution of the re-scaled problem (3.78)–(3.85) and asymptotic solution (dashed) of (3.106)–(3.108) at (a) $t = 0.5$ and (b) $t = 1.0$. The parameter values are $\mathcal{D} = 1$, $\mathcal{U} = 1$, $\phi_0 = 0.5$, $\mathcal{M} = 2$, and $\delta = 10^{-3}$.

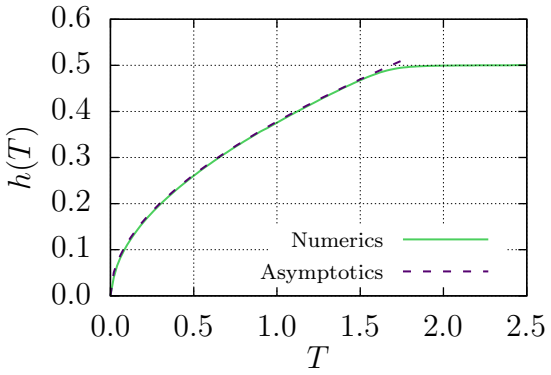

Figure 3.5: Position of the reaction front from the numerical solution of the re-scaled problem (3.78)–(3.85) and asymptotic approximation (3.126). The parameter values are $\mathcal{D} = 1$, $\mathcal{U} = 1$, $\phi_0 = 0.5$, $\mathcal{M} = 2$, and $\delta = 10^{-3}$.

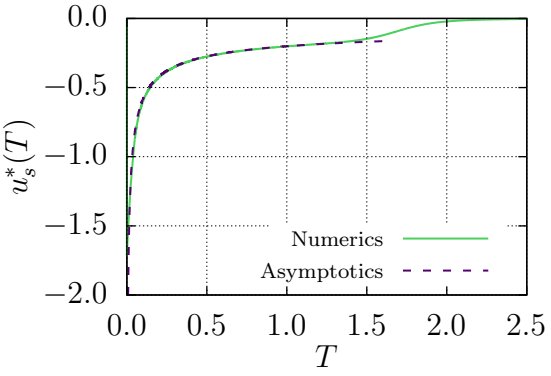

Figure 3.6: Solid velocity at the top of the bed of particles from the numerical solution of the re-scaled problem (3.78)–(3.85) and asymptotic approximation (3.129). The parameter values are $\mathcal{D} = 1$, $\mathcal{U} = 1$, $\phi_0 = 0.5$, $\mathcal{M} = 2$, and $\delta = 10^{-3}$.

solved this paradigm problem numerically and found the leading-order asymptotic behaviour, we now consider another paradigm problem that is more representative of the chemistry of our full system.

3.3.2 Three-reaction system

We now consider a system with three solids, three gases, and three reactions—similar to our full system, but we still assume the gas density is constant, and the gas flows at constant speed. We also make the additional assumption that molar densities of the solids are equal, so that there is no solid flow induced by the reactions. We consider the paradigm reactions

$$\mathcal{G}_1 + 2\mathcal{S}_1 \to \mathcal{S}_2 + \mathcal{G}_2, \tag{3.130}$$

$$\mathcal{G}_2 + \mathcal{S}_3 \to \mathcal{G}_1 + \mathcal{G}_3, \tag{3.131}$$

$$\mathcal{G}_3 + \mathcal{S}_1 \to 2\mathcal{G}_2, \tag{3.132}$$

which are analogous to (1.5)–(1.7), with net reaction

$$3\mathcal{S}_1 + \mathcal{S}_3 \to \mathcal{S}_2 + 2\mathcal{G}_2, \tag{3.133}$$

which is analogous to (1.9).

We follow a similar methodology as in the first paradigm problem. We consider the dimensionless model

$$\frac{\partial S_1}{\partial t} = S_1^{2/3}(-2g_1 - g_3), \tag{3.134}$$

$$\frac{\partial S_2}{\partial t} = S_1^{2/3} g_1, \tag{3.135}$$

$$\frac{\partial S_3}{\partial t} = -S_3^{2/3} g_2, \tag{3.136}$$

$$\delta\left(\frac{\partial g_1}{\partial t} + \mathcal{U}\frac{\partial g_1}{\partial z} - \mathcal{D}\frac{\partial^2 g_1}{\partial z^2}\right) = -S_1^{2/3} g_1 + S_3^{2/3} g_2, \tag{3.137}$$

$$\delta\left(\frac{\partial g_2}{\partial t} + \mathcal{U}\frac{\partial g_2}{\partial z} - \mathcal{D}\frac{\partial^2 g_2}{\partial z^2}\right) = S_1^{2/3} g_1 - S_3^{2/3} g_2 + 2S_1^{2/3} g_3, \tag{3.138}$$

$$\delta\left(\frac{\partial g_3}{\partial t} + \mathcal{U}\frac{\partial g_3}{\partial z} - \mathcal{D}\frac{\partial^2 g_3}{\partial z^2}\right) = S_3^{2/3} g_2 - S_1^{2/3} g_3. \tag{3.139}$$

Here, S_1, S_2, and S_3 are analogous to the volume fractions of carbon, silicon carbide, and quartz respectively, and g_1, g_2, and g_3 are analogous to the concentrations of

silicon monoxide, carbon monoxide, and carbon dioxide, respectively, and we will refer to the variables in this way. We assume we have a prescribed amount of carbon and quartz and no silicon carbide initially, so that

$$S_1 = \lambda_1, \quad S_2 = 0, \quad S_3 = \lambda_3, \quad \text{at } t = 0, \tag{3.140}$$

and we assume that $\lambda_1 \geq 3\lambda_3$ so that the system has an excess of carbon. Furthermore, we suppose that there are no reactive gases present in the system initially and so we write

$$g_1 = 0, \quad g_2 = 0, \quad g_3 = 0, \quad \text{at } t = 0. \tag{3.141}$$

We assume that the flux of carbon monoxide through the bottom of the crucible is prescribed, and that there is no flux of silicon monoxide or carbon dioxide here. Thus, we write

$$\mathcal{U}g_1 - \mathcal{D}\frac{\partial g_1}{\partial z} = 0, \quad \mathcal{U}g_2 - \mathcal{D}\frac{\partial g_2}{\partial z} = \mathcal{U}, \quad \mathcal{U}g_3 - \mathcal{D}\frac{\partial g_3}{\partial z} = 0, \quad \text{at } z = 0. \tag{3.142}$$

Finally, we assume that the concentration of the gaseous components just above the solid layer are maintained at zero and so we write

$$g_1 = 0, \quad g_2 = 0, \quad g_3 = 0, \quad \text{at } z = 1. \tag{3.143}$$

We again assume that $\mathcal{U}$, $\mathcal{D}$, λ_1, and λ_3 are $\mathcal{O}(1)$, while $\delta \ll 1$.

We begin by solving the system (3.134)–(3.143) numerically to help guide scalings for the asymptotics. Surprisingly, we find that the gas concentrations are $\mathcal{O}(\delta^{-1})$ and that the system evolves on a fast timescale of $\mathcal{O}\big(\delta^{1/2}\big)$. We use the same scheme and implementation as in the first paradigm problem. However, we do not need to transform the domain as we have neglected the motion of the solid. We show two snapshots of the solution in Figure 3.7, where we plot δg_i rather than g_i for ease of visualization. We see that, as with the previous problem, a moving reaction front develops. The difference between this problem and the previous one is that, here, the reactions are self-sustaining and there is a net production of g_2—we are not limited by the transport of gas to the reaction front. Therefore, we expect a large amount of gas to be produced. Since δ is the concentration ratio of gas to solid, it is unsurprising that an $\mathcal{O}(1)$ amount of solid produces an $\mathcal{O}(\delta^{-1})$ amount of gas. To explore the behaviour of the system further, we transform to the short timescale and

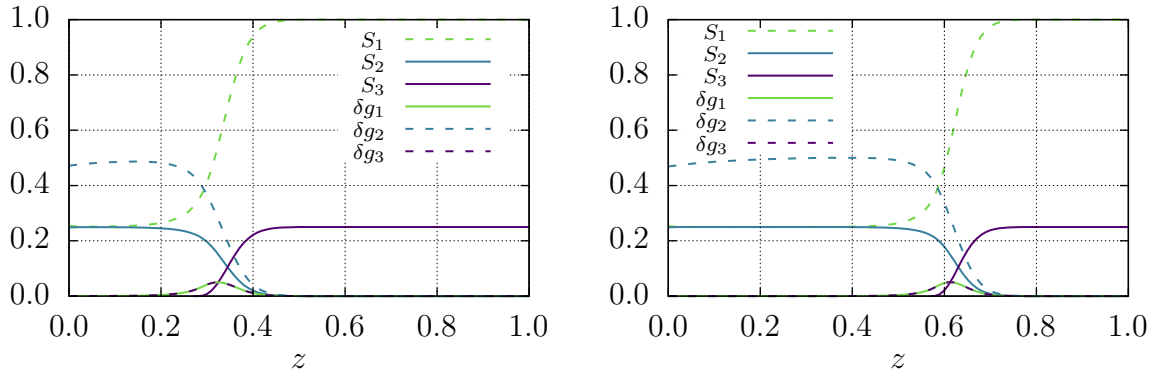

(a) (b)

Figure 3.7: Numerical solution of the problem (3.134)–(3.143) (a) $t = 0.005$ and (b) $t = 0.007$. The parameter values are $\mathcal{D} = 1$, $\mathcal{U} = 1$, $\lambda_1 = 1$, $\lambda_3 = 0.25$ and $\delta = 10^{-3}$. Note that we plot δg_i rather than g_i for ease of visualization.

the large-gas-concentration scale by using

$$t = \delta^{1/2} T, \quad g_i = \frac{G_i}{\delta}. \tag{3.144}$$

The transformed system reads

$$\delta^{1/2}\frac{\partial S_1}{\partial T} = S_1^{2/3}(-2G_1 - G_3), \tag{3.145}$$

$$\delta^{1/2}\frac{\partial S_2}{\partial T} = S_1^{2/3} G_1, \tag{3.146}$$

$$\delta^{1/2}\frac{\partial S_3}{\partial T} = -S_3^{2/3} G_2, \tag{3.147}$$

$$\delta^{1/2}\frac{\partial G_1}{\partial T} + \delta\left(\mathcal{U}\frac{\partial G_1}{\partial z} - \mathcal{D}\frac{\partial^2 G_1}{\partial z^2}\right) = -S_1^{2/3} G_1 + S_3^{2/3} G_2, \tag{3.148}$$

$$\delta^{1/2}\frac{\partial G_2}{\partial T} + \delta\left(\mathcal{U}\frac{\partial G_2}{\partial z} - \mathcal{D}\frac{\partial^2 G_2}{\partial z^2}\right) = S_1^{2/3} G_1 - S_3^{2/3} G_2 + 2S_1^{2/3} G_3, \tag{3.149}$$

$$\delta^{1/2}\frac{\partial G_3}{\partial T} + \delta\left(\mathcal{U}\frac{\partial G_3}{\partial z} - \mathcal{D}\frac{\partial^2 G_3}{\partial z^2}\right) = S_3^{2/3} G_2 - S_1^{2/3} G_3, \tag{3.150}$$

with initial conditions given by (3.140) and (3.141), and boundary conditions given by

$$\mathcal{U}G_1 - \mathcal{D}\frac{\partial G_1}{\partial z} = 0, \quad \mathcal{U}G_2 - \mathcal{D}\frac{\partial G_2}{\partial z} = \delta\mathcal{U}, \quad \mathcal{U}G_3 - \mathcal{D}\frac{\partial G_3}{\partial z} = 0, \quad \text{at } z = 0, \tag{3.151}$$

and with (3.143) holding at $z = 1$.

3.3.2.1 Outer solutions

We take the limit $\delta \to 0$ and solve the leading-order system to find the outer solutions ahead and behind the front. We begin with the leading-order versions of gas equations (3.148)–(3.150), which we write as

$$\mathbf{0} = \begin{pmatrix} -(S_1^0)^{2/3} & (S_3^0)^{2/3} & 0 \\ (S_1^0)^{2/3} & -(S_3^0)^{2/3} & 2(S_1^0)^{2/3} \\ 0 & (S_3^0)^{2/3} & -(S_1^0)^{2/3} \end{pmatrix} \begin{pmatrix} G_1^0 \\ G_2^0 \\ G_3^0 \end{pmatrix}. \tag{3.152}$$

The determinant d of this matrix is

$$d = 2(S_1^0)^{4/3}(S_3^0)^{2/3}. \tag{3.153}$$

Ahead of the reaction front S_1^0 and S_3^0 are both positive so the determinant is non-zero, and so all the G_i^0 are zero for $z > h^0(T)$. Since we have assumed an excess of carbon, we must have $S_3^0 = 0$ behind the reaction front, $z < h^0(T)$. Substituting this into (3.152), and solving the resulting system yields that $G_1^0 = G_3^0 = 0$ for $z < h^0(T)$, and therefore, $G_1^0 = G_3^0 = 0$ everywhere outside of the reaction front. Similar to the previous problem, we cannot determine G_2^0 at leading order.

With $G_1^0 = 0$ and $G_3^0 = 0$ in both outer regions, $G_2^0 = 0$ ahead of the front, and $S_3^0 = 0$ behind the front, no reactions take place in the outer regions at leading order. So, S_1^0, S_2^0, and S_3^0 are uniform in both outer regions. Ahead of the front we maintain the initial conditions in (3.140), whereas, behind the front we have $S_3^0 = 0$. We cannot yet determine the values of S_1^0 and S_2^0 in $z < h^0(T)$, where h is the position of the reaction front. However, intuitively, by the net reaction (3.133) we expect λ_3 amount of quartz to consume $3\lambda_3$ amount of carbon. We would expect to see that $S_1^0 = \lambda_1 - 3\lambda_3$ behind the front. Similarly, we would expect $S_2^0 = \lambda_3$, as we see in Figure 3.7.

3.3.2.2 Inner solution

We scale into the narrow layer around the moving reaction front located at $z = h(\tau)$ using the substitutions

$$\zeta = \frac{z - h(\tau)}{\delta^{1/2}}, \quad \tau = T, \tag{3.154}$$

and we obtain the following leading-order boundary layer equations

$$-\frac{\mathrm{d}h^0}{\mathrm{d}\tau}\frac{\partial S_1^0}{\partial \zeta} = -(S_1^0)^{2/3}(2G_1^0 + G_3^0), \tag{3.155}$$

$$-\frac{\mathrm{d}h^0}{\mathrm{d}\tau}\frac{\partial S_2^0}{\partial \zeta} = (S_1^0)^{2/3}G_1^0, \tag{3.156}$$

$$-\frac{\mathrm{d}h^0}{\mathrm{d}\tau}\frac{\partial S_3^0}{\partial \zeta} = -(S_3^0)^{2/3}G_2^0, \tag{3.157}$$

$$-\frac{\mathrm{d}h^0}{\mathrm{d}\tau}\frac{\partial G_1^0}{\partial \zeta} - \mathcal{D}\frac{\partial^2 G_1^0}{\partial \zeta^2} = -(S_1^0)^{2/3}G_1^0 + (S_3^0)^{2/3}G_2^0, \tag{3.158}$$

$$-\frac{\mathrm{d}h^0}{\mathrm{d}\tau}\frac{\partial G_2^0}{\partial \zeta} - \mathcal{D}\frac{\partial^2 G_2^0}{\partial \zeta^2} = (S_1^0)^{2/3}G_1^0 - (S_3^0)^{2/3}G_2^0 + 2(S_1^0)^{2/3}G_3^0, \tag{3.159}$$

$$-\frac{\mathrm{d}h^0}{\mathrm{d}\tau}\frac{\partial G_3^0}{\partial \zeta} - \mathcal{D}\frac{\partial^2 G_3^0}{\partial \zeta^2} = (S_3^0)^{2/3}G_2^0 - (S_1^0)^{2/3}G_3^0. \tag{3.160}$$

We must match the solutions to (3.155)–(3.160) with the outer solutions ahead and behind the reaction front. Substituting (3.156) and (3.157) into (3.158) we find that

$$-\frac{\mathrm{d}h^0}{\mathrm{d}\tau}\frac{\partial G_1^0}{\partial \zeta} - \mathcal{D}\frac{\partial^2 G_1^0}{\partial \zeta^2} = \frac{\mathrm{d}h^0}{\mathrm{d}\tau}\frac{\partial S_2^0}{\partial \zeta} + \frac{\mathrm{d}h^0}{\mathrm{d}\tau}\frac{\partial S_3^0}{\partial \zeta}, \tag{3.161}$$

which may be integrated to yield

$$-\left(\frac{\mathrm{d}h^0}{\mathrm{d}\tau}G_1^0 + \mathcal{D}\frac{\partial G_1^0}{\partial \zeta}\right) = \frac{\mathrm{d}h^0}{\mathrm{d}\tau}(S_2^0 + S_3^0 - \lambda_3), \tag{3.162}$$

where we have used the fact that $G_1^0 \to 0$, $S_2^0 \to 0$, and $S_3^0 \to \lambda_3$ as $\zeta \to \infty$. We repeat this process for the other two gases to yield

$$-\left(\frac{\mathrm{d}h^0}{\mathrm{d}\tau}G_2^0 + \mathcal{D}\frac{\partial G_2^0}{\partial \zeta}\right) = \frac{\mathrm{d}h^0}{\mathrm{d}\tau}(2S_1^0 + 3S_2^0 - S_3^0 - 2\lambda_1 + \lambda_3), \tag{3.163}$$

$$-\left(\frac{\mathrm{d}h^0}{\mathrm{d}\tau}G_3^0 + \mathcal{D}\frac{\partial G_3^0}{\partial \zeta}\right) = \frac{\mathrm{d}h^0}{\mathrm{d}\tau}(-S_1^0 - 2S_2^0 + S_3^0 + \lambda_1 - \lambda_3). \tag{3.164}$$

We now consider the behaviour as $\zeta \to -\infty$ in order to match the outer solution behind the front. Recalling that, as $\zeta \to -\infty$, $S_3^0 \to 0$ and $G_1^0 \to 0$, so that $\partial G_1^0/\partial \zeta \to 0$ also, from (3.162) we find that

$$S_2^0 \to \lambda_3, \quad \text{as } \zeta \to -\infty, \tag{3.165}$$

which tells us that the amount of silicon carbide we produce is equal to the initial amount of quartz, as expected in this excess carbon case. From (3.164), we then

find that

$$S_1^0 \to \lambda_1 - 3\lambda_3, \quad \text{as } \zeta \to -\infty. \tag{3.166}$$

This is in agreement with our intuition and our numerical findings in Figure 3.7. Finally, from (3.163), we find that

$$\frac{\mathrm{d}h^0}{\mathrm{d}\tau} G_2^0 + \mathcal{D}\frac{\partial G_2^0}{\partial \zeta} \to 2\lambda_3 \frac{\mathrm{d}h^0}{\mathrm{d}\tau}, \quad \text{as } \zeta \to -\infty. \tag{3.167}$$

However, if the derivative of G_2^0 in (3.167) is non-zero, $G_2^0 \to \infty$ as $\zeta \to -\infty$, and so it must be that $\partial G_2^0/\partial\zeta \to 0$, and thus,

$$G_2^0 \to 2\lambda_3, \quad \text{as } \zeta \to -\infty. \tag{3.168}$$

We determine the speed of the reaction front by first noticing that G_1^0 and G_3^0 both satisfy the same equations and have the same conditions at $\pm\infty$, and so $G_1^0 \equiv G_3^0$. We then rewrite (3.155) as

$$\frac{\mathrm{d}h^0}{\mathrm{d}\tau}\frac{\partial S_1^0}{\partial \zeta} = 3(S_1^0)^{2/3} G_1^0, \tag{3.169}$$

and, by rearranging (3.169) and integrating over the boundary layer, we find

$$\begin{aligned}
\int_{-\infty}^{\infty} G_1^0 \,\mathrm{d}\zeta &= \frac{1}{3}\frac{\mathrm{d}h^0}{\mathrm{d}\tau}\int_{-\infty}^{\infty} (S_1^0)^{-2/3}\frac{\partial S_1^0}{\partial \zeta}\,\mathrm{d}\zeta, && (3.170)\\
&= \frac{\mathrm{d}h^0}{\mathrm{d}\tau}(S_1^0)^{1/3}\Big|_{-\infty}^{\infty}, && (3.171)\\
&= \frac{\mathrm{d}h^0}{\mathrm{d}\tau}\Big(\lambda_1^{1/3} - (\lambda_1 - 3\lambda_3)^{1/3}\Big), && (3.172)
\end{aligned}$$

and so, the speed of the front is given by

$$\frac{\mathrm{d}h^0}{\mathrm{d}\tau} = \frac{\displaystyle\int_{-\infty}^{\infty} G_1^0 \,\mathrm{d}\zeta}{\lambda_1^{1/3} - (\lambda_1 - 3\lambda_3)^{1/3}}. \tag{3.173}$$

In Figure 3.8, we compare the position of the front found from the simulation with (3.173), where we have extracted G_1^0 from the numerical solution. We find good agreement between the two solutions. We also notice that h^0 is approximately linear for $0.3 \leq T \leq 0.7$. Within this time interval the amount of G_1^0 in the system is

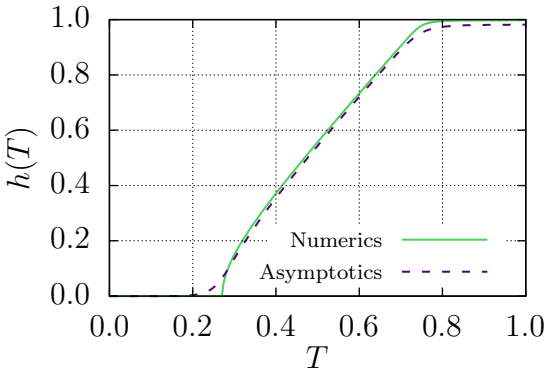

Figure 3.8: Position of the reaction front from the numerical solution of the problem (3.134)–(3.143) and asymptotic approximation (3.173). The parameter values are $\mathcal{D} = 1$, $\mathcal{U} = 1$, $\lambda_1 = 1$, $\lambda_3 = 0.25$ and $\delta = 10^{-3}$.

constant, and so $\mathrm{d}h^0/\mathrm{d}\tau$ is also constant by (3.173).

In the first paradigm problem, the reaction was limited by the transport of the gas into the reaction front, and so $\mathrm{d}h^0/\mathrm{d}\tau$ was proportional to the flux. In this second paradigm problem, our system is self-sustaining once the process has initiated and is not reliant on the supplied gas from the inlet at $z = 0$. We would therefore expect the reaction front to move linearly since carbon monoxide is produced within the reaction front. Silicon monoxide, the species key in determining the front speed in (3.173), is produced by the reaction of carbon monoxide and quartz. Therefore, since the system is self-sustaining and carbon monoxide is produced in the reaction front, the reaction speed is constant, and thus the amount of silicon monoxide is constant. Hence, we find a constant front speed.

3.4 Analysis of the multiphase model

Having gained experience on some simpler problems, we now return to the full problem summarized in Section 3.2. For the remainder of the chapter, we assume $\mathscr{D}_{\mathrm{SiO}} = \mathscr{D}_{\mathrm{CO}} = \mathscr{D}_{\mathrm{CO_2}}$ and $\theta_{\mathrm{SiO}} = \theta_{\mathrm{CO}} = \theta_{\mathrm{CO_2}} = \theta_{\mathrm{bg}}$ for simplicity, and so $\mathrm{Da}_{\mathrm{SiO}} = \mathrm{Da}_{\mathrm{CO}} = \mathrm{Da}_{\mathrm{CO_2}}$, $\mathrm{Pe}_{\mathrm{SiO}} = \mathrm{Pe}_{\mathrm{CO}} = \mathrm{Pe}_{\mathrm{CO_2}}$, and $\chi_{\mathrm{SiO}} = \chi_{\mathrm{CO}} = \chi_{\mathrm{CO_2}} = \chi_{\mathrm{bg}}$ and we omit the subscripts. Furthermore, we assume the permeability κ and gas viscosity μ are constant.

In the second paradigm problem we saw large gas concentrations. This is unphysical, since large concentration gradients will drive a diffusive gas flow. In this section, we reintroduce the coupling between the gas concentrations and gas flow and solve the full model summarized in Section 3.2. We will assume $\delta \ll 1$ and briefly consider two parameter regimes: $\mathrm{Da} = \mathcal{O}(\delta)$, in which we will see transport-limited

behaviour as in the second paradigm problem, and $\mathrm{Da} = \mathcal{O}(1)$, in which we will see more uniform dynamics owing to the increased transport. We will then consider the physically relevant parameters given in Table 3.2.

The details of the numerical methods used for the full multiphase model, as well as numerical optimizations, and convergence tests are given in Appendix A.

We suppose that $\mathrm{Da} = 10^{-3}$ and $\delta = 10^{-3}$ ($\ll 1$), $\mathrm{Pe} = 1$ (to more easily compare with the paradigm problem), and use the values in Table 3.2 for the rest of the parameters. We take $\delta = 10^{-3}$ instead of $\delta = 10^{-4}$ as in Table 3.2 for numerical stability and convergence. In this transport-limited case, the reactions dominate the transport of the gas, as we had in the second paradigm problem. In Figure 3.9 we present the numerical solution to (3.6), (3.17), (3.51)–(3.55), (3.57)–(3.59), (3.62), (3.63), and (3.76) with these parameters, for two times. We plot δC_i and $\delta^{1/2} u_s$ instead of C_i and u_s for ease of visualization since the gas concentrations and solid velocity are large. We see that, throughout the reaction front, the unreacted quartz is converted to product silicon carbide. One notable characteristic of this system is that α_{C}, the volume fraction of carbon, remains nearly uniform. This uniformity can be attributed to the constitutive law (3.17) describing dense packing, and the fact that the volume fraction of silicon carbide behind the reaction front is comparable to the volume fraction of quartz ahead of the reaction front. We emphasize that the entire reaction process occurs within a relatively short timeframe, due to the large gas concentrations. Indeed, we find that the reaction front reaches the top surface at $t = 0.0363$. It is worth noting that, while silicon monoxide and carbon dioxide are necessary intermediates of the process, they are confined to the region around the reaction front. With the exception of the uniformity of α_{C}, the dynamics are the same to those in the three-reaction, second paradigm problem.

We briefly show that the leading-order equations of the full model have the same structure as in the second paradigm problem. In the limit $\delta \to 0$ the leading-order gas equations, from (3.57)–(3.59), reduce to

$$\begin{pmatrix} -\left(n_{\mathrm{C}}\alpha_{\mathrm{C}}^2\right)^{1/3} & \left(n_{\mathrm{SiO_2}}\alpha_{\mathrm{SiO_2}}^2\right)^{1/3} & 0 \\ \left(n_{\mathrm{C}}\alpha_{\mathrm{C}}^2\right)^{1/3} & -\left(n_{\mathrm{SiO_2}}\alpha_{\mathrm{SiO_2}}^2\right)^{1/3} & 2\left(n_{\mathrm{C}}\alpha_{\mathrm{C}}^2\right)^{1/3} \\ 0 & \left(n_{\mathrm{SiO_2}}\alpha_{\mathrm{SiO_2}}^2\right)^{1/3} & -\left(n_{\mathrm{C}}\alpha_{\mathrm{C}}^2\right)^{1/3} \end{pmatrix} \begin{pmatrix} C_{\mathrm{SiO}} \\ C_{\mathrm{CO}} \\ C_{\mathrm{CO_2}} \end{pmatrix} = \mathbf{0}. \tag{3.174}$$

The determinant d of the matrix given in (3.174) is

$$d = 2\left(n_{\mathrm{SiO_2}}\alpha_{\mathrm{SiO_2}}^2\right)^{1/3}\left(n_{\mathrm{C}}\alpha_{\mathrm{C}}^2\right)^{2/3}, \tag{3.175}$$

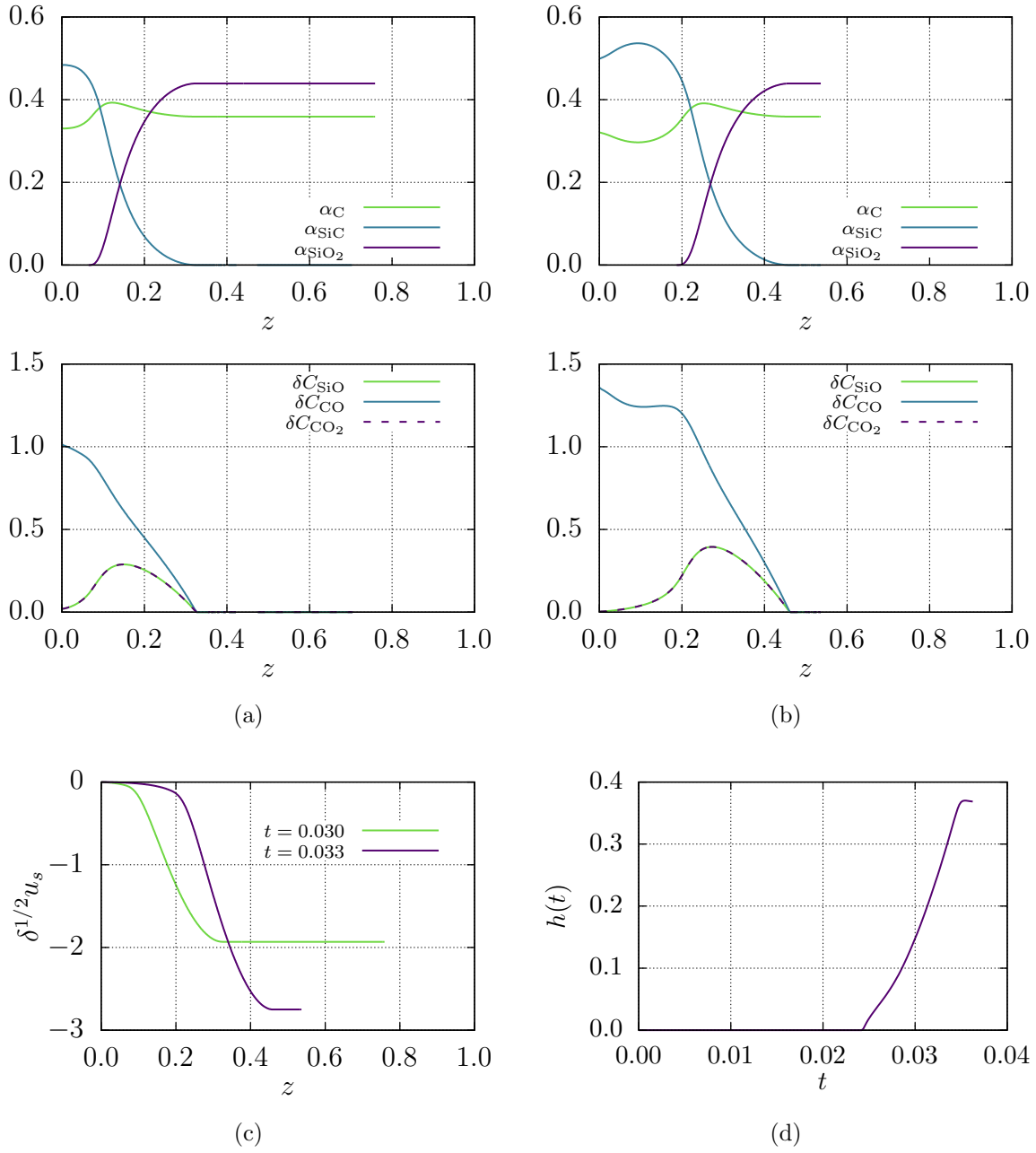

Figure 3.9: Numerical solution of (3.6), (3.17), (3.51)–(3.55), (3.57)–(3.59), (3.62), (3.63), and (3.76). We show α_C, α_{SiC}, α_{SiO_2}, δC_{SiO}, δC_{CO}, and δC_{CO_2} versus z at (a) $t = 0.030$, and (b) $t = 0.033$. In (c), we show $\delta^{1/2} u_s$ vs z for these two times, and in (d) we show the position of the reaction front. The parameter values are $\mathrm{Da} = 10^{-3}$, $\mathrm{Pe} = 1$, $\delta = 10^{-3}$ and the other parameter values are given in Table 3.2. Note that we plot δC_i and δu_s rather than C_i and u_s for ease of visualization.

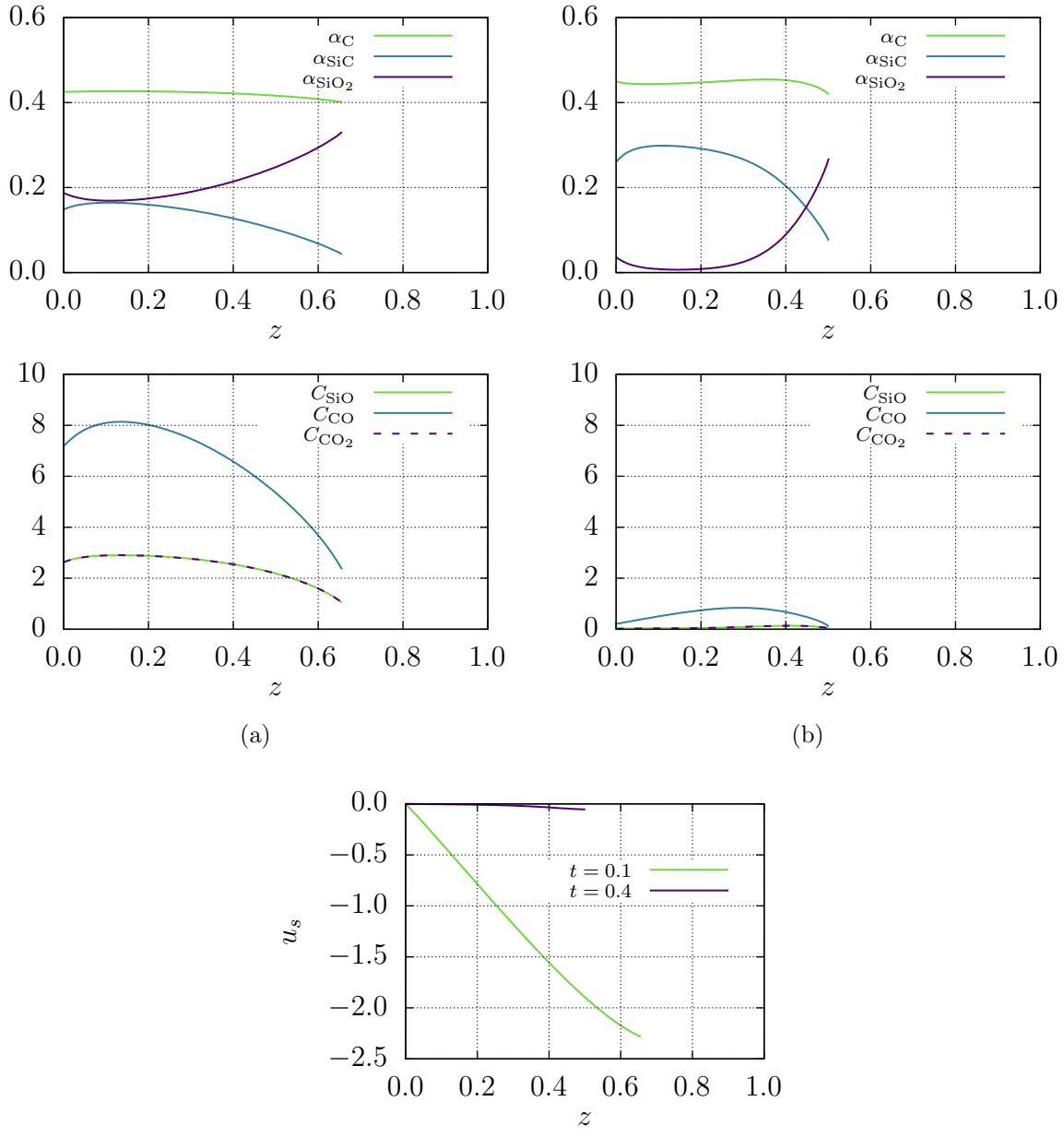

Figure 3.10: Numerical solution of (3.6), (3.17), (3.51)–(3.55), (3.57)–(3.59), (3.62), (3.63), and (3.76). We show α_C, α_{SiC}, α_{SiO_2}, C_{SiO}, C_{CO}, and C_{CO_2} versus z at (a) $t = 0.1$, and (b) $t = 0.4$. In (c), we show u_s vs z for these two times. The parameter values are Da $= 1$, Pe $= 1$, $\delta = 10^{-3}$ and the other parameter values are given in Table 3.2.

and so, when $\alpha_{\mathrm{SiO_2}} > 0$ and $\alpha_{\mathrm{C}} > 0$, only the trivial solution exists (since $n_{\mathrm{SiO_2}}$ and n_{C} are bounded below by 1). We again have a moving reaction front $h(t)$. Ahead of the front $\alpha_{\mathrm{SiO_2}} = \alpha^0_{\mathrm{SiO_2}} > 0$ and $\alpha_{\mathrm{C}} = \alpha^0_{\mathrm{C}} > 0$, and therefore $C_{\mathrm{SiO}} = C_{\mathrm{CO}} = C_{\mathrm{CO_2}} = 0$ in this region. Behind the front however, $\alpha_{\mathrm{SiO_2}} = 0$ by our assumption that the system has a slight excess of carbon. It then follows from solving (3.174) with $\alpha_{\mathrm{SiO_2}} = 0$ that $C_{\mathrm{SiO}} = C_{\mathrm{CO_2}} = 0$ for $z < h(t)$. Due to the highly nonlinear coupling of the variables, we cannot make further analytic progress.

We now suppose that Da = 1, Pe = 1, $\delta = 10^{-3}$, and the rest of the parameters are as given in Table 3.2, *i.e.* transport is considerably larger than in the previous simulation. We present the numerical solution to (3.6), (3.17), (3.51)–(3.55), (3.57)–(3.59), (3.62), (3.63), and (3.76) with these parameters for two times in Figure 3.10. In this scenario, we see that the gas concentrations are $\mathcal{O}(1)$, and therefore, that the gas must be transported much more easily, and is transported upward and out of the crucible. The dynamics are therefore different than the previous example. One feature we observe is a more spatially uniform conversion of carbon and quartz into silicon carbide. Unlike previous examples where the gas tended to remain localized near the reaction front, here, gases are efficiently transported throughout the system. The transport leads to a more uniform chemical transformation, albeit over a much larger timescale than in the solution in the previous example. The increased gas transport and more uniform reactions cause an approximately linear velocity profile of the solid. This contrasts with earlier observations of sharp changes in the solid velocity profile within the reaction front. Additionally, the gas concentrations, and therefore pressure—which are $\mathcal{O}(1)$ here—are more representative of real-world conditions, and are inherently more safe. As we would expect, the increased gas transport also leads to a more uniform distribution of the gas concentrations. However, the reduced gas concentrations affect the speed of the reactions. In this case, the reaction takes an $\mathcal{O}(1)$ amount of time to reach completion, unlike in the first example.

3.4.1 Numerical solutions

To better understand the effect of the dimensionless parameters on the dynamics, we now examine in detail four points within the parameter space. We will then transition to analyzing macroscale metrics as we sweep through the parameter space. To assess carbon utilization and silicon carbide production in the multiphase model we re-write

(2.97) and (2.98) in Cartesian coordinates

$$U_{\mathrm{C}}(t) = 1 - \frac{1}{\alpha_{\mathrm{C}}^0} \int_0^{H(t)} \alpha_{\mathrm{C}}(z,t)\,\mathrm{d}z, \tag{3.176}$$

$$Y_{\mathrm{SiC}}(t) = \frac{1}{\mathcal{M}_{\mathrm{SiC}}\alpha_{\mathrm{SiO_2}}^0} \int_0^{H(t)} \alpha_{\mathrm{SiC}}(z,t)\,\mathrm{d}z, \tag{3.177}$$

respectively.

Case I: We consider the system with default parameter values given in Table 3.2, and we present the results in Figure 3.11. With these parameters, the spatial variation in solid volume fractions and gas concentrations is localized to a thin layer near the top of the pellet bed where the volume fraction of carbon and silicon carbide and the gas concentrations decrease and the volume fraction of quartz increases. The carbon volume fraction α_{C} exhibits a slight increase over time. Both quartz and silicon carbide share similar spatial profiles but inverted. The profiles for silicon monoxide and carbon dioxide are identical since they follow the same dynamics for these parameter choices and both exhibit weak spatial variation except at the upper boundary; the concentrations decrease with time. Conversely, carbon monoxide presents a different behaviour due to the boundary conditions (3.68)—the concentration approaches a linear steady-state profile. Approximately 50% of the carbon is consumed by the time the quartz is fully consumed, while around 60% of the silicon in the initial quartz is converted to silicon carbide by this time. Initially, the pressure spikes rapidly to about 6, followed by a steady decrease back to 1 over time.

Case II: We consider the case where $\chi = 50$, considerably smaller than in Case I, reducing the gas escape through the top of the pellets, and the rest of the parameter values as given in Table 3.2. We show the result in Figure 3.12. We see that the gas concentrations and pressure get very large, as the gas struggles to escape. The spatial profiles for the solid volume fractions and gas concentrations become nearly uniform. Unlike the previous example, there is no boundary layer near the top surface because the flux through the top of the bed of pellets is greatly reduced. This uniformity is expected as advection, and to a lesser extent diffusion, equilibrate the gases throughout the crucible, and so the gases are well mixed. Owing to Darcy's law, gradients in the pressure, and thus gas concentrations, are equilibrated by the gas flow. We observe exponential growth in both carbon utilization and silicon yield, until a final carbon utilization of 0.571 and silicon yield of 0.667. The pressure also grows exponentially due to the decreased ability of gas to escape. The exponential concentration and pressure growth, evidenced by the logarithmic time spacing in Figure 3.12, increase

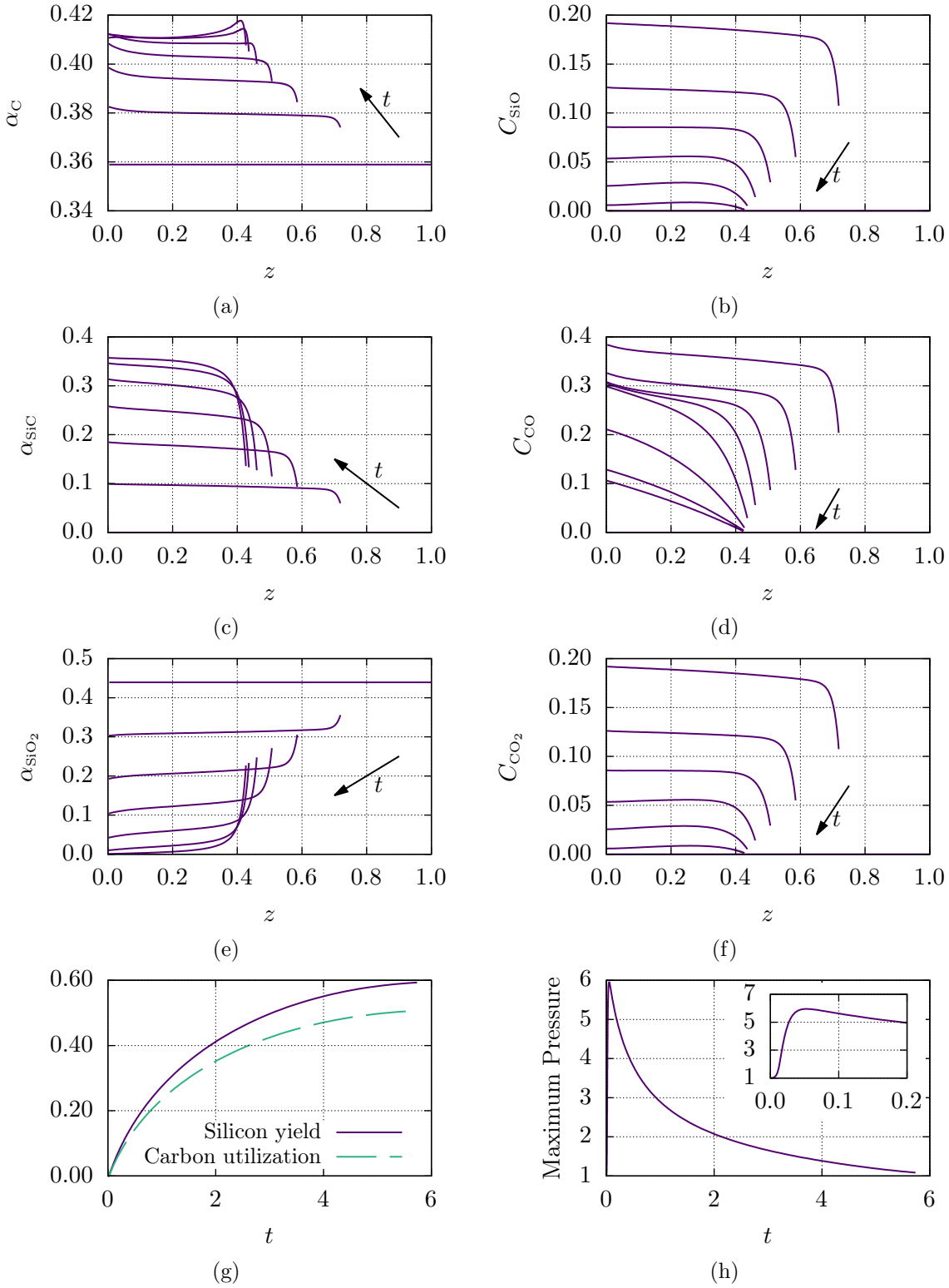

Figure 3.11: Graphs of the numerical solution of (3.6), (3.17), (3.51)–(3.55), (3.57)–(3.59), (3.62), (3.63), and (3.76). Parameter values taken from Table 3.2. Lines in (a)–(f) are plotted for $t = 0.0, 0.72, 1.43, 2.15, 2.87, 3.58, 4.30, 5.02, 5.74$.

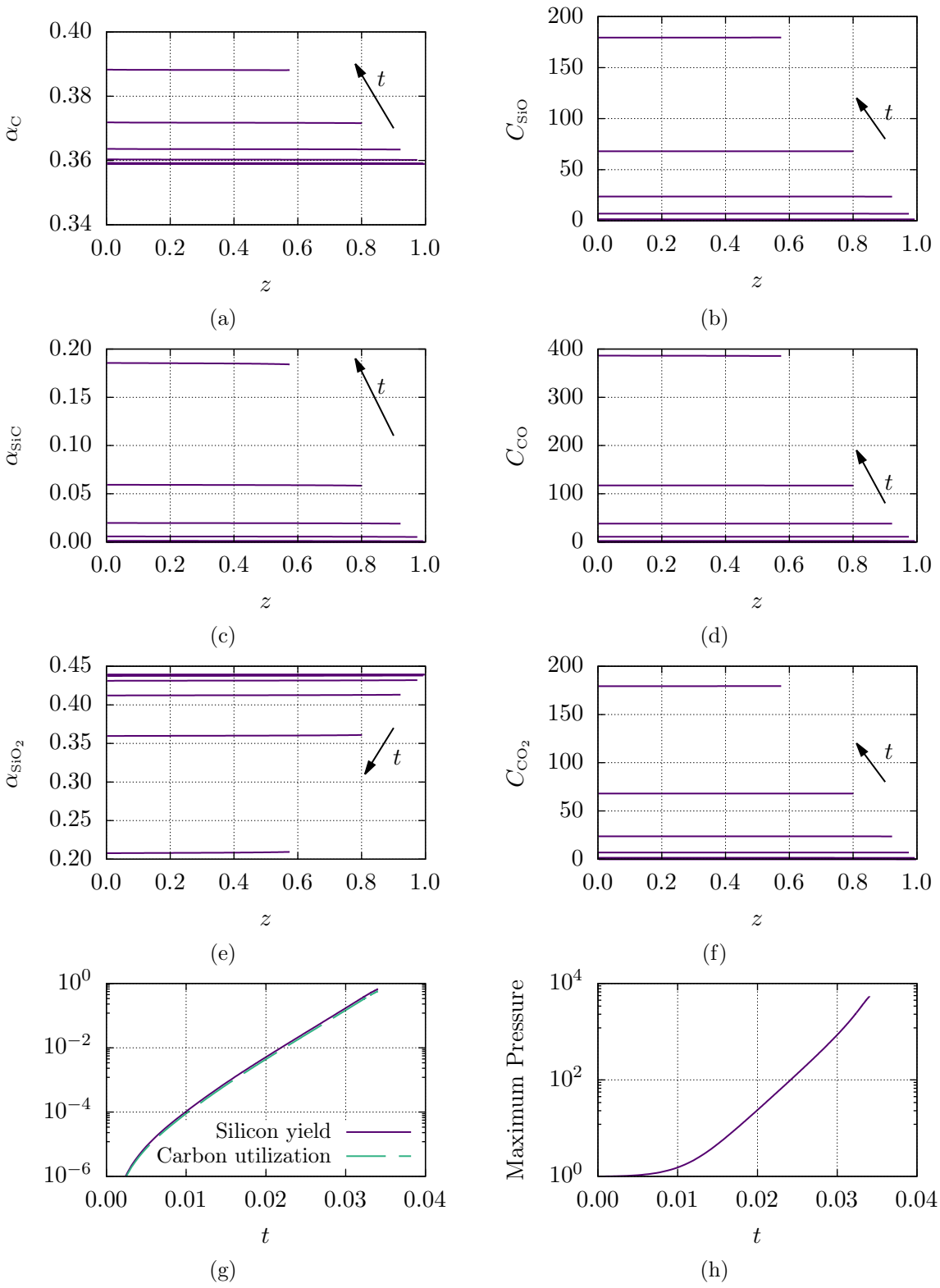

Figure 3.12: Graphs of the numerical solution of (3.6), (3.17), (3.51)–(3.55), (3.57)–(3.59), (3.62), (3.63), and (3.76). Parameter values taken from Table 3.2, except we take $\chi = 50$. Lines in (a)–(f) are plotted for $t = 0.0, 0.014, 0.021, 0.025, 0.029, 0.032, 0.034$.

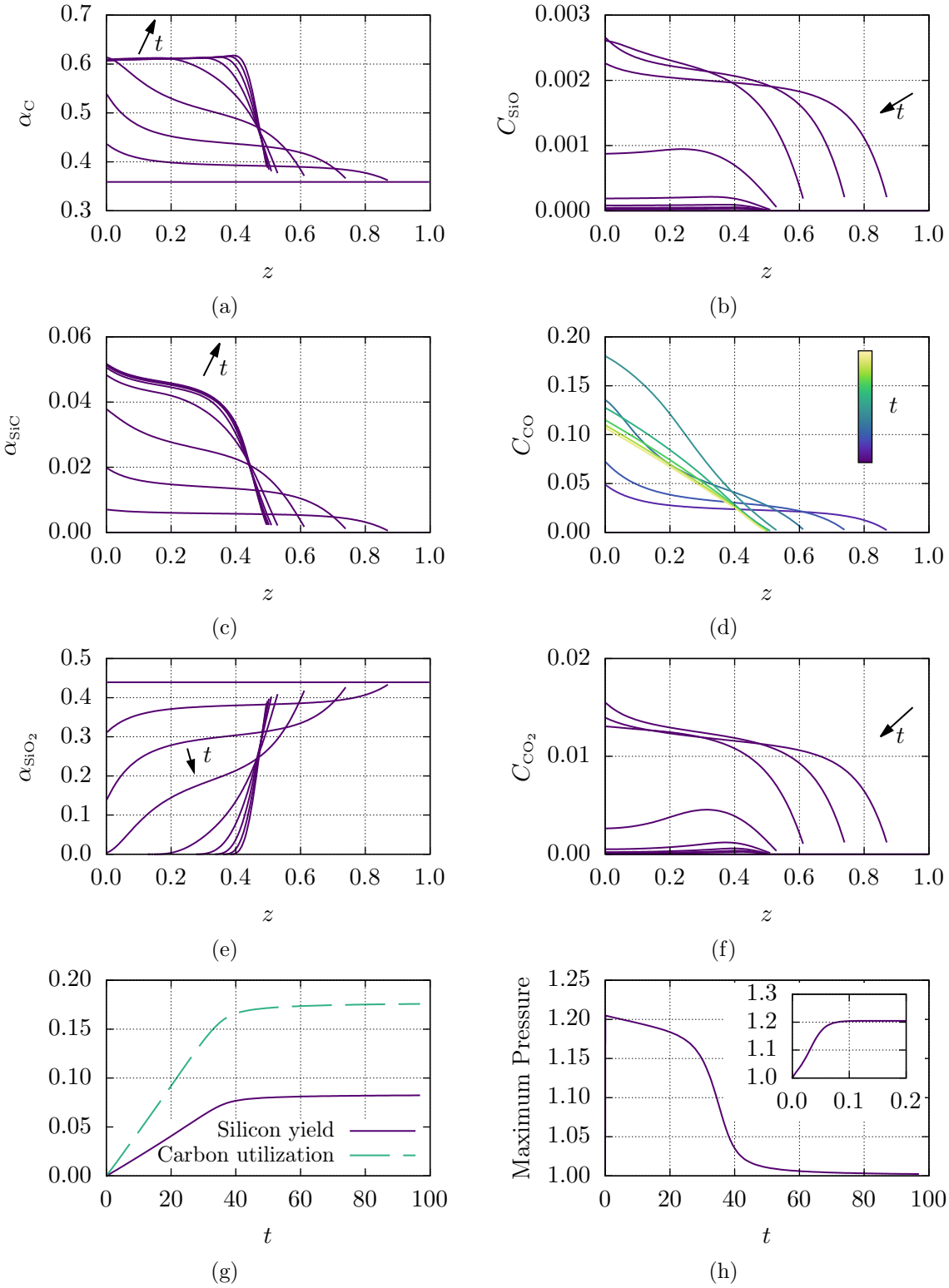

Figure 3.13: Graphs of the numerical solution of (3.6), (3.17), (3.51)–(3.55), (3.57)–(3.59), (3.62), (3.63), and (3.76). Parameter values taken from Table 3.2, except we take $\mathcal{C}_{SiO} = 100$ and $\mathcal{C}_{CO_2} = 10$. Lines in (a)–(f) are plotted for $t = 0.0, 12.11, 24.23, 36.34, 48.45, 60.56, 72.68, 84.79, 96.90$.

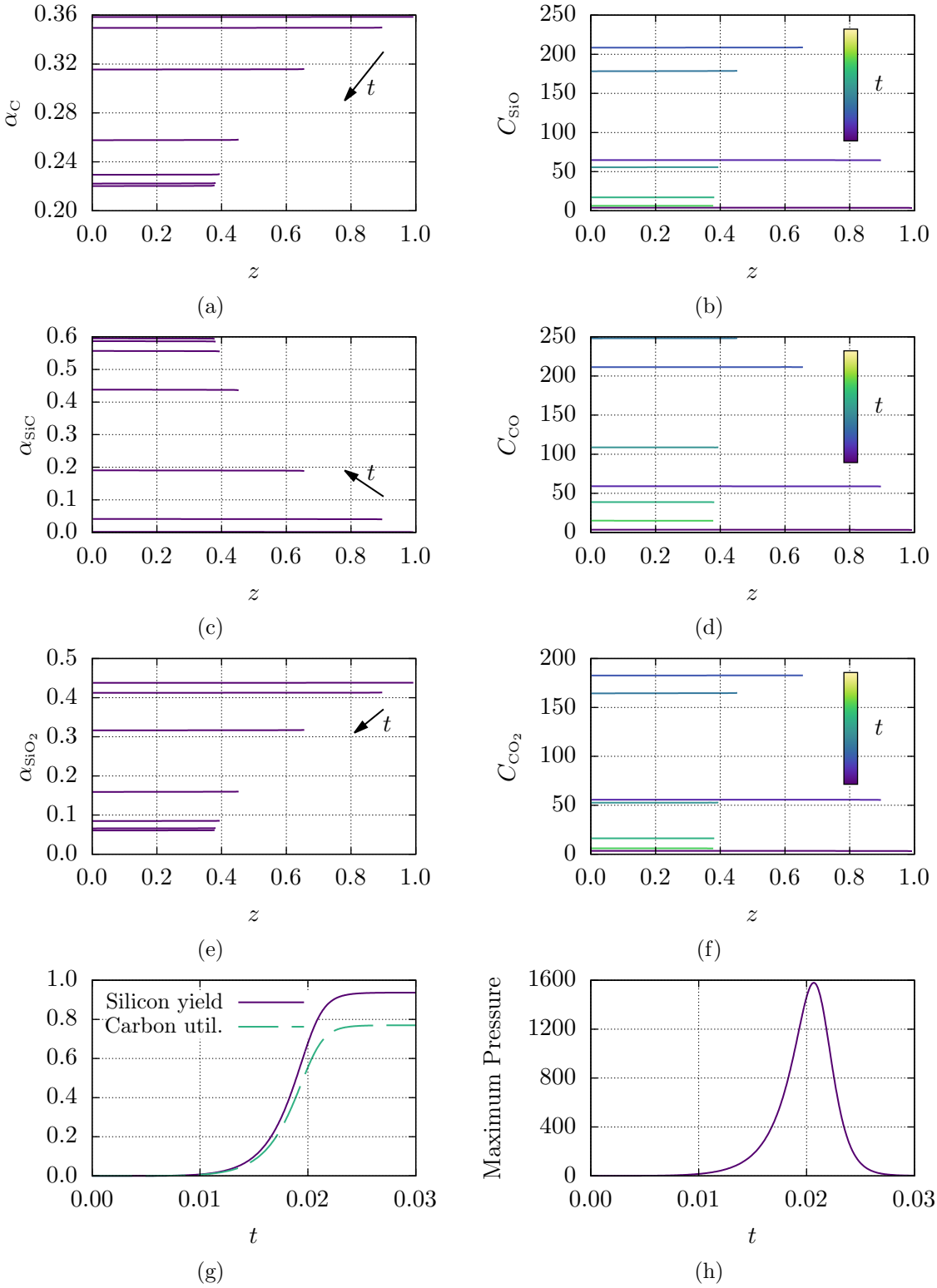

Figure 3.14: Graphs of the numerical solution of (3.6), (3.17), (3.51)–(3.55), (3.57)–(3.59), (3.62), (3.63), and (3.76). Parameter values taken from Table 3.2, except we take $\mathcal{C}_{SiO} = 0.01$ and $\mathcal{C}_{CO_2} = 0.1$. Lines in (a)–(f) are plotted for $t = 0.010, 0.016, 0.019, 0.021, 0.023, 0.024, 0.025$.

the reaction rate. This leads to exponential increases in both carbon utilization and silicon yield.

Case III: We consider the case where $\mathcal{C}_{\mathrm{SiO}} = 100$ and $\mathcal{C}_{\mathrm{CO_2}} = 10$, and we show the results in Figure 3.13. The quartz reaction proceeds faster than the Boudouard reaction, which in turn is faster than the silicon carbide reaction with this choice of parameters. The profiles for the three solids are similar, and form a boundary layer at the outlet. Silicon carbide production is minimal due to the slow associated reaction. The quartz reacts quickly, but most of the carbon is consumed by the Boudouard reaction instead of the silicon carbide reaction. Consequently, most of the silicon monoxide and carbon dioxide produced by the quartz reaction are transported out of the crucible without reacting with carbon. Despite the fast quartz reaction, its consumption is slow—limited by the carbon monoxide fed in at the inlet. Only about 20% of the carbon is consumed, and the silicon yield is less than 10%. The maximum pressure is approximately 1.2 due to the limited gas production.

Case IV: In our final example, we consider the scenario where all the reactions are fast, with the silicon carbide reaction fastest, followed by the Boudouard reaction, with the quartz reaction being the slowest ($\mathcal{C}_{\mathrm{SiO}} = 0.01$ and $\mathcal{C}_{\mathrm{CO_2}} = 0.1$). We show the results in Figure 3.14. There is almost no spatial variation of the volume fractions or gas concentrations in this case. Most of the carbon reacts, leading to significant silicon carbide production, and the profiles for the three solids remain similar to each other, with the volume fraction of silicon carbide being inverted. Again, the rapid silicon carbide reaction results in exponential gas production. Any silicon monoxide produced by the quartz reaction quickly reacts with carbon, and the carbon dioxide produced also reacts swiftly with carbon, generating more carbon monoxide, which can then react with quartz again. This cycle results in a net production of carbon monoxide, causing gas concentrations to grow exponentially. This is reflected in the pressure, which increases exponentially to about 1600 before decaying as reactants are depleted. Approximately 80% of the carbon is utilized, and the silicon yield is nearly 100%, with very little silicon monoxide lost through the top of the pellets—almost all of the silicon monoxide reacts to form silicon carbide.

The pressure differences across the four cases highlights significant concerns for maintaining safe operating conditions. While the dimensionally scaled results show pressures in the range of 1.2–5400 atm, only Case III is suitable for the target set by Elkem ASA. Elkem ASA would prefer maximum pressures less than 1.2 atm, and no more than 3.0 atm. The other three cases exhibit much higher pressures, beyond the safety threshold. Case II and Case IV reach unphysical values that would cause the

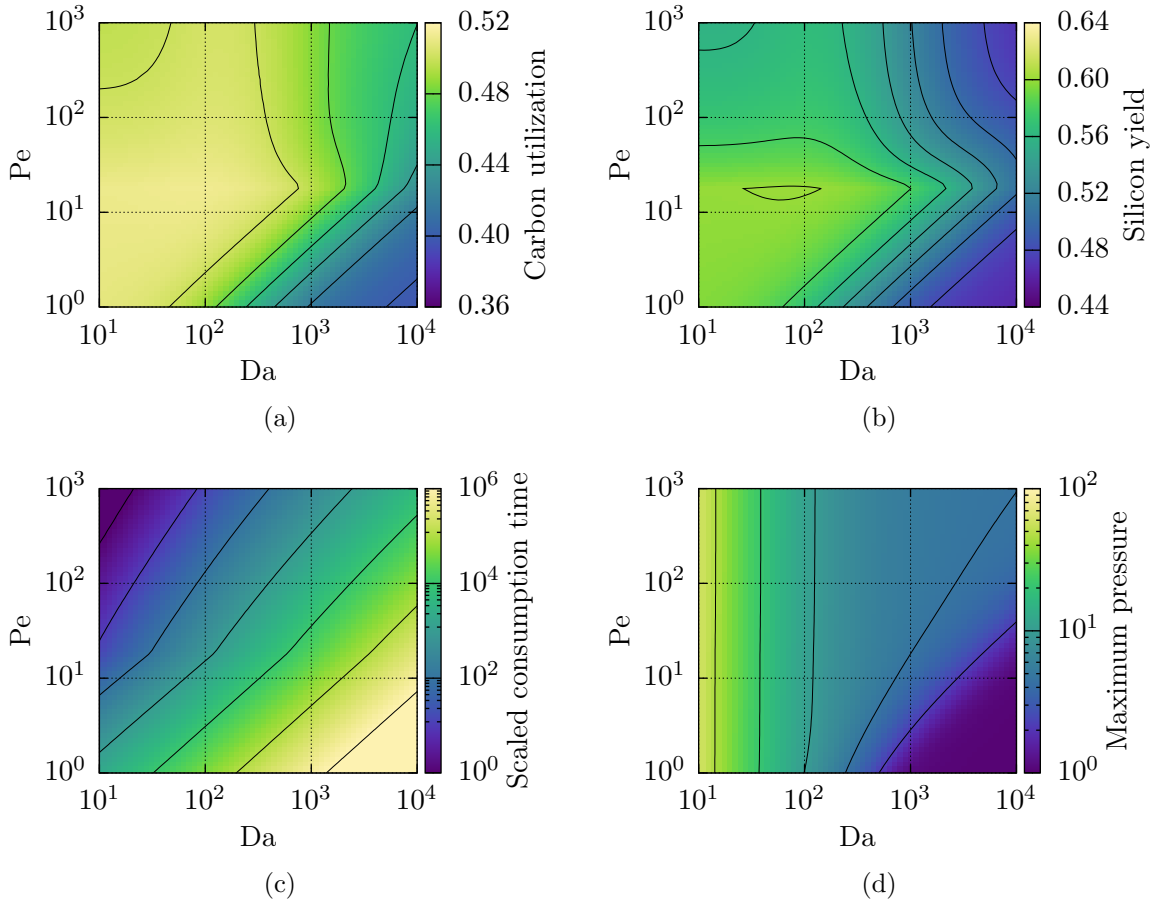

Figure 3.15: Da–Pe plane. (a) Carbon utilization and (b) silicon yield, given by (3.176) and (3.177), respectively, at the quartz consumption time. (c) Scaled quartz consumption time, given by (3.178), and (d) maximum pressure. The default values are given in Table 3.2.

crucible to fail in reality. Thus, we have the challenge of managing gas dynamics in the system, as excessively high pressures would lead to equipment failure, with safe pressure levels being a critical factor for practical operations.

3.4.2 Parameter sweeps

We now shift to sweeping through the parameter space. We will characterize a set of parameters by the carbon utilization fraction and silicon yield, as given by (3.176) and (3.177), at the quartz consumption time, as well as the quartz consumption time itself, and the maximum pressure. These macroscale metrics will help inform us of the dynamics and efficiency of a particular set of parameters.

In Figure 3.15 we show the carbon utilization fraction, silicon yield, scaled quartz consumption time, and maximum pressure while sweeping through the Damköhler number Da, and Péclet number Pe holding all other parameters constant. We see

that the carbon utilization fraction and silicon yield fraction are fairly uniform for $\mathrm{Da} \lesssim 10^3$. We note that the timescaling used in (3.49) depends on many of the same dimensional parameters as Da, and Pe. In order to make conclusions about the dimensional quartz consumption time we consider the scaled quartz consumption time

$$\mathcal{T}_1 = \frac{\mathrm{Da}}{\mathrm{Pe}} t^* = \frac{\mathcal{D}}{(H^0)^2} \left(\frac{\rho_{\mathrm{SiO_2}}/m_{\mathrm{SiO_2}}}{k_3 (n^0_{\mathrm{SiO_2}})^{1/3} c^*_{\mathrm{CO}}} \right) t^*, \tag{3.178}$$

which has the same dependence on k_3, $n^0_{\mathrm{SiO_2}}$, and c^*_{CO} as in (3.49). Here, t^* is the dimensionless quartz consumption time, such that $\alpha_{\mathrm{SiO_2}}(t^*) = 10^{-3}$. In this way we are able to draw conclusions for experiments where the initial bed height H^0 is constant. In Figure 3.15c we see that the scaled quartz consumption time, (3.178), varies specifically with the effective transport, which increases towards the lower right. Moving to the right increases advection, and moving down increases diffusion. In the upper left region, advection is slow relative to the reactions and diffusion is slow relative to advection. Thus, we find that the reactions dominate the dynamics and the quartz is fully consumed quickly. However, in the lower right region, the transport dominates the reactions and the quartz consumption time correspondingly increases. We find little variation in the maximum pressure as the Péclet number varies. Increasing Pe reduces the relative impact of diffusion, and so there is little effect on the maximum pressure. Diffusion is most impactful for large Da and small Pe, and we find that in this region the maximum pressure is smallest since diffusion helps equalize the pressure throughout the crucible.

We now move on to sweeping through the $\mathcal{C}_{\mathrm{SiO}}$–$\mathcal{C}_{\mathrm{CO_2}}$ plane, as shown in Figure 3.16. In the quadrant $\mathcal{C}_{\mathrm{SiO}} \ll 1$ and $\mathcal{C}_{\mathrm{CO_2}} \ll 1$ the quartz reaction is the slowest of the reactions. Any silicon monoxide and carbon dioxide produced by the quartz reaction quickly reacts with the carbon and so the carbon utilization and silicon yield are large. In the region $\mathcal{C}_{\mathrm{SiO}} \gg 1$ and $\mathcal{C}_{\mathrm{CO_2}} \ll 1$ the silicon carbide reaction is the slowest and the Boudouard reaction is the fastest. Therefore, we do not produce a lot of silicon carbide and the silicon yield is very low. However, since the Boudouard reaction is the fastest we find that the carbon utilization is roughly one third. In this case, we expect an effective carbon to quartz mole ratio of $1:1$, but we provide an initial ratio of $3.5:1$. Thus, we only consume about 30% of the carbon. In the region $\mathcal{C}_{\mathrm{SiO}} \ll 1$ and $\mathcal{C}_{\mathrm{CO_2}} \gg 1$ we have the opposite behaviour with the silicon carbide reaction being the fastest, and the Boudouard reaction being the slowest. Here, any silicon monoxide quickly reacts with the carbon to create silicon carbide. Thus, the silicon yield is very high, and the carbon utilization is roughly 0.66. Here, our effective mole ratio

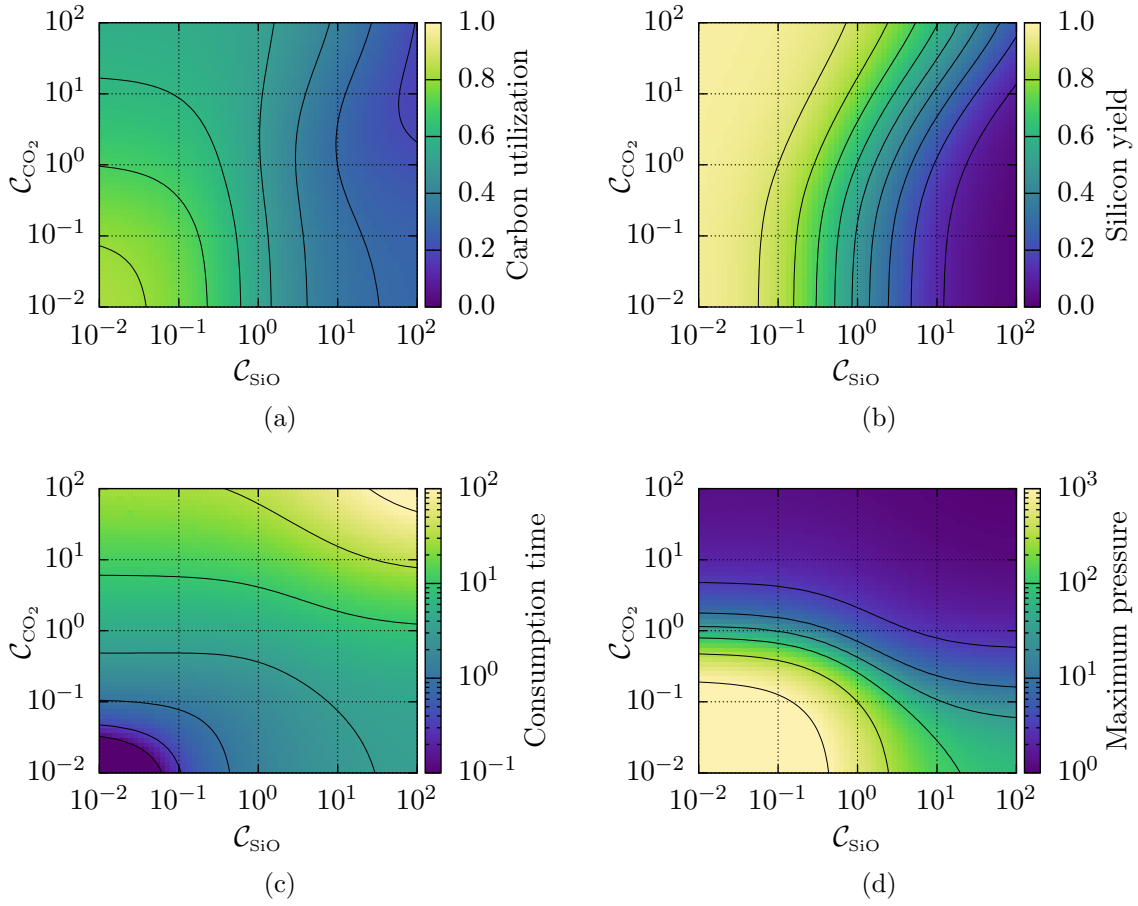

Figure 3.16: $\mathcal{C}_{\mathrm{SiO}}$–$\mathcal{C}_{\mathrm{CO_2}}$ plane. (a) Carbon utilization and (b) silicon yield, as given by (3.176) and (3.177), respectively, at the quartz consumption time. (c) Quartz consumption time, and (d) maximum pressure. The default values are given in Table 3.2.

is 2 : 1. Finally, for $\mathcal{C}_{\mathrm{SiO}} \gg 1$ and $\mathcal{C}_{\mathrm{CO_2}} \gg 1$ the quartz reaction is the fastest. In this region the carbon utilization fraction and silicon yield transition from the lower right behaviour to the upper left behaviour. For large values of $\mathcal{C}_{\mathrm{CO_2}}$ the quartz consumption time increases. The Boudouard reaction is slow for $\mathcal{C}_{\mathrm{CO_2}} \gg 1$, which is key to replenish carbon monoxide to facilitate the consumption of the quartz. In this regime, the system is reliant on the inlet supply of carbon monoxide to react with the quartz. Thus, the quartz consumption time is large for $\mathcal{C}_{\mathrm{CO_2}} \gg 1$. In this regime, the Boudouard reaction is negligible, and so the system is dependent on the supplied carbon monoxide from the inlet. The inlet flux is small compared to the gas generated by the Boudouard reaction, and so the consumption time is much larger. Finally, we examine the maximum pressure. As $\mathcal{C}_{\mathrm{CO_2}}$ increases, the maximum pressure decreases as the system is limited by the inlet gas flow, and does not generate large amounts of gas.

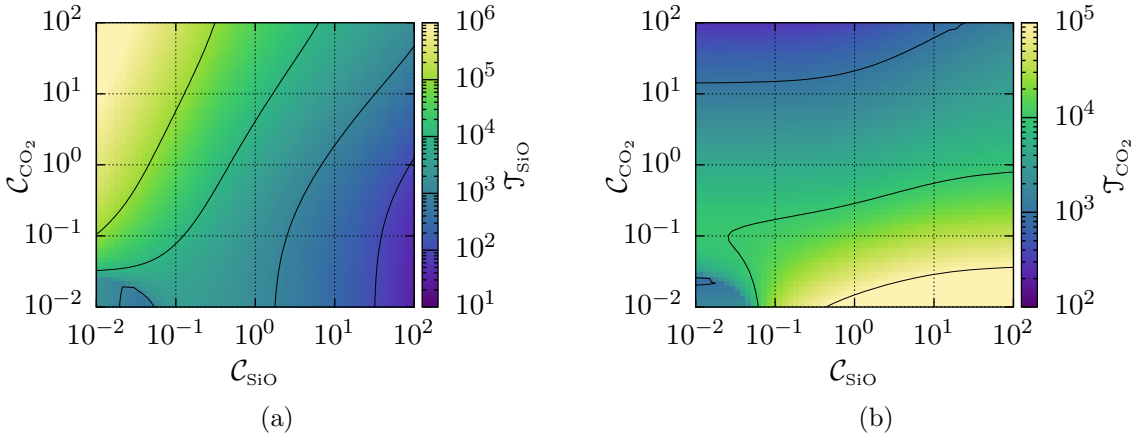

Figure 3.17: Scaled quartz consumption times given by (a) (3.179) and (b) (3.180).

Again, owing to the non-dimensionalization of the system, it is difficult to make dimensional conclusions from the dimensionless quartz consumption time. Therefore, we consider the two scaled quartz consumption times

$$\mathcal{T}_{\mathrm{SiO}} = \frac{t^*}{\delta\,\mathcal{C}_{\mathrm{SiO}}} = \left(\frac{k_2 (n_{\mathrm{C}}^0)^{1/3} \rho_{\mathrm{SiO_2}}/m_{\mathrm{SiO_2}}}{k_3 (n_{\mathrm{SiO_2}}^0)^{1/3} c_{\mathrm{CO}}^*}\right) t^*, \tag{3.179}$$

where we consider k_1 constant, and

$$\mathcal{T}_{\mathrm{CO_2}} = \frac{t^*}{\delta\,\mathcal{C}_{\mathrm{CO_2}}} = \left(\frac{k_1 (n_{\mathrm{C}}^0)^{1/3} \rho_{\mathrm{SiO_2}}/m_{\mathrm{SiO_2}}}{k_3 (n_{\mathrm{SiO_2}}^0)^{1/3} c_{\mathrm{CO}}^*}\right) t^*, \tag{3.180}$$

were we consider k_2 constant. We show these quantities in Figure 3.17. For constant k_1 the silicon carbide reaction speed is constant and $\mathcal{C}_{\mathrm{SiO}}$ varies the speed of the quartz reaction, and so $\mathcal{C}_{\mathrm{CO_2}}$ varies the relative speed of the quartz reaction and the Boudouard reaction. Unsurprisingly, the scaled quartz consumption time decreases as $\mathcal{C}_{\mathrm{SiO}}$ increases. In this case, $\mathcal{C}_{\mathrm{SiO}}$ is directly related to the speed of the quartz reaction and so increasing this naturally decreases the time to consume the quartz. As we increase $\mathcal{C}_{\mathrm{CO_2}}$ the relative speed of the quartz reaction to the Boudouard reaction also increases. As $\mathcal{C}_{\mathrm{CO_2}}$ increases so does the quartz consumption time. The system is more dependent on the inlet supply of carbon monoxide as $\mathcal{C}_{\mathrm{CO_2}}$ increases, and thus the quartz consumption time also increases. We show how $\mathcal{T}_{\mathrm{CO_2}}$, given by (3.180), varies with $\mathcal{C}_{\mathrm{SiO}}$ and $\mathcal{C}_{\mathrm{CO_2}}$ in Figure 3.17b. Now, for constant k_2, $\mathcal{C}_{\mathrm{CO_2}}$ varies the speed of the quartz reaction, and $\mathcal{C}_{\mathrm{SiO}}$ varies the relative speed of the quartz reaction and the silicon carbide reaction. In this case, we find less variation than in Figure 3.17a. Since we consider k_2 to be fixed in this plot, the speed of the Boudouard reaction

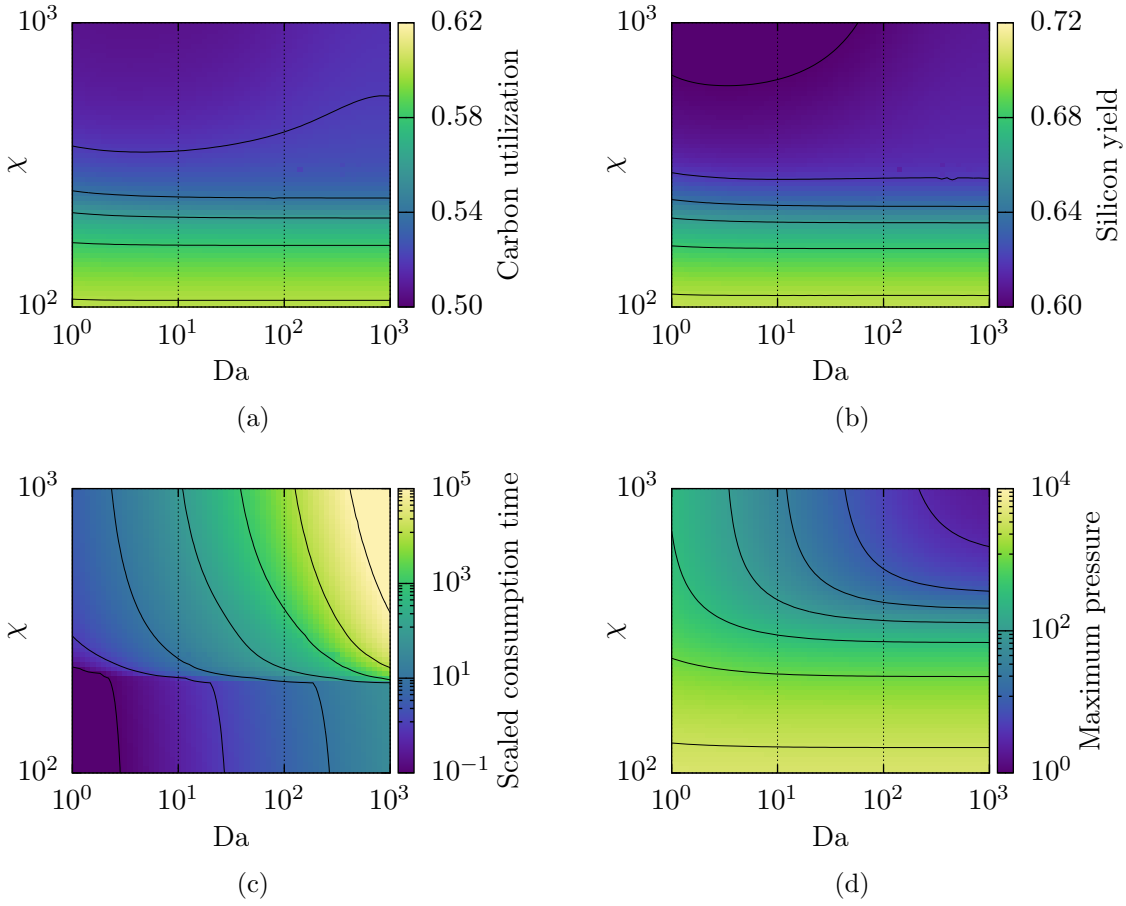

Figure 3.18: Da–χ plane. (a) Carbon utilization and (b) silicon yield, as given by (3.176) and (3.177), respectively, at the quartz consumption time. (c) Scaled quartz consumption time, given by (3.181), and (d) maximum pressure. The default values are given in Table 3.2.

is also fixed. As we have seen in several examples so far, the Boudouard reaction is important to generate a self-sustaining system. The speed of the quartz reaction or the silicon carbide reaction are less relevant is this regard, and hence, we see less variation in the scaled consumption time in Figure 3.17b than in Figure 3.17a.

Finally, in Figure 3.18, we consider the Da–χ plane. Carbon utilization and silicon yield show negligible variation with changes in Da. The influence of χ on these metrics is moderate, with fluctuations of approximately 20%. Larger χ leads to reduced carbon utilization and silicon yield, attributed to the easier gas escape and lower gas concentrations generated. Conversely, lower χ values restrict gas escape, resulting in higher carbon utilization and silicon yield due to faster reactions caused by higher gas concentrations. We note that the moderate carbon utilization and silicon yield are a result of stopping the simulation once the quartz has been consumed. At this point there are still large concentrations of silicon monoxide and carbon dioxide,

which would continue to react with the carbon. The carbon utilization and silicon yield would continue increasing after the quartz has been consumed, as we saw in Figure 3.12. The scaled consumption time

$$\mathcal{T}_3 = \mathrm{Da}\, t^* = \frac{\kappa P_{\mathrm{atm}}}{\mu (H^0)^2} \left(\frac{\rho_{\mathrm{SiO_2}}/m_{\mathrm{SiO_2}}}{k_3 (n^0_{\mathrm{SiO_2}})^{1/3} c^*_{\mathrm{CO}}} \right) t^*, \tag{3.181}$$

follows a similar trend, increasing with both Da and χ. Larger Da enhances gas transport to the top of the pellets, and large χ facilitates easier escape. We see that the maximum pressure has three regimes. For small values of χ, the gas generated cannot escape efficiently regardless of Da, leading to large concentrations and pressures. In contrast, for large Da and large χ, the gas is easily transported to the top of the pellets and escapes, resulting in low maximum pressure, as the generated gas is swiftly removed from the system. The transition regime occurs with small Da and large χ, where the reaction rates outpace the transport, causing a build up of concentrations and pressure. However, since χ is large, the gas may still escape the crucible, preventing the maximum pressure from reaching levels as high as observed when χ is small.

3.5 Conclusions

In this chapter, we derived a multiphase model for a homogeneous bed of fine quartz and carbon particles, under the assumption that solid motion is primarily governed by gravity and that the bed remains well-packed. The system involves a crucible filled with quartz and carbon particles with space for gas to flow. The crucible is heated to 1600 °C. The gases react with the solid particles, leading to consumption of the quartz and carbon, and causing a downward movement of the solid material as voids are filled. Simultaneously, gas generation drives upward flow within the crucible. An inert gas is initially present, with carbon monoxide injected at the bottom, and the crucible's top remains open to allow gas escape.

We considered a one-dimensional multiphase flow, tracking the volume fractions of carbon, silicon carbide, and quartz and the gas concentrations. Number density of carbon and quartz particles was also considered, since the reaction rates depend on this property. The governing equations describe the behaviour of 13 variables and depend on 22 dimensionless parameters.

We studied two paradigm problems to explore the behaviour of this system. The first problem was a one-reaction system with solid advection, where we observed

a reaction front. The speed of this front was influenced by the gas flux into the reaction layer, resembling a diffusion flame. In the large Péclet number limit, the front position exhibited linear behaviour due to dominant advection, while in the small Péclet limit, the position followed a $t^{1/2}$ dependency as diffusion became dominant. Both analytical and numerical solutions were employed to explore this scenario. The second paradigm problem, which more accurately reflects our chemistry, involved self-sustaining reactions leading to significant gas concentrations within the reaction layer. In this case, silicon monoxide was produced directly within the reaction layer to convert carbon into silicon carbide, unlike the previous example where the reaction was limited by gas transport from the inlet. Consequently, the reaction front position was linear and directly proportional to the amount of silicon monoxide present. We solved this problem using asymptotic methods, as well as numerically.

Returning to the full model, we solved the system numerically. We observed that, for small Da and Pe $= \mathcal{O}(1)$ values, the behaviour mirrored that of our second paradigm problem, with reactions dominating the system. This led to large gas concentrations due to rapid gas production outpacing transport. When both Da and Pe were $\mathcal{O}(1)$, the gas was transported more efficiently throughout the particle bed. As a result, the reaction became more uniform across the crucible, eliminating the distinct reaction front observed previously. This uniformity also contributed to more manageable concentrations and pressures, as gas flow was driven by concentration gradients.

We examined in detail four examples within the parameter space. First, using default values, we observed behaviour similar to the second example but with a boundary layer at the top of the particle bed due to the Péclet number being large. This resulted in moderate carbon utilization, silicon yield, and maximum pressure. Second, with default parameters, but $\chi = 50$, the gas struggled to escape, leading to spatially uniform dynamics. Advection and diffusion equilibrated the concentrations, resulting in exponential gas production, rapid reactions, and short consumption time. This scenario exhibited high carbon utilization and silicon yield, with an unphysically large maximum pressure. Third, using default parameters, but $\mathcal{C}_{\mathrm{SiO}} = 100$ and $\mathcal{C}_{\mathrm{CO_2}} = 10$, a boundary layer at the top was observed. Silicon monoxide and carbon dioxide were produced faster than they were consumed, causing significant gas loss through the crucible top, leading to low carbon utilization, very low silicon yield, and a maximum pressure of about 1.2. Lastly, with $\mathcal{C}_{\mathrm{SiO}} = 0.01$ and $\mathcal{C}_{\mathrm{CO_2}} = 0.1$, we again observed spatially uniform dynamics, with very fast reactions, resulting in high carbon utilization and very high silicon yield. This scenario also led to exponential gas production, which is unsafe and unphysical due to the rapid build up of gas.

We moved on to parameter sweeps to better understand the macroscale metrics as dimensionless parameters varied. Within the Da–Pe plane, there were not large variations in carbon utilization or silicon yield. Consumption time depended on effective transport; faster transport led to slower reactions as more gas escaped. For small Da and large Pe, transport was very slow compared to reactions, leading to short consumption times. The maximum pressure depended more strongly on Da than Pe, with lower Da causing higher pressures due to reduced transport. Within the $\mathcal{C}_{\mathrm{SiO}}$–$\mathcal{C}_{\mathrm{CO_2}}$ plane, there were $\mathcal{O}(1)$ variations in carbon utilization and silicon yield, both of which depended more strongly on $\mathcal{C}_{\mathrm{SiO}}$ than on $\mathcal{C}_{\mathrm{CO_2}}$. Smaller $\mathcal{C}_{\mathrm{SiO}}$ led to higher carbon utilization and silicon yield, and increasing $\mathcal{C}_{\mathrm{CO_2}}$ also increased silicon yield, but to a lesser extent. For small $\mathcal{C}_{\mathrm{SiO}}$ and $\mathcal{C}_{\mathrm{CO_2}}$, both the silicon carbide and Boudouard reactions were fast, leading to a self-sustaining system with very fast reactions and the smallest consumption time. For large $\mathcal{C}_{\mathrm{SiO}}$ and $\mathcal{C}_{\mathrm{CO_2}}$, the system depended on the inlet carbon monoxide and the consumption time was much longer. Similarly, for the maximum pressure, small $\mathcal{C}_{\mathrm{SiO}}$ and $\mathcal{C}_{\mathrm{CO_2}}$ resulted in the largest maximum pressure due to the reactions being fastest here, while both $\mathcal{C}_{\mathrm{SiO}}$ and $\mathcal{C}_{\mathrm{CO_2}}$ being large resulted in the smallest maximum pressure. For the Da–χ plane, both carbon utilization and silicon yield depended more strongly on χ than on Da. For small χ, the gas could not escape the crucible, leading to fast reactions and high maximum pressure. The scaled consumption time increased with both Da and χ, as increasing transport and flux at the top of the pellets slowed the process.

Elkem ASA aims to maximize silicon yield while maintaining safe pressures. From the parameter sweeps, several key trends emerged. To maintain safe pressures, the Damköhler number Da should be large, the Péclet number Pe should be small, and the carbon monoxide concentration ratio $\mathcal{C}_{\mathrm{CO}}$ should be large. For good silicon yield, the silicon monoxide concentration ratio $\mathcal{C}_{\mathrm{SiO}}$ should be small. Increasing Da can be achieved by increasing the initial radius of the quartz or decreasing the initial bed height. Decreasing Pe can be accomplished by reducing the permeability κ, though this may lead to higher pressures. The requirement to decrease $\mathcal{C}_{\mathrm{SiO}}$ while increasing $\mathcal{C}_{\mathrm{CO}}$ can be interpreted as maximizing the rate of the silicon carbide reaction while minimizing the rate of the Boudouard reaction. However, in practice, reaction rates are difficult to control, making this challenging to implement. Due to nonlinear interactions and complex dependencies, these general principles may not necessarily lead to an optimal solution. Therefore, further investigation is required.

Looking ahead to Chapter 4, our focus will shift to identifying strategies to control the maximum pressure while maximizing silicon yield. Given that excessive pressure

poses a significant risk to the structural integrity of the crucible, particularly in the more extreme cases, optimization is critical in finding solutions that balance gas production and gas pressure.

Chapter 4

Optimization of the multiphase model

We have developed a multiphase model for silicon carbide production and conducted initial parameter sweeps to understand the general impact of the parameters on the silicon yield and carbon utilization. The next step is to refine and optimize this process to maximize silicon yield. Pressure plays a significant role in the process, and will be considered in the optimization. Although our current focus is on maximizing silicon yield, our optimization methods are flexible enough to accommodate other objectives, such as chemical selectivity, should they become priorities in future work. In Section 4.1, we introduce optimization techniques, focusing on derivative-free methods, which are particularly suited to our problem. These include direct search methods such as DIRECT [137] and DIRECT-L [138], as well as model-based approaches like BOBYQA [139]. This section sets the stage for the optimization strategies we employ. In Section 4.2, we delve into the specific objective and optimization method we implement, with a discussion on constraining pressure to acceptable levels. In Section 4.3, we examine two examples in detail, one where we do not allow the maximum pressure to exceed 3.0, and one where we do not let it exceed 1.2. Additionally, we conduct stability analysis to identify the most influential model parameters, providing insights into which aspects of the system are most critical to achieving optimal results. In Section 4.4, we shift the focus toward understanding the effects of dimensional parameters. We specifically investigate the initial height of the bed of pellets, the permeability of the pellet bed, and the mass transfer coefficient at the top of the bed of pellets. We also explore prescribing a fixed dimensional duration for the experiment rather than allowing it to run to completion. Finally, in Section 4.5, we summarize the findings from our optimization efforts and provide conclusions on the

overall effectiveness of the model.

4.1 Introduction

Derivative-based and derivative-free methods are the two primary classes of methods in optimization [140]. Derivative-based methods rely on accurate calculations of the objective function and its derivatives. The derivatives play a critical role in determining search directions and deciding when to terminate the optimization process [141]. Methods like analytic differentiation [142], where derivatives are computed manually based on an analytic form of the objective function, or algorithmic differentiation [142], which automates this process symbolically, are common approaches. However, these methods require access to the objective's analytic form or the ability to differentiate the code, which is impractical for our scenario. `ForwardDiff.jl` [143] provides automatic differentiation for native Julia functions. However, this is not compatible with `SUNDIALS`, which is not written in Julia. An alternative is to approximate the derivatives by finite differences [144]. However, this requires $d + 1$ evaluations for forward (or backward) differences and $2d$ evaluations for central difference, for a d dimensional space. Methods that use high-order derivatives, such as Newton's method, require even more objective evaluations. In the finite differences case, derivative-based methods are impractical for large dimensionality or very expensive objective calculations.

Given that our model is costly to evaluate accurately and might involve (numerical) noise, derivative-free optimization methods are more suitable [141]. These methods operate without requiring derivative information, making them robust for scenarios where the objective function is treated as a black box. Our parameter space has relatively low dimensionality, and the objective is smooth but expensive to compute, aligning well with the strengths of derivative-free optimization techniques [141]. Derivative-free optimization methods have a wide range of applications in mathematics, physics, engineering, chemistry, computer science, economics, and finance [140, 141, 145–152].

For our optimization strategy, we will start with a global direct search method to explore the full parameter space and identify the general vicinity of the optimal solution. Direct search methods are known for their global exploration capabilities, making them suitable for our initial phase. Once we have identified the most promising region or neighbourhood of the parameter space, we will transition to a model-based local optimization method.

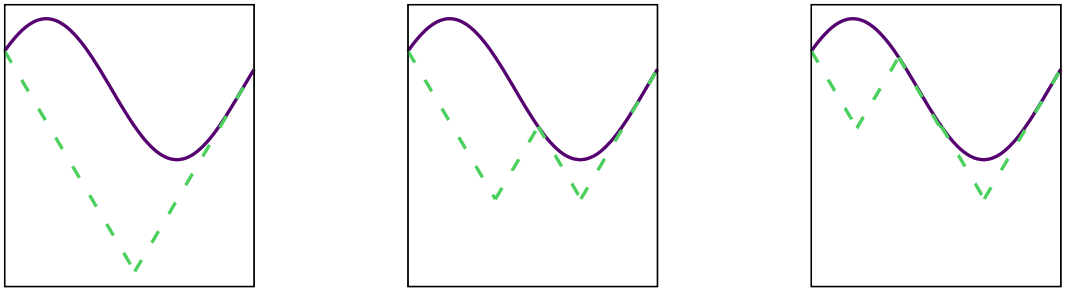

(a) First iteration. (b) Second iteration. (c) Third iteration.

Figure 4.1: Shubert's algorithm. A function (purple line) is approximated (green dashed line) from below by piecewise linear functions with slope $\pm K$, where K is a Lipschitz constant of the function. (a) In the first iteration, the function is evaluated at the endpoints and the approximation is built. (b), (c) In subsequent iterations, the function is evaluated at a minimum of the approximation and the approximation is refined.

4.1.1 Direct search methods

We first introduce Shubert's method so that we can build up to the DIRECT algorithm. Shubert's method [153], is used for the global minimization of a univariate continuous function f over a bounded interval $[a, b]$. This method assumes that f is Lipschitz continuous so that for all $x, x' \in [a, b]$ we have that

$$|f(x) - f(x')| \leq K|x - x'|. \tag{4.1}$$

Alternatively, for our purposes we assume the derivative of the function satisfies

$$f'(x) \leq K \tag{4.2}$$

for all $x \in [a, b]$. Additionally, we assume that some upper bound on K is known.

Shubert's method iteratively refines a piecewise linear lower bound for f, where each segment has a slope of $\pm K$. The algorithm begins by evaluating $f(a)$ and $f(b)$. Based on the Lipschitz condition (4.1) we know that for all $x \in [a, b]$

$$f(x) \geq f(a) - K(x - a), \tag{4.3}$$
$$f(x) \geq f(b) + K(x - b), \tag{4.4}$$

which gives lines of slope $\pm K$ passing through the points $(a, f(a))$ and $(b, f(b))$. These lines are used to form the initial piecewise approximation, as shown in Figure 4.1a. Next, we find the minimum of this piecewise approximation and evaluate the function

at this point. Using this new value, the approximation is updated by applying the same procedure. More specifically, for the minimum point c from the first iteration, we impose

$$f(x) \geq f(c) - K(x - c) \quad \text{for} \quad x \geq c, \tag{4.5}$$

$$f(x) \geq f(c) + K(x - c) \quad \text{for} \quad x \leq c, \tag{4.6}$$

resulting in a 'W'-shaped approximation, as depicted in Figure 4.1b. If there are multiple minima in the approximation, one is chosen at random for the next step.

This iterative process continues (Figure 4.1c), and after several iterations we approach the true minimum of the function. Additionally, notice that the sum of (4.3) and (4.4) evaluated at the midpoint gives

$$f(c_i) \geq \frac{1}{2}(f(b_i) + f(a_i)) - \frac{K}{2}(b_i - a_i), \tag{4.7}$$

for any interval $[a_i, b_i]$ with midpoint c_i. The first term of the right-hand side favours intervals with good function evaluations (leading to local searching), while the second term favours small intervals or large values of K (leading to global searching). Thus, the Lipschitz constant K acts as a balancing factor between local and global searching, with larger K skewing the method toward global exploration.

Shubert's method and similar Lipschitz-based methods have three considerable drawbacks. First, estimating the Lipschitz constant K can be challenging, as it often cannot be easily computed. In many applications, the objective function might be based on time-consuming simulations or large finite element computations, making K difficult to determine. Second, the speed of convergence is often slow. In practice, the Lipschitz constant is typically large, either due to the nature of the objective or because it must be chosen as an upper bound on the derivative, which can significantly slow the algorithm's progress. Third, the computational complexity increases rapidly with dimensionality. In the initialization phase, we must evaluate the objective at the endpoints of the interval. While this is manageable in one or a few dimensions, for an d-dimensional problem, we must evaluate the objective 2^d times before we can begin, which becomes impractical for high-dimensional problems or expensive objective functions.

The DIRECT (DIviding RECTangles) algorithm, developed in 1993 by Jones, Perttunen, and Stuckman [137], is a deterministic global optimization method designed to alleviate the issues with Shubert's method. First, with regard to large

values of K, the DIRECT algorithm simultaneously searches using all possible values of K, as we will explain in more detail shortly. Second, DIRECT adapts the search process by dynamically balancing global exploration and local exploitation, ensuring that the algorithm converges efficiently. Third, regarding complexity, instead of evaluating the objective at the endpoints of intervals as in Shubert's method, DIRECT evaluates the objective at the midpoints of hyper-rectangles (generalizations of rectangles in higher dimensions). This significantly reduces the computational burden in higher dimensions, as any hyper-rectangle has a single centre point, regardless of dimensionality. An additional advantage of the DIRECT algorithm over other direct search methods is that it only requires the specification of one hyperparameter. DIRECT is known to be insensitive to this value, making the method robust and easy to apply in practice [137].

We now describe the DIRECT algorithm in one dimension in detail. In Figure 4.2, we illustrate the first few iterations of DIRECT. We initialize by evaluating the objective function at the midpoint of the initial interval. In the first iteration, we divide the interval into three equal sub-intervals, where the original midpoint becomes the centre of the middle sub-interval. The objective function is then evaluated at the midpoints of the two newly created intervals (Figure 4.2a, top). Next, for each interval, we plot a point corresponding to the width of the interval and the objective value at the midpoint (Figure 4.2a, bottom). In the first iteration all three intervals have the same length, and so the points are vertically aligned. Using this plot, we determine the 'potentially optimal' intervals by identifying the convex hull[1]. Any point on the boundary of the convex hull is potentially optimal. We divide each potentially optimal interval into three smaller intervals, repeating the above process. In our example, the only potentially optimal interval in the first iteration is the rightmost one. We divide this region into three smaller sub-intervals, compute the objective at the two new midpoints, and update the plot (Figure 4.2b).

We continue by identifying the potentially optimal intervals based on the updated convex hull (Figure 4.2b, bottom) and repeat the process. In the third iteration, shown in Figure 4.2c, we divide the two potentially optimal intervals from the second iteration, compute the objective at their midpoints, and update the convex hull plot accordingly. This results in identifying three potentially optimal intervals after the third iteration, and we proceed by repeating the division and evaluation steps iteratively, refining our search for the global minimum. In the first few iterations of our

[1]The convex hull of a set of points is the smallest convex shape that encloses the set of points, for example, see [154].

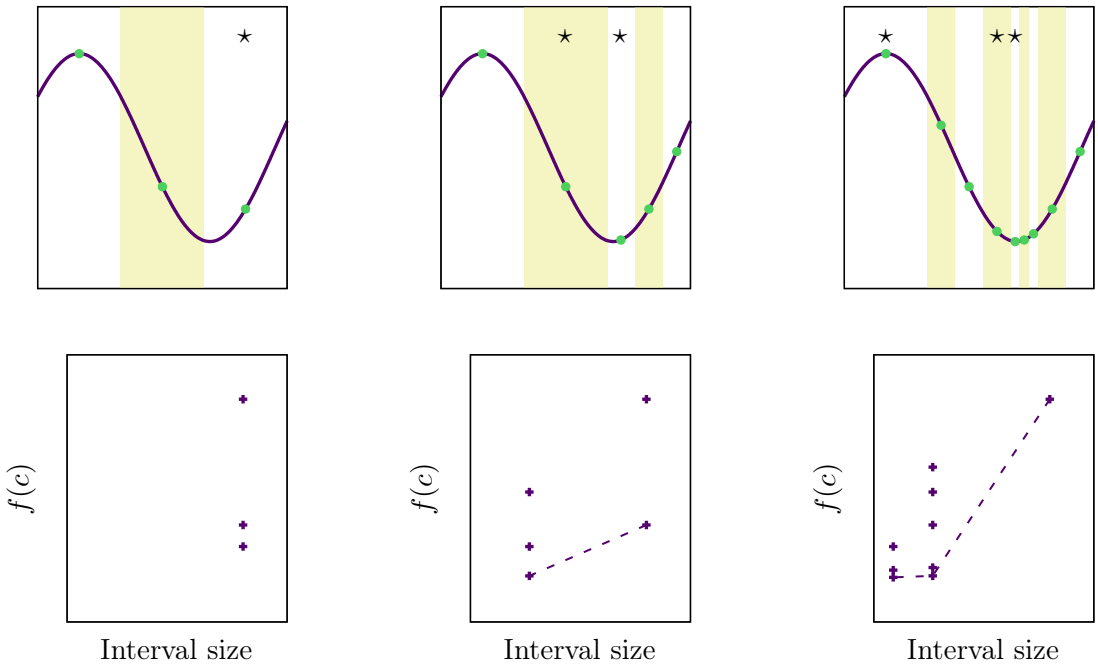

(a) First iteration (b) Second iteration (c) Third iteration

Figure 4.2: DIRECT algorithm. (a) In the first iteration, the interval is divided into three sub-intervals (top, white and yellow stripes) and the function (top, purple line) is evaluated at the midpoints (top, green dots). Interval size–function value pairs are recorded (bottom, purple crosses). (b) In the second iteration, the interval that contains the best function value is divided into three sub-intervals, and the function is evaluated at the two new midpoints. The interval size–function value pairs are updated, and the convex hull (bottom, purple dashed line) is computed. (c) In subsequent iterations, any interval size–function value pair on the boundary of the convex hull, and thus is potentially optimal (top, stars), is sub-divided by the same method as the second iteration.

simple example, the points forming the convex hull correspond to the best function evaluation for a particular interval size. However, this relationship does not hold in general.

The slope of a line on the plot of function evaluation versus interval size corresponds to a Lipschitz constant. We consider two cases: for large K, the best strategy is to search near the top right point, which corresponds to the largest interval. Despite having the worst objective value, the large interval size, along with large K, means the minimum may be in this interval. In this case, the large K may compensate for the difference in objective value caused by the wider interval. Large K biases us to search large intervals. Conversely, for small K, the top right point cannot contain a potential minimum because the objective value is too large. Thus, we focus on searching intervals with low objective values, prioritizing those with smaller sizes.

Small K biases us to search small intervals. This relationship between K and global versus local searching is further emphasized by DIRECT's adaptive search method. In DIRECT, by constructing the convex hull, we effectively search across all relevant values of K in each iteration, given the current state. The convex hull helps us determine the critical K values. In the third iteration of our example, for large K, the top right point is the best candidate for further search; for very small K, the bottom left point is preferred; and for intermediate K values, the bottom middle point is optimal. Since DIRECT does not require explicit knowledge of K, it searches in all three intervals corresponding to these points.

For generalization to higher dimensions, refer to [137]. In higher-dimensional spaces, DIRECT generalizes to using hyper-rectangles. Moreover, DIRECT is guaranteed to converge to the global minimum of continuous functions in d dimensions. As the number of iterations approaches infinity, each (hyper-)rectangle is subdivided an infinite number of times, ensuring that the entire search space is explored. In this way, the points evaluated form a dense subset of the original hyper-rectangle.

DIRECT-L [138] is a variation of the DIRECT algorithm that introduces a local search component to improve convergence speed, particularly in the final stages of optimization. While DIRECT is primarily focused on global exploration, DIRECT-L modifies the division strategy to emphasize local search more heavily once promising regions are identified. This is achieved by adjusting the selection of hyper-rectangles for further division, giving preference to those that show greater potential for containing the optimum. By doing so, DIRECT-L can often converge more quickly to the global optimum compared to the original DIRECT algorithm, especially in low dimensionality problems or where the landscape of the objective function has few local minima or is smooth.

Both DIRECT and DIRECT-L are widely used in practical optimization problems due to their robustness and ability to handle complex objective functions. They are particularly well-suited for applications in engineering and fields where the objective function may be difficult or expensive to evaluate. Direct search methods provide a reliable means of finding global optima without requiring derivative information, making them versatile tools in the optimization toolkit. However, in general, model-based methods are more efficient than direct search methods, particularly when the objective is smooth [141].

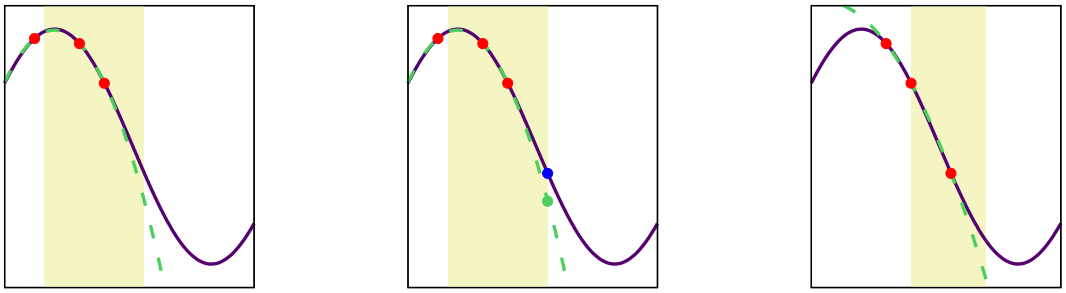

(a) Model. (b) Evaluate candidate step. (c) Update model.

Figure 4.3: One iteration of a model-based derivative-free optimization method. (a) Objective we wish to minimize (purple line), previous objective evaluations (red points), current model of objective (green dashed line), candidate, or trust, interval (yellow shading). (b) Minimum of model within candidate region (green point), and objective evaluation at the minimizer (blue). (c) Recompute model and new candidate region.

4.1.2 Model-based methods

Model-based optimization methods, such as BOBYQA (Bound Optimization BY Quadratic Approximation) [139], are designed to handle complex and expensive-to-evaluate objective functions by creating a model of the objective function. This model is computationally cheap to evaluate and is iteratively refined based on evaluations of the actual objective function. BOBYQA, developed in 2009 by Powell [139], constructs and updates a quadratic model of the objective function within a trust region framework. We show an example iteration of BOBYQA in Figure 4.3. At each iteration, it optimizes the quadratic model within the trust region (Figure 4.3b) to propose new evaluation points. The trust region is adjusted according to the model's predictive accuracy, and the quadratic model is updated accordingly (Figure 4.3c). This process continues until convergence criteria are met. BOBYQA is inherently a local optimization method, and therefore, the optimum found depends on the initial point. Although model-based methods are more efficient, their usability are limited by having good initial guesses of the optimum.

4.2 Optimization method

In the following analysis we maximize the objective function

$$f = Y_{\text{SiC}}(t^*) - \Lambda \left(\text{ramp} \left(\max_{z,t} P - P_{\text{pen}} \right) \right)^2, \tag{4.8}$$

Table 4.1: Parameters, their descriptions, lower bound, and upper bound used for optimization.

Param.	Description	Lower bound	Upper bound
Da	Damköhler number	10	1000
Pe	Péclet number	1	1000
χ	Dimensionless mass transfer coefficient	10	3000
$\mathcal{C}_{\mathrm{SiO}}$	Silicon monoxide concentration ratio	0.01	100
$\mathcal{C}_{\mathrm{CO_2}}$	Carbon dioxide concentration ratio	0.01	100

which depends on the parameters in Table 3.2. Here, $Y_{\mathrm{SiC}}(t^*)$ is the silicon yield given by (3.177), at the quartz consumption time t^*, and the second term penalizes a maximum pressure over P_{pen}, where

$$\mathrm{ramp}(x) = \max\{x, 0\} \tag{4.9}$$

is the ramp function, and Λ is the coefficient of the penalization. We take the square of the ramp term so that f is everywhere differentiable. Although we use derivative-free methods, it is still beneficial to have a differentiable objective, particularly for a model-based method. In all of our analysis, for simplicity, we take $\Lambda = 1$.

We optimize the objective function over the five parameters Da, Pe, χ, $\mathcal{C}_{\mathrm{SiO}}$, and $\mathcal{C}_{\mathrm{CO_2}}$ within the bounds given in Table 4.1. Since we are interested in optimizing over a wide range of parameter values we employ a two-step hybrid method. We start with DIRECT-L allowing for a global exploration to identify the neighbourhood of the global optimum. Once this promising region is found, we switch to BOBYQA leveraging its more efficient local search capabilities to quickly converge to the optimum. We optimize with respect to the log of the parameters in the first phase since we allow the parameters to vary by multiple orders of magnitude. This modification helps the solver find the optimal neighbourhood more quickly than if using the parameters themselves (owing to the linear dividing in DIRECT). As we saw in the parameter sweeps in Chapter 3, $\mathcal{O}(1)$ variations in the silicon yield typically required $\mathcal{O}(100)$ variations in the parameters. In the second, local, phase we optimize with respect to the parameters themselves. In this phase, we are more interested in the local landscape, and the size of the bounds do not effect BOBYQA's behaviour. Practically, we conduct the optimization by calling the NLOpt (non-linear optimization) library [155] from within Julia. We specify an objective tolerance of 10^{-4} for DIRECT-L in the

first phase, and a tolerance of 10^{-5} for BOBYQA in the second phase.

4.3 Results

We recall from the parameter sweeps in Chapter 3 that the silicon yield is typically very flat within the parameter space. The silicon yield may only vary by a few percent as the parameters vary by orders of magnitude. The flatness within the parameter space will be further intensified as we examine the local neighbourhood around an optimum point.

We apply the method described in the previous section, with a penalty pressure of $P_{\text{pen}} = 3.0$. We find that the optimal value of f is 0.9961, which is achieved for $\text{Da} = 37.6$, $\text{Pe} = 907.7$, $\chi = 632.2$, $\mathcal{C}_{\text{SiO}} = 0.01$, $\mathcal{C}_{\text{CO}_2} = 95.2$, and takes about 4 hours on a standard desktop computer. We note that we report the optimal objective value to more significant figures than is physical or that can be determined by our model. A laboratory-scale experiment could not be constructed with the accuracy in the parameters or silicon yield needed to achieve four significant figures. Furthermore, since we use a macroscale multiphase model there are higher-order corrections terms in δ that we have not accounted for. Finally, the accuracy of this number is dependent on the spacial discretization and tolerance used for the model solution.

Here, the silicon carbide reaction is the fastest ($\mathcal{C}_{\text{SiO}} \ll 1$), while the Boudouard reaction is the slowest ($\mathcal{C}_{\text{CO}_2} \gg 1$). The rapid silicon carbide reaction ensures a high silicon yield. Any silicon monoxide produced reacts quickly with carbon to form silicon carbide. Conversely, the slow Boudouard reaction helps maintain a reasonable maximum pressure. We show the time evolution in Figure 4.4. Similar to earlier examples, the three solid volume fractions exhibit comparable profiles to each other. We also observe a sharp boundary layer at the top of the particle bed. Silicon monoxide and carbon dioxide have similar profiles and time evolutions. Carbon monoxide reacts with quartz and as the quartz is consumed the carbon monoxide is transported farther up the crucible. We achieve a silicon yield of 99.61% at the quartz consumption time since the silicon carbide reaction is significantly faster than the other two reactions. The final carbon utilization is around 60%. The slow Boudouard reaction makes it almost negligible, meaning almost all reacted carbon forms silicon carbide. Thus, the mole ratio of carbon to quartz is effectively $2 : 1$ instead of $3 : 1$ as in the net reaction (1.9). Since we started with an excess carbon to quartz ratio of $3.5 : 1$, we expect to react $4/7$, or about 57.1%, of the carbon. Our simulation shows a carbon utilization of 58.5%, slightly higher because of the Boudouard reaction. The pressure

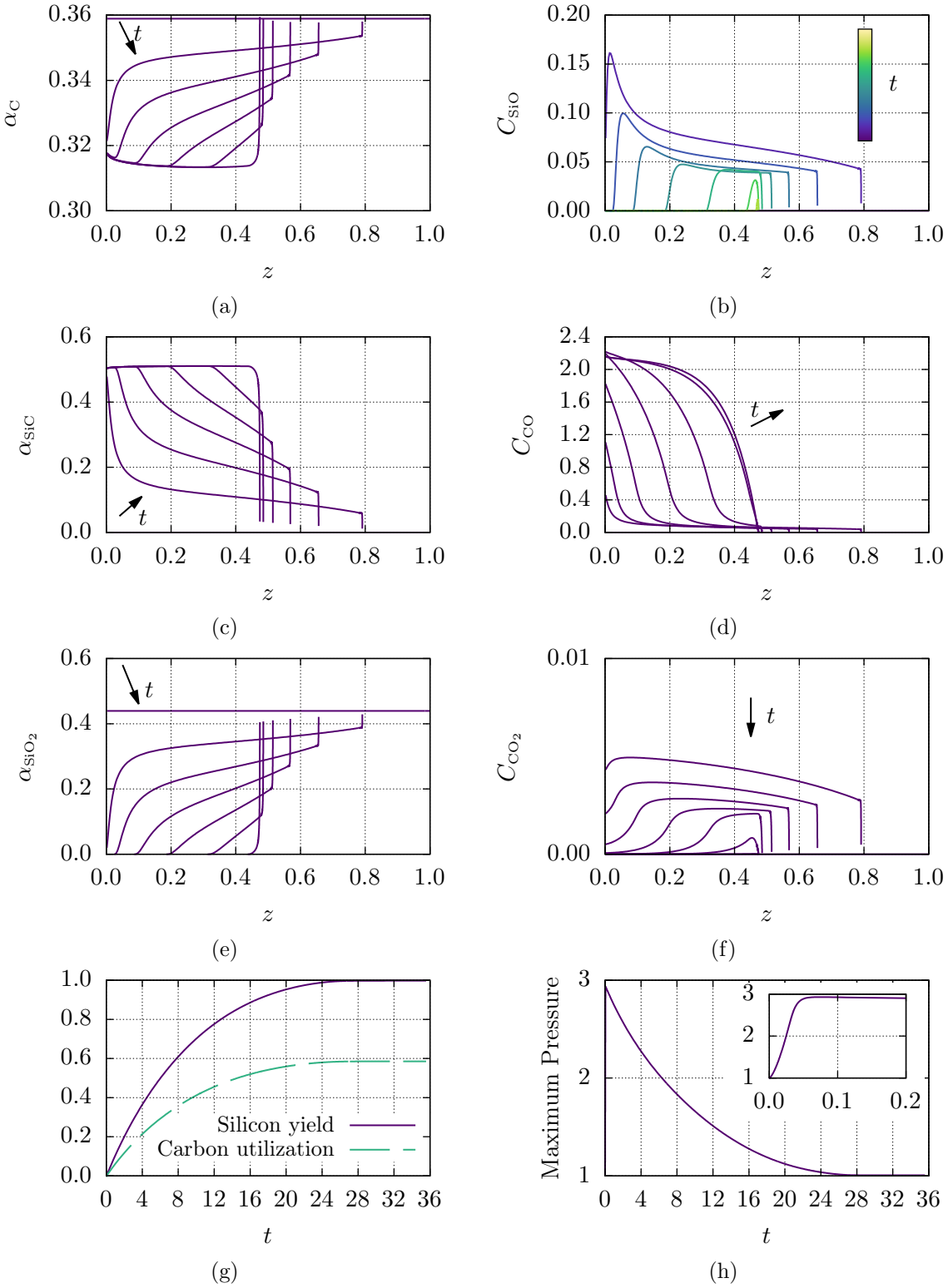

Figure 4.4: Graphs of the numerical solution of (3.6), (3.17), (3.51)–(3.55), (3.57)–(3.59), (3.62), (3.63), and (3.76). Parameter values taken from Table 3.2, except we take Da = 37.6, Pe = 907.7, $\chi = 632.2$, $\mathcal{C}_{SiO} = 0.01$, and $\mathcal{C}_{CO_2} = 95.2$, the optimal values when $P_{pen} = 3.0$. Lines in (a)–(f) are plotted for $t = 0.0, 5.93, 11.86, 17.78, 23.71, 29.64, 35.57$.

quickly spikes to a maximum of 2.932, just below our limit of 3.0, and then steadily decreases back to the equilibrium pressure of 1.0.

We now examine the sensitivity of the objective around the optimum with respect to the parameters. We recall from the parameter sweeps, the silicon yield is most impacted by $\mathcal{C}_{\text{SiO}}$, with the silicon yield increasing as $\mathcal{C}_{\text{SiO}}$ decreases. We numerically compute the Hessian around the optimum point found. This requires 51 model evaluations[2], and takes about 5 hours. The Hessian matrix provides a measure of sensitivity since its elements are second-order partial derivatives of the objective function with respect to the parameters. We find that the Hessian is

$$H = \begin{pmatrix} -4.50 \cdot 10^{-4} & -2.30 \cdot 10^{-6} & -3.52 \cdot 10^{-6} & -4.86 \cdot 10^{-3} & -2.93 \cdot 10^{-5} \\ -2.30 \cdot 10^{-6} & -1.00 \cdot 10^{-6} & 3.03 \cdot 10^{-8} & 1.46 \cdot 10^{-6} & 4.88 \cdot 10^{-7} \\ -3.53 \cdot 10^{-6} & 3.03 \cdot 10^{-8} & -1.03 \cdot 10^{-6} & -5.93 \cdot 10^{-6} & -8.37 \cdot 10^{-7} \\ -4.86 \cdot 10^{-3} & 1.46 \cdot 10^{-6} & -5.93 \cdot 10^{-6} & 5.43 & -7.88 \cdot 10^{-5} \\ -2.93 \cdot 10^{-5} & 4.88 \cdot 10^{-7} & -8.37 \cdot 10^{-7} & -7.88 \cdot 10^{-5} & -3.98 \cdot 10^{-5} \end{pmatrix}. \tag{4.10}$$

The eigenvectors of the Hessian indicate the principal directions in which the objective function is most sensitive, helping us understand how changes in parameters affect the silicon yield. The eigenvalues of H are

$$\begin{aligned} \lambda_1 &= 5.43, \\ \lambda_2 &= -4.56 \cdot 10^{-4}, \\ \lambda_3 &= -3.78 \cdot 10^{-5}, \\ \lambda_4 &= -1.02 \cdot 10^{-6}, \\ \lambda_5 &= -9.47 \cdot 10^{-7}, \end{aligned} \tag{4.11}$$

[2]Numerically computing the Hessian with central differences requires $2d^2 + 1$ evaluations for a d dimensional Hessian.

with eigenvectors

$$V = \begin{pmatrix} 0.000896 & -1.00 & -0.0703 & -0.000965 & 0.00909 \\ -2.69 \cdot 10^{-7} & -0.00496 & -0.0177 & -0.656 & -0.751 \\ 1.09 \cdot 10^{-6} & -0.00786 & 0.0160 & 0.751 & -0.660 \\ -1.00 & -0.0008943 & -4.85 \cdot 10^{-5} & -2.12 \cdot 10^{-7} & 7.59 \cdot 10^{-6} \\ 1.45 \cdot 10^{-5} & -0.0703 & 1.00 & -0.02378 & -0.00208 \end{pmatrix}. \quad (4.12)$$

There is some degree of numerical noise in the computation of the Hessian matrix, which also affects the eigenvalues and eigenvectors obtained from the analysis. In a perfect world, $\lambda_i = 0$ since we sought a maximum. However, four of the eigenvalues are small in magnitude and negative, while the final eigenvalue is 5.43. The eigenvector associated with $\lambda_1 = 5.43$ suggests decreasing $\mathcal{C}_{\text{SiO}}$ to improve the objective. However, the optimum point found has $\mathcal{C}_{\text{SiO}} = 0.01$, which is the lower bound we supplied (Table 4.1). Therefore, we are at the maximum objective within the bounds.

We will now further investigate the silicon yield, objective value, and maximum pressure around this optimum point. Specifically, we will examine the effects of each of the five parameters on these metrics, providing insight into how variations in parameter values influence the system's performance.

We note that by computing the Hessian and considering the following parameter sweeps, we gain additional insights into the objective function. However, these additional calculations are computationally expensive. While we could marginally refine and improve the objective value found by the solver, the gains we would realize are within the prescribed tolerance of the solver. Of course, tightening these tolerances could further improve the solution, but this would come at the cost of increased computation time both in the number of iterations of the optimization as well as tightening the tolerance of the model. We note that numerically computing the Hessian took a comparable amount of computational time as the entire optimization process.

We begin by examining the effect of Da, as shown in Figure 4.5. For values of Da less than 37.6 (indicated by the square), the objective function (dashed line) decreases due to the maximum pressure exceeding our penalty threshold of 3.0. From the plot, it is evident that decreasing Da slightly increases the silicon yield, as the current maximum pressure at Da = 37.6 is 2.932, allowing for a slight improvement in the objective value. This behaviour is also reflected in the second column of the eigenvector matrix V. The second most significant eigen-direction corresponds to a

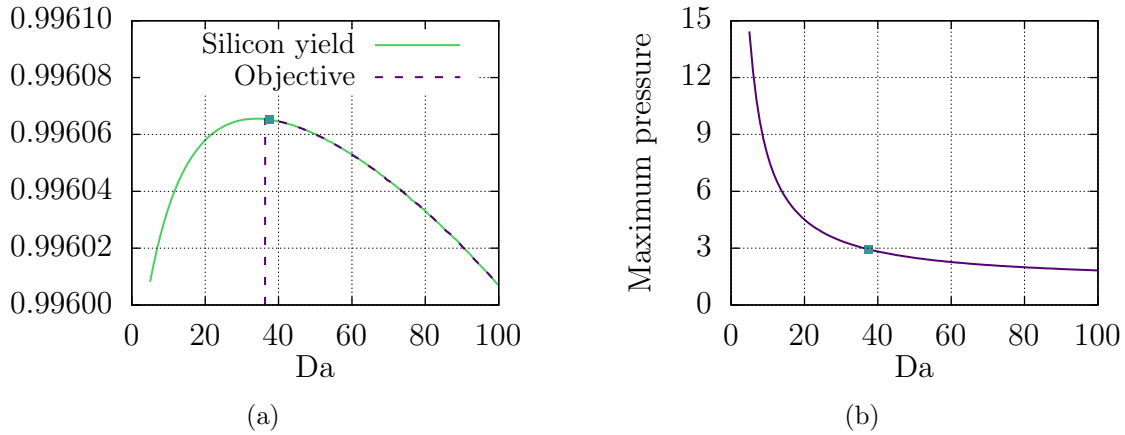

Figure 4.5: (a) Silicon yield at the quartz consumption time and objective, given by (3.177) and (4.8), respectively, and (b) maximum pressure. Parameter values taken from Table 3.2, except we take Pe = 907.7, $\chi = 632.2$, $\mathcal{C}_{\mathrm{SiO}} = 0.01$, and $\mathcal{C}_{\mathrm{CO}_2} = 95.2$. The teal square denotes the optimal point found for $P_{\mathrm{pen}} = 3.0$.

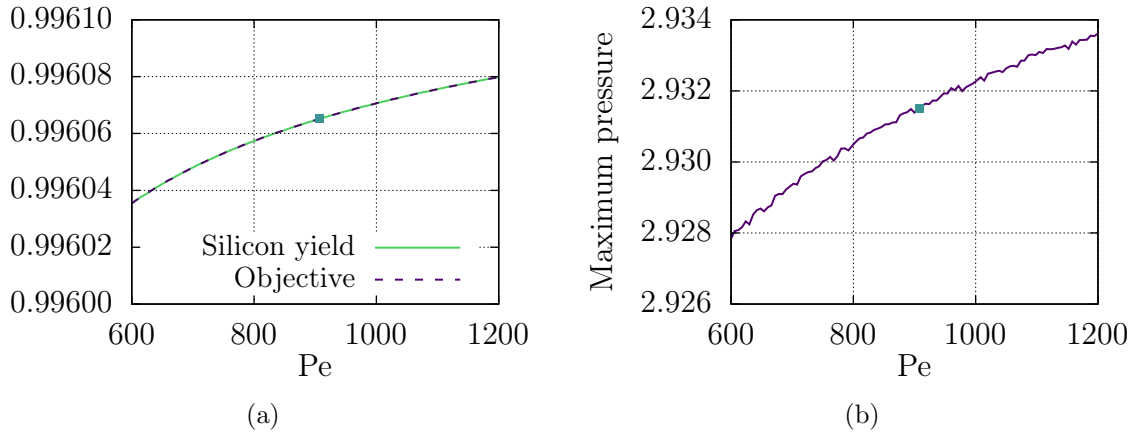

Figure 4.6: (a) Silicon yield at the quartz consumption time and objective, given by (3.177) and (4.8), respectively, and (b) maximum pressure. Parameter values taken from Table 3.2, except we take Da = 37.6, $\chi = 632.2$, $\mathcal{C}_{\mathrm{SiO}} = 0.01$, and $\mathcal{C}_{\mathrm{CO}_2} = 95.2$. The teal square denotes the optimal point found for $P_{\mathrm{pen}} = 3.0$.

decrease in Da, indicating its importance in optimizing the system. However, the impact of this direction is relatively small, as indicated by the magnitude of the corresponding eigenvalue, $\lambda_2 = -4.56 \times 10^{-4}$. We re-emphasize that this marginal increase in the silicon yield is within the tolerance of the optimization and would not be measurable in a laboratory.

In Figure 4.6, we show the results for Pe. Here, we find that the maximum pressure over the interval $600 \leq \mathrm{Pe} \leq 1200$ does not exceed the penalty threshold of 3.0. As a result, the silicon yield and the objective function are equal across this interval. The dependence of pressure on Pe is weak, with the maximum pressure varying by only

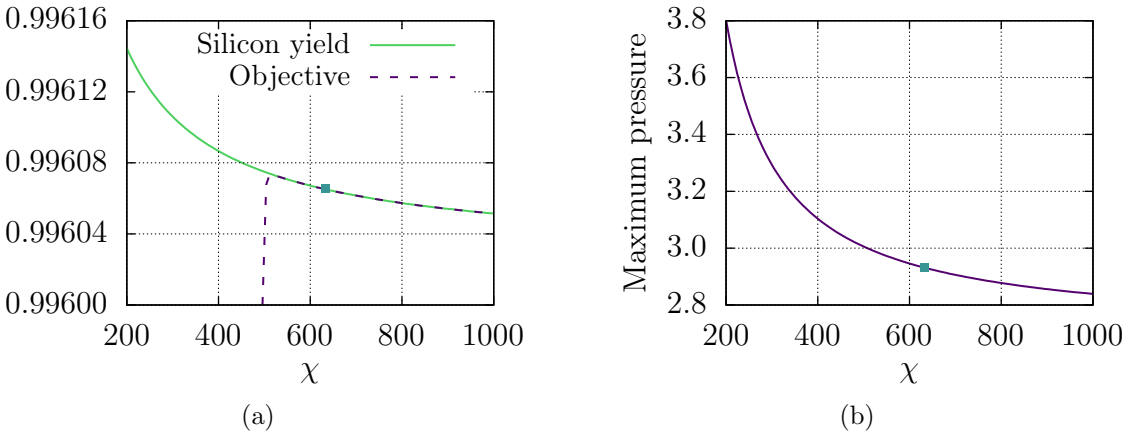

Figure 4.7: (a) Silicon yield at the quartz consumption time and objective, given by (3.177) and (4.8), respectively, and (b) maximum pressure. Parameter values taken from Table 3.2, except we take Da = 37.6, Pe = 907.7, $\mathcal{C}_{\mathrm{SiO}} = 0.01$, and $\mathcal{C}_{\mathrm{CO_2}} = 95.2$. The teal square denotes the optimal point found for $P_{\mathrm{pen}} = 3.0$.

about 0.2% over a factor of 2 in Pe. This weak dependence is consistent with our earlier findings during parameter sweeps. Increasing Pe up to the specified limit of 1000 would lead to a slight increase in the objective value, but only by approximately 10^{-5}. This small effect is further reflected in the eigenvalues of H, which are on the order of 10^{-6}, indicating that Pe has minimal impact on the objective in this neighbourhood.

In Figure 4.7, we show the effect of varying χ. From the plot, it appears that decreasing χ improves the objective value. The optimal value seems to be around $\chi \approx 500$, rather than $\chi = 632.2$ found by the solver. However, similar to what we observed with Pe, the variation in the objective with respect to χ is small. Changes in χ have only a marginal effect on the overall optimization.

In Figure 4.8, we show the results for $\mathcal{C}_{\mathrm{SiO}}$. As observed in the parameter sweeps and confirmed by the Hessian's eigenvectors, $\mathcal{C}_{\mathrm{SiO}}$ is the most impactful parameter on the silicon yield. The solver found a value of $\mathcal{C}_{\mathrm{SiO}} = 0.01$, which was the lower bound provided. The first column of the eigenvector matrix V, associated with the largest eigenvalue, indicates that decreasing $\mathcal{C}_{\mathrm{SiO}}$ would further improve the objective. Indeed, we observe that the objective increases as $\mathcal{C}_{\mathrm{SiO}}$ is reduced below the lower bound, suggesting that a smaller value for $\mathcal{C}_{\mathrm{SiO}}$ leads to even better performance.

In Figure 4.9, we show the results for $\mathcal{C}_{\mathrm{CO_2}}$. Once again, the solver returns a value close to the provided bound, in this case, $\mathcal{C}_{\mathrm{CO_2}} = 95.2$, compared to the upper bound of $\mathcal{C}_{\mathrm{CO_2}} = 100$. From the parameter sweeps, we observed that $\mathcal{C}_{\mathrm{CO_2}}$ had a significant impact on the maximum pressure, which is also evident here. Interestingly,

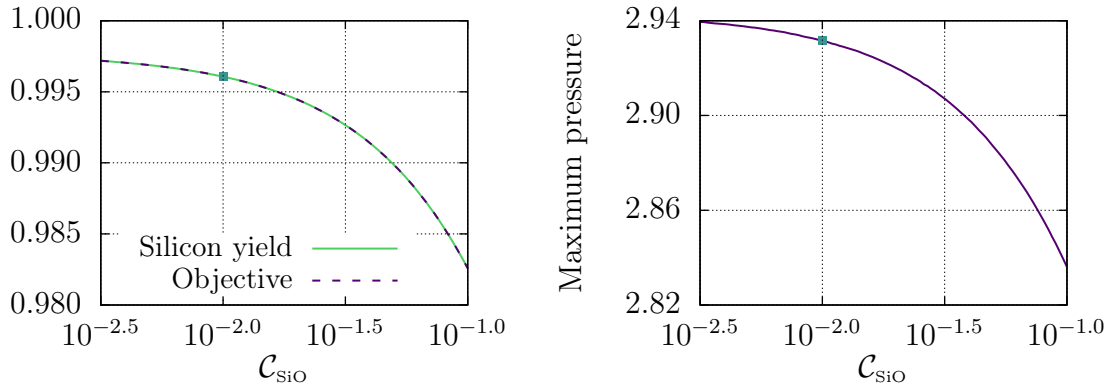

Figure 4.8: (a) Silicon yield at the quartz consumption time and objective, given by (3.177) and (4.8), respectively, and (b) maximum pressure. Parameter values taken from Table 3.2, except we take $\mathrm{Da} = 37.6$, $\mathrm{Pe} = 907.7$, $\chi = 632.2$, and $\mathcal{C}_{\mathrm{CO_2}} = 95.2$. The teal square denotes the optimal point found for $P_{\mathrm{pen}} = 3.0$.

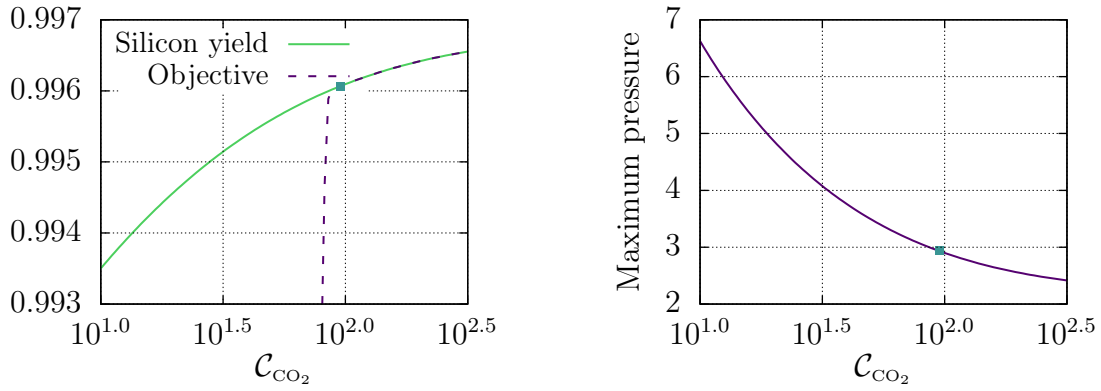

Figure 4.9: (a) Silicon yield at the quartz consumption time and objective, given by (3.177) and (4.8), respectively, and (b) maximum pressure. Parameter values taken from Table 3.2, except we take $\mathrm{Da} = 37.6$, $\mathrm{Pe} = 907.7$, $\chi = 632.2$, and $\mathcal{C}_{\mathrm{SiO}} = 0.01$. The teal square denotes the optimal point found for $P_{\mathrm{pen}} = 3.0$.

the feasible interval where the maximum pressure remains below 3.0 is narrow. For values of $\mathcal{C}_{\mathrm{CO_2}} \lesssim 80$, the maximum pressure exceeds the penalty pressure of 3.0. We also find that the objective increases as $\mathcal{C}_{\mathrm{CO_2}}$ approaches and surpasses 100, as indicated by the third column of V. However, similar to Da, Pe, and χ, the magnitude of the associated eigenvalue is small, suggesting that while $\mathcal{C}_{\mathrm{CO_2}}$ impacts the objective, its influence is not as strong as $\mathcal{C}_{\mathrm{SiO}}$.

These findings provide further evidence of the general trends we observed during the parameter sweeps are perhaps more relevant since they are centred around an optimal point. While we saw trends indicating marginal gains in the objective value,

we cannot necessarily apply all these trends simultaneously, particularly due to the interplay between Pe and χ, as demonstrated by the final two columns of V.

We repeat our optimization procedure with a penalty pressure $P_{\text{pen}} = 1.2$. We find that the optimized parameter values are Da = 916.8, Pe = 1.0, $\chi = 143.1$, $\mathcal{C}_{\text{SiO}} = 0.01$, and $\mathcal{C}_{\text{CO}_2} = 100.0$. With these parameters, we obtained a silicon yield of 0.9941 and a maximum pressure of 1.203. We note again that the accuracy of the objective value is not physical. The solution with these parameters is plotted in Figure 4.10. The dynamics in this case are nearly uniform in space due to fast diffusion. The gas concentrations are small because of the low $\mathcal{C}_{\text{SiO}}$ and high $\mathcal{C}_{\text{CO}_2}$. The silicon carbide reaction proceeds rapidly, while the Boudouard reaction is slow. This slow Boudouard reaction results in a low maximum pressure, as we observed previously. Since the Boudouard reaction is negligible, again the effective carbon-to-quartz ratio is approximately 2 : 1. Given that we supplied a 3.5 : 1 ratio, we expect to consume roughly $4/7 = 0.5714$ of the carbon. At the end of the simulation, 0.5749 of the carbon had been consumed, which is in line with this expectation. The maximum pressure quickly reaches 1.203 before decaying back to 1.0 over time.

The Hessian at the optimal point found by the solver is given by

$$H = \begin{pmatrix} -4.59 \cdot 10^{-9} & 1.93 \cdot 10^{-6} & -3.32 \cdot 10^{-7} & -3.57 \cdot 10^{-5} & -8.00 \cdot 10^{-8} \\ 1.93 \cdot 10^{-6} & -0.000830 & 0.000150 & 0.0186 & 3.62 \cdot 10^{-5} \\ -3.32 \cdot 10^{-7} & 0.000150 & -2.76 \cdot 10^{-5} & -0.00471 & -6.61 \cdot 10^{-6} \\ -3.57 \cdot 10^{-5} & 0.0186 & -0.00471 & 0.365 & -0.000543 \\ -8.00 \cdot 10^{-8} & 3.62 \cdot 10^{-5} & -6.61 \cdot 10^{-6} & -0.000543 & -1.69 \cdot 10^{-6} \end{pmatrix}. \tag{4.13}$$

The eigenvalues of H are

$$\begin{aligned} \lambda_1 &= 0.366, \\ \lambda_2 &= -0.00186, \\ \lambda_3 &= -2.87 \cdot 10^{-6}, \\ \lambda_4 &= -1.46 \cdot 10^{-7}, \\ \lambda_5 &= 3.71 \cdot 10^{-10}, \end{aligned} \tag{4.14}$$

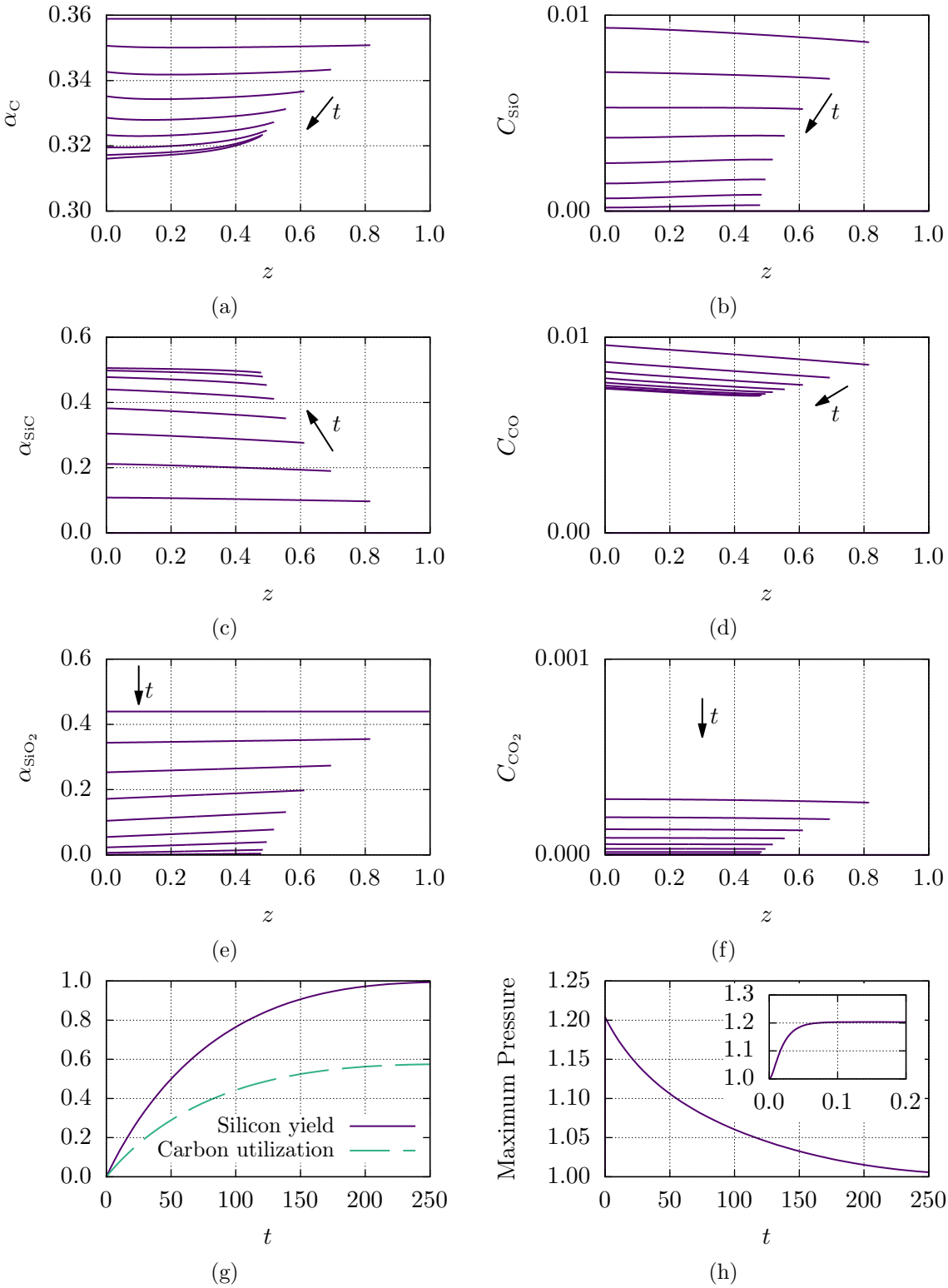

Figure 4.10: Graphs of the numerical solution of (3.6), (3.17), (3.51)–(3.55), (3.57)–(3.59), (3.62), (3.63), and (3.76). Parameter values taken from Table 3.2, except we take Da = 916.8, Pe = 1.0, χ = 143.1, $\mathcal{C}_{SiO}$ = 0.01, and $\mathcal{C}_{CO_2}$ = 100.0, the optimal values when P_{pen} = 1.2. Lines in (a)–(f) are plotted for t = 0.0, 31.27, 62.55, 93.82, 125.10, 156.38, 187.65, 218.92, 250.20.

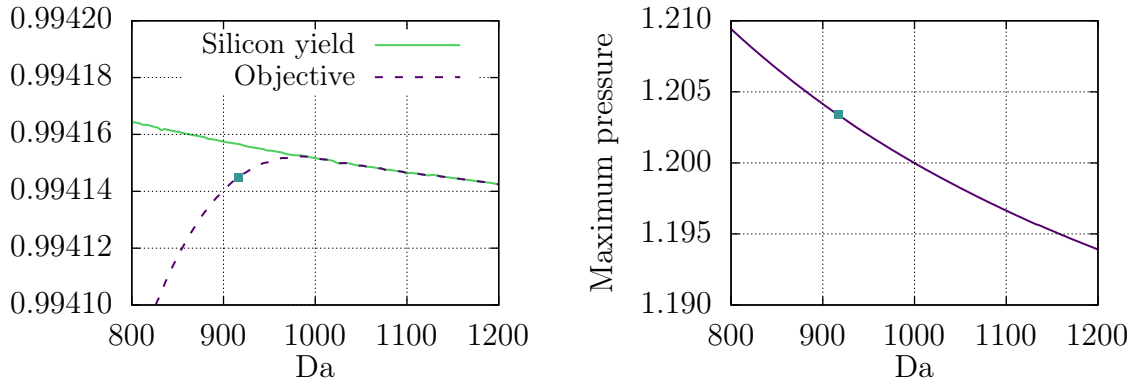

Figure 4.11: (a) Silicon yield at the quartz consumption time and objective, given by (3.177) and (4.8), respectively, and (b) maximum pressure. Parameter values taken from Table 3.2, except we take $\mathrm{Pe} = 1.0$, $\chi = 143.1$, $\mathcal{C}_{\mathrm{SiO}} = 0.01$, and $\mathcal{C}_{\mathrm{CO_2}} = 100.0$. The teal square denotes the optimal point found for $P_{\mathrm{pen}} = 1.2$.

with associated eigenvectors

$$V = \begin{pmatrix} 9.72 \cdot 10^{-5} & -0.00206 & 0.0104 & -0.0404 & 1.00 \\ -0.0506 & 0.975 & -0.207 & 0.0657 & 0.00683 \\ 0.0128 & -0.214 & -0.967 & 0.138 & 0.0152 \\ -0.990 & -0.0522 & -0.00171 & -0.000101 & 3.44 \cdot 10^{-6} \\ 0.00148 & -0.0350 & 0.149 & 0.987 & 0.0383 \end{pmatrix}. \tag{4.15}$$

Once again, we observe that only one eigenvalue is non-negligible. This eigenvalue is associated with decreasing $\mathcal{C}_{\mathrm{SiO}}$. We note for the optimal solution found, $\mathcal{C}_{\mathrm{SiO}}$ is the lower boundary (Table 4.1), and so we cannot reduce it further.

Once again, we examine the plots of the silicon yield, objective function, and maximum pressure as we vary the five parameters around the optimum point identified by the solver.

Beginning with Da, in Figure 4.11, we observe that the silicon yield, objective, and maximum pressure are all relatively uniform across the parameter range. Visually, the objective could be slightly improved by increasing Da, although the improvement would be minimal, on the order of 10^{-5}. Increasing Da would lead to a decrease in silicon yield, but it would also reduce the maximum pressure, which in turn improves the objective. This behaviour is reflected in the final column of the eigenvector matrix V, where a slight increase in the objective is indicated by a small magnitude for the corresponding eigenvalue $\lambda_2 = -0.00186$. This suggests that while increasing Da

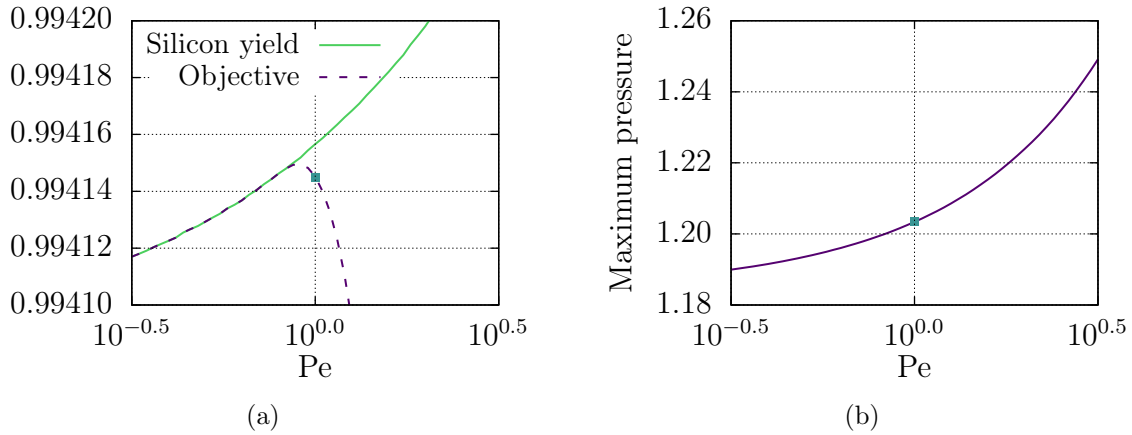

Figure 4.12: (a) Silicon yield at the quartz consumption time and objective, given by (3.177) and (4.8), respectively, and (b) maximum pressure. Parameter values taken from Table 3.2, except we take Da = 916.8, $\chi = 143.1$, $\mathcal{C}_{\text{SiO}} = 0.01$, and $\mathcal{C}_{\text{CO}_2} = 100.0$. The teal square denotes the optimal point found for $P_{\text{pen}} = 1.2$.

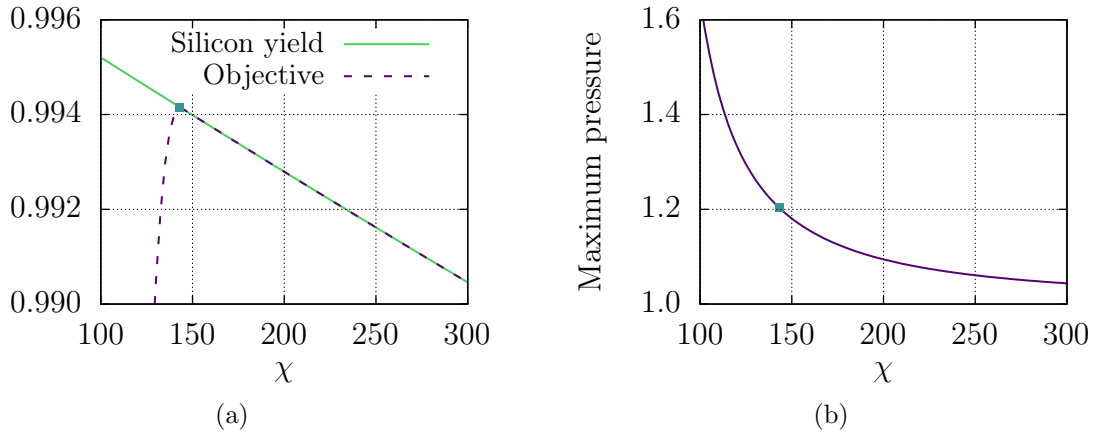

Figure 4.13: (a) Silicon yield at the quartz consumption time and objective, given by (3.177) and (4.8), respectively, and (b) maximum pressure. Parameter values taken from Table 3.2, except we take Da = 916.8, Pe = 1.0, $\mathcal{C}_{\text{SiO}} = 0.01$, and $\mathcal{C}_{\text{CO}_2} = 100.0$. The teal square denotes the optimal point found for $P_{\text{pen}} = 1.2$.

could enhance the objective, the overall impact would be minor.

In Figure 4.12 we show the results when we vary Pe. The solver finds a value of Pe = 1.0, equal to the minimum bound we set. For all relevant values of Pe the maximum pressure is greater than 1.2. Decreasing Pe farther would improve the objective, but as before, this would also decrease the silicon yield. However, the variations in the objective are small, on the order of 10^{-5}, indicating only a marginal improvement by varying Pe.

In Figure 4.13 we show the results when we vary χ. It appears that the solver has identified the optimal point for this parameter. Increasing χ results in a decrease

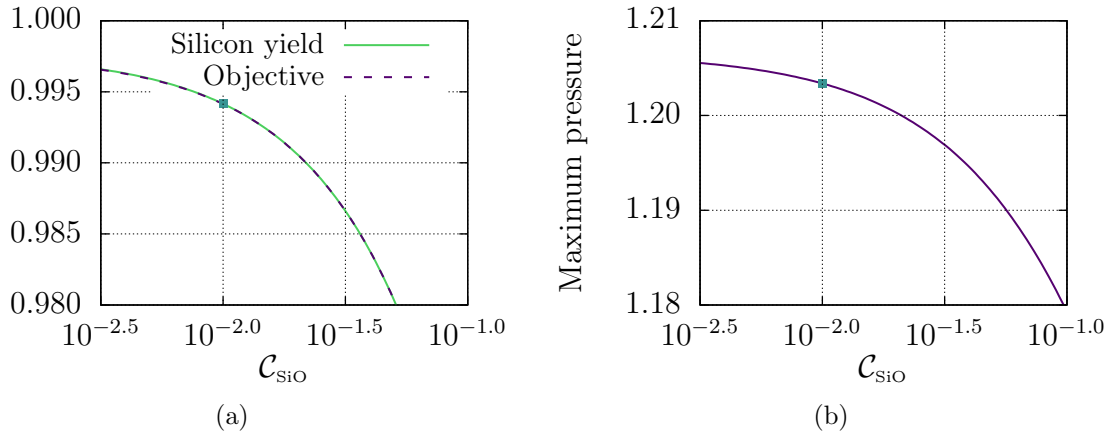

Figure 4.14: (a) Silicon yield at the quartz consumption time and objective, given by (3.177) and (4.8), respectively, and (b) maximum pressure. Parameter values taken from Table 3.2, except we take Da = 916.8, Pe = 1.0, $\chi = 143.1$, and $\mathcal{C}_{\mathrm{CO_2}} = 100.0$. The teal square denotes the optimal point found for $P_{\mathrm{pen}} = 1.2$.

in the silicon yield, while decreasing χ leads to an increase in the pressure, which in turn decreases the objective function. Thus, adjusting χ in either direction from this point negatively affects the objective.

We show in Figure 4.14 the results when we vary $\mathcal{C}_{\mathrm{SiO}}$. As with previous cases, $\mathcal{C}_{\mathrm{SiO}}$ is the most impactful parameter on both the silicon yield and the objective. The eigenvector associated with the largest eigenvalue suggests that decreasing $\mathcal{C}_{\mathrm{SiO}}$ improves the objective function. Indeed, we observe that the objective increases as $\mathcal{C}_{\mathrm{SiO}}$ decreases below 0.01. However, this value is the lower bound we provided to the solver, so we do not explore beyond this point, limiting further improvements to the objective in this direction.

Finally, in Figure 4.15 we show the results when we vary $\mathcal{C}_{\mathrm{CO_2}}$. Once again, the solver finds the upper bound, returning $\mathcal{C}_{\mathrm{CO_2}} = 100.0$. The silicon yield remains relatively flat as we vary $\mathcal{C}_{\mathrm{CO_2}}$, but there is a noticeable effect on the maximum pressure. Similar to the previous example with a penalty pressure of 3.0, we observe a narrow range of $\mathcal{C}_{\mathrm{CO_2}}$ values for which the maximum pressure is below 1.2. Additionally, the objective function experiences a small increase as $\mathcal{C}_{\mathrm{CO_2}}$ exceeds 100, as indicated by the fourth column of V. However, as with Da, Pe, and χ the magnitude of the associated eigenvalue is small, suggesting that the impact of further increasing $\mathcal{C}_{\mathrm{CO_2}}$ is relatively limited.

For a penalty pressure of 3.0, we found that Pe and $\mathcal{C}_{\mathrm{CO_2}}$ are large and $\mathcal{C}_{\mathrm{SiO}}$ is small. However, only $\mathcal{C}_{\mathrm{SiO}}$ actually reaches the boundary in this case (Table 4.1). From additional parameter sweeps, it was clear that both Pe and $\mathcal{C}_{\mathrm{CO_2}}$ would prefer

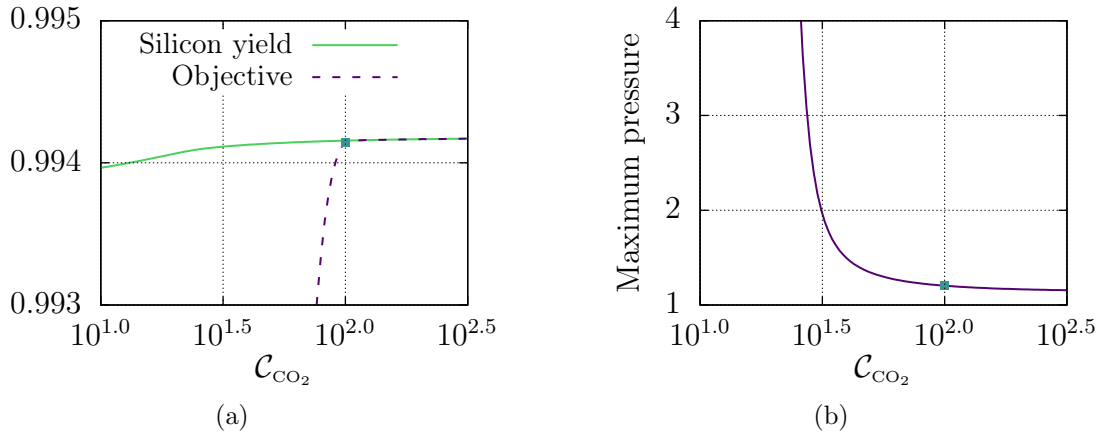

Figure 4.15: (a) Silicon yield at the quartz consumption time and objective, given by (3.177) and (4.8), respectively, and (b) maximum pressure. Parameter values taken from Table 3.2, except we take Da = 916.8, Pe = 1.0, $\chi = 143.1$, and $\mathcal{C}_{\mathrm{SiO}} = 0.01$. The teal square denotes the optimal point found for $P_{\mathrm{pen}} = 1.2$.

to be as large as possible, even though they do not hit their bounds in this case. For the lower penalty pressure of 1.2, the same three parameters sat at the boundaries of the optimization. However, in this case, Pe is minimized, which is surprising. In both penalty pressure cases, Da and χ are internally optimized, and do not reach the boundaries of their respective parameter ranges.

4.4 Dimensional optimization

In the previous section, the connection between dimensional quantities and the dimensionless parameter set was not clearly defined. The relationship between them is nonlinear and not a bijection, making the inverse mapping somewhat ill-defined. To address this, we conduct parameter sweeps over some of the dimensional quantities.

We treat the dimensionless parameters Pe, χ, $\mathcal{C}_{\mathrm{SiO}}$, and $\mathcal{C}_{\mathrm{CO_2}}$ as independent variables in our model. The Damköhler number Da is then determined by

$$\mathrm{Da} = \frac{\Gamma}{H^0\theta}\chi, \tag{4.16}$$

which relates Da and χ by the dimensional parameters H^0 and θ, and we introduce $\Gamma = \kappa P_{\mathrm{atm}}/\mu$. A taller pellet bed, H^0, may lead to more pronounced concentration gradients and longer reaction times due to increased mass and length. The mass transfer coefficient θ at the top of the bed affects the efficiency of gas escape. Higher θ values give better mass transfer, potentially reducing the maximum pressure and

influencing the reaction rate. The additional parameter Γ reflects how easily gas advects through the pellet bed. Higher permeability facilitates better gas advection, affecting pressure distribution. The permeability is not precisely known, and so Γ acts a proxy for the permeability.

To better compare our results with laboratory-scale experiments, we run simulations for a *fixed dimensional time* rather than until all the quartz has reacted as we have done previously. This approach helps identify transient behaviours and reaction progress over a specified period, as is done industrially. The timescale in the dimensionless setup is ambiguous as we vary the parameters, and could range from seconds to days. By fixing the dimensional time, we can better interpret the results and their practical implications. The maximum dimensionless time, $t_{\max}$, can then be computed as

$$t_{\max} = \frac{\mathrm{Da}\,\theta^2}{\chi^2\Gamma} t_{\max}^{\dim}, \tag{4.17}$$

where $t_{\max}^{\dim}$ is the maximum dimensional time, which we set to 1 hour.

We first consider the case where $H^0 = 3$ m, $\Gamma = 1.0$ m^2/s, $\theta = 10.0$ m/s, and $P_{\text{pen}} = 3.0$. We find a final silicon yield of 0.7941, a maximum pressure of 3.151, and an objective of 0.7714. We find that the optimal set of parameters is $\mathrm{Da} = 30.9$ (by (4.16)), $\mathrm{Pe} = 206.4$, $\chi = 940.6$, $\mathcal{C}_{\mathrm{SiO}} = 0.034$, and $\mathcal{C}_{\mathrm{CO_2}} = 99.6$. The resulting time evolution is shown in Figure 4.16. Generally, the time evolution is similar to Figure 4.4 up to $t \approx 12$. Each of Da, $\mathcal{C}_{\mathrm{SiO}}$, and $\mathcal{C}_{\mathrm{CO_2}}$ have similar values as in Figure 4.4, and we have seen that Pe and χ are less impactful on the overall dynamics. Of course, in this case we stop the simulation after 1 hour, whereas in Figure 4.4 we simulated until the quartz was fully consumed.

To better understand the effects of the dimensional parameters on the system's behaviour, we perform parameter sweeps over H^0, Γ, and θ. We show the results[3] for a penalty pressure of $P_{\text{pen}} = 3.0$ in Figure 4.17. For each line within the sub-plots we fix Γ and θ, while we vary H^0. We then repeat this, fixing a new θ, and again varying H^0 to obtain the additional lines. We then repeat this process in the other sub-plots for three more values of Γ.

We observe that increasing the height of the pellet bed leads to a decrease in the optimal objective value. This result is due to two effects. First, with more material to react and a *fixed* reaction time, the percentage of conversion decreases.

[3]Again, each point requires ~ 4 hours of CPU time. Figure 4.17 contains $21 \times 4 \times 4 = 336$ points, and takes ~ 1350 CPU hours of computation.

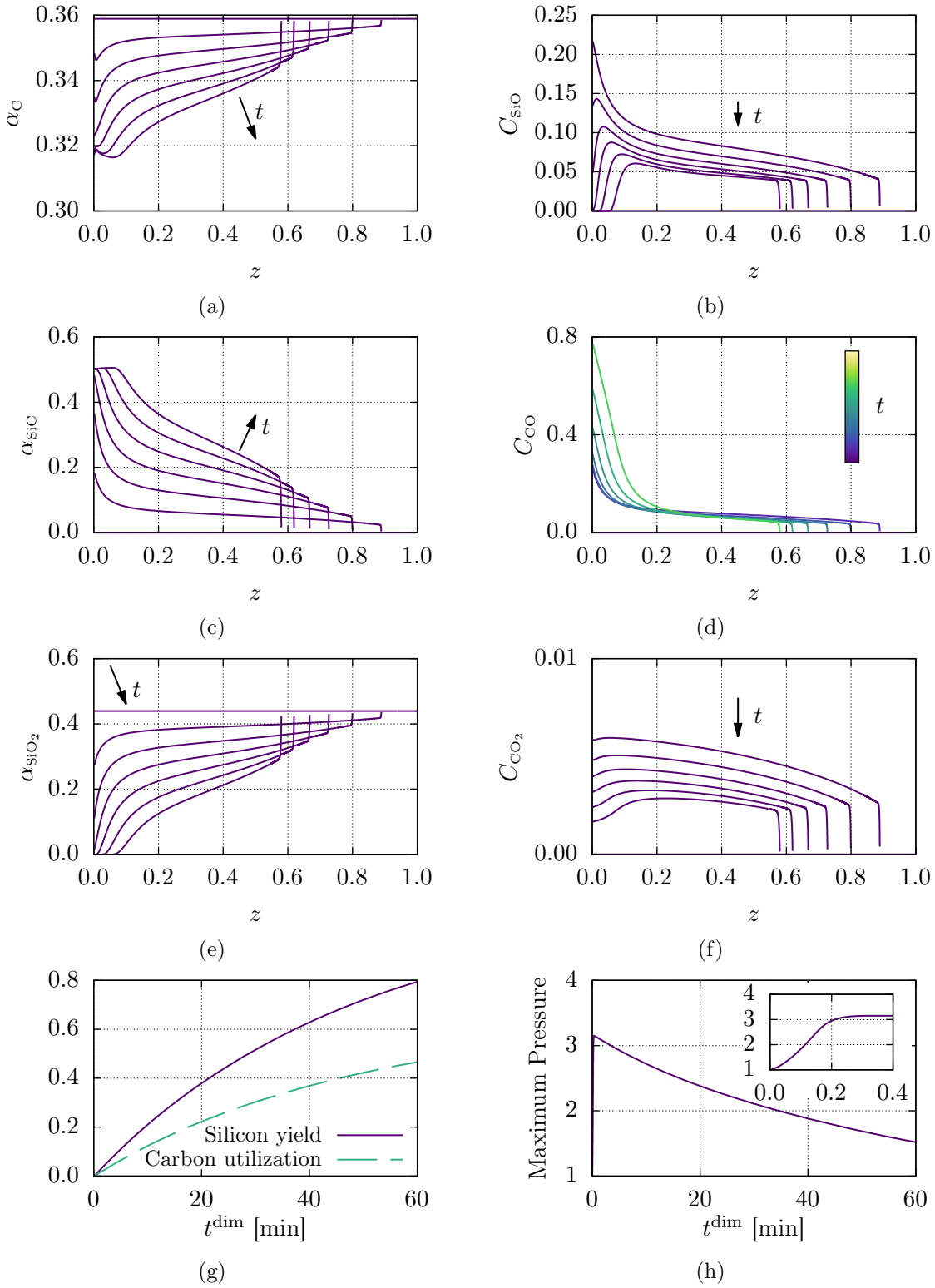

Figure 4.16: Graphs of the numerical solution of (3.6), (3.17), (3.51)–(3.55), (3.57)–(3.59), (3.62), (3.63), and (3.76). Parameter values taken from Table 3.2, except we take Da = 30.9 (by (4.16)), Pe = 206.4, $\chi = 940.6$, $\mathcal{C}_{SiO} = 0.034$, and $\mathcal{C}_{CO_2} = 99.6$, the optimal parameters for $H^0 = 3$ m, $\Gamma = 1.0$ m^2/s, $\theta = 10.0$ m/s, and $P_{pen} = 3.0$. Lines in (a)–(f) are plotted for $t^{dim} = 0.0, 10.0, 20.0, 30.0, 40.0, 50.0, 60.0$ min.

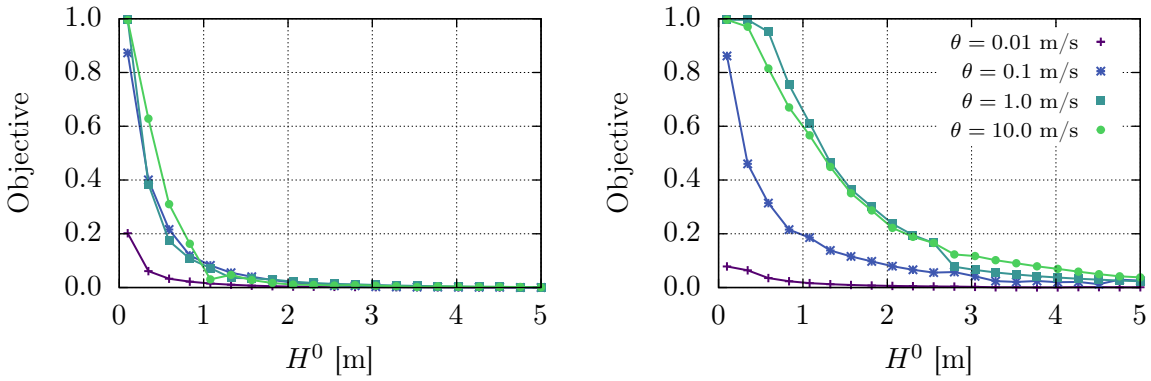

(a) $\Gamma = 0.01$ m^2/s.

(b) $\Gamma = 0.1$ m^2/s.

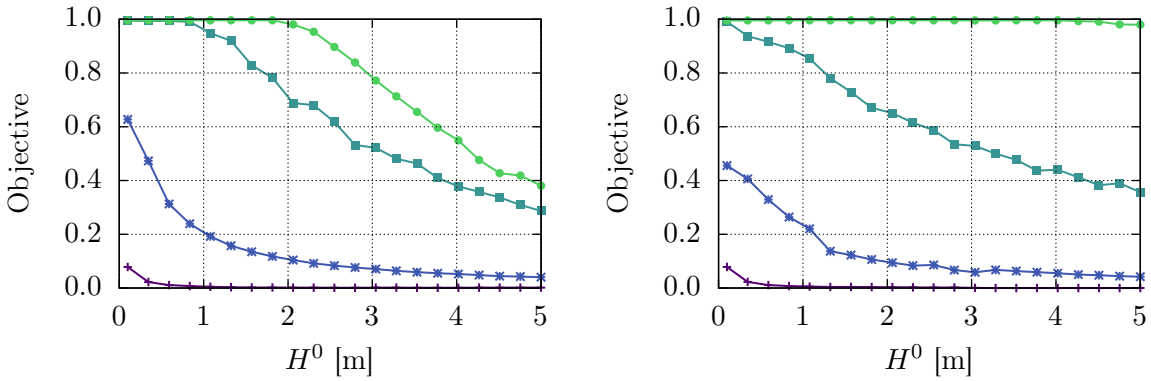

(c) $\Gamma = 1.0$ m^2/s.

(d) $\Gamma = 10.0$ m^2/s.

Figure 4.17: Dependence of optimal objective value, from (4.8), with $P_{\text{pen}} = 3.0$, on the initial bed height H^0, for $\theta = 0.01, 0.1, 1.0, 10.0$ m/s in each sub-plot, and for $\Gamma = 0.01, 0.1, 1.0, 10.0$ m^2/s across sub-plots. We optimize over the parameters Da (from (4.16)), Pe, χ, $\mathcal{C}_{\text{SiO}}$, and $\mathcal{C}_{\text{CO}_2}$ with bounds given in Table 4.1, other parameter values are taken from Table 3.2.

Second, as the height increases, the gas must travel a greater distance to escape the crucible, which can result in a pressure build up depending on the effectiveness of the transport. Additionally, increasing θ improves the objective value. When θ is too small, gas becomes trapped in the crucible, causing pressure to build up and reduce the objective. In contrast, increasing Γ generally enhances the objective value. Increasing Γ improves gas transport within the particle bed, helping to equilibrate pressure and concentration levels, thereby aiding in satisfying the pressure constraint.

We now examine the optimal parameter values for a given Γ and θ while varying the initial bed height H^0. In Figure 4.18 we present the optimal parameter values for the line with green circles in Figure 4.17c. From these plots, we observe that for $H^0 \lesssim 2$ m, the optimal Pe values are large. However, for $H^0 \gtrsim 2$ m, the optimal

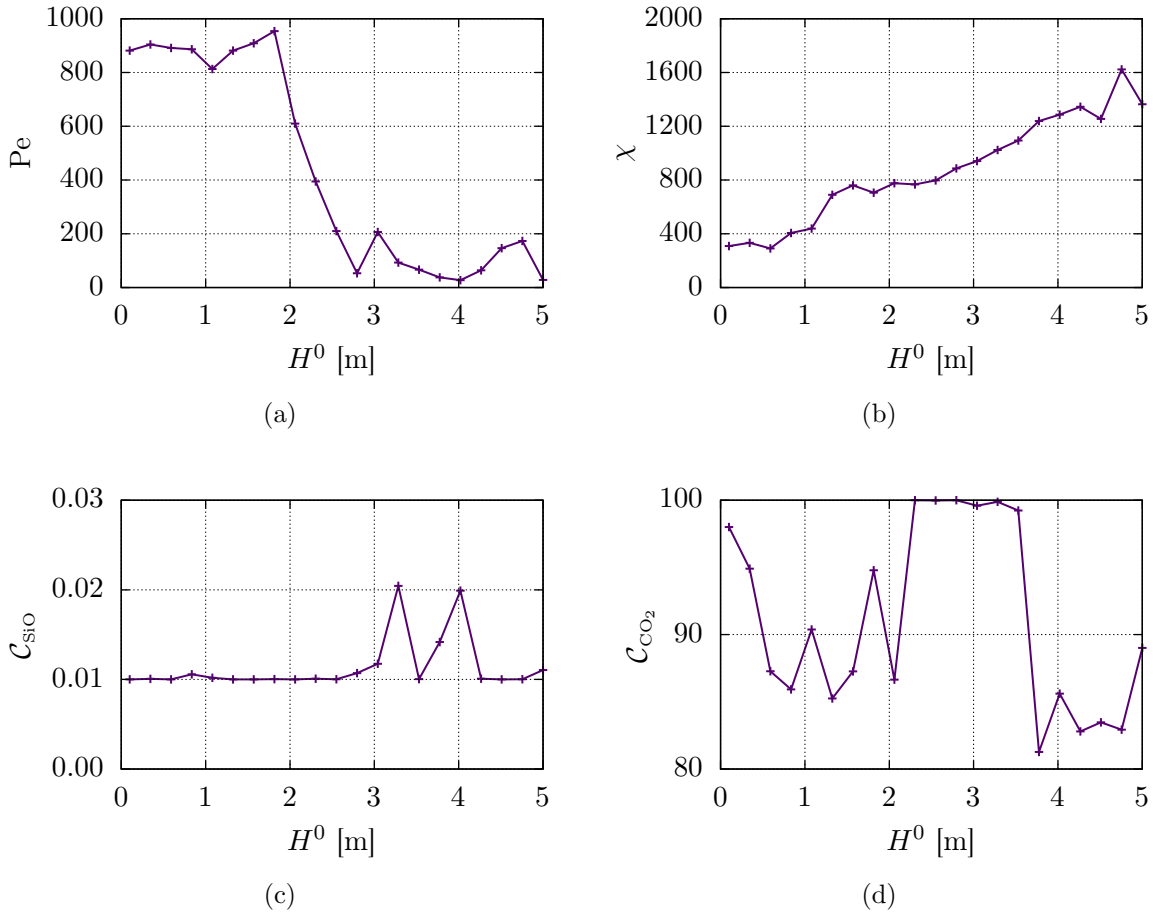

Figure 4.18: Parameter values that achieve the maximum objective value, from (4.8) with $P_{\text{pen}} = 3.0$, for $\Gamma = 1.0$ m^2/s, $\theta = 10.0$ m/s (green circles in Figure 4.17c). Note that Da is computed by (4.16).

Pe values decrease significantly. This critical height of $H^0 = 2$ m corresponds to the point where the objective value begins to deviate from 1, as shown in Figure 4.17c. For χ, we find a steady increase as the initial bed height increases. With a higher initial bed height, more material is available, resulting in the production of more gas. Consequently, χ must increase to maintain a maximum pressure below the penalty threshold. As expected, for $\mathcal{C}_{\mathrm{SiO}}$, the optimal value remains small across all bed heights, though we observe some numerical noise in the range between 3 m and 4 m. Finally, for $\mathcal{C}_{\mathrm{CO_2}}$, we see that the values are consistently large, as we saw in previous cases, but the results exhibit considerable noise, and a clear trend is difficult to discern.

Optimizing a very flat objective function, such as ours, and setting only the objective tolerance can lead to noticeable errors in the parameters. This occurs because a flat objective function is insensitive to variations in certain parameters, as we saw

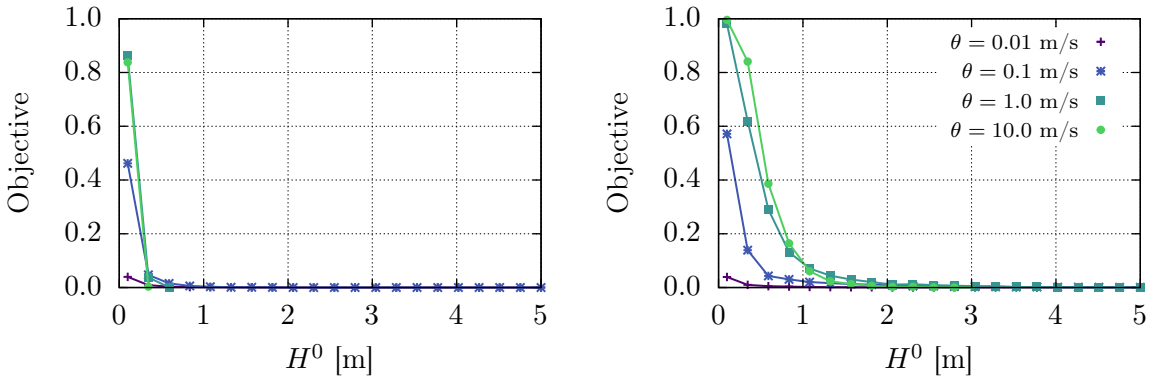

(a) $\Gamma = 0.01$ m^2/s.

(b) $\Gamma = 0.1$ m^2/s.

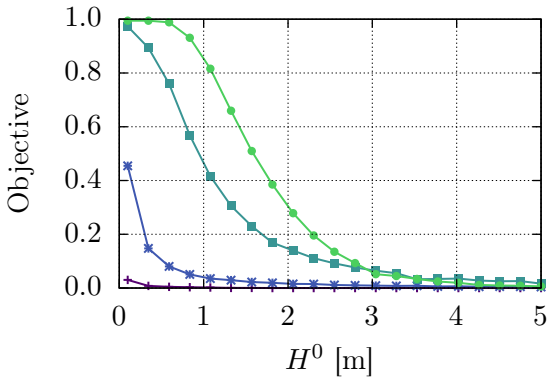

(c) $\Gamma = 1.0$ m^2/s.

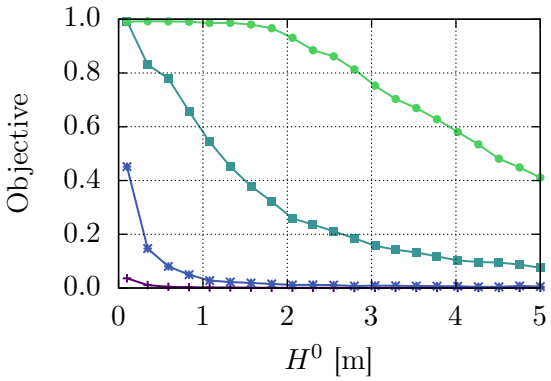

(d) $\Gamma = 10.0$ m^2/s.

Figure 4.19: Dependence of optimal objective value, from (4.8), with $P_{\text{pen}} = 1.2$, on the initial bed height H^0, for $\theta = 0.01, 0.1, 1.0, 10.0$ m/s in each sub-plot, and for $\Gamma = 0.01, 0.1, 1.0, 10.0$ m^2/s across sub-plots. We optimize over the parameters Da (from (4.16)), Pe, χ, $\mathcal{C}_{\text{SiO}}$, and $\mathcal{C}_{\text{CO}_2}$ with bounds given in Table 4.1, other parameter values are taken from Table 3.2.

in the parameter sweeps. Thus, even significant changes in the parameters may result in only minimal changes in the objective value. In such cases, the optimization process converges successfully based on the objective tolerance alone. However, the parameters themselves could deviate from their true optimal values.

We now repeat our dimensional parameter sweeps for $P_{\text{pen}} = 1.2$; the results are shown in Figure 4.19. Unsurprisingly, we observe the same general trends as in the $P_{\text{pen}} = 3.0$ case. Specifically, increasing Γ or θ raises the objective value for the same reasons as before: improved gas transport and pressure equilibration help the system perform better under the given constraints. However, since $P_{\text{pen}} = 1.2$ is lower, the optimal objective value is correspondingly reduced. For $\Gamma = 0.01$ m^2/s (Figure 4.19a), we find that, regardless of θ, almost no conversion to silicon carbide occurs without

exceeding the maximum pressure of 1.2, except in cases with shallow initial particle beds. Recall that, for $P_{\text{pen}} = 3.0$ with $\Gamma = 1.0$ m^2/s (Figure 4.17c) and $\Gamma = 10.0$ m^2/s (Figure 4.17d), we achieved near-perfect silicon conversion for an initial bed heights of $H^0 \leq 2.0$ m. In this lower penalty pressure case, however, we only attain an objective value of approximately 0.3 when $\Gamma = 1.0$ m^2/s (Figure 4.19c), but obtain near-perfect conversion when $\Gamma = 10.0$ m^2/s (Figure 4.19d) and $H^0 \lesssim 2.0$ m.

4.5 Conclusions

We have demonstrated that it is possible to achieve near-perfect silicon conversion while maintaining a maximum pressure below 3.0 or 1.2. This is primarily achieved by minimizing $\mathcal{C}_{\text{SiO}}$ and maximizing $\mathcal{C}_{\text{CO}_2}$. This strategy can be interpreted as maximizing the rate of the silicon carbide reaction while minimizing the rate of the Boudouard reaction. Among the five parameters we considered, $\mathcal{C}_{\text{SiO}}$ is by far the most impactful in increasing the silicon yield, making it the key parameter to optimize for conversion efficiency. On the other hand, $\mathcal{C}_{\text{CO}_2}$ plays a critical role in satisfying the pressure constraint. In contrast, the parameters Da, Pe, and χ are generally less significant, provided that there is sufficient transport within the crucible and adequate gas flux at the top of the system. As long as these conditions are met, variations in these parameters have only a marginal impact on the overall performance of the system.

Our dimensional conclusions are as follows. Increasing the height of the bed decreases the maximum silicon yield achievable since the overall amount of gas produced increases and the gas has farther to travel before being removed from the system. Increasing Γ also increases the silicon yield. Recall that Γ is a proxy for the permeability, and so increasing Γ allows the gas to be advected through the bed of particles more easily. Thus, it is easier for the system to maintain a pressure below the penalty pressure. Similarly, increasing θ increases the optimal silicon yield. Increasing θ increases the flux through the top of the bed of particles, and so the gas can more freely escape the crucible. We again found that minimizing $\mathcal{C}_{\text{SiO}}$ and maximizing $\mathcal{C}_{\text{CO}_2}$ were key to an optimal silicon yield. We were able to convert a considerable amount of the initial quartz to silicon carbide while maintaining pressures under 3.0 and 1.2 for a wide range of bed heights and permeabilities.

From the optimization results, several practical conclusions can be drawn, alleviating some of the uncertainty of practical implementation from the previous chapter. The most critical factor for maximizing silicon yield is minimizing the silicon monoxide concentration ratio $\mathcal{C}_{\text{SiO}}$, while the most important factor for maintaining a safe

maximum pressure is maximizing the carbon monoxide concentration ratio $\mathcal{C}_{\mathrm{CO}}$. As previously stated, the Damköhler number Da, the Péclet number Pe, and the dimensionless mass transfer coefficient χ are less significant in comparison. The general strategies for achieving these conditions remain consistent with those outlined in the previous chapter, along with the associated difficulties in controlling reaction rates. Further evidence now supports the conclusion that shallower beds have the potential for higher silicon yield, aligning with expectations from the previous chapter. Interestingly, increasing the permeability κ generally led to increased silicon yield, despite also increasing Pe.

Chapter 5

Conclusions

To conclude, in Section 5.1, we provide a summary of the research conducted, emphasizing our key results. In Section 5.2, we explore potential directions for future research.

5.1 Summary of modelling and results

In Chapter 2 we formulated and analyzed a model to investigate the behaviour of a single quartz–carbon pellet under experimental conditions. Our approach involved developing a spherically symmetric model that captured the essential chemical reactions and mass transfer processes for the pellet. After reducing the model to a quasi-steady state owing to the density difference between the solid and gas, we solved the model numerically, simplifying the analysis to focus on four key dimensionless parameters, which allowed us to more effectively explore the dynamics and parameter space.

Our analysis revealed two distinct regimes within the parameter space: a reaction-limited regime and a diffusion-limited regime. In the reaction-limited regime, most of the silicon monoxide produced at the quartz surface diffuses out of the pellet and is lost. Conversely, in the diffusion-limited regime, the majority of the silicon monoxide is converted to silicon carbide, as the chemical reactions dominate the transport of the gas. We characterized the system dynamics using two metrics: the carbon utilization fraction and the silicon yield, both of which were computed at the time that the quartz was fully consumed. The carbon utilization fraction quantifies the amount of carbon that has reacted, while the silicon yield measures the fraction of initial quartz converted to silicon carbide, indicating how much silicon monoxide escaped from the pellet. A diffusion-limited system is optimal for maximizing both carbon utilization and silicon yield, as the silicon monoxide reacts with carbon before it has

the chance to diffuse out of the pellet. Through numerical exploration, we identified a critical ratio of initial quartz radius to pellet radius of approximately 0.8, marking the transition between a carbon-limited system and a quartz-limited system, given our initial porosity of 0.3. This 0.8 ratio aligned with calculations based on the initial mole ratio.

In Chapter 3 we developed and analyzed a multiphase model for a homogeneous bed of quartz and carbon particles, assuming that the solid motion is driven by gravity, so that the bed remains well-packed, and that the gaseous components form a compressible mixture. We explored two paradigm problems to understand the system's behaviour. The first paradigm problem involved a single chemical reaction with solid advection, where a reaction front formed and its speed was determined by the gas flux into the reaction layer. In the limit of large Péclet number, advection dominates, resulting in a linear reaction front position, while for small Péclet number, diffusion dominates, and the front position scaled as $t^{1/2}$. In the second paradigm problem, which more accurately reflects the chemistry of the full system, we found that the self-sustaining reactions produce significant gas concentrations within the reaction layer, leading to a linear relationship between reaction front speed and the total amount of silicon monoxide present in the system.

Numerical solutions of the full model revealed that, for small Damköhler number and Péclet number $\mathcal{O}(1)$, the system behaves similarly to the second paradigm problem—with rapid gas production leading to high local concentrations and high pressures. When both the Damköhler number and the Péclet number were $\mathcal{O}(1)$, transport improved, resulting in more uniform concentrations and lower pressures. This uniformity stopped reaction front formation and stabilized gas concentrations.

Parameter sweeps revealed how the dimensionless parameters influence carbon utilization, silicon yield, and maximum pressure pressure. In the Damköhler number–Péclet number plane, we found that the variations in carbon utilization and silicon yield are small, with transport playing a key role in determining reaction rates. While varying the relative speed of the reactions, we found that carbon utilization and silicon yield are most sensitive to the ratio of the speed of the silicon carbide reaction to the quartz reaction, with better utilization and yield when the silicon carbide reaction was much faster. Finally, we found that high pressures and fast consumption occurs when the mass transfer coefficient at the top of the bed of particles is too small, emphasizing the importance of gas flux through the top of the bed of pellets in managing system pressures and reaction rates.

In Chapter 4 we established a framework for choosing the dimensionless parame-

ters in the model, within prescribed bounds, in order to optimize the silicon yield, and demonstrated that near-perfect silicon conversion can be achieved in finite time while maintaining a maximum pressure below 3.0 or 1.2. This was primarily accomplished by maximizing the silicon carbide reaction speed and minimizing the Boudouard reaction speed. Typically, we found that the optimal solution had the associated parameters $\mathcal{C}_{\mathrm{SiO}}$ and $\mathcal{C}_{\mathrm{CO_2}}$ on the boundary supplied to the solver. Among the five dimensionless parameters considered, $\mathcal{C}_{\mathrm{SiO}}$ was the most influential at improving silicon yield, making it the critical parameter for conversion efficiency. Conversely, $\mathcal{C}_{\mathrm{CO_2}}$ is key for meeting pressure constraints. The Damköhler number, Péclet number, and the dimensionless parameter associated with the mass flux at the top of the bed of particles are generally less significant, provided that transport within the crucible and gas flux through the top of the particle bed are sufficient. With these conditions met, variations in these parameters have only a marginal impact on system performance.

Our analysis of the influence of dimensional parameters on the silicon yield led to several conclusions. Increasing the bed height reduces the maximum achievable silicon yield, as more gas is produced and the gas must travel a greater distance to escape the system. On the other hand, increasing the permeability of the particle bed improved the silicon yield. This is achieved by facilitating gas transport through the particle bed, and thus, helps to maintain pressures below the penalty pressure. Similarly, increasing the mass transfer coefficient at the top of the bed of pellets enhances the silicon yield by increasing the gas flux through the top of the bed. The increased gas flux allows gas to escape more easily from the crucible. Maximizing the speed of the silicon carbide reaction and minimizing the speed of the Boudouard reaction remain crucial for optimizing the silicon yield, as they enable significant conversion of quartz to silicon carbide while keeping the maximum pressure low across a wide range of bed heights and permeabilities.

5.2 Future work

There are promising avenues for future work, stemming from the models built in this thesis, that are of interest both from a mathematical perspective and for Elkem ASA.

In Chapter 2 we considered the most physically relevant limit for silicon carbide production. However, one possible continuation would be to investigate further sub-limits. Other distinguished limits are also within the ranges in Table 2.2 and may be instructive. More experimental evidence could help reduce the wide parameter ranges and suggest particular sub-limits to consider. In particular, reducing the

ranges of the rate constants would be the most helpful, since their values are not known experimentally. Asymptotic analysis of the sub-limits would provide further insight into the mechanisms for silicon carbide production.

Another consideration is the effect of temperature. In our model, we assume the pellet is isothermal. However, this assumption is not likely to be the case in an industrial-scale furnace, and the reaction rates will increase with temperature, probably following an Arrhenius law. Incorporating the temperature dependence into the model would better capture the physics and to explore how temperature alters the pellet's evolution. An instructive extension would be to find the optimal temperature to maximize the efficiency of the process.

Another extension would be to relax our assumption of neglecting gravity in the single pellet model. We neglected gravity in order to maintain spherical symmetry, thus, our model and solution only depended on the radial distance. However, as the quartz core shrinks we would expect the quartz to remain in contact with the bottom of the carbon shell. Incorporating gravity would involve solving an axisymmetric model that is more representative of the underlying physics and geometry.

We directly wrote bulk reaction terms within the carbon layer, and estimated the effective rate constants. However, another approach would be to use the method of homogenization (see [156]) to derive the form and effective rate constants from the microstructure of the pores and surface reactions. Homogenization would allow us to encapsulate the pore-scale structure into our model on the scale of the porous pellet. Furthermore, our single pellet model is the first stage in developing a model for the operation of a furnace containing many pellets. However, it would be computationally expensive to track the gas behaviour in every pellet. One alternative would be to use the method of homogenization to upscale the single pellet model to a model that holds over the scale of the furnace and that captures the microscale factors in the effective parameters. Homogenization has been used to describe similar multiscale processes, for example, the electrical current distribution within a silicon furnace [73], a grain model with applications to silicon processing [45, 157], reactive decontamination [72], and reactive filtration [158].

There are also potential improvements and extensions needed to refine the accuracy and applicability of the multiphase model, examined in Chapter 3, so that it better approximates real-world conditions and industrial scales.

Examining a well-mixed model of the system would be instructive, since some of our examples showed spatially uniform dynamics. By removing the spatial complexity, we may gain deeper insights into the fundamental behaviour of the system and identify

key parameters more easily. This could lead to improved predictability and control over the reactions and overall process.

Our model for the solid dynamics should be made more realistic. We currently use a constitutive law that forces the inter-quartz voids to be densely packed with carbon particles. Additionally, we assumed a single velocity for the solid mixture as a whole. However, considering the significant difference in particle size between quartz and carbon it would be better to use a two-particle-size granular flow model, such as presented in [159–162]. This model would account for the (potential) independent movement of quartz and carbon particles. Carbon, being smaller, might flow faster than the larger quartz particles, affecting the dynamics and efficiency of the reactions.

As with the single pellet model, the coupling of reaction rates with temperature through Arrhenius laws is another important aspect to consider. Incorporating this temperature dependency would add constraints on the effective reaction rates within our model. For example, we treat the parameters $\mathcal{C}_{\mathrm{SiO}}$ and $\mathcal{C}_{\mathrm{CO}}$ as independent, however, their ratio will depend only on the temperature under an Arrhenius model (*cf.* (3.47) and (3.61)). Furthermore, revisiting the isothermal assumption is also crucial for larger systems where temperature variations are likely more impactful. In traditional furnaces, heating is applied only at the bottom of the furnace and so non-constant temperatures are likely. In an industrial-scale silicon carbide reactor, heating may not be uniformly distributed across the entire depth of particles. Temperature gradients can significantly influence reaction rates, gas dynamics, and material properties, making it essential to incorporate temperature dependence into the model for more accurate predictions. However, additional experimental evidence would be needed to guide the development of a temperature-dependent model, for example, to determine the values of the parameters for the Arrhenius laws.

Our model would benefit from being extended to 2D, most likely axisymmetric. We derived a 1D model based on the long and thin nature of a laboratory-scale crucible, but traditional industrial silicon furnaces are wider than they are tall and exhibit significant radial effects. An axisymmetric model would better capture these dynamics, improving the applicability to industrial-scale operations.

Lastly, considering a continuous operation setup for our model would align more closely with traditional silicon production methods. Our current model is inspired by laboratory-scale batch experiments. In contrast, industrial silicon production involves continuous operation, where quartz and carbon are periodically added to the top of the furnace to replenish consumed materials, and liquid silicon is continuously tapped off from the bottom. A natural next step would be to modify the boundary conditions to

replicate the periodic addition of quartz and carbon at the top of the particle bed and the continuous or periodic extraction of materials from the bottom of the bed. Given that silicon carbide is a solid, devising methods for its removal would be necessary to reflect industrial processes accurately. This continuous operation model would provide a more realistic framework for optimizing and scaling-up the production of silicon carbide.

In Chapter 4, a key improvement would be better estimates of the model parameters. Much of the previously discussed future work would have secondary consequences on the optimization. For instance, refining the model through temperature dependence and more accurate reaction rate parameters would lead to more tightly constrained bounds for the optimization. Improved parameter estimates could also reduce the number of parameters to optimize over, making the optimization faster and computationally cheaper. For example, incorporating temperature dependence would allow us to further constrain the optimization by linking reaction rates to temperature, giving a more physically realistic model, at the expense of having to solve an energy equation.

In the current work, we used the weighting factor $\Lambda = 1$ in the objective function, balancing the penalty for exceeding the pressure threshold with the silicon yield. However, as observed in Figure 4.16, the optimal objective can still occur when the maximum pressure is above the penalty pressure. Increasing Λ would more strongly enforce the pressure constraint, reducing the occurrence of exceeding the penalty pressure. This is particularly important in industrial applications where maintaining pressures below a critical value is essential for safe and efficient operation.

We found that, in general, optimizing the system involved maximizing the speed of the silicon carbide reaction while minimizing the speed of the Boudouard reaction. In this regime, the carbon utilization was around 60%, as the Boudouard reaction played a minimal role. Another possible extension is to include the initial mole ratio of carbon to quartz as a parameter in the optimization process. Since this is an easily controllable parameter in both laboratory and industrial settings, optimizing over the mole ratio could further increase carbon utilization, reducing waste and improving efficiency. However, there is a trade-off. Decreasing the initial amount of carbon will slow down the silicon carbide reaction, potentially lowering the overall efficiency. Therefore, we must balance carbon utilization with reaction speed.

Finally, to help address the flatness of the objective function, we may wish to extend to multi-objective optimization by incorporating the chemical selectivity of the system.

Mathematical modelling plays a crucial role in the design and operation of silicon carbide furnaces. The complex interactions are often challenging to observe. By abstracting these processes into models, our approach offers a deeper understanding that contrasts the large-scale simulations typically used in furnace design. This enhanced understanding allows for more informed decisions on material selection and process parameters, ultimately improving furnace efficiency and silicon yield. In addition, the models provide a foundation for future innovations in furnace geometry and operational strategies, contributing to the long-term sustainability and optimization of silicon carbide production.

Appendix A

Numerical methods

In Section A.1, we derive the finite volume discretization we implement in our numerical solution of the multiphase model presented in Chapter 3. We then discuss our choice of non-uniform grid and show how our implementation converges. In Section A.2, we describe how the Jacobian can be computed in constant time and show the computational advantage of using a sparse linear solver over a dense linear solver.

A.1 Finite volume method discretization

The dimensionless conservation equations for the solid volume fractions and solid number densities take the form (*cf.* (3.51)–(3.55))

$$\frac{\partial \alpha}{\partial t} + \frac{\partial}{\partial z}(u_s \alpha) = R_\alpha, \tag{A.1}$$

where $\alpha \in \{\alpha_{\mathrm{C}}, \alpha_{\mathrm{SiC}}, \alpha_{\mathrm{SiO_2}}, n_{\mathrm{C}}, n_{\mathrm{SiO_2}}\}$ and R_α are the associated reaction terms for the α species. In practice, to determine u_s, we divide (3.51) by η, and add (3.52) and (3.53), then, from (3.17), we find

$$\frac{\partial u_s}{\partial z} = f, \tag{A.2}$$

where

$$f = -\frac{\alpha_{\mathrm{gas}} \mathcal{M}_{\mathrm{C}}}{\eta}(n_{\mathrm{C}} \alpha_{\mathrm{C}}^2)^{1/3}(2C_{\mathrm{SiO}} + C_{\mathrm{CO_2}}) - \alpha_{\mathrm{gas}}(n_{\mathrm{SiO_2}} \alpha_{\mathrm{SiO_2}}^2)^{1/3} C_{\mathrm{CO}} + \alpha_{\mathrm{gas}} \mathcal{M}_{\mathrm{SiC}}(n_{\mathrm{C}} \alpha_{\mathrm{C}}^2)^{1/3} C_{\mathrm{SiO}} \tag{A.3}$$

is related to the change in volume due to the three chemical reactions. The dimensionless gas conservation equations take the form (*cf.* (3.57)–(3.59) and (3.62))

$$\delta\left[\frac{\partial}{\partial t}(\alpha_{\text{gas}}C)+\frac{\partial}{\partial z}\left(-\text{Da}\,\alpha_{\text{gas}}C\frac{\partial P}{\partial z}-\frac{\text{Da}}{\text{Pe}}\alpha_{\text{gas}}\rho\frac{\partial}{\partial z}\left(\frac{C}{\rho}\right)\right)\right]=R_C, \tag{A.4}$$

where $C\in\{C_{\text{SiO}},C_{\text{CO}},C_{\text{CO}_2},\rho\}$.

Since we have a moving interface at the top of our domain, we first perform a change of coordinates in order to allow us to solve the problem on a fixed domain. We write

$$\tau=t,\quad \xi=\frac{z}{H(t)}, \tag{A.5}$$

so that $\xi=0$ is the bottom of the crucible and $\xi=1$ denotes the moving interface at the top of the bed of particles. It then follows that

$$\frac{\partial}{\partial t}=\frac{\partial\tau}{\partial t}\frac{\partial}{\partial\tau}+\frac{\partial\xi}{\partial t}\frac{\partial}{\partial\xi}=\frac{\partial}{\partial\tau}-\frac{\xi H'}{H}\frac{\partial}{\partial\xi}, \tag{A.6}$$

and

$$\frac{\partial}{\partial z}=\frac{\partial\tau}{\partial z}\frac{\partial}{\partial\tau}+\frac{\partial\xi}{\partial z}\frac{\partial}{\partial\xi}=\frac{1}{H}\frac{\partial}{\partial\xi}. \tag{A.7}$$

Applying the change of coordinates (A.6) and (A.7) to (A.1), multiplying by H, and writing in conservative form, we find

$$\frac{\partial}{\partial\tau}(H\alpha)+\frac{\partial}{\partial\xi}\left(\frac{(u_s-H'\xi)H\alpha}{H}\right)=HR_\alpha. \tag{A.8}$$

We introduce the conserved quantities $\widetilde{\alpha}=H\alpha$ and $\widetilde{C}=H\alpha_{\text{gas}}C$, as well as $\widetilde{P}=H\alpha_{\text{gas}}P$ and $\widetilde{\alpha}_{\text{gas}}=H\alpha_{\text{gas}}$, and write (A.8) as

$$\frac{\partial\widetilde{\alpha}}{\partial\tau}+\frac{\partial\mathcal{F}_s}{\partial\xi}=HR_{\widetilde{\alpha}}, \tag{A.9}$$

where

$$\mathcal{F}_s=\left(\frac{u_s-H'\xi}{H}\right)\widetilde{\alpha} \tag{A.10}$$

is the solid flux in the new coordinates, and $R_{\widetilde{\alpha}}$ are the associated reaction terms for the α species written in terms of the conservative variables. Similarly, writing (A.2)

in the transformed coordinates and conservative variables we find

$$\frac{1}{H}\frac{\partial u_s}{\partial \xi} = \widetilde{f}, \tag{A.11}$$

where $\widetilde{f}$ is f written in terms of conservative variables. Finally, applying the change of coordinates (A.6) and (A.7) to (A.4) we find

$$\delta\left(\frac{\partial \widetilde{C}}{\partial \tau} + \frac{\partial \mathcal{F}_g}{\partial \xi}\right) = HR_{\widetilde{C}}, \tag{A.12}$$

where

$$\mathcal{F}_g = -\frac{H'\xi\widetilde{C}}{H} - \frac{\mathrm{Da}}{H^2}\widetilde{C}\frac{\partial}{\partial \xi}\left(\frac{\widetilde{P}}{\widetilde{\alpha}_{\mathrm{gas}}}\right) - \frac{\mathrm{Da}}{H^2\mathrm{Pe}}\widetilde{\rho}\frac{\partial}{\partial \xi}\left(\frac{\widetilde{C}}{\widetilde{\rho}}\right) \tag{A.13}$$

is the transformed gas flux, where we have introduced $\widetilde{\rho} = H\alpha_{\mathrm{gas}}\rho$.

We discretize space using the finite volume method. Finite volume methods are particularly useful for solving conservation equations since they remain conservative at the discrete level [163]. The domain is partitioned into regions called cells that the differential equations are integrated over. Then, using the divergence theorem, the cell integrals can be converted to surface integrals of the flux.

For a general grid with points $\{\xi^i\}$, we first define a secondary grid $\{\xi^{i+1/2}\}$ where $\xi^{i+1/2} = (\xi^{i+1} + \xi^i)/2$. There are two ways of defining cells [164]. First, in a *vertex centred scheme* the secondary grid defines the vertices of cells so that the mass balance equations hold over the intervals $[\xi^{i-1/2}, \xi^{i+1/2}]$. The vertices are centred with respect to the original grid. The alternative scheme is a *cell centred scheme*. In this case, the primary grid defines the cells $[\xi^i, \xi^{i+1}]$, and the secondary grid defines the centres of the cells. In practice, cell centred schemes are less common owing to their lack of stability [164, 165]. We proceed with a vertex centred scheme.

For a grid with primary grid points $\{\xi^i\}$ and secondary grid points $\{\xi^{i+1/2}\}$, we let [164]

$$h_i = \frac{1}{2}(\xi^{i+1} - \xi^{i-1}), \quad h_i^- = \xi^i - \xi^{i-1}, \quad h_i^+ = \xi^{i+1} - \xi^i, \tag{A.14}$$

where h_i is the 'volume' of the ith cell, and $h_i^{\pm}$ are the distances to the neighbouring

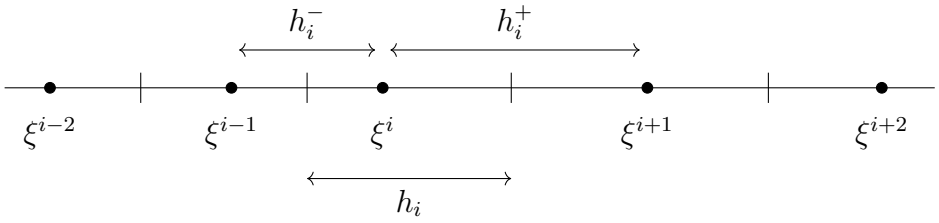

Figure A.1: Vertex centred scheme for finite volume methods in 1D.

grid points, as shown in Figure A.1. Integrating (A.9) over the ith cell we find

$$\int_{\xi^{i-1/2}}^{\xi^{i+1/2}} \frac{\partial \widetilde{\alpha}}{\partial \tau}\,\mathrm{d}\xi + \mathcal{F}_s|_{\xi^{i-1/2}}^{\xi^{i+1/2}} = H \int_{\xi^{i-1/2}}^{\xi^{i+1/2}} R_{\widetilde{\alpha}}\,\mathrm{d}\xi. \tag{A.15}$$

We let $\widetilde{\alpha}^i = \widetilde{\alpha}(\xi^i)$, $\mathcal{F}_s^i = \mathcal{F}_s(\xi^i)$, and $R_{\widetilde{\alpha}}^i = R_{\widetilde{\alpha}}(\xi^i)$, and approximate the integrals as [163, 166]

$$\int_{\xi^{i-1/2}}^{\xi^{i+1/2}} \frac{\partial \widetilde{\alpha}}{\partial \tau}\,\mathrm{d}\xi \approx h_i \frac{\partial \widetilde{\alpha}^i}{\partial \tau}, \quad \int_{\xi^{i-1/2}}^{\xi^{i+1/2}} R_{\widetilde{\alpha}}\,\mathrm{d}\xi \approx h_i R_{\widetilde{\alpha}}^i. \tag{A.16}$$

We find

$$\frac{\partial \widetilde{\alpha}^i}{\partial \tau} + \frac{\mathcal{F}_s^{i+1/2} - \mathcal{F}_s^{i-1/2}}{h_i} = H R_{\widetilde{\alpha}}^i. \tag{A.17}$$

We approximate $\mathcal{F}_s^{i+1/2}$ with the upwind scheme [164]

$$\mathcal{F}_s^{i+1/2} = \begin{cases} \dfrac{-H'\xi^{i+1/2} + u_s^{i+1/2}}{H}\widetilde{\alpha}^i & \text{for } \dfrac{-H'\xi^{i+1/2} + u_s^{i+1/2}}{H} > 0, \\ \dfrac{-H'\xi^{i+1/2} + u_s^{i+1/2}}{H}\widetilde{\alpha}^{i+1} & \text{for } \dfrac{-H'\xi^{i+1/2} + u_s^{i+1/2}}{H} < 0. \end{cases} \tag{A.18}$$

Applying the same process to (A.11), we find

$$\frac{u_s^{i+1/2} - u_s^{i-1/2}}{h_i} = H\widetilde{f}^i. \tag{A.19}$$

We note that we *solve u_s on the secondary grid* since it is a flux; $u_s^{i+1/2}$ does not need to be interpolated.

Similarly, integrating (A.12) over the ith cell and dividing by h_i, we find

$$\delta\left(\frac{\partial\widetilde{C}^i}{\partial\tau}+\frac{\mathcal{F}_g^{i+1/2}-\mathcal{F}_g^{i-1/2}}{h_i}\right)=HR_{\widetilde{C}}^i. \tag{A.20}$$

We approximate the fluxes through the cell vertices with linear interpolation and central difference so that

$$\begin{aligned}\mathcal{F}_g^{i+1/2}=-\frac{H'\xi^{i+1/2}}{H}\left(\frac{\widetilde{C}^{i+1}+\widetilde{C}^i}{2}\right)-\frac{\mathrm{Da}}{H^2}\left(\frac{\widetilde{C}^{i+1}+\widetilde{C}^i}{2}\right)\frac{\left(\dfrac{\widetilde{P}^{i+1}}{\widetilde{\alpha}_{\mathrm{gas}}^{i+1}}-\dfrac{\widetilde{P}^i}{\widetilde{\alpha}_{\mathrm{gas}}^i}\right)}{h_i^+}+\\ \frac{\mathrm{Da}}{H^2\mathrm{Pe}}\left(\frac{\widetilde{\rho}^{i+1}+\widetilde{\rho}^i}{2}\right)\frac{\left(\dfrac{\widetilde{C}^{i+1}}{\widetilde{\rho}^{i+1}}-\dfrac{\widetilde{C}^i}{\widetilde{\rho}^i}\right)}{h_i^+}.\end{aligned} \tag{A.21}$$

We assume that our grid is defined in such a way that $\xi^{1/2}=0$ and $\xi^{n+1/2}=1$, where n is the number of points in our spatial discretization, since our model prescribes flux boundary conditions. From (3.68), we have that

$$u_s^{1/2}=0, \tag{A.22}$$

and since $\xi^{1/2}=0$ by construction, it must be that $\mathcal{F}_s^{1/2}=0$ by (A.18). Thus,

$$\frac{\partial\widetilde{\alpha}^1}{\partial\tau}+\frac{\mathcal{F}_s^{1+1/2}}{h_1}=HR_{\widetilde{\alpha}}^1, \tag{A.23}$$

$$\frac{u_s^{1+1/2}}{h_1}=H\widetilde{f}^1, \tag{A.24}$$

from (A.17) and (A.19), respectively. For the gas concentration conservation equations we find (*cf.* (3.68))

$$\delta\left(\frac{\partial\widetilde{C}^1}{\partial\tau}+\frac{\mathcal{F}_g^{1+1/2}-q_{\widetilde{C}}^{\mathrm{in}}}{h_1}\right)=HR_{\widetilde{C}}^1, \tag{A.25}$$

where $q_{\widetilde{C}}^{\mathrm{in}}$ is the inlet flux of $\widetilde{C}$.

Similarly, at the surface of the pellet bed (*cf.* (3.70)–(3.73) and (3.76))

$$H' = u_s^{n+1/2}, \tag{A.26}$$

$$\frac{\partial \widetilde{\alpha}^n}{\partial \tau} - \frac{\mathcal{F}_s^{n-1/2}}{h_n} = HR_{\widetilde{\alpha}}^n, \tag{A.27}$$

$$\delta\left(\frac{\partial \widetilde{C}^n}{\partial \tau} + \frac{q_{\widetilde{C}}^{\text{out}} - \mathcal{F}_g^{n-1/2}}{h_n}\right) = HR_{\widetilde{C}}^n. \tag{A.28}$$

A.1.1 Non-uniform grids

In deriving the discretized equations for our system, we allowed for a non-uniform grid by allowing the step-size between vertices to vary. This flexibility is crucial because we expect a sharp boundary layer at $\xi = 1$ for some parameter regimes. Using a uniform grid to capture these layers would be computationally prohibitive. To address this challenge, we employ a Shishkin grid [163, 164, 167, 168], a well-known method for generating piecewise uniform grids.

A Shishkin grid divides the domain into two regions, $[0, 1-\sigma]$ and $[1-\sigma, 1]$ (assuming the boundary layer is at $\xi = 1$), with $n/2$ uniformly spaced points in each sub-domain. The point $1-\sigma$ is known as the grid transition point; we take σ to be [163]

$$\sigma = \min\left\{\frac{2}{\text{Pe}}\log n,\ \frac{1}{2}\right\}. \tag{A.29}$$

For small values of Pe, we obtain a globally uniform grid since no boundary layer is expected. As Pe increases, σ decreases and the grid transition point moves closer to 1, allowing the grid to resolve the boundary layer behaviour. Although scalings of σ other than (A.29) are possible provided certain necessary conditions are satisfied [167], this choice is the simplest.

The coarse grid, in the interval $[0, 1-\sigma]$, has uniform spacing

$$h = \frac{2(1-\sigma)}{n}, \tag{A.30}$$

bounded by

$$\frac{1}{n} \leq h \leq \frac{2}{n}, \tag{A.31}$$

while the fine grid, in the interval $[1-\sigma, 1]$, which resolves the boundary layer,

has spacing

$$h = \frac{2\sigma}{n}, \tag{A.32}$$

$$= \frac{4}{\mathrm{Pe}}\left(\frac{\log n}{n}\right), \tag{A.33}$$

$$\ll \frac{1}{\mathrm{Pe}}. \tag{A.34}$$

One advantage of using a Shishkin grid is that the boundary layer can be resolved with a constant number of points, independent of the size of Pe, ensuring that computation time does not scale with Pe. However, since the grid is piecewise uniform, it is not differentiable at the transition point $1-\sigma$, which often makes this region the most challenging to handle when using a Shishkin grid.

A.1.2 Convergence

We now test the convergence of our numerical implementation. The test is performed using the parameter values given in Table 3.2, except we take $\mathrm{Pe} = 1000$ and solve to a dimensionless time of 3.0. We use a large Pe value to create a sharp boundary layer at $\xi = 1$. The maximum time of 3.0 is chosen to focus on testing our spatial discretization, rather than the tolerances of the time integrations. Additionally, if we were to simulate up to the quartz consumption time, no quartz would remain, and most of the gas would have either reacted or escaped through the top of the bed of pellets, which would be a poor case for testing convergence.

We first compute the solution using $n = 5000$ spatial points, and we will calculate the error of other solutions relative to this reference solution. The L_1 norm is commonly used to measure error for conservation law equations [166]. We compute the error as

$$E_1(n) = \left\| Q^n(\xi) - Q^{5000}(\xi) \right\|_{L_1}, \tag{A.35}$$

$$= \int_0^1 \left| Q^n(\xi) - Q^{5000}(\xi) \right| \mathrm{d}\xi, \tag{A.36}$$

where Q denotes any of the variables, and $Q^n(\xi)$ is the linear interpolation of the solution that we obtain with n spatial points. The integral is discretized using the trapezoid rule with 10^4 points. The results are shown in Figure A.2.

We observe linear convergence for each variable. This result is expected, as the discretization for u_s in (A.19) is first-order, and we employ an upwinding scheme

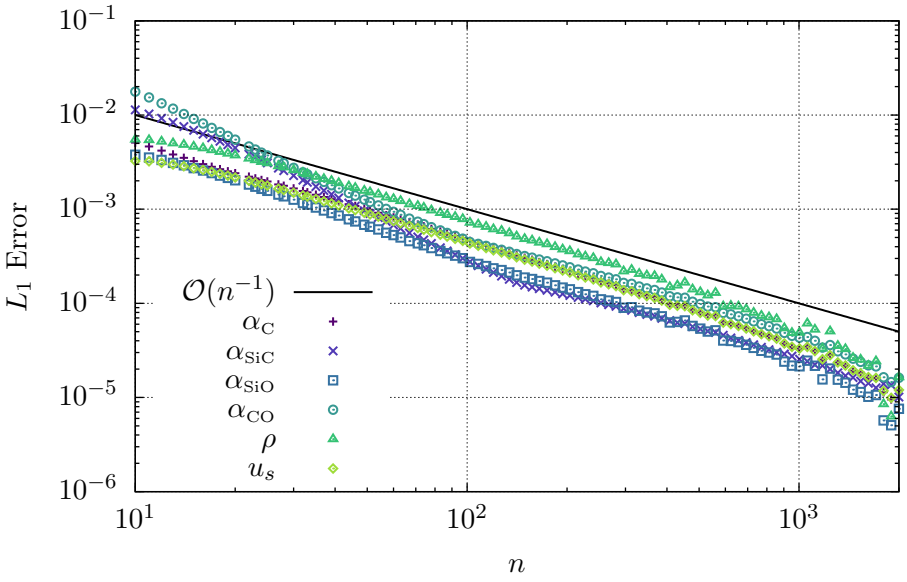

Figure A.2: Convergence of L_1 error of the numerical solution.

for the solid flux in (A.18). Furthermore, in a vertex centered scheme with a non-differentiable grid, convergence is expected to be worse than quadratic but not worse than linear [164].

A.2 Jacobian sparsity

The numerical system has $10n+1$ equations and unknowns and therefore the Jacobian has dimension $(10n+1) \times (10n+1)$. However, the Jacobian is composed mostly of blocks of (tri)diagonal matrices, as shown in Figure A.3. Therefore, by exploiting the sparsity we should expect significant speed-up of the numerical solution. In addition to using a sparse linear solver, we also more efficiently compute the Jacobian numerically than the naive approach.

For a function $\mathbf{f}(x_1, \cdots, x_m)$ the Jacobian is given by

$$\mathbf{J} = \begin{bmatrix} \frac{\partial \mathbf{f}}{\partial x_1} & \cdots & \frac{\partial \mathbf{f}}{\partial x_m} \end{bmatrix}, \tag{A.37}$$

which we approximate with finite difference as

$$\mathbf{J} = \frac{1}{\epsilon} \Big[\mathbf{f}(\mathbf{x} + \epsilon\, \mathbf{e}_1) - \mathbf{f}(\mathbf{x}) \quad \cdots \quad \mathbf{f}(\mathbf{x} + \epsilon\, \mathbf{e}_m) - \mathbf{f}(\mathbf{x}) \Big]. \tag{A.38}$$

Calculating $\mathbf{J}$ requires $m+1$ evaluations of $\mathbf{f}$ (or more for higher-order schemes). For large m or expensive $\mathbf{f}$ this can be very costly. However, for sparse $\mathbf{J}$ we can exploit

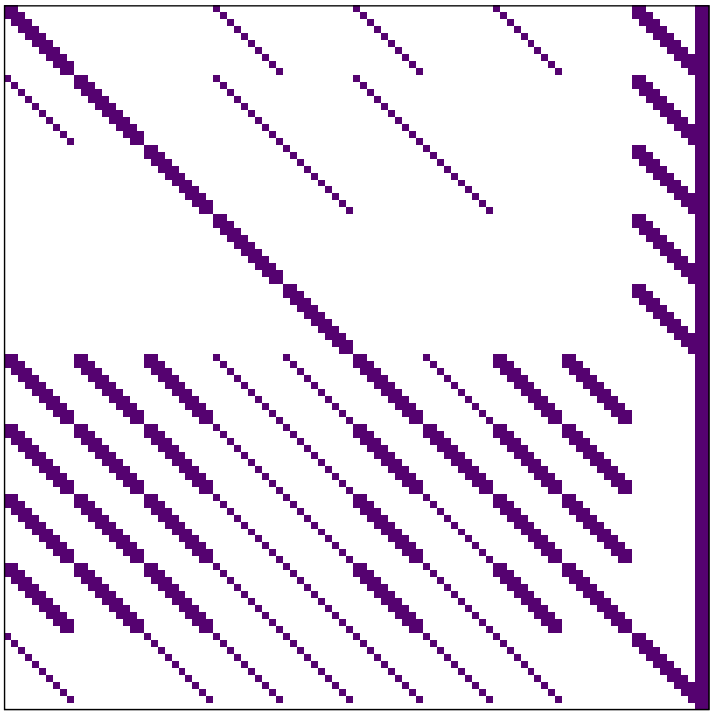

Figure A.3: Sparsity of the Jacobian. A purple square represents a non-zero value ($n = 10$).

the sparsity in order to approximate the Jacobian more efficiently.

First proposed by Curtis, Powell, and Reid [169], we partition the columns of $\mathbf{J}$ into subsets, referred to as colours, such that no two columns in a subset have a non-zero element in a common row. We then only need to evaluate $\mathbf{f}$ once per subset to determine all of the columns of $\mathbf{J}$ in that subset. We highlight the partitioning in Figure A.4 for a matrix with tridiagonal sparsity. The ith column and the $(i+3)$th column of a tridiagonal matrix are orthogonal. Therefore, we only need to evaluate

$$\mathbf{f}\left(\mathbf{x} + \epsilon \sum_i \mathbf{e}_{3i+k}\right) \tag{A.39}$$

for $k = 0, 1, 2$, as well as $\mathbf{f}(\mathbf{x})$. The columns are then separated again to fully determine $\mathbf{J}$. In the case of tridiagonal sparsity, we reduce the number of $\mathbf{f}$ calls from $m + 1$ to 4.

Actually determining how to partition the columns is non-trivial. The partitioning is cast as a graph colouring problem [170], which is NP-hard, but heuristics exist for efficient solutions [171]. Similar methods also exist for efficiently computing the Hessian [172, 173]. For a more complete description of matrix colouring see [174],

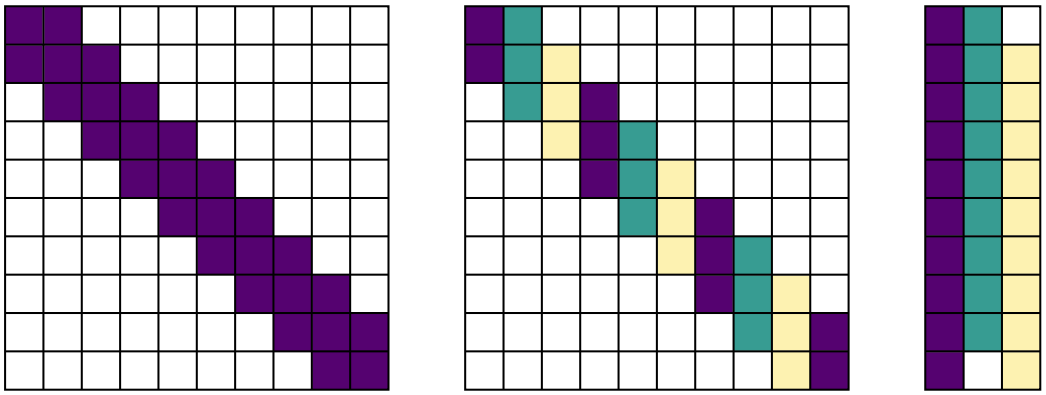

(a) (b) (c)

Figure A.4: (a) Tridiagonal sparsity. (b) Colour the columns so that all columns of a colour are mutually orthogonal. (c) Combine columns of a given colour into a single column to reduce the dimensionality.

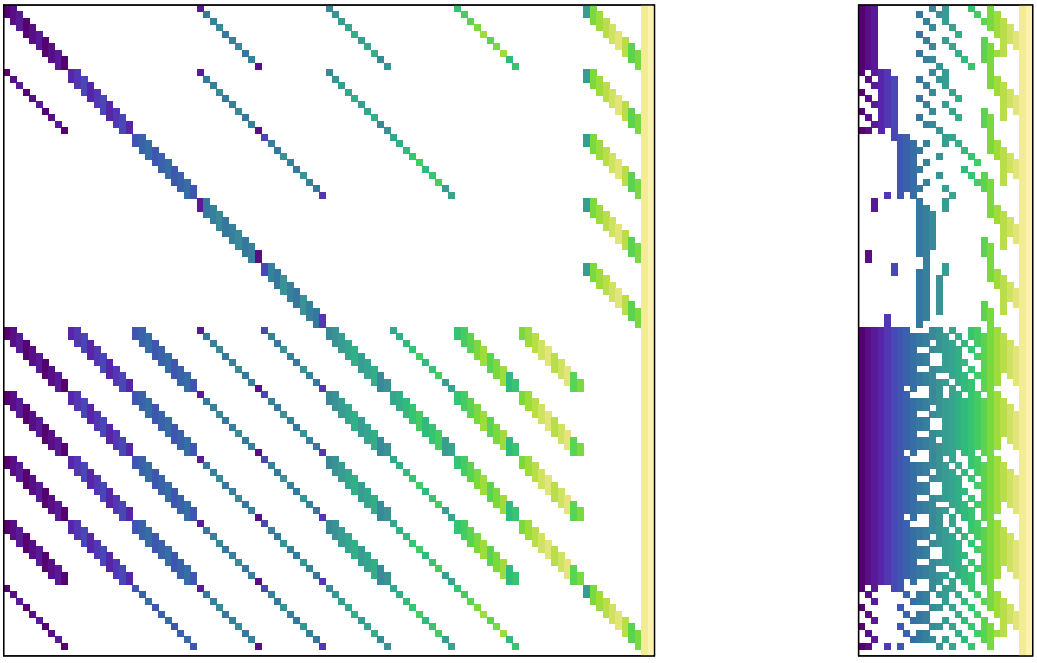

(a) (b)

Figure A.5: (a) Column colours found by `matrix_colors` such that all columns of a colour are mutually orthogonal. (b) 27 combined columns.

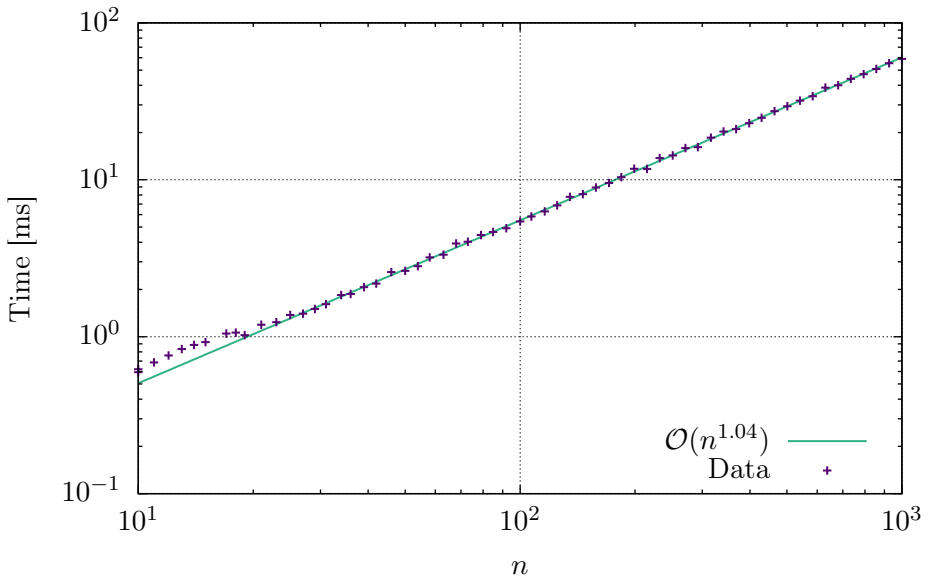

Figure A.6: Scaling of the computation time of the matrix colouring problem (median time of 100 runs).

and for graph colouring problems in general see [175].

We now turn to colouring the Jacobian for our problem. A clear lower bound for the number of function calls required is one more than the maximum number of non-zero elements in a row of the Jacobian. In our case, the maximum number of non-zero entries in a row is 25, and so at least 26 function calls are required to approximate the Jacobian. The `matrix_colors` function in `SparseDiffTools.jl` finds a solution to our colouring problem with 27 colours (Figure A.5). Thus, we reduce the number of function calls from $10n + 2$ to 28 (for $n \geq 6$). Furthermore, solving the matrix colouring problem is computationally cheap and is only required once; the colours are reused at each time-step. In Figure A.6 we show the median time of 100 runs of solving our matrix colouring problem. The time grows linearly with n. For $n = 1000$ the solution takes less than 100 ms.

In Figure A.7 we show the time in seconds to compute the complete solution using a dense Jacobian and dense linear solver, as well as finding the matrix colours and exploiting the sparsity of the Jacobian by using a sparse linear solver. Over the entire interval tested, $10 \leq n \leq 1000$, the sparse setup outperforms the dense solution in terms of speed. Even for smaller problems, the added overhead of solving the matrix colouring problem and using a sparse solver does not slow down the overall solution. Predicting the time complexity for problems like our system is challenging, but our results show that the dense solution scales as $\mathcal{O}(n^{2.57})$, while the sparse solution scales

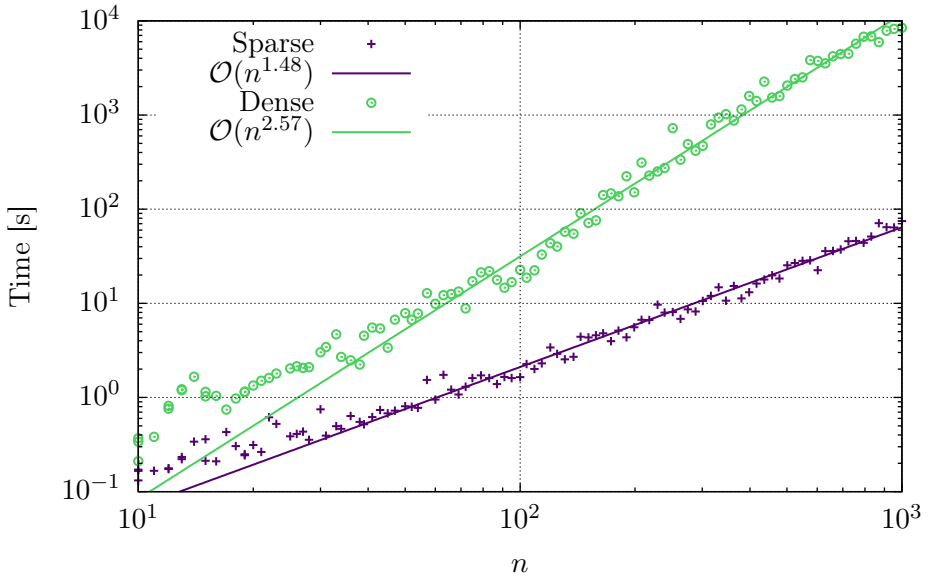

Figure A.7: Time complexity of dense and sparse solvers.

more efficiently at $\mathcal{O}(n^{1.48})$. Notably, for problems with $n = 1000$, the sparse solver, which also takes advantage of the matrix colouring, is more than 100 times faster than the dense solution!

References

[1] B. Metherall, C. J. W. Breward, C. P. Please, J. M. Oliver, and B. M. Sloman, "Modelling the reduction of quartz in a quartz–carbon pellet", *Journal of Engineering Mathematics*, vol. 141, no. 1, 2023. DOI: 10.1007/s10665-023-10277-4.

[2] J. Andrews, A. Azemar, A. Bhattacharya, C. Egan, A. Lacey, B. Metherall, and N. Ryan, "Mathematical modelling of a silicon carbide (SiC) pilot furnace", *Mathematics in Industry Reports*, 2024. DOI: 10.33774/miir-2024-54jzl.

[3] A. A. Yaroshevsky, "Abundances of chemical elements in the Earth's crust", *Geochemistry International*, vol. 44, no. 1, 2006. DOI: 10.1134/S001670290601006X.

[4] A. Schei, J. K. Tuset, and H. Tveit, *Production of High Silicon Alloys*. Trondheim, Norway: Tapir Trondheim, 1998.

[5] E. Scheepers, Y. Yang, A. T. Adema, R. Boom, and M. A. Reuter, "Process modeling and optimization of a submerged arc furnace for phosphorus production", *Metallurgical and Materials Transactions B*, vol. 41, no. 5, 2010. DOI: 10.1007/s11663-010-9403-3.

[6] J. Kunze and R. Degel, "New trends in submerged arc furnace technology", in *Proceedings of the Tenth International Ferroalloy Congress*, 2004. URL: https://www.pyro.co.za/InfaconX/050.pdf.

[7] A. M. Valderhaug, "Modelling and control of submerged-arc ferrosilicon furnaces", PhD thesis, The Norwegian Institute of Technology, Trondheim, Norway, 1992. URL: http://hdl.handle.net/11250/260770.

[8] E. K. Luckins, "Mathematical modelling of electrical, thermal, and chemical processes occurring within a silicon furnace", PhD thesis, University of Oxford,

Oxford, UK, 2021. URL: https://ora.ox.ac.uk/objects/uuid:ca50df39-3887-438c-8f54-1221c81cd92d.

[9] T. Hannesson, *The Si process drawings*, Elkem, Iceland, 2016. URL: https://www.elkem.is/globalassets/iceland/si-process.pdf.

[10] K. Wiik, "Kinetics of reactions between silica and carbon", PhD thesis, The Norwegian Institute of Technology, Trondheim, Norway, 1990. URL: http://hdl.handle.net/11250/2396774.

[11] S. Halvorsen, "A unidimensional dynamic model for the (ferro) silicon process", in *Electric Furnace Conference Proceedings*, vol. 50, 1992.

[12] M. Kadkhodabeigi, H. Tveit, and S. T. Johansen, "Modelling the tapping process in submerged arc furnaces used in high silicon alloys production", *Iron and Steel Institute of Japan International*, vol. 51, no. 2, 2011. DOI: 10.2355/isijinternational.51.193.

[13] E. Myrhaug, J. Tuset, and H. Tveit, "Reaction mechanisms of charcoal and coke in the silicon process", in *Proceedings of the Tenth International Ferroalloy Congress*, 2004. URL: https://www.pyro.co.za/InfaconX/007.pdf.

[14] R. González-Fariña, "Modelling the mechanisms of microsilica particle formation and growth", PhD thesis, University of Oxford, Oxford, UK, 2020. URL: https://ora.ox.ac.uk/objects/uuid:df016039-4c40-43ca-91a6-ffe0575aae77.

[15] R. Alizadeh, E. Jamshidi, and G. Zhang, "Transformation of methane to synthesis gas over metal oxides without using catalyst", *Journal of Natural Gas Chemistry*, vol. 18, no. 2, 2009. DOI: 10.1016/S1003-9953(08)60105-X.

[16] H. Lindgaard, "High temperature decomposition of methane on quartz pellets", Master's thesis, Norwegian University of Science and Technology, Trondheim, Norway, 2015. URL: http://hdl.handle.net/11250/2352173.

[17] H. Ale Ebrahim and E. Jamshidi, "Kinetic study of zinc oxide reduction by methane", *Transactions of the Institution of Chemical Engineers*, vol. 79, no. 1, 2001. DOI: 10.1205/026387601528534.

[18] O. Ostrovski and G. Zhang, "Reduction and carburization of metal oxides by methane-containing gas", *American Institute of Chemical Engineers Journal*, vol. 52, no. 1, 2006. DOI: 10.1002/aic.10628.

[19] B. Monsen, L. Kolbeinsen, S. Prytz, V. Myrvågnes, and K. Tang, "Possible use of natural gas for silicon or ferrosilicon production", in *Proceedings of the Thirteenth International Ferroalloy Congress*, 2013. URL: https://www.researchgate.net/profile/Leiv-Kolbeinsen/publication/255960793_Possible_Use_of_Natural_Gas_For_Silicon_or_Ferrosilicon_Production/links/54427fae0cf2e6f0c0f93118/Possible-Use-of-Natural-Gas-For-Silicon-or-Ferrosilicon-Production.pdf.

[20] M. Ksiazek, M. Tangstad, H. Dalaker, and E. Ringdalen, "Reduction of SiO_2 to SiC using natural gas", *Metallurgical and Materials Transactions E*, vol. 1E, no. 3, 2014. DOI: 10.1007/s40553-014-0027-4.

[21] F. Li, "SiC production using SiO_2 and C agglomerates", PhD thesis, Norwegian University of Science and Technology, Trondheim, Norway, 2017. URL: http://hdl.handle.net/11250/2465202.

[22] J. G. Lee, P. D. Miller, and I. B. Cutler, "Carbothermal reduction of silica", in *Reactivity of Solids*, New York: Springer, 1977. DOI: 10.1007/978-1-4684-2340-2_102.

[23] A. Agarwal and U. Pal, "Influence of pellet composition and structure on carbothermic reduction of silica", *Metallurgical and Materials Transactions B*, vol. 30, no. 2, 1999. DOI: 10.1007/s11663-999-0059-9.

[24] J. J. Biernacki and G. P. Wotzak, "Thermogravimetric study of the C + SiO_2 reaction", *Journal of Thermal Analysis*, vol. 39, no. 5, 1989. DOI: 10.1007/BF01912940.

[25] J. L. Blumenthal, M. J. Santy, and E. A. Burns, "Kinetic studies of high-temperature carbon-silica reactions in charred silica-reinforced phenolic resins", *American Institute of Aeronautics and Astronautics Journal*, vol. 4, no. 6, 1966. DOI: 10.2514/3.3603.

[26] J. B. Henderson and M. R. Tant, "A study of the kinetics of high-temperature carbon-silica reactions in an ablative polymer composite", *Polymer Composites*, vol. 4, no. 4, 1983. DOI: 10.1002/pc.750040408.

[27] P. Kennedy and B. North, "The production of fine silicon carbide powder by the reaction of gaseous silicon monoxide with particulate carbon", *Proceedings of the British Ceramic Society*, no. 33, 1983.

[28] S. E. Khalafalla and L. A. Haas, "Kinetics of carbothermal reduction of quartz under vacuum", *Journal of the American Ceramic Society*, vol. 55, no. 8, 1972. DOI: 10.1111/j.1151-2916.1972.tb11324.x.

[29] N. Klinger, E. L. Strauss, and K. L. Komarek, "Reactions between silica and graphite", *Journal of the American Ceramic Society*, vol. 49, no. 7, 1966. DOI: 10.1111/j.1151-2916.1966.tb13287.x.

[30] J. G. Lee and I. B. Cutler, "Formation of silicon carbide from rice hulls", *American Ceramic Society Bulletin*, vol. 54, no. 2, 1975.

[31] P. D. Miller, J. G. Lee, and I. B. Cutler, "The reduction of silica with carbon and silicon carbide", *Journal of the American Ceramic Society*, vol. 62, no. 3–4, 1979. DOI: 10.1111/j.1151-2916.1979.tb19041.x.

[32] B. Ozturk and R. J. Fruehan, "The rate of formation of SiO by the reaction of CO or H_2 with silica and silicate slags", *Metallurgical Transactions B*, vol. 16, no. 4, 1985. DOI: 10.1007/BF02667516.

[33] T. Shimoo, F. Mizutaki, S. Ando, and H. Kimura, "Mechanism of formation of SiC by reaction of SiO with graphite and CO", *Journal of the Japan Institute of Metals*, vol. 52, no. 3, 1988. DOI: 10.2320/jinstmet1952.52.3_279.

[34] F. K. van Dijen and R. Metselaar, "The chemistry of the carbothermal synthesis of β-SiC: Reaction mechanism, reaction rate and grain growth", *Journal of the European Ceramic Society*, vol. 7, no. 3, 1991. DOI: 10.1016/0955-2219(91)90035-X.

[35] A. W. Weimer, K. J. Nilsen, G. A. Cochran, and R. P. Roach, "Kinetics of carbothermal reduction synthesis of beta silicon carbide", *American Institute of Chemical Engineers Journal*, vol. 39, no. 3, 1993. DOI: 10.1002/aic.690390311.

[36] I. Bjerle, F. Xu, and Z. Ye, "Useful experimental technique for the study of heterogeneous reactions", *Chemical Engineering & Technology*, vol. 15, no. 3, 1992. DOI: 10.1002/ceat.270150303.

[37] S. Yagi and D. Kunii, "Studies on combustion of carbon particles in flames and fluidized beds", *Symposium (International) on Combustion*, vol. 5, no. 1, 1955. DOI: 10.1016/S0082-0784(55)80033-1.

[38] F. Li, M. Tangstad, and E. Ringdalen, "Carbothermal reduction of quartz and carbon pellets at elevated temperatures", *Metallurgical and Materials Transactions B*, vol. 49B, no. 3, 2018. DOI: 10.1007/s11663-018-1195-x.

[39] F. Li, M. Tangstad, and I. Solheim, "Quartz and carbon black pellets for silicon production", in *Proceedings of the Fourteenth International Ferroalloy Congress*, 2015. URL: https://www.researchgate.net/profile/Fei-Li-65/publication/313987298_Quartz_and_Carbon_Black_Pellets_for_Silicon_Production/links/58b5530caca272b99390f447/Quartz-and-Carbon-Black-Pellets-for-Silicon-Production.pdf.

[40] F. Li and M. Tangstad, "Use of agglomerated raw materials in Si production", in *Silicon for the Chemical and Solar Industry XIII*, 2016. URL: https://www.ntnu.no/trykk/publikasjoner/Silicon%20for%20the%20chemical%20and%20solar%20industry%20XIII/HTML/files/assets/common/downloads/page0267.pdf.

[41] F. Li and M. Tangstad, "Carbothermal reduction of quartz with carbon from natural gas", *Metallurgical and Materials Transactions B*, vol. 48B, no. 2, 2017. DOI: 10.1007/s11663-016-0887-3.

[42] B. M. Sloman, "Mathematical modelling of silicon furnaces", PhD thesis, University of Oxford, Oxford, UK, 2018. URL: https://ora.ox.ac.uk/objects/uuid:3d43921c-078a-4390-a943-c761e750a9ea.

[43] B. M. Sloman, C. P. Please, R. A. Van Gorder, A. M. Valderhaug, R. G. Birkeland, and H. Wegge, "A heat and mass transfer model of a silicon pilot furnace", *Metallurgical and Materials Transactions B*, vol. 48, no. 5, 2017. DOI: 10.1007/s11663-017-1052-3.

[44] B. M. Sloman, C. P. Please, and R. A. Van Gorder, "Asymptotic analysis of a silicon furnace model", *SIAM Journal on Applied Mathematics*, vol. 78, no. 2, 2018. DOI: 10.1137/17m1122335.

[45] B. M. Sloman, C. P. Please, and R. A. Van Gorder, "Homogenization of a shrinking core model for gas–solid reactions in granular particles", *SIAM Journal on Applied Mathematics*, vol. 79, no. 1, 2019. DOI: 10.1137/17M1159634.

[46] B. M. Sloman, C. P. Please, and R. A. Van Gorder, "Melting and dripping of a heated material with temperature-dependent viscosity in a thin vertical tube", *Journal of Fluid Mechanics*, vol. 905, 2020. DOI: 10.1017/jfm.2020.727.

[47] N. E. Kamfjord, "Mass and energy balances of the silicon process: Improved emission standards", PhD thesis, Norwegian University of Science and Technology, Trondheim, Norway, 2012. URL: https://ntnuopen.ntnu.no/ntnu-xmlui/bitstream/handle/11250/249043/549454_FULLTEXT02.pdf.

[48] B. F. Lund, "Rigorous simulation models for improved process operation", PhD thesis, Norwegian University of Science and Technology, Trondheim, Norway, 2005.

[49] M. Takla, N. Kamfjord, H. Tveit, and S. Kjelstrup, "Energy and exergy analysis of the silicon production process", *Energy*, vol. 58, 2013. DOI: 10.1016/j.energy.2013.04.051.

[50] P. Fidjestol and M. Dastol, "The history of silica fume in concrete from novelty to key ingredient in high performance concrete", in *Proceedings of the Congresso Brasileiro do Concreto*, 2008. URL: http://www.ibracon.org.br/eventos/50cbc/plenarias/per_fidjestol.pdf.

[51] D. T. Mueller and R. L. Dillenbeck, "The versatility of silica fume as an oilwell cement admixture", in *SPE Oklahoma City Oil and Gas Symposium*, 1991. DOI: 10.2118/21688-MS.

[52] R. González-Fariña, A. Münch, J. M. Oliver, and R. A. Van Gorder, "Modeling microsilica particle formation and growth due to the combustion reaction of silicon monoxide with oxygen", *SIAM Journal on Applied Mathematics*, vol. 80, no. 2, 2020. DOI: 10.1137/19m1287080.

[53] C. W. Söderberg, "Electrode for electric furnaces and process for manufacturing the same", 1,440,724, 1923. URL: https://patentimages.storage.googleapis.com/87/af/9c/f05dace9cc857a/US1440724.pdf.

[54] R. Innvaer and L. Olsen, "Practical use of mathematical models for Soderberg electrodes", in *Proceedings of the AIME Conference*, 1980.

[55] C. Ray, P. Sahoo, and S. Rao, "Electrode management—investigation into soft breaks at 48MVA FeCr closed furnace", in *Proceedings of the Eleventh International Ferroalloy Congress*, 2007. URL: https://www.pyrometallurgy.co.za/InfaconXI/741-Ray.pdf.

[56] P. Wilkinson, S. Ganguly, P. Williams, and L. Jensen, "Impact of electrode paste on Soderberg electrode performance", in *Proceedings of the Ninth International Ferroalloy Congress*, 2001. URL: https://www.pyro.co.za/InfaconIX/510-Wilkinson.pdf.

[57] L. Olsen, A. Arnesen, I. Bencze, and R. Innvaer, "Temperature distribution in Soderberg electrodes", in *Proceedings of the Seventh International Congress of Electro-heat*, 1972.

[58] A. Skjeldestad, M. Tangstad, L. Lindstad, and B. Larsen, "Temperature profiles in Søderberg electrodes", in *Proceedings of the Fourteenth International Ferroalloy Congress*, 2015. URL: https://www.pyro.co.za/InfaconXIV/327-Skjeldestad.pdf.

[59] T. Bergstrøm, S. Cowley, A. C. Fowler, and P. E. Seward, "Segregation of carbon paste in a smelting electrode", *IMA Journal of Applied Mathematics*, vol. 43, no. 1, 1989. DOI: 10.1093/imamat/43.1.83.

[60] A. Fitt and P. Howell, "The manufacture of continuous smelting electrodes from carbon–paste briquettes", *Journal of Engineering Mathematics*, vol. 33, no. 4, 1998. DOI: 10.1023/a:1004317014216.

[61] A. A. Lacey, "Thermal runaway in a non-local problem modelling Ohmic heating. Part II: General proof of blow-up and asymptotics of runaway", *European Journal of Applied Mathematics*, vol. 6, no. 3, 1995. DOI: 10.1017/s0956792500001807.

[62] R. A. Van Gorder, A. Kamilova, R. G. Birkeland, and A. L. Krause, "Locating the baking isotherm in a Søderberg electrode: Analysis of a moving thermistor model", *SIAM Journal on Applied Mathematics*, vol. 81, no. 4, 2021. DOI: 10.1137/20m1314276.

[63] A. A. Kamilova, "Modelling and analysis of paste flow in high performance Soderberg electrodes", PhD thesis, University of Oxford, Oxford, UK, 2021. URL: https://ora.ox.ac.uk/objects/uuid:fe65fdfa-3765-4df0-a47b-47d499da0086.

[64] G. Saevarsdottir and J. Bakken, "Current distribution in submerged arc furnaces for silicon metal/ferrosilicon production", in *Proceedings of the Twelfth International Ferroalloy Congress*, 2010. URL: https://pyrometallurgy.co.za/InfaconXII/717-Saevarsdottir.pdf.

[65] A. Bermúdez, M. C. Muñiz, F. Pena, and J. Bullón, "Numerical computation of the electromagnetic field in the electrodes of a three-phase arc furnace", *International Journal for Numerical Methods in Engineering*, vol. 46, no. 5, 1999. DOI: 10.1002/(sici)1097-0207(19991020)46:5<649::aid-nme664>3.0.co;2-c.

[66] M. Dhainaut, "Simulation of the electric field in a submerged arc furnace", in *Proceedings of the Tenth International Ferroalloy Congress*, 2004. URL: https://www.pyrometallurgy.co.za/InfaconX/079.pdf.

[67] Y. Tesfahunegn, T. Magnusson, M. Tangstad, and G. Saevarsdottir, "Effect of electrode shape on the current distribution in submerged arc furnaces for silicon production—a modelling approach", *Journal of the Southern African Institute of Mining and Metallurgy*, vol. 118, no. 6, 2018.

[68] Y. A. Tesfahunegn, T. Magnusson, M. Tangstad, and G. Saevarsdottir, "Comparative study of AC and DC solvers based on current and power distributions in a submerged arc furnace", *Metallurgical and Materials Transactions B*, vol. 51, no. 2, 2020. DOI: 10.1007/s11663-020-01794-z.

[69] J. Alexis, M. Ramirez, G. Trapaga, and P. Jönsson, "Modeling of a DC electric arc furnace—heat transfer from the arc", *Iron and Steel Institute of Japan International*, vol. 40, no. 11, 2000. DOI: 10.2355/isijinternational.40.1089.

[70] G. A. Saevarsdottir, "High current AC arcs in silicon and ferrosilicon furnaces.", PhD thesis, Norwegian University of Science and Technology, Trondheim, Norway, 2002.

[71] A. Westermoen, "Modelling of dynamic arc behaviour in a plasma reactor", PhD thesis, Norwegian University of Science and Technology, Trondheim, Norway, 2007. URL: http://hdl.handle.net/11250/248693.

[72] E. Luckins, C. J. W. Breward, I. M. Griffiths, and Z. Wilmott, "Homogenisation problems in reactive decontamination", *European Journal of Applied Mathematics*, vol. 31, no. 5, 2020. DOI: 10.1017/S0956792519000263.

[73] E. K. Luckins, J. M. Oliver, C. P. Please, B. M. Sloman, and R. A. Van Gorder, "Homogenised model for the electrical current distribution within a submerged arc furnace for silicon production", *European Journal of Applied Mathematics*, vol. 33, no. 5, 2022. DOI: 10.1017/S0956792521000243.

[74] E. K. Luckins, J. M. Oliver, C. P. Please, B. M. Sloman, A. M. Valderhaug, and R. A. Van Gorder, "Modelling alternating current effects in a submerged arc furnace", *IMA Journal of Applied Mathematics*, vol. 87, no. 3, 2022. DOI: 10.1093/imamat/hxac012.

[75] E. K. Luckins, J. M. Oliver, C. P. Please, B. M. Sloman, and R. A. Van Gorder, "Modelling and analysis of an endothermic reacting counter-current flow", *Journal of Fluid Mechanics*, vol. 949, 2022. DOI: 10.1017/jfm.2022.702.

[76] R. W. Winters and R. E. Davies, "The role of countercurrent mechanisms in urine concentration: A review", *Annals of Internal Medicine*, vol. 54, no. 4, 1961. DOI: 10.7326/0003-4819-54-4-810.

[77] J. Merchuk, Y. Rosenblat, and I. Berzin, "Fluid flow and mass transfer in a counter-current gas–liquid inclined tubes photo-bioreactor", *Chemical Engineering Science*, vol. 62, no. 24, 2007. DOI: 10.1016/j.ces.2007.08.058.

[78] I. A. Sutherland, "Recent progress on the industrial scale-up of counter-current chromatography", *Journal of Chromatography A*, vol. 1151, no. 1–2, 2007. DOI: 10.1016/j.chroma.2007.01.143.

[79] J. W. Mitchell and G. E. Myers, "An analytical model of the counter-current heat exchange phenomena", *Biophysical Journal*, vol. 8, no. 8, 1968. DOI: 10.1016/s0006-3495(68)86527-0.

[80] Deendarlianto, T. Höhne, D. Lucas, and K. Vierow, "Gas–liquid countercurrent two-phase flow in a PWR hot leg: A comprehensive research review", *Nuclear Engineering and Design*, vol. 243, 2012. DOI: 10.1016/j.nucengdes.2011.11.015.

[81] H. Byrne and J. Norbury, "Stable solutions for a catalytic converter", *SIAM Journal on Applied Mathematics*, vol. 54, no. 3, 1994. DOI: 10.1137/s0036139991217872.

[82] H. Byrne and J. Norbury, "The effect of solid conversion on travelling combustion waves in porous media", *Journal of Engineering Mathematics*, vol. 32, no. 4, 1997. DOI: 10.1023/a:1004261121570.

[83] R.-J. Koopmans, J. S. Shrimpton, G. T. Roberts, and A. J. Musker, "A one-dimensional multicomponent two-fluid model of a reacting packed bed including mass, momentum and energy interphase transfer", *International Journal of Multiphase Flow*, vol. 57, 2013. DOI: 10.1016/j.ijmultiphaseflow.2013.06.005.

[84] S. H. Yi, B. R. Cho, and C. H. Rhee, "Prediction of channelling caused by breakthrough of cohesive zone in blast furnace", *Ironmaking & Steelmaking*, vol. 25, no. 4, 1998. URL: https://www.proquest.com/docview/236453340.

[85] A. Shajii and J. P. Freidberg, "Theory of low Mach number compressible flow in a channel", *Journal of Fluid Mechanics*, vol. 313, 1996. DOI: 10.1017/s0022112096002157.

[86] H. M. Kvamsdal, G. Haugen, and H. F. Svendsen, "Flue-gas cooling in post-combustion capture plants", *Chemical Engineering Research and Design*, vol. 89, no. 9, 2011. DOI: 10.1016/j.cherd.2011.02.029.

[87] A. A. Rostami, A. S. Mujumdar, and N. Saniei, "Flow and heat transfer for gas flowing in microchannels: A review", *Heat and Mass Transfer*, vol. 38, no. 4–5, 2002. DOI: 10.1007/s002310100247.

[88] R. J. Cooper, J. Billingham, and A. C. King, "Flow and reaction in solid oxide fuel cells", *Journal of Fluid Mechanics*, vol. 411, 2000. DOI: 10.1017/s0022112099008150.

[89] A. C. King, J. Billingham, and R. J. Cooper, "Performance modelling of solid oxide fuel cells", *Combustion Theory and Modelling*, vol. 5, no. 4, 2001. DOI: 10.1088/1364-7830/5/4/308.

[90] M. Shirley, "Material flow in a silicon furnace", PhD thesis, University of Oxford, Oxford, UK, 2022. URL: https://ora.ox.ac.uk/objects/uuid:f012c56d-272d-46be-b87d-cb3a9945a2d9.

[91] A. Kovács, C. J. W. Breward, K. E. Einarsrud, S. A. Halvorsen, E. Nordgård-Hansen, E. Manger, A. Münch, and J. M. Oliver, "A heat and mass transfer problem for the dissolution of an alumina particle in a cryolite bath", *International Journal of Heat and Mass Transfer*, vol. 162, 2020. DOI: 10.1016/j.ijheatmasstransfer.2020.120232.

[92] W. Nachbar, F. Williams, and S. S. Penner, "The conservation equations for independent coexistent continua and for multicomponent reacting gas mixtures", *Quarterly of Applied Mathematics*, vol. 17, no. 1, 1959. DOI: 10.1090/qam/102982.

[93] S. Whitaker, "Derivation and application of the Stefan–Maxwell equations", *Revista Mexicana De Ingeniería Química*, vol. 8, no. 3, 2009. URL: https://www.redalyc.org/pdf/620/62016349001.pdf.

[94] N. G. Cogan and J. P. Keener, "The role of the biofilm matrix in structural development", *Mathematical Medicine and Biology*, vol. 21, no. 2, 2004. DOI: 10.1093/imammb/21.2.147.

[95] J. E. F. Green, "Mathematical modelling of cell aggregation in liver tissue engineering", PhD thesis, University of Nottingham, Nottingham, UK, 2006. URL: https://www.proquest.com/dissertations-theses/mathematical-modelling-cell-aggregation-liver/docview/301699011/se-2.

[96] J. Szekely, J. W. Evans, and H. Y. Sohn, *Gas–Solid Reactions*. New York: Academic Press, Inc., 1976.

[97] J. Meija, T. B. Coplen, M. Berglund, *et al.*, "Atomic weights of the elements 2013 (IUPAC Technical Report)", *Pure and Applied Chemistry*, vol. 88, no. 3, 2016. DOI: 10.1515/pac-2015-0305.

[98] J. O. Hirschfelder, C. F. Curtiss, and R. B. Bird, *Molecular Theory of Gases and Liquids*. New York: John Wiley & Sons, Inc., 1964.

[99] R. Brun, *Introduction to reactive gas dynamics*. Oxford University Press, 2009.

[100] R. Prud'homme, *Flows of Reactive Fluids*, 1 ed., vol. 94 of *Fluid Mechanics and Its Applications*. Boston: Birkhäuser Boston, 2010. DOI: 10.1007/978-0-8176-4659-2.

[101] J. Bezanson, A. Edelman, S. Karpinski, and V. B. Shah, "Julia: A fresh approach to numerical computing", *SIAM Review*, vol. 59, no. 1, 2017. DOI: 10.1137/141000671.

[102] C. Rackauckas and Q. Nie, "DifferentialEquations.jl–A performant and feature-rich ecosystem for solving differential equations in Julia", *Journal of Open Research Software*, vol. 5, no. 1, 2017. DOI: 10.5334/jors.151.

[103] A. C. Hindmarsh, P. N. Brown, K. E. Grant, S. L. Lee, R. Serban, D. E. Shumaker, and C. S. Woodward, "SUNDIALS: Suite of nonlinear and differential/algebraic equation solvers", *ACM Transactions on Mathematical Software*, vol. 31, no. 3, 2005. DOI: 10.1145/1089014.1089020.

[104] Y. Ma, S. Gowda, R. Anantharaman, C. Laughman, V. Shah, and C. Rackauckas, *ModelingToolkit: A composable graph transformation system for equation-based modeling*, 2021. arXiv: 2103.05244.

[105] M. R. Booty and B. J. Matkowsky, "Modes of burning in filtration combustion", *European Journal of Applied Mathematics*, vol. 2, no. 1, 1991. DOI: 10.1017/S0956792500000371.

[106] R. Prud'Homme, *Évaporation et Combustion de Gouttes dans les Moteurs*. Editions Techniques de l'Ingenieur, 2009. DOI: 10.51257/a-v1-bm2521.

[107] J. Young and B. Todd, "Modelling of multi-component gas flows in capillaries and porous solids", *International Journal of Heat and Mass Transfer*, vol. 48, no. 25–26, 2005. DOI: 10.1016/j.ijheatmasstransfer.2005.07.034.

[108] C. J. W. Breward, H. M. Byrne, and C. E. Lewis, "The role of cell–cell interactions in a two-phase model for avascular tumour growth", *Journal of Mathematical Biology*, vol. 45, no. 2, 2002. DOI: 10.1007/s002850200149.

[109] C. S. Bohun and C. Breward, "Yolk dynamics in amphibian embryos", in *Proceedings of the Fields–MITACS Industrial Problems Workshop*, 2006. URL: http://miis.maths.ox.ac.uk/miis/229/1/fmipw1-3.pdf.

[110] H. F. Winstanley, M. Chapwanya, M. J. McGuinness, and A. C. Fowler, "A polymer–solvent model of biofilm growth", *Proceedings of the Royal Society A: Mathematical, Physical and Engineering Sciences*, vol. 467, no. 2129, 2010. DOI: 10.1098/rspa.2010.0327.

[111] J. R. King and J. M. Oliver, "Thin-film modelling of poroviscous free surface flows", *European Journal of Applied Mathematics*, vol. 16, no. 4, 2005. DOI: 10.1017/s095679250500584x.

[112] R. F. Katz and Y. Takei, "Consequences of viscous anisotropy in a deforming, two-phase aggregate. Part 2. Numerical solutions of the full equations", *Journal of Fluid Mechanics*, vol. 734, 2013. DOI: 10.1017/jfm.2013.483.

[113] Y. Takei and R. F. Katz, "Consequences of viscous anisotropy in a deforming, two-phase aggregate. Part 1. Governing equations and linearized analysis", *Journal of Fluid Mechanics*, vol. 734, 2013. DOI: 10.1017/jfm.2013.482.

[114] P. Howell and M. Muldoon, "Two-phase modelling of air bubbles in ice cream", *Mathematics in Industry Reports*, 2021. DOI: 10.33774/miir-2021-fb24s.

[115] A. C. Fowler, *Mathematical Models in the Applied Sciences.* Vol. 54. Cambridge University Press, 1998.

[116] D. A. Drew, "Mathematical modeling of two-phase flow.", *Technical Summary Report Wisconsin University*, 1982.

[117] D. A. Drew and S. L. Passman, *Theory of Multicomponent Fluids*, vol. 135. Springer Science & Business Media, 1999. DOI: 10.1007/b97678.

[118] C. F. Curtiss and R. B. Bird, "Multicomponent diffusion", *Industrial & Engineering Chemistry Research*, vol. 38, no. 7, 1999. DOI: 10.1021/ie9901123.

[119] L. D. Landau and E. M. Lifshitz, *Fluid Mechanics*, 2 ed., trans. by J. B. Sykes and W. H. Reid, vol. 6 of *Course of Theoretical Physics*. London: Pergamon Press, 1987.

[120] R. Clausius, "Ueber die Art der Bewegung, welche wir Wärme nennen", *Annalen Der Physik*, vol. 176, no. 3, 1857. DOI: 10.1002/andp.18571760302.

[121] A. Krönig, "Grundzüge einer Theorie der Gase", *Annalen der Physik*, vol. 175, no. 10, 1856. DOI: 10.1002/andp.18561751008.

[122] C. E. Brennen, *Fundamentals of Multiphase Flow*. Cambridge University Press, 2005.

[123] A. W. Jenike and R. Shield, "On the plastic flow of Coulomb solids beyond original failure", *Journal of Applied Mechanics*, vol. 26, no. 4, 1959. DOI: 10.1115/1.4012119.

[124] T. Nguyen, C. Brennen, and R. Sabersky, "Gravity flow of granular materials in conical hoppers", *Journal of Applied Mechanics*, vol. 46, no. 3, 1979. DOI: 10.1115/1.3424601.

[125] J. L. Finney, "Random packings and the structure of simple liquids. I. The geometry of random close packing", *Proceedings of the Royal Society of London A*, vol. 319, no. 1539, 1970. DOI: 10.1098/rspa.1970.0189.

[126] W. Jodrey and E. Tory, "Computer simulation of isotropic, homogeneous, dense random packing of equal spheres", *Powder Technology*, vol. 30, no. 2, 1981. DOI: 10.1016/0032-5910(81)80003-4.

[127] G. D. Scott and D. M. Kilgour, "The density of random close packing of spheres", *Journal of Physics D: Applied Physics*, vol. 2, no. 6, 1969. DOI: 10.1088/0022-3727/2/6/311.

[128] A. Gamba, "Random packing of equal spheres", *Nature*, vol. 256, no. 5517, 1975. DOI: 10.1038/256521c0.

[129] E. Tory, W. Jodrey, and D. Pickard, "Simulation of random sequential adsorption: Efficient methods and resolution of conflicting results", *Journal of Theoretical Biology*, vol. 102, no. 3, 1983. DOI: 10.1016/0022-5193(83)90379-X.

[130] S. Torquato, T. M. Truskett, and P. G. Debenedetti, "Is random close packing of spheres well defined?", *Physical Review Letters*, vol. 84, no. 10, 2000. DOI: 10.1103/PhysRevLett.84.2064.

[131] J. G. Berryman, "Random close packing of hard spheres and disks", *Physical Review A*, vol. 27, no. 2, 1983. DOI: 10.1103/PhysRevA.27.1053.

[132] W. S. Jodrey and E. M. Tory, "Computer simulation of close random packing of equal spheres", *Physical Review A*, vol. 32, no. 4, 1985. DOI: 10.1103/PhysRevA.32.2347.

[133] F. M. White, *Viscous Fluid Flow*, 2 ed., of *McGraw-Hill Series in Mechanical Engineering*. New York: McGraw-Hill, 1991.

[134] E. L. Cussler, *Diffusion: Mass Transfer in Fluid Systems*, 3 ed., Cambridge University Press, 2009. DOI: 10.1017/cbo9780511805134.

[135] R. B. Bird, W. E. Stewart, and E. N. Lightfoot, *Transport Phenomena*, 2 ed., John Wiley & Sons, Inc., 2002.

[136] R. M. Corless, G. H. Gonnet, D. E. G. Hare, D. J. Jeffrey, and D. E. Knuth, "On the Lambert W function", *Advances in Computational Mathematics*, vol. 5, no. 1, 1996. DOI: 10.1007/BF02124750.

[137] D. R. Jones, C. D. Perttunen, and B. E. Stuckman, "Lipschitzian optimization without the Lipschitz constant", *Journal of Optimization Theory and Applications*, vol. 79, no. 1, 1993. DOI: 10.1007/bf00941892.

[138] J. M. Gablonsky and C. T. Kelley, "A locally-biased form of the DIRECT algorithm", *Journal of Global Optimization*, vol. 21, no. 1, 2001. DOI: 10.1023/a:1017930332101.

[139] M. J. D. Powell, "The BOBYQA algorithm for bound constrained optimization without derivatives", Department of Applied Mathematics and Theoretical Physics, Cambridge University, Cambridge, UK, Tech. Rep. NA2009/06, 2009.

[140] C. Audet and W. Hare, *Derivative-Free and Blackbox Optimization*. Springer International Publishing, 2017. DOI: 10.1007/978-3-319-68913-5.

[141] A. R. Conn, K. Scheinberg, and L. N. Vicente, *Introduction to derivative-free optimization*, vol. 8 of *MPS-SIAM Series on Optimization*. SIAM, 2009. DOI: 10.1137/1.9780898718768.

[142] A. Griewank and A. Walther, *Evaluating Derivatives: Principles and Techniques of Algorithmic Differentiation*, 2 ed., SIAM, 2008. DOI: 10.1137/1.9780898717761.

[143] J. Revels, M. Lubin, and T. Papamarkou, *Forward-mode automatic differentiation in Julia*, 2016. arXiv: 1607.07892.

[144] R. L. Burden and J. D. Faires, *Numerical Analysis*, 9 ed., Brooks/Cole, Cengage Learning, 2011.

[145] C. Audet and J. E. Dennis Jr, "A pattern search filter method for nonlinear programming without derivatives", *SIAM Journal on Optimization*, vol. 14, no. 4, 2004. DOI: 10.1137/s105262340138983x.

[146] C. Audet and D. Orban, "Finding optimal algorithmic parameters using derivative-free optimization", *SIAM Journal on Optimization*, vol. 17, no. 3, 2006. DOI: 10.1137/040620886.

[147] C. Audet, "A survey on direct search methods for blackbox optimization and their applications", in *Mathematics Without Boundaries: Surveys in Interdisciplinary Research*, P. M. Pardalos and T. M. Rassias, Eds. New York, NY: Springer New York, 2014. DOI: 10.1007/978-1-4939-1124-0_2.

[148] R. Duvigneau and M. Visonneau, "Hydrodynamic design using a derivative-free method", *Structural and Multidisciplinary Optimization*, vol. 28, 2004. DOI: 10.1007/s00158-004-0414-z.

[149] K. R. Fowler, J. P. Reese, C. E. Kees, *et al.*, "Comparison of derivative-free optimization methods for groundwater supply and hydraulic capture community problems", *Advances in Water Resources*, vol. 31, no. 5, 2008. DOI: 10.1016/j.advwatres.2008.01.010.

[150] T. Levina, Y. Levin, J. McGill, and M. Nediak, "Dynamic pricing with online learning and strategic consumers: An application of the aggregating algorithm", *Operations research*, vol. 57, no. 2, 2009. DOI: 10.1287/opre.1080.0577.

[151] A. L. Marsden, M. Wang, J. E. Dennis, and P. Moin, "Optimal aeroacoustic shape design using the surrogate management framework", *Optimization and Engineering*, vol. 5, 2004. DOI: 10.1023/B:OPTE.0000033376.89159.65.

[152] R. Oeuvray and M. Bierlaire, "A new derivative-free algorithm for the medical image registration problem", *International Journal of Modelling and Simulation*, vol. 27, no. 2, 2007. DOI: 10.2316/journal.205.2007.2.205-4367.

[153] B. O. Shubert, "A sequential method seeking the global maximum of a function", *SIAM Journal on Numerical Analysis*, vol. 9, no. 3, 1972. DOI: 10.1137/0709036.

[154] S. Boyd and L. Vandenberghe, *Convex Optimization*. Cambridge University Press, 2004. DOI: 10.1017/cbo9780511804441.

[155] S. G. Johnson, *The NLopt nonlinear-optimization package*, https://github.com/stevengj/nlopt, 2007.

[156] G. A. Pavliotis and A. M. Stuart, *Multiscale methods: Averaging and homogenization*, vol. 53 of *Texts in Applied Mathematics*. Springer Science & Business Media, 2008. DOI: 10.1007/978-0-387-73829-1.

[157] E. H. Myrhaug, "Non-fossil reduction materials in the silicon process—properties and behaviour", PhD thesis, Norwegian University of Science and Technology, Trondheim, Norway, 2003. URL: https://www.osti.gov/etdeweb/biblio/20559402.

[158] K. B. Kiradjiev, C. J. W. Breward, I. Griffiths, and D. W. Schwendeman, "A homogenized model for a reactive filter", *SIAM Journal on Applied Mathematics*, vol. 81, no. 2, 2021. DOI: 10.1137/19M1305495.

[159] Y. Gu, A. Ozel, and S. Sundaresan, "Rheology of granular materials with size distributions across dense-flow regimes", *Powder Technology*, vol. 295, 2016. DOI: 10.1016/j.powtec.2016.03.035.

[160] H. Iddir and H. Arastoopour, "Modeling of multitype particle flow using the kinetic theory approach", *American Institute of Chemical Engineering Journal*, vol. 51, no. 6, 2005. DOI: 10.1002/aic.10429.

[161] H. Iddir, H. Arastoopour, and C. M. Hrenya, "Analysis of binary and ternary granular mixtures behavior using the kinetic theory approach", *Powder Technology*, vol. 151, 2005. DOI: 10.1016/j.powtec.2004.11.033.

[162] P. Zamankhan, "Kinetic theory of multicomponent dense mixtures of slightly inelastic spherical particles", *Physical Review E*, vol. 52, no. 5, 1995. DOI: 10.1103/physreve.52.4877.

[163] H.-G. Roos, M. Stynes, and L. Tobiska, *Robust Numerical Methods for Singularly Perturbed Differential Equations*, 2 ed., of *Springer Series in Computational Mathematics*. Springer Berlin Heidelberg, 2008. DOI: 10.1007/978-3-540-34467-4.

[164] W. Hundsdorfer and J. Verwer, *Numerical Solution of Time-Dependent Advection-Diffusion-Reaction Equations*, 1 ed., of *Springer Series in Computational Mathematics*. Springer Berlin Heidelberg, 2003. DOI: 10.1007/978-3-662-09017-6.

[165] P. Balland and E. Süli, "Analysis of the cell-vertex finite volume method for hyperbolic problems with variable coefficients", *SIAM Journal on Numerical Analysis*, vol. 34, no. 3, 1997. DOI: 10.1137/s0036142994264882.

[166] R. J. LeVeque, *Finite Volume Methods for Hyperbolic Problems* of *Cambridge Texts in Applied Mathematics*. Cambridge University Press, 2002.

[167] P. Farrell, A. Hegarty, J. M. Miller, E. O'Riordan, and G. I. Shishkin, *Robust Computational Techniques for Boundary Layers*. Chapman and Hall/CRC, 2000. DOI: 10.1201/9781482285727.

[168] J. J. H. Miller, E. O'Riordan, and G. I. Shishkin, *Fitted numerical methods for singular perturbation problems*. World Scientific, 1996. DOI: 10.1142/2933.

[169] A. R. Curtis, M. J. Powell, and J. K. Reid, "On the estimation of sparse Jacobian matrices", *Journal of the Institute of Mathematics and its Applications*, vol. 13, no. 1, 1974. DOI: 10.1093/imamat/13.1.117.

[170] T. F. Coleman and J. J. Moré, "Estimation of sparse Jacobian matrices and graph coloring problems", *SIAM Journal on Numerical Analysis*, vol. 20, no. 1, 1983. DOI: 10.1137/0720013.

[171] G. N. Newsam and J. D. Ramsdell, "Estimation of sparse Jacobian matrices", *SIAM Journal on Algebraic Discrete Methods*, vol. 4, no. 3, 1983. DOI: 10.1137/0604041.

[172] T. F. Coleman and J. J. Moré, "Estimation of sparse Hessian matrices and graph coloring problems", *Mathematical Programming*, vol. 28, no. 3, 1984. DOI: 10.1007/bf02612334.

[173] M. J. D. Powell and P. L. Toint, "On the estimation of sparse Hessian matrices", *SIAM Journal on Numerical Analysis*, vol. 16, no. 6, 1979. DOI: 10.1137/0716078.

[174] A. H. Gebremedhin, F. Manne, and A. Pothen, "What color is your Jacobian? Graph coloring for computing derivatives", *SIAM Review*, vol. 47, no. 4, 2005. DOI: 10.1137/s0036144504444711.

[175] B. Toft, "Colouring, stable sets and perfect graphs", in *Handbook of Combinatorics*, R. L. Graham, M. Grötschel, and L. Lovász, Eds., vol. 1, MIT Press, Cambridge, USA, 1996.